Low Dimensional Structures and Devices Group
Department of Physics and Astronomy
University of Sheffield

The University Of Sheffield.

Probing Nuclear Spin Bath Dynamics in a Self-Assembled Quantum Dot with Optically Detected NMR

Andreas Michael Waeber

Submitted for the degree of Doctor of Philosophy

Supervisors: Dr. Evgeny A. Chekhovich
Prof. Alexander I. Tartakovskii
Prof. Maurice S. Skolnick

March 2016

Abstract

This thesis describes experiments using optically detected nuclear magnetic resonance (NMR) techniques to probe and control the nuclear spin bath evolution in single self-assembled InGaAs quantum dots at large external magnetic fields. Strong non-resonant optical pumping is used to create spin bath polarisations $\gtrsim 60\%$ in dynamic nuclear polarisation. Changes of the nuclear magnetisation under resonant radio frequency (rf) excitation of nuclear Zeeman transitions are detected in low-power photoluminescence spectroscopy measurements of the hyperfine shifts of the exciton transition lines.

Continuous wave rf excitation shows strong inhomogeneous broadening of the NMR spectra in a quantum dot owing to strain-induced quadrupolar interactions. Hahn echo measurements reveal comparatively long nuclear spin phase memory times $T_{\mathrm{M,n}}^{\mathrm{HE}} \sim 1 - 4$ ms which are attributed to strong suppression of nuclear spin fluctuations due to the inhomogeneous broadening.

Further progress towards full control of the spin bath evolution is made using a set of new multiple pulse NMR sequences combining features of Hahn and solid echoes. Measurements demonstrate that spin bath coherence times of up to ~ 20 ms can be achieved within the experimental limitations of this work. Use of these NMR sequences in combination with electron/hole spin control techniques is expected to increase central spin coherence times significantly.

The equilibrium spin bath coherence properties are probed using a novel, weakly-invasive rf frequency comb NMR method. Frequency combs with varying tooth spacing are used to determine the homogeneous NMR lineshapes. The sensitivity of the homogeneous linewidths to fluctuations in the spin bath is used to probe the bath dynamics. Few-second-long spin flip-flop correlation times are revealed, demonstrating the potential of self-assembled InGaAs quantum dots to serve as a highly stable host system for spin qubits.

Acknowledgements

The success of this work would not have been possible without the help of many others. I would therefore like to take the opportunity to thank all those who contributed to the success of this work and made my time with the LDSD group such a pleasant experience.

Firstly, I am very grateful to **Sasha Tartakovskii** and **Maurice Skolnick** for making this project possible, creating such a nourishing research environment and always providing guidance and support when needed. I am particularly thankful to my supervisor **Evgeny Chekhovich**, whose mentorship and guidance over the past years were invaluable and whose work ethic and dedication have been truly inspirational. It has been a privilege to work with you.

Furthermore, I would like to thank my co-workers **Ata Ulhaq** and **Gau Ragunathan** for the fruitful collaboration and numerous thought-provoking discussions, as well as **Joe Maguire** for his contributions in the course of his SURE project.

All experimental physics requires a working setup. A big thank you to **Paul Kemp-Russell**, **Simon Dixon**, **Jonathan Mercer** and their colleagues in the workshop for their readiness to help whenever something needed to be fixed "really urgently" on a Friday afternoon... I am also indebted to **Chris Vickers**, **Phil Taylor** and **Pete Robinson** who worked tirelessly to help quench the thirst of our anadipsic cryostat systems.

My thanks also goes to the people involved in the growth and processing of the samples studied in the course of this project. One of the two samples on which the majority of the results discussed in this work were obtained was provided by our collaborators **Anthony Bennett**, **Mark Stevenson** and **Andrew Shields** from Toshiba Research Europe Ltd in Cambridge and grown and processed by **Ian Farrer**, **Jonas Nilsson** and **David Ritchie** at the Cavendish Laboratory in Cambridge. All other samples were grown by **Mark Hopkinson** or **Ed Clark** and **Nasser Babazadeh**, **Ken Kennedy** and **Ben Royall** were involved in the processing.

I would also like to thank all the past and present members of the LDSD group who have made my time here so enjoyable. In particular, I thank (in alphabetical order) **Chris Bentham**, **Zofia Bishop**, **Alistair Brash**, **Giuseppe Buonaiuto**, **Emiliano Cancellieri**, **Jasmin Chana**, **Rikki Coles**, **Qingqing Duan**, **Scott Dufferwiel**, **Branislav Dzurnak**, **Andrew Foster**, **Tillmann Godde**, **Tim Godden**, **David Hurst**, **Feng Li**, **Feng Liu**, **Tom Lyons**, **John O'Hara**, **David Price**, **John Quilter**, **Stefan Schwarz**, **Robbie Schofield**, **Danny Sercombe**, **Jasminder Sidhu**, **Lloyd Tinkler**, **Deivis Vaitiekus** and **Charles Whittaker** for countless interesting discussions and debates on a Friday evening or during a tea break. This group would not been the same without you.

I had the great fortune that my PhD position was part of the Marie Sklodowska-Curie ITN S^{3}NANO. As such I would also like to acknowledge the support of the European Union in form of funding and regular network meetings. Within the network, my special thanks goes to **Sally Greenhough**, who organised many of the events in addition to her administrative role within LDSD and the groups of **Leo Kouwenhoven** at the TU Delft and **Mete Atatüre** at the Cavendish Laboratory in Cambridge - in particular **Ed Laird**, **Fei Pei** and **Maja Cassidy** who were happy to share their vast experience with spin resonance techniques and **Ben Pingault**, **Helena Knowles** and **Dhiren Kara** who introduced me to their work on defect centres in diamond. Concerning funding I also wish to acknowledge the EPSRC which has provided the financial backbone for this project via the Programme Grant EP/J007544/1.

Last but not least, I thank my family for their support and patience throughout the entire 21 years which I have now accumulated studying in some way or other. In particular, I wish to thank my parents **Brunhilde Waeber** and **Lorenz Waeber**, and my sister **Daniela Waeber**.

Publications

Articles

A. M. Waeber, M. Hopkinson, I. Farrer, D. A. Ritchie, J. Nilsson, R. M. Stevenson, A. J. Bennett, A. J. Shields, G. Burkard, A. I. Tartakovskii, M. S. Skolnick, and E. A. Chekhovich. "Few-second-long correlation times in a quantum dot nuclear spin bath probed by frequency-comb NMR spectroscopy", *Nature Physics*, 12:688 (2016). doi:10.1038/nphys3686

P.-L. Ardelt, K. Gawarecki, K. Müller, **A. M. Waeber**, A. Bechtold, K. Oberhofer, J. M. Daniels, F. Klotz, M. Bichler, T. Kuhn, H. J. Krenner, P. Machnikowski, G. Abstreiter and J. J. Finley. "Coulomb Mediated Hybridization of Excitons in Coupled Quantum Dots", *Physical Review Letters*, 116:077401 (2016). doi:10.1103/PhysRevLett.116.077401

Conference Contributions

A. M. Waeber, I. Farrer, D. A. Ritchie, J. Nilsson, R. M. Stevenson, A. J. Bennett, A. J. Shields, A. I. Tartakovskii, M. S. Skolnick, and E. A. Chekhovich. "Increased Nuclear Spin Coherence in Strained Quantum Dots under π-pulse trains", IOP Quantum Dot Day, 12$^{\text{th}}$ January 2015, Cambridge (talk)

A. M. Waeber, M. Hopkinson, I. Farrer, D. A. Ritchie, J. Nilsson, R. M. Stevenson, A. J. Bennett, A. J. Shields, A. I. Tartakovskii, M. S. Skolnick, and E. A. Chekhovich. "Increased Nuclear Spin Coherence in InGaAs Quantum Dots under multiple pulse NMR", UK Semiconductors, 1$^{\text{st}}$-2$^{\text{nd}}$ July 2015, Sheffield (talk)

A. M. Waeber, M. Hopkinson, I. Farrer, D. A. Ritchie, J. Nilsson, R. M. Stevenson, A. J. Bennett, A. J. Shields, A. I. Tartakovskii, M. S. Skolnick, and E. A. Chekhovich. "Increased Nuclear Spin Coherence in InGaAs Quantum Dots under multiple pulse NMR", EP2DS-21/MSS-17, 26$^{\text{th}}$-31$^{\text{st}}$ July 2015, Sendai, Japan (talk)

Contents

List of Figures

$\chi\alpha\lambda\epsilon\pi\alpha\ \tau\alpha\ \kappa\alpha\lambda\alpha$
Plato - The Republic (Book IV, 435c)

1 Introduction

The work discussed in this thesis concerns the study and control of the nuclear spin bath dynamics in individual self-assembled InGaAs quantum dots. What might at first glance appear to be a rather specialised and niche topic is in fact part of a concerted effort by research groups in solid state and atomic physics worldwide to find a physical system suitable for building a quantum computer.

In the early 1980s, Y. Manin[1, 2] and R. Feynman[3] noted independently that the simulation of quantum physics with classical computers is an exponentially complex problem and can quickly become infeasible irrespective of the processing power available. The solution Feynman proposed to overcome this limitation was to use a quantum computer instead, i.e. a computer relying on quantum mechanical effects for information processing[3, 4]. Such a system would also be well-suited to solve several other complex problems which exceed the capabilities of classical computers such as the factorisation of large numbers (Shor's algorithm, [5]) and accelerated database search (Grover's algorithm, [6]).

The basic building blocks of a quantum computer are called *qubits* in analogy to the digital bits in classical computing. Potential qubit candidates have been identified in many systems including trapped ions[7, 8], superconducting circuits[9], dopants in silicon[10–12] and diamond[13], as well as electrostatically defined and self-assembled quantum dots[14–16]. This list is by no means exhaustive and many other materials are also under consideration.

A comprehensive discussion of specific requirements for a practical quantum com-

puter was first given by D. DiVincenzo in 2000[17]. A more recent review of quantum computers by T. Ladd et al. states 3(+1) general criteria for a fault-tolerant quantum computer[18]:

(i) The addition of further qubits to the system does not increase the demands on resources exponentially (*scalability*). These "resources" can include e.g. fabrication aspects or the technology required for qubit control (electronic gates, lasers, low-temperature environment,...).

(ii) All possible quantum computer operations can be realised using a finite set of quantum gates (*universal logic*).

(iii) The state of the quantum system can be initialised and measured efficiently (*correctability*).

(iv) The qubit coherence times are long enough to achieve (i)-(iii).

Self-assembled quantum dots in III-V semiconductors are of particular interest for quantum information applications due to their strong interaction with light. Their large optical dipole moment allows ultrafast coherent optical control of charge spins[19, 20] and makes the system ideally suited for spin-photon interfacing. This opens additional pathways for scalability as quantum communication via photons acting as "flying" qubits can be used to connect spatially distant qubit ensembles[17]. One of the most active research areas involving self-assembled quantum dots is the development of optical circuits for all-optical quantum computing[21–23], where the quantum dots can be used as efficient on-demand single photon sources[24, 25].

On the other hand, self-assembled quantum dots are facing two major challenges in their suitability for quantum information processing. Firstly, their formation in molecular beam epitaxy is a stochastic process resulting in a random spatial distribution of dots with varying optical properties. Although progress has been made in the deterministic site-controlled growth of quantum dots in recent years, the optical characteristics of such samples are still noticeably inferior[26, 27]. The optical transition energies can be tuned to a significant extent by electric and magnetic

fields, making entanglement between spins in distant quantum dots feasible[28]. However, despite these encouraging developments further progress will be required to make spin qubits in self-assembled quantum dot scalable.

The second drawback which self-assembled quantum dots share with their electrostatically defined counterparts is the presence of a large number ($\sim 10^4 - 10^6$) of non-zero nuclear spins. The mutual electromagnetic interaction with the nuclear spin bath severely limits the coherence time of a central electron or hole spin[29, 30]. Several ways have been explored to increase the central spin coherence. One intuitive approach is to abandon III-V semiconductors altogether and to chose a nuclear-spin-free host material instead. Recent results in electrostatically defined quantum dots in isotopically purified Si[31, 32] and Si/SiGe heterostructures[33] have shown that electron spin coherence times can indeed be extended in this way. Other approaches have included the suppression of coupling to the bath by nuclear spin state narrowing[34–36] and dynamic nuclear polarisation[37, 38].

In order to create a stable, predictable environment for the central spin, a full understanding of the nuclear spin bath dynamics is needed. Recent progress with optically detected nuclear magnetic resonance (ODNMR) techniques has made it possible to probe the inhomogeneously broadened NMR spectra in InGaAs quantum dots[39, 40], and nuclear spin Hahn echo experiments[41, 42] have provided a first direct measurement of the spin bath coherence.

Here, we present our most recent advances in the control and study of nuclear spin bath coherence in self-assembled InGaAs quantum dots using novel pulsed and continuous wave NMR techniques. The work is structured as follows:

In **chapter 2**, we introduce self-assembled quantum dots and their optical properties. After a brief discussion of the epitaxial growth techniques used in the fabrication of quantum dot samples, we study the three-dimensional confinement potential analytically and show how discrete bound energy states emerge for electrons and holes in a quantum dot. A look at optical interband transitions and correction

terms to the energy states concludes this short review. The influence of electric and magnetic fields on the system is treated in the second part of this chapter, where we show that the optical transition energies can be altered significantly by external fields.

In **chapter 3**, we study the quantum dot spin system in greater detail. A discussion of the electron- and hole-nuclear hyperfine interaction is followed by a review of the dominant relaxation and decoherence mechanisms for carrier and nuclear spins in a quantum dot. We then look at how resonant interaction with a radio frequency (rf) field allows the control and manipulation of a spin system in nuclear magnetic resonance (NMR).

In **chapter 4**, we present the low temperature magneto-photoluminescence setup used for the measurements discussed in this work. The implementation of optically detected NMR is explored and further details of the two studied sample structures are given.

In **chapter 5**, we measure the nuclear Hahn echo decay for ^{75}As and ^{71}Ga in individual InGaAs quantum dots. The quenching of nuclear spin bath fluctuations due to strain-induced quadrupolar interactions is studied experimentally in a gated p-i-n diode sample which allows control over the charge population in the studied dot. Hahn echo experiments confirm recent findings of extended nuclear spin phase memory times in a charge-free quantum dot.

In **chapter 6**, we look at advanced pulsed NMR protocols aimed at further suppression of the nuclear spin bath decoherence. Carr-Purcell pulse sequences are used to refocus the spin bath dephasing due to interactions with a fluctuating environment. We discuss the spin-locking origin of unexpectedly large increases in the observed nuclear spin phase memory time and design a set of new combined Hahn and solid echo sequences using average Hamiltonian theory. We show that these new sequences allow noticeably increased control over the spin bath evolution and discuss experimental limitations to the performance of the sequences.

In **chapter 7**, we introduce the novel concept of frequency comb NMR which allows us to weakly probe the dynamics of the spin bath without many of the limitations associated with pulsed NMR. The homogeneous lineshape of ^{75}As and ^{71}Ga is probed and the few-second-long homonuclear spin flip-flop correlation times of the ^{71}Ga central and satellite NMR transitions are measured experimentally using this technique.

In **chapter 8**, we give a brief summary of the findings presented in this work and discuss possible future directions that could be explored based on our results.

2 Self-Assembled Quantum Dots

The behaviour of a charge carrier strongly bound in a three-dimensional potential is governed by quantum mechanics and often contradicts classical expectations. The best-known example of such a system is an individual atom with its discrete electron binding energies and optical transitions. However, similar quantised states and transition energies can also be observed in larger systems. In recent decades, the semiconductor community has identified various nanocrystal structures with such properties which are collectively referred to as *quantum dots* or *artificial atoms*.

Since the first report on size-dependent absorption energies in CuCl nanocrystals by Ekimov[43], quantum dots have been realised in systems including colloidal crystals[44], two-dimensional electron gases with electrostatic confinement[45], thickness fluctuations in a quantum well[46] and self-assembled nanoscale islands formed with heteroepitaxial growth[47]. Depending on the design and compound materials, a dot can confine electrons, holes or excitons (bound electron-hole pairs).

All the work presented in this thesis was done on self-assembled InGaAs quantum dots embedded in a GaAs matrix. In this chapter, an overview of the basic properties of such a system is given. Section 2.1 discusses the growth of quantum dots in molecular beam epitaxy (MBE). The discrete energy structure of the trapped electrons and holes in a quantum dot is derived in section 2.2.1 and the optical properties of the system are explored in 2.2.2. In the final section 2.3, the influence of electric and magnetic fields on the energy spectrum is discussed.

2.1 Growth of InGaAs Quantum Dots

The experimental work of this project was done on individual InGaAs quantum dots grown on a GaAs substrate using molecular beam epitaxy (MBE). Epitaxial growth of heterostructures can occur in three distinct modes depending on the surface energies of substrate γ_S and film γ_F as well as the interface energy γ_{SF}[48]. If $\gamma_S > \gamma_F + \gamma_{SF}$, the total surface energy is minimised when the deposited material forms a uniform layer, covering the substrate. This is commonly referred to as the *Franck-van der Merve* growth mode. In the opposite case, the *Volmer-Weber* mode, $\gamma_S < \gamma_F + \gamma_{SF}$ and instead of a uniform film small islands of the deposited material form at the substrate surface. The third mode is a combination of the first two: in many cases a slight mismatch in the lattice constants of substrate and overlayer material allows for the formation of one or two epitaxial monolayers (ML) before strain increases the interface energy to a point where nucleation is favourable. In this way, the deposited material can form uniform nanoscale islands with defect-free substrate interfaces.

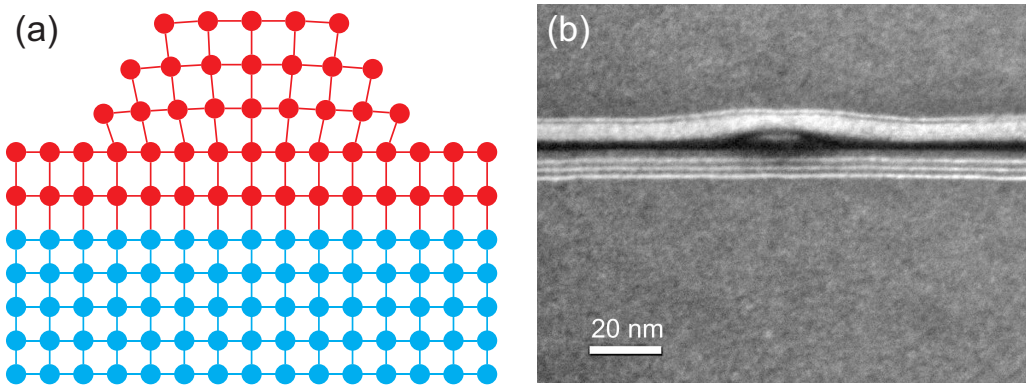

Figure 2.1: (a) The lattice mismatch between GaAs (blue) and InGaAs (red) causes strain which leads to the formation of quantum dot islands after the initial deposition of $1-2$ monolayers of InGaAs. This mechanism is commonly known as the Stranski-Krastanov growth mode. (b) Transmission electron microscope (TEM) image of an MBE grown self-assembled InGaAs/GaAs quantum dot. The lens-shaped dot is clearly contrasted against the GaAs/AlGaAs short-period superlattice in which it is embedded to prevent charge tunnelling (more details on the sample structure will be given in chapter 4.4.1).

This *Stranski-Krastanov* mode is used for the epitaxial growth of self-assembled quantum dots. The lattice constant of the ternary $In_xGa_{1-x}As$ compound depends on the indium concentration and can have values of up to $a = 6.06$ Å for pure InAs compared to $a = 5.65$ Å for the GaAs substrate[49]. After an initial wetting layer deposition of $1 - 2$ ML, strain relaxation along the growth direction results in the formation of stochastically distributed three-dimensional InGaAs islands across the sample surface[50, 51] (see figure 2.1a). In principle these few-nanometre islands already constitute quantum dots. However, for practical applications an additional capping layer of GaAs is added to prevent non-radiative charge recombination via surface states and to provide full three-dimensional confinement within the GaAs host material. The size, shape, density and compound content of quantum dots can be controlled via several growth parameters including temperatures, pressures and flux rates.

In the samples used in this project the basic structure outlined above was modified by adding GaAs/AlGaAs short-period superlattices as charge tunnel barriers above and below the dot layer (see figure 2.1b). This system was embedded in a planar microcavity consisting of several GaAs/AlGaAs bilayers to enhance the light extraction efficiency. A more detailed description of the sample structures will be given in chapter 4.4.

A major obstacle for the use of self-assembled quantum dots in quantum information applications is the lack of control over nucleation sites. The Stranski-Krastanov process is fundamentally stochastic and does not lend itself easily to the growth of ordered structures. Pre-patterned substrates[52, 53] are a promising route towards scalable systems although due to defect-rich dot-substrate interfaces the optical properties of quantum dots grown in this fashion are still inferior[26, 27]. Alternatively, site control can be achieved in conventionally grown samples with dot registration techniques: using the position of a suitable quantum dot relative to a set of registration markers, the fabrication of the desired structure can be centred

around the dot, allowing e.g. for optimised coupling in photonic structures[54, 55]. For the experiments presented here, site control was not a necessary prerequisite as we studied single dots that were not embedded in a lateral structure. However, we relied on a set of micrometre sized Ti/Au surface markers for the purpose of relocating individual quantum dots relative to the marker positions.

2.2 Discrete Energy States in a Quantum Dot

The conduction band (CB) and valence band (VB) offset between the InGaAs dot and the surrounding GaAs matrix results in a three-dimensional confinement potential inside the quantum dot. Here, we show how this gives rise to discrete bound energy states for confined charges before we discuss inter- and intraband optical transition rules. Finally, we look at the influence of fine structure corrections arising from exchange interaction.

2.2.1 Three-Dimensional Confinement

A quantitative theoretical description of the electronic structure inside a quantum dot is difficult to obtain since the dot-matrix interface is diffuse. However, the calculation of bound energy states in the presence of internal strain is not trivial even if clear interfaces and symmetric dot shapes are assumed. Theoretical models based on effective mass and eight-band $\mathbf{k}\cdot\mathbf{p}$ theory have been developed for various dot geometries including lens-[56, 57], disc-[58] and pyramid-like[59, 60] shapes. Here we will only discuss a basic model which describes the main features of the electronic structure qualitatively.

The confining potential of a self-assembled quantum dot is strongly anisotropic. The epitaxial growth technique results in flat islands with lateral dimensions exceeding the height by a factor of five to ten (see e.g. the TEM image in figure 2.1b).

Therefore, electron confinement is significantly stronger along the growth direction

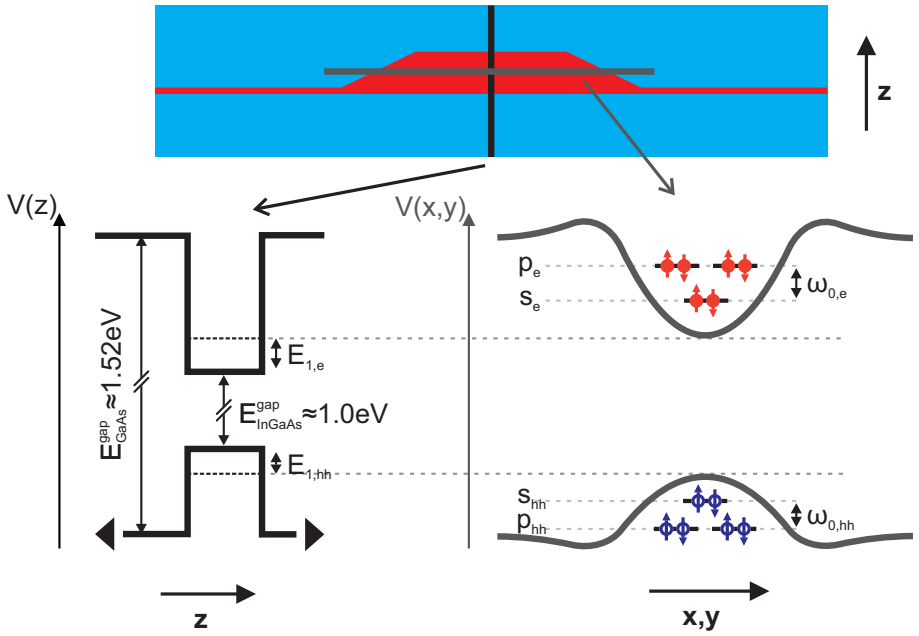

Figure 2.2: The strong confinement along the growth direction $\hat{e}_z$ in a quantum dot can be treated as a finite well problem, giving only one discrete bound ground state each for electron and heavy hole. The weaker in-plane confinement is modelled as a two-dimensional harmonic potential with an atom-like shell structure in conduction and valence band.

$\hat{e}_z$ than it is in the x-y plane and the vertical motion can be treated separately[56]. Assuming a finite square well, the time-independent Schrödinger equation is

$$\left(-\frac{\hbar^2}{2m^*}\frac{\partial^2}{\partial z^2} + V(z)\right)\Phi_j(z) = E_j\Phi_j(z)\ , \tag{2.1}$$

where m^* is the effective mass of the charge carrier and the potential $V(z)$ is zero inside the well and V_0 otherwise. In the well, we find two sets of symmetric ($\propto \cos(k_j z)$) and antisymmetric ($\propto \sin(k_j z)$) solutions for the wavefunction $\Phi_j(z)$ with $k_j = \sqrt{2m^*_{\mathrm{dot}}E_j/\hbar^2}$. The energy of a confined electron in state j is given by

$$\sqrt{\frac{m^*_{\mathrm{bulk}}(V_0 - E_j)}{m^*_{\mathrm{dot}}E_j}} = \tan\left(\frac{d}{2}\sqrt{\frac{2m^*_{\mathrm{dot}}E_j}{\hbar^2}} + \mathrm{mod}(j+1,2)\cdot\frac{\pi}{2}\right)\ , \tag{2.2}$$

where d denotes the dot height or well width, and odd $j = 1, 3, \ldots$ and even $j = 2, 4, \ldots$ are associated with symmetric and antisymmetric wavefunctions, respectively. This transcendental equation can only be solved numerically or graphi-

cally for a given set of parameters. It should be noted that the lowest bound state $j = 1$ in a quantum well is symmetric and always exists.

Using realistic values for d, V_0 and m^*, we can derive approximate energy levels E_j for charges in the conduction (CB) and valence band (VB) of an InGaAs quantum dot. From the TEM image in figure 2.1b we derive a dot height of $d \approx 5$ nm. Previous continuous wave (cw) NMR experiments on quantum dots from one of the samples studied in this project (sample A) have revealed an average indium content of $\sim 20\%$ in the dot volume overlapping with the electron wavefunction[39]. While the full stoichiometry of the quantum dot is unknown, we shall assume an $In_{0.2}Ga_{0.8}As$ dot in the following. The exact band gap in $In_{0.2}Ga_{0.8}As$ is difficult to determine as it also depends on temperature and internal strain composition[61, 62]. However, a rough estimate taking into account all three parameters gives a band gap in the region of $E^{\text{gap}}_{\text{InGaAs}} \approx 1.0$ eV at liquid helium temperatures. This is markedly smaller than the substrate band gap $E^{\text{gap}}_{\text{GaAs}} \approx 1.52$ eV[63]. The band alignment in InGaAs/GaAs heterostructures is of type I; the potential energy within the quantum dot is lowered in the CB and raised in the VB. Measurements of the relative CB offset ratio have found $\Delta E^{\text{CB}}/\Delta E^{\text{gap}} \approx 0.6$ independent of the indium content[64]. Based on these findings, the CB energy offset is $V_0 \approx 0.30\ eV$.

The electron effective mass in bulk GaAs $m^*_{\text{bulk,e}} = 0.067 m_{0,\text{e}}$ is well-established from cyclotron resonance and Shubnikov-de Haas experiments[49]. For the effective mass inside the $In_{0.2}Ga_{0.8}As$ dot we use a bulk value $m^*_{\text{dot,e}} = 0.054 m_{0,\text{e}}$, neglecting small corrections arising from the confinement[65]. With these parameters we obtain a single bound solution for the ground state $j = 1$ at $E_{1,\text{e}} \approx 110$ meV above the CB edge inside the dot (see figure 2.2).

The treatment of the bound energy states for holes (unoccupied electron states) in the VB is more complex as the underlying band structure must be considered. The CB is formed of s-shell Bloch functions ($L = 0$) and is only spin degenerate ($S_{\text{z}} = \pm\frac{1}{2}$). By contrast, the VB is formed by hybridised p-shell electrons with

orbital angular momentum $L = 1$. Therefore, the total angular momentum is given by $\boldsymbol{J}_\mathrm{h} = \boldsymbol{L} + \boldsymbol{S}$, resulting in three distinct hole sub-bands: *heavy hole* (hh, $J_\mathrm{hh} = \frac{3}{2}, J_\mathrm{hh,z} = \pm\frac{3}{2}$), *light hole* (lh, $J_\mathrm{lh} = \frac{3}{2}, J_\mathrm{lh,z} = \pm\frac{1}{2}$) and *split-off band* (s-o, $J_\mathrm{so} = \frac{1}{2}, J_\mathrm{so,z} = \pm\frac{1}{2}$). The s-o band can be neglected in our discussion as it is separated from the hh and lh bands by a spin-orbit splitting of $\Delta_\mathrm{so} \approx 350$ meV[66].

For heavy and light holes, we can assume a confinement energy of $V_0 \approx 0.20\ eV$. The effective masses in bulk GaAs are $m^*_\mathrm{bulk,hh} = 0.51 m_\mathrm{0,e}$ and $m^*_\mathrm{bulk,lh} = 0.082 m_\mathrm{0,e}$ and linear interpolation gives $m^*_\mathrm{dot,hh} = 0.49 m_\mathrm{0,e}$ and $m^*_\mathrm{dot,lh} = 0.071 m_\mathrm{0,e}$ for the $\mathrm{In_{0.2}Ga_{0.8}As}$ alloy[67]. From the resulting ground state energy levels $E_\mathrm{1,hh} \approx 25$ meV and $E_\mathrm{1,lh} \approx 80$ meV determined with equation (2.2), we can already conclude that the lowest VB energy state inside the dot will have hh character. This has been confirmed experimentally[68] and is in notable contrast to bulk (In)GaAs where the hh and lh band maxima are degenerate at the Γ point[67].

So far we have not considered the motion in the x-y plane. A good description of the in-plane confinement is given by the rotationally symmetric two-dimensional parabolic potential $V(x, y) = \frac{1}{2} m^* \omega_0^2 (x^2 + y^2)$[56, 69] with solutions

$$E_{k,l} = \hbar\omega_0 (k + l + 1)\ , \tag{2.3}$$

where $k, l = 0, 1, 2\ldots$ and ω_0 is a constant level spacing. By introducing the quantum number $n = k + l$ and treating the z confinement as a fixed energy offset, we can describe the quantum dot energy levels as a two-dimensional shell structure with (2n+1)-degenerate levels s, p, d ... for $n = 0, 1, 2\ldots$ in analogy to the subshell labels of an atom. Experiments have shown that this simple model is surprisingly accurate for the lower energy levels in both CB and VB as long as electron-electron interactions can be neglected, and typical intershell spacings of $\omega_\mathrm{0,e} = 15 - 60$ meV and $\omega_\mathrm{0,hh} = 10 - 40$ meV have been reported by several groups[56, 70–72].

2.2.2 Excitons and Optical Transitions

GaAs and the ternary InGaAs compound are both direct bandgap semiconductors as their CB energy minimum and VB energy maximum are both located at the Γ point. This makes the quantum dot system well suited for optical experiments because the crystal momentum is trivially conserved under radiative interband transitions without the need for additional phonon absorption or emission. In both materials the bandgap is sufficiently large to ensure a negligible thermal population of the CB at low temperatures. Under optical excitation at $\hbar\omega \geq E^{\mathrm{gap}}$ $(+E_{1,\mathrm{e}} + E_{1,\mathrm{hh}})$ single VB electrons in the bulk (dot) can be promoted into the CB by absorbing a photon, leaving behind a hole in the VB. Analogously, an electron in the CB can recombine with a VB hole emitting a photon.

The Coulomb interaction between the oppositely charged and spatially separated electron and hole can lead to the formation of a bound quasi-particle called an *exciton*. Although the localisation of charge carriers inside a quantum dot is dominated by the confinement potential and not by the Coulomb interaction, this term has also been adopted in the quantum dot literature and will be used here to refer to a confined electron-hole pair. However, the confinement in the quantum dot does also increase the Coulomb interaction and lowers the optical transition energy by an excitonic binding energy $E_{\mathrm{B}} \approx 10 - 20$ meV depending on the dot size[69, 73]. By comparison, excitons in bulk GaAs possess a considerably smaller binding energy of $E_{\mathrm{B}}^{\mathrm{bulk}} = 4.2$ meV[74].

Not every excitonic state inside a quantum dot can be created optically. A single photon carries a net angular momentum of $J_{\gamma,\mathrm{z}} = \pm 1$ and has intrinsic parity $\pi_\gamma = -1$. In the previous section, we briefly mentioned that the envelope wavefunctions of bound states in a square well have alternating symmetry. This is likewise the case for the solutions of the two-dimensional harmonic oscillator. We also saw that the Bloch functions of CB and VB have opposite parity. Therefore only interband transitions between states with the same symmetry are dipole-allowed (e.g. $s_{\mathrm{h}} \leftrightarrow s_{\mathrm{e}}$,

$p_h \leftrightarrow p_e$,...). For intraband transitions, the Bloch functions of both states are identical and only excitation and relaxation between states with $\Delta L = \pm 1$ is allowed (e.g. $s_e \leftrightarrow p_e$)[75]. However, in real InGaAs quantum dots these selection rules can be weakened by an asymmetric dot geometry and parity-forbidden transitions are often observed[76].

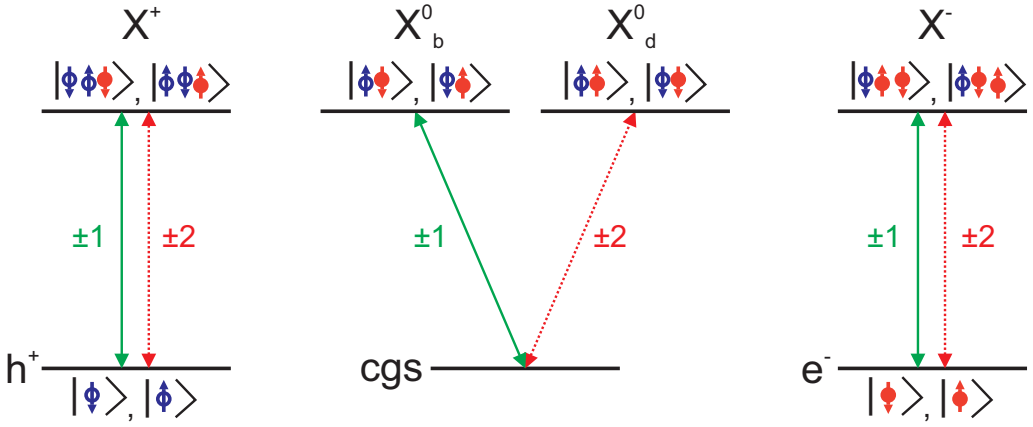

Figure 2.3: Positive (left, X^+) and negative trions (right, X^-) have two possible spin configurations which are both optically accessible. For the neutral exciton (centre), only the two bright states $X^0{}_b$ can be created whereas formation of the dark $X^0{}_d$ states is optically forbidden.

In addition to conservation of parity we have to consider the angular momentum: in principle, a neutral ground state exciton (X^0) consisting of a single electron-hole pair can have four different spin configurations. However, since the photon carries unity angular momentum, only two of these states, $|\Uparrow\downarrow\rangle$ with $J_{ex} = +1$ and $|\Downarrow\uparrow\rangle$ with $J_{ex} = -1$ are optically active (here $\Uparrow$ and $\uparrow$ denote the hole and electron spin). Accordingly, these states are called *bright* whereas the two states with parallel spin alignment $|\Uparrow\uparrow\rangle$, $|\Downarrow\downarrow\rangle$ ($J_{ex} = \pm 2$) are referred to as *dark* excitons.

The excitonic binding energies and selection rules discussed in this section strongly depend on the population of the quantum dot. For example, a singly charged exciton or trion can be formed when the dot already contains a charge prior to the optical generation of an electron-hole pair. Such a resident charge can be introduced in a controlled fashion by embedding the dot layer in a diode structure[71, 77] or by doping the sample[78].

As illustrated in figure 2.3, the single positive ($|\Uparrow\downarrow\Downarrow\uparrow\rangle$, $|\Downarrow\uparrow\Uparrow\downarrow\rangle$) and negative trion states ($|\Uparrow\downarrow\Uparrow\downarrow\rangle$, $|\Downarrow\uparrow\Downarrow\uparrow\rangle$) can all be formed optically. Due to different Coulomb interaction strengths, X^- transition energies are red shifted by $3-8$ meV compared to X^0, whereas X^+ transitions are generally blue shifted[71, 79, 80]. While "forbidden" excitation paths also exist for trions, these cannot be distinguished in the absence of a magnetic field since the initial and final spin states are degenerate.

However, forbidden trion transitions have been observed optically in magnetic fields[81]. Similarly, dark neutral excitons can be observed at low optical excitation powers[82, 83]. In both cases, mixing of heavy and light hole states due to reduced dot symmetry or a tilted dot quantisation axis can lead to a finite coupling strength for the forbidden $\Delta J = \pm 2$ transitions[84, 85].

2.2.3 Exchange Interactions and Fine Structure

Although we have introduced the electron and hole spin in the discussion above, we have neglected the energy corrections associated with spin exchange interaction so far. We have seen that the attractive Coulomb interaction between electron and hole lowers the X^0 transition energy by up to 20 meV and that the addition of a second electron (hole) decreases (increases) the binding energy by a few meV. Crucially, this interaction does not depend on the charge spin configuration and the initial and final states of the excitonic transitions shown in figure 2.3 are fully degenerate if the Pauli exclusion principle is not taken into account.

In this section we will look at the effect of spin exchange on the energy spectrum. For a neutral exciton with electron spin $\boldsymbol{S}_\mathrm{e}$ and hole spin $\boldsymbol{J}_\mathrm{h}$, the spin-spin coupling can be described as[86, 87]

$$\mathcal{H}_\mathrm{exch} = a_\mathrm{z} J_\mathrm{h,z} S_\mathrm{e,z} + \sum_{i=\mathrm{x,y,z}} b_i J^3_{\mathrm{h},i} S_{\mathrm{e},i} \ , \tag{2.4}$$

where a_i, b_i are the spin-spin coupling constants. The exchange Hamiltonian can also

be expressed in the basis of bright ($|+1\rangle$, $|-1\rangle$) and dark exciton states ($|+2\rangle$, $|-2\rangle$). This basis is particularly insightful as it contains the exchange coupling terms between the "pure" $\Delta j = \pm 1, \pm 2$ transitions in an explicit form[88]:

$$\mathcal{H}_{\text{exch}} = \frac{1}{2} \begin{pmatrix} \delta_0 & \delta_\text{b} & 0 & 0 \\ \delta_\text{b} & \delta_0 & 0 & 0 \\ 0 & 0 & -\delta_0 & \delta_\text{d} \\ 0 & 0 & \delta_\text{d} & -\delta_0 \end{pmatrix} . \tag{2.5}$$

Here, $\delta_0 = 1.5(a_\text{z} + 2.25 b_\text{z})$ is the splitting between bright and dark excitons with typical values $\delta_0 \approx 100 - 400$ μeV[83, 88] depending on the dot size. The two dark exciton states are split by $\delta_\text{d} = 0.75(b_\text{x} + b_\text{y}) \lesssim 50$ meV, which is generally too small

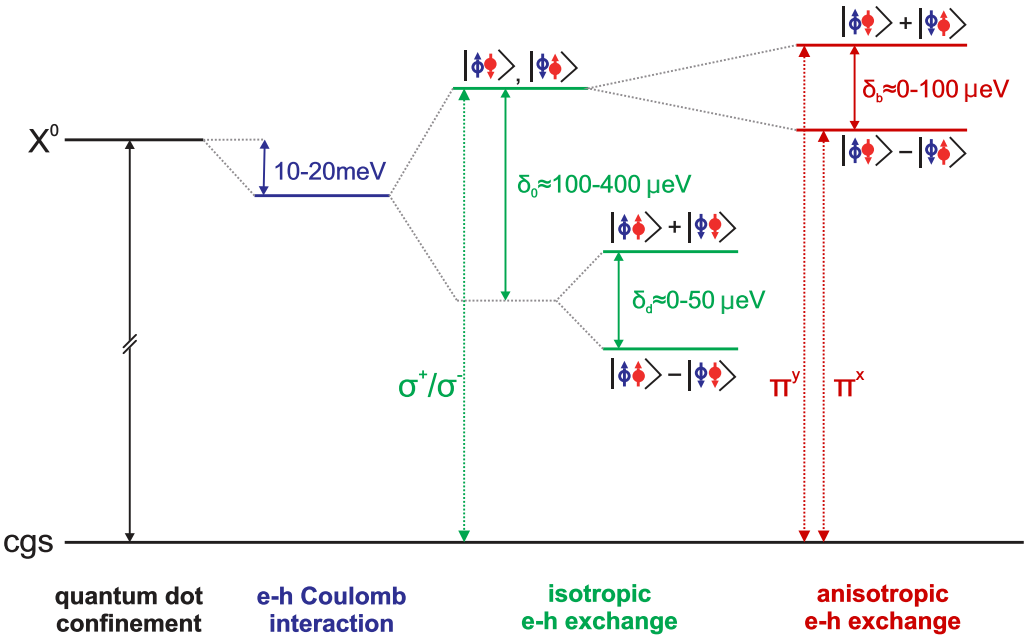

Figure 2.4: Spin-independent Coulomb interaction between electron and hole reduces the transition energy of a neutral exciton by up to 20meV (blue). The spin degeneracy between bright and dark states is lifted by isotropic exchange interactions (δ_0 and δ_d, green). The bright exciton transitions are circularly polarised (σ^+/σ^-), whereas the dark exciton transitions are optically forbidden. A further anisotropic exchange term results in a fine structure splitting δ_b between the two bright exciton states (red). Due to the changed spin eigenstates, the fine structure split exciton transitions are linearly polarised ($\pi^\text{y}/\pi^\text{x}$).

to be resolved in photoluminescence spectroscopy[83]. Both δ_0 and δ_d are present in every quantum dot and can be summarised as the isotropic electron-hole exchange splitting, indicated in green in figure 2.4.

In addition, anisotropic exchange interaction (red in figure 2.4) can split the two degenerate bright states by $\delta_b = 0.75(b_x - b_y)$ if the dot does not possess full rotational symmetry in the x-y plane and $b_x \neq b_y$. This fine structure splitting (FSS) depends strongly on the individual dot and is usually within a range $\delta_b \approx 0 - 100\ \mu$eV[83, 88]. Based on these literature values and our own experimental findings (see section 2.3.2) we can therefore also conclude that $|b_x|, |b_y| \lesssim 70\ \mu$eV.

The anisotropic exchange also affects the optical transition rules: as it mixes the bright states, the total angular momentum $J_{ex} = \pm 1$ is no longer a good quantum number. Therefore the two fine structure split states cannot be addressed selectively with circularly polarised light. Instead, linear polarisation is observed for the two bright exciton transitions in the absence of a magnetic field[88].

By contrast, negative and positive trions show no FSS. In both cases the initial state is formed by a single trapped charge which naturally is not affected by exchange interaction. The final state is formed by a hole (electron) interacting with an electron pair (hole pair) in the spin-singlet state and in accordance with the Kramers degeneracy theorem for fermions has no exchange energy either[89, 90]. Hence the presence of FSS is a useful indicator for the identification of an unknown optical transition.

2.3 Exciton States in Electric and Magnetic Fields

The excitonic transitions introduced in the previous sections are sensitive to both electric and magnetic fields. An external electric field can couple to the dipole moment of the exciton and lead to a linear and quadratic *Stark shift* of the transition energies. Magnetic fields affect the excitonic spectrum in two ways: the diamag-

netism of the exciton gives rise to a quadratic shift that allows conclusions on the lateral size of the quantum dot. In addition, the *Zeeman interaction* lifts level degeneracies and influences the selection rules for optical transitions. Depending on the alignment of optical axis and magnetic field, the "pure" bright and dark states can either be fully restored or fully mixed.

2.3.1 Electric Fields

The electron and hole of a neutral exciton X^0 are not only energetically but also spatially separated. While the hole wave function is located towards the indium-rich apex of the dot, the electron is localised in the base region[91]. This separation of the two charge carriers within the dot leads to a finite permanent electric dipole moment $\boldsymbol{p}_{\mathrm{d},0} = e \cdot \boldsymbol{r}$ for the exciton. Here, e is the elementary charge and $\boldsymbol{r}$ is the displacement vector for the hole wavefunction relative to the centre of the electron wavefunction. In an external electric field $\boldsymbol{F}$ the two wavefunctions get shifted and an additional dipole moment is induced. The magnitude of this field-induced term depends on the polarisability α of the exciton.

$$\boldsymbol{p}_{\mathrm{d}} = e \cdot \boldsymbol{r} + \alpha \cdot \boldsymbol{F} \,. \tag{2.6}$$

Coupling of the dipole moment $\boldsymbol{p}_{\mathrm{d}}$ to the applied electric field leads to a shift of the excitonic transition energy which has terms linear and quadratic in $\boldsymbol{F}$. This is the first and second order *Stark effect*[92]. If we denote the transition energy at zero field as E_0 we can write

$$\Delta E_{\mathrm{Stark}} = E_0 - \boldsymbol{p}_{\mathrm{d}} \cdot \boldsymbol{F} = E_0 - \boldsymbol{p}_{\mathrm{d},0} \cdot \boldsymbol{F} - \alpha \cdot \boldsymbol{F}^2 \tag{2.7}$$

It should be noted at this point that all excitonic states possess an intrinsic dipole moment. Observation of the Stark effect is therefore not limited to X^0.

Because of the strong confinement in a quantum dot even shifts exceeding the

Coulomb binding energy will not ionise the exciton. This specific behaviour is referred to as the *quantum confined Stark effect* (QCSE)[93]. Further distinction is made between the DC Stark effect typically observed in gated structures and the AC Stark effect which can have much larger field amplitudes and is often induced by applying high-power optical excitation[94].

The intrinsic dipole of an exciton confined in a single quantum dot is small compared to the induced dipole and the Stark shift observed in embedded diode structures is typically dominated by the quadratic component. However, strong linear Stark shifts have been observed in coupled vertically stacked quantum dots where electron and hole can be located in separate dots[95].

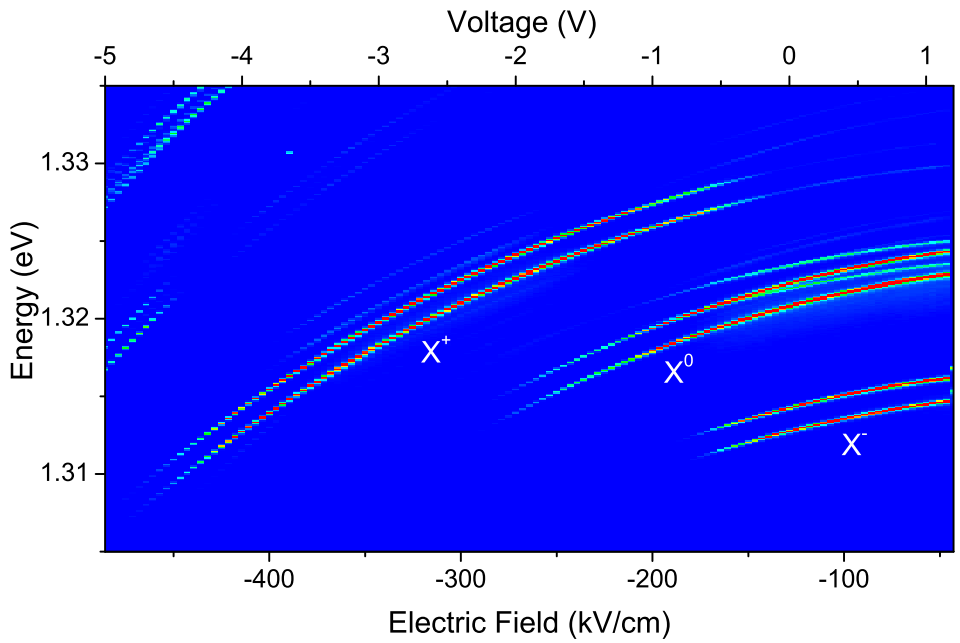

Figure 2.5: Bias-dependent photoluminescence (PL) map of a quantum dot in one of the samples used in this project (sample B) at $B_{0,z} = 8$ T and low optical excitation power. The charge population of the dot is controlled by the applied electric field and X^+, X^0 and X^- can be observed within distinct voltage ranges. $Al_{0.75}Ga_{0.25}As$ barriers on either side of the dot layer suppress electron and hole tunnelling and permit tuning of the PL emission energy over a range of up to 25 meV (see chapter 4.4.2 and [96] for a description of the sample structure).

The DC quantum confined Stark effect is present in all electrically gated quantum dot structures and has found widespread application as a tool for tuning optical

transitions into resonance e.g. with a cavity[97, 98], a photon from another quantum dot for interference[99] and entanglement experiments[28] or a laser for resonant excitation[100]. The tuning range of the Stark shift in a quantum dot mainly depends on the design of the diode structure and is limited by charge tunnelling at large biases. By placing the dot layer between two large bandgap barriers, Stark shifts of up to 25 meV have been achieved[96, 101].

Figure 2.5 shows a bias dependent photoluminescence (PL) map for a dot in such a "giant Stark shift" sample which was used in the present work (sample B). The electric field values stated were calculated from the bias voltage using $F = -\frac{V_{\mathrm{bi}} - V_{\mathrm{bias}}}{d}$ where $V_{\mathrm{bi}} = 1.8$ V is the built-in bias of the diode and $d = 140$ nm is the thickness of the intrinsic layer. From fitting of the neutral exciton transition with equation (2.7), we obtained $p_{\mathrm{d},0} = -8.1\ \mu\mathrm{eV\ kV^{-1}\ cm}$ and $\alpha = -0.010\ \mu\mathrm{eV\ kV^{-2}\ cm^2}$ for the intrinsic dipole and polarisability, in good agreement with previous values reported for this structure[96]. A more detailed description of the sample will be given in chapter 4.4.2.

2.3.2 Magnetic Fields

In the presence of an external magnetic field $\boldsymbol{B}_0$, level splittings between otherwise degenerate excitonic states appear as the constituent electron and hole spins couple to $\boldsymbol{B}_0$ via the Zeeman interaction. In addition, the field induces a diamagnetic response in the form of a quadratic transition energy shift.

Two types of magnetic field configurations are of particular interest in the study of quantum dots. The *Faraday geometry* describes a system in which the optical excitation axis and quantum dot growth axis are aligned parallel to the external field vector $\boldsymbol{B}_0 \parallel \hat{e}_{\mathrm{z}}$. By contrast, a configuration where the optical axis is perpendicular to the magnetic field $\boldsymbol{B}_0 \perp \hat{e}_{\mathrm{z}}$ is referred to as a *Voigt geometry*.

The orientation of $\boldsymbol{B}_0$ has a strong influence on the observed Zeeman splitting of the excitonic states and affects the optical selection rules as we will see for the

example of X^0. Here, the general Zeeman Hamiltonian describing the interaction between a magnetic field $\boldsymbol{B}_0$ and the electron ($\boldsymbol{S}_\mathrm{e}$) and hole spin ($\boldsymbol{J}_\mathrm{h}$) is given by

$$\mathcal{H}_\mathrm{Z} = \mu_\mathrm{B}(\boldsymbol{B}_0^\mathsf{T} \cdot \boldsymbol{g}_\mathrm{e} \cdot \boldsymbol{S}_\mathrm{e} + \boldsymbol{B}_0^\mathsf{T} \cdot \boldsymbol{g}_\mathrm{h} \cdot \boldsymbol{J}_\mathrm{h}) \,, \tag{2.8}$$

where $\boldsymbol{g}_{\mathrm{e/h}}$ denotes the electron and hole g factor tensors. Their principal axes coincide with the main crystal axes[102] and we choose the laboratory frame accordingly without loss of generality. We find that in Faraday geometry ($\boldsymbol{B}_0 = B_{0,\mathrm{z}}\hat{e}_\mathrm{z}$) the pure exciton states $|\pm1\rangle$, $|\pm2\rangle$ are eigenstates of the Zeeman Hamiltonian. Taking into account the FSS contributions discussed in section 2.2.3 and the quadratic diamagnetic shift, we obtain the energy shifts listed in table 2.1a[88] and illustrated on the left side of figure 2.6. We note that at low magnetic fields, the fine structure splitting δ_b (δ_d) dominates and the energy levels remain mixed, i.e. the optical transitions of the bright excitons remain linearly polarised as shown in figure 2.4. However, circular polarisation of the optical transitions is restored at higher magnetic fields when $\mu_\mathrm{B}|(g_{\mathrm{h,z}} - g_{\mathrm{e,z}})|B_{0,\mathrm{z}} \gg \delta_\mathrm{b}$.

(a) Faraday geometry
$\Delta E_{\mathrm{b,F}}(B_\mathrm{z}) = \gamma_2 B_\mathrm{z}^2 + \frac{\delta_0}{2} \pm \frac{1}{2}\sqrt{\delta_\mathrm{b}^2 + \mu_\mathrm{B}^2(g_{\mathrm{h,z}} - g_{\mathrm{e,z}})^2 B_\mathrm{z}^2}$
$\Delta E_{\mathrm{d,F}}(B_\mathrm{z}) = \gamma_2 B_\mathrm{z}^2 - \frac{\delta_0}{2} \pm \frac{1}{2}\sqrt{\delta_\mathrm{d}^2 + \mu_\mathrm{B}^2(g_{\mathrm{h,z}} + g_{\mathrm{e,z}})^2 B_\mathrm{z}^2}$
(b) Voigt geometry
$\Delta E_{\mathrm{b,V}}(B_\mathrm{x}) = \gamma_2 B_\mathrm{x}^2 + \frac{1}{4}\left(\pm(\delta_\mathrm{b} + \delta_\mathrm{d}) + \sqrt{(2\delta_0 \pm \delta_\mathrm{b} \mp \delta_\mathrm{d})^2 + 4\mu_\mathrm{B}^2(g_{\mathrm{h,x}} \mp g_{\mathrm{e,x}})^2 B_\mathrm{x}^2}\right)$
$\Delta E_{\mathrm{d,V}}(B_\mathrm{x}) = \gamma_2 B_\mathrm{x}^2 + \frac{1}{4}\left(\pm(\delta_\mathrm{b} + \delta_\mathrm{d}) - \sqrt{(2\delta_0 \pm \delta_\mathrm{b} \mp \delta_\mathrm{d})^2 + 4\mu_\mathrm{B}^2(g_{\mathrm{h,x}} \mp g_{\mathrm{e,x}})^2 B_\mathrm{x}^2}\right)$

Table 2.1: Energy shifts ΔE for a neutral exciton in an external magnetic field (after [88]). The first term describes the diamagnetic shift while the subsequent terms summarise the exchange and Zeeman interactions that lift the spin degeneracy of the excitonic transitions. In Voigt geometry, $\boldsymbol{B}_0 || \hat{e}_\mathrm{x}$ is assumed. Analogous expressions for $\boldsymbol{B}_0 || \hat{e}_\mathrm{y}$ are given in [88].

Application of an in-plane field $\boldsymbol{B}_0 = B_{0,\mathrm{x}}\hat{e}_\mathrm{x}$ mixes the bright and dark exciton states strongly, giving the dark states non-zero oscillator strength. Therefore, four optically active and linearly polarised transitions are observed in Voigt geometry.

Here, the energy splittings scale with the in-plane g factors $g_{\mathrm{e/h,x}}$. A recent comprehensive study by Schwan et al. has shown the electron g tensor in a quantum dot to be approximately isotropic[102]. By contrast, the in-plane hole g factor is typically an order of magnitude smaller than $g_{\mathrm{h,z}}$[102, 103]. This anisotropy arises from the splitting of heavy and light hole band in the three-dimensional confinement of the quantum dot (see section 2.2.1) and is influenced by the dot geometry and strain composition[104].

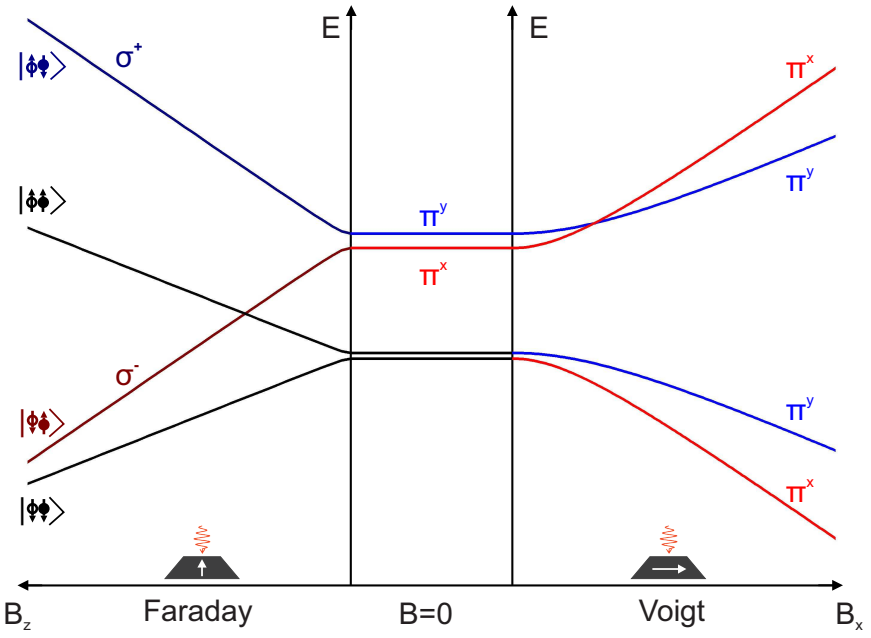

Figure 2.6: Scheme of the B-field dependent splitting of the neutral exciton states. In Faraday geometry the circularly polarised eigenstates along $\hat{e}_z$ are restored at large magnetic fields. In Voigt geometry the bright and dark exciton states are mixed and the optical transitions are linearly polarised.

The full Hamiltonian describing the interaction of the exciton with a magnetic field also contains two terms proportional to $\boldsymbol{B}_0^2$, which are responsible for the excitonic diamagnetic shift[105]. The first term arises from the altered canonical momentum $\boldsymbol{p} \rightarrow \boldsymbol{p} + \frac{q}{c}\boldsymbol{A}$ (with momentum operator $\boldsymbol{p}$ and vector potential $\boldsymbol{A}$). As Walck et al. showed[106], it is possible to remove the second quadratic contribution (a second-order Zeeman term) using a gauge transformation and to link the diamag-

netic coefficient γ_2 directly to the lateral dimensions of the electron and hole wave function. In a quantum dot this gives[107]

$$\gamma_2 = \frac{e^2}{8}\left[\frac{\langle r_{\mathrm{e}}^2\rangle}{m_{\mathrm{e}}^*} + \frac{\langle r_{\mathrm{h}}^2\rangle}{m_{\mathrm{h}}^*}\right] , \tag{2.9}$$

where m_{e}^* and m_{h}^* denote the effective electron and hole mass, respectively, and $\langle r_{\mathrm{e/h}}^2\rangle$ is the mean lateral extension of the wavefunction.

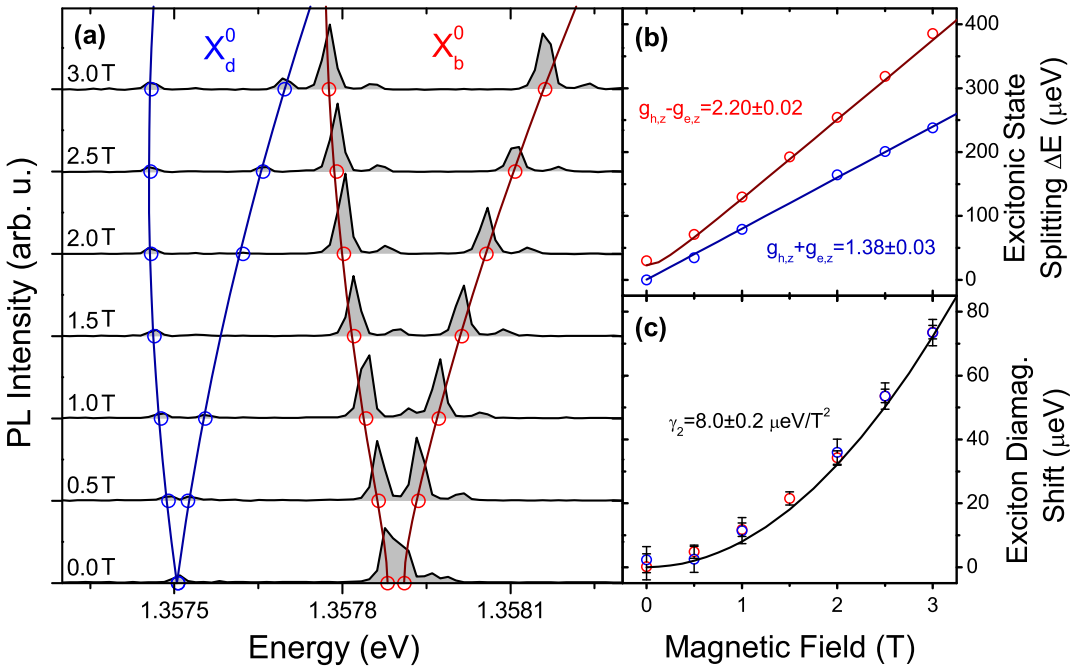

Figure 2.7: B-field dependent measurement in Faraday geometry at low optical excitation power ($P \approx 0.001 P_{\mathrm{Sat,X^0}}$). (a) PL spectra and fitted splittings for dark (blue) and bright (red) X^0 transitions. The bright-dark exciton splitting is $\delta_0 = 391 \pm 4$ μeV. (b) and (c) show the energy splittings and diamagnetic shifts of the bright and dark excitons separately for clarity. A fine structure splitting of $\delta_{\mathrm{b}} = 30 \pm 4$ μeV is measured whereas δ_{d} is not resolved. The electron and hole g factors are $g_{\mathrm{e,z}} = -0.41 \pm 0.03$ and $g_{\mathrm{h,z}} = 1.79 \pm 0.03$. These results agree well with literature values, as does the observed diamagnetic shift of $\gamma_2 = 8.0 \pm 0.2$ μeV/T^2[83, 102, 103].

An example of the Faraday magnetic field dependence of the bright and dark X^0 transition energies in sample A (see chapter 4.4) is shown in figure 2.7. The left panel shows the low-power PL spectra of all four transitions. The bright and dark ex-

citon splittings and diamagnetic shifts are extracted separately for clarity and shown in b and c. Using the expressions for $\Delta E_{\mathrm{b,F}}$ and $\Delta E_{\mathrm{d,F}}$ given in table 2.1a for fitting, we get a diamagnetic coefficient of $\gamma_2 = 8.0 \pm 0.2\ \mu\mathrm{eV/T^2}$, which is in good agreement with values reported for comparable samples[83]. Under the assumption of equal lateral dimensions for the electron and hole wavefunctions, we obtain $\sqrt{\langle r^2_{\mathrm{e/h}} \rangle} \approx 3.7$ nm. This agrees well with results from similar structures[108]. The electron and hole g factors along the growth axis can be extracted from the different Zeeman splittings of the bright and dark states. We obtain $g_{\mathrm{e,z}} = -0.41 \pm 0.03$ and $g_{\mathrm{h,z}} = 1.79 \pm 0.03$, again in good agreement with typical values from literature[83, 102, 103].

2.4 Summary

Epitaxially grown self-assembled quantum dots provide a three-dimensional confinement potential for electrons and holes. The strong confinement results in discrete energy levels inside the dot in the valence and conduction band similar to the electron shell structure found in atoms. Excitons can be formed in the quantum dot under optical excitation and the charge state can be controlled passively by doping or actively by gating the structure. The electric field in a diode sample also allows tuning of the exciton transition energies via the quantum confined Stark effect. Using external magnetic fields $\boldsymbol{B}_0$, one can fully restore the pure optical transitions of a neutral exciton which are generally mixed due to exchange interaction arising from imperfections in the physical geometry of the quantum dot. At large $\boldsymbol{B}_0$, exciton states can be addressed spin-selectively with circularly polarised light.

3 The Quantum Dot Spin System

In the previous chapter we have seen that the optical properties of a quantum dot make it possible to create electron-hole pairs spin-selectively. This has been used to initialise individual electron and hole spins with high fidelity by ionising a polarised exciton in a gated structure, making use of differences in the electron and hole tunnelling times at a given bias[77, 109]. Alternative initialisation schemes have employed the finite mixing of states to shelve an electron or hole spin in a long-lived trion ground state that is not addressed by the state-selective optical excitation[81, 110]. Based on these and similar techniques, coherent optical control schemes for single charge spins have been implemented[19, 111], demonstrating the potential of single quantum dots for quantum information technologies.

Isotope	Natural abundance	Nuclear spin I	Electron hyperfine coupling constant A^e (μeV / GHz)	Gyromagnetic ratio $\gamma^* = \gamma/2\pi$ (MHz/T)
^{69}Ga	60.1%	3/2	42† / 64†	10.248
^{71}Ga	39.9%	3/2	42† / 64†	13.021
^{75}As	100%	3/2	46 / 70	7.315
^{113}In	4.3%	9/2	56† / 85†	9.365
^{115}In	95.7%	9/2	56† / 85†	9.386

Table 3.1: Properties of all stable nuclear isotopes in an InGaAs quantum dot. Hyperfine constants A^e are taken from [112], with † marking average values for elements with two stable isotopes. All other parameters are adapted from [113].

In a perfect qubit, the charge carrier spin would be completely isolated from its environment and only interact with given neighbouring spins under controlled con-

ditions. However, this picture is strongly idealised compared to a real self-assembled InGaAs quantum dot where all constituent atoms carry a non-zero nuclear spin (see table 3.1). In this chapter we discuss the general properties of the spin system in a quantum dot. In section 3.1, we look at the various effects of the hyperfine interaction between a confined electron or hole spin and the nuclear spin bath. In section 3.2, we discuss the spin relaxation timescales T_1 and T_2 before studying the relevant mechanisms for charge and nuclear spin relaxation in a quantum dot. Finally, the theoretical framework of nuclear magnetic resonance (NMR) is introduced in section 3.3.

3.1 Hyperfine Interaction

Following the initial proposal for the use of confined charge carrier spins in quantum dots as qubits[14], it was quickly realised that the electromagnetic interaction of the carrier spin with an ensemble of $\sim 10^5$ nuclear spins would be the dominant source of spin qubit decoherence at low temperatures[29, 30]. On the other hand, the nuclear spin system itself is strongly decoupled from the environment and typically possesses extremely long spin relaxation times $T_{1,\mathrm{n}} > 1$ h[85, 114, 115].

The electromagnetic or *hyperfine* interaction between a central charge carrier spin $\boldsymbol{S}$ and the nuclear spin bath $\boldsymbol{I}_n$ is commonly treated analytically in terms of three separate contributions. The isotropic *Fermi contact interaction* arises from the overlap of the charge carrier and nuclear Bloch wave functions. By contrast, the dipolar coupling between nuclear and charge spins is an anisotropic long-range interaction. A third mechanism is the coupling of the charge carrier orbital angular momentum $\boldsymbol{L}_n$ to the n-th nuclear spin $\boldsymbol{I}_n$. As we will now show, all three of these contributions to the hyperfine interaction can be derived directly from the Pauli equation for a charged spin-$\frac{1}{2}$ particle in the presence of a nuclear magnetic

dipole $\boldsymbol{\mu}_n$[116]

$$\mathcal{H} = \frac{1}{2m}\left(\boldsymbol{p} + \frac{q}{c}\boldsymbol{A}_n\right)^2 + 2\mu_\mathrm{B}\boldsymbol{S}\cdot(\boldsymbol{\nabla}_n \times \boldsymbol{A}_n)\,, \quad \boldsymbol{A}_n = \boldsymbol{\nabla}_n \times \frac{\boldsymbol{\mu}_n}{r_n}\,, \tag{3.1}$$

where $\boldsymbol{r}_n$ denotes the location of the n-th nucleus relative to the position of the charge carrier, $\boldsymbol{A}_n$ is the vector potential of the nuclear magnetic moment $\boldsymbol{\mu}_n$ and $\boldsymbol{p}$ is the momentum operator of the central particle. For a localised charge carrier interacting with the $\sim 10^4 - 10^5$ nuclei of a quantum dot, the interaction terms in equation (3.1) can be expressed as[29, 117]

$$\begin{aligned}\mathcal{H}_\mathrm{hf} =& \frac{v_0}{2}\frac{16\pi}{3}\mu_\mathrm{B}\gamma\sum_n |u(\boldsymbol{r}_n)|^2|\Psi(\boldsymbol{r}_n)|^2\boldsymbol{S}\cdot\boldsymbol{I}_n \\ &+ 2\mu_\mathrm{B}\gamma\left(\frac{3(\boldsymbol{I}_n\cdot\boldsymbol{r}_n)(\boldsymbol{S}\cdot\boldsymbol{r}_n)}{r_n^5} - \frac{\boldsymbol{S}\cdot\boldsymbol{I}_n}{r_n^3}\right) \\ &+ 2\mu_\mathrm{B}\gamma\frac{\boldsymbol{L}_n\cdot\boldsymbol{I}_n}{r_n^3}\,.\end{aligned} \tag{3.2}$$

Here, the first term describes the contact interaction with unit cell volume v_0, nuclear gyromagnetic ratio γ (assuming only one isotope for now), charge carrier Bloch function $u(\boldsymbol{r}_n)$ at the n-th nucleus and envelope wave function $\Psi(\boldsymbol{r}_n)$ at the n-th lattice site. The second term accounts for the dipolar hyperfine interaction and the final term describes the spin-orbit coupling with $\boldsymbol{L}_n = \boldsymbol{r}_n \times \boldsymbol{p}$.

From equation (3.2) it is clear that the relative coupling strengths of electron and hole spins to the nuclear spin bath will differ considerably. The electron Bloch function in the CB has s-symmetry. Hence, no spin-orbit coupling occurs and the hyperfine interaction strength is determined by the isotropic Fermi contact term[118]. By contrast, the p-symmetry of the VB results in a vanishing heavy hole Bloch function at the lattice sites. This initially led to the assumption that the hole hyperfine interaction would be Ising-like and potentially allow for drastically increased dephasing times compared to the hyperfine induced electron spin dephasing[117, 119]. However, recent experiments have revealed a considerable d-orbital contribution to

the heavy hole Bloch function which results in a non-vanishing transverse term for the hole-nuclear spin coupling[120].

Because of the strong Fermi contact interaction, the long-range dipolar contribution can be neglected in the description of electron hyperfine coupling. One can define an isotope-specific electron hyperfine constant $A^{\mathrm{e}} = \frac{16\pi}{3}\mu_{\mathrm{B}}\gamma|u(0)|^2$ which is independent of $\boldsymbol{r}_n$ as the Bloch amplitude is maximum at all lattice sites in the crystal[118]. We are now taking into account j different isotopes with N_j nuclear spins, and obtain[112, 121]

$$\mathcal{H}_{\mathrm{hf}}^{\mathrm{e}} = \frac{v_0}{2}\sum_j A_j^{\mathrm{e}} \sum_n^{N_j} |\Psi(\boldsymbol{r}_j)|^2 \left(2I_{n,\mathrm{z}}S_{\mathrm{e,z}} + \left[I_n^+ S_{\mathrm{e}}^- + I_n^- S_{\mathrm{e}}^+\right]\right). \tag{3.3}$$

Experimental values for the hyperfine constants of all stable isotopes present in InGaAs quantum dots are listed in table 3.1. The first term ($\propto 2I_{n,\mathrm{z}}S_{\mathrm{e,z}}$) causes a shift in the electron and nuclear spin transition energies whereas the second term ($\propto [I_n^+ S_{\mathrm{e}}^- + I_n^- S_{\mathrm{e}}^+]$) is responsible for the flip-flops between two spins $\boldsymbol{S}_{\mathrm{e}}$ and $\boldsymbol{I}_n$.

As discussed above, the Fermi contact term in equation (3.2) vanishes for the hole hyperfine interaction. The spin-orbit term can be incorporated into the dipolar coupling, and in analogy to A^{e} we can define a heavy hole hyperfine constant

$$A^{\mathrm{h}} = \frac{16}{5}\mu_{\mathrm{B}}\gamma \left\langle \frac{1}{r_n^3} \right\rangle_{\mathrm{u.c.}}, \tag{3.4}$$

where $\langle \ldots \rangle_{\mathrm{u.c.}}$ is the Bloch amplitude expectation value over one unit cell[117, 119]. This definition of A^{h} implies another approximation as it neglects long-range interactions beyond the unit cell which give only minor corrections. Experimentally, values of $A^{\mathrm{h}} \approx 0.1 \cdot A^{\mathrm{e}}$ have been reported[122–124]. For a pure heavy hole, theoretical analysis predicts an Ising-like hyperfine interaction[119]

$$\mathcal{H}_{\mathrm{hf}}^{\mathrm{hh}} = v_0 \sum_j A_j^{\mathrm{h}} \sum_n^{N_j} |\Psi(\boldsymbol{r}_n)|^2 I_{n,\mathrm{z}}S_{\mathrm{h,z}}, \tag{3.5}$$

with hole pseudo-spin $S_\mathrm{h} = \pm 1/2$. In this case, the hole hyperfine coupling could be suppressed effectively by applying an in-plane magnetic field[117, 125] or by narrowing the nuclear spin state distribution[126]. Initial theoretical and experimental work attributed non-vanishing flip-flop terms in the hole hyperfine Hamiltonian to mixing of heavy and light hole states[117, 122]. This led to the proposition of an altered heavy hole hyperfine Hamiltonian[119]

$$\mathcal{H}_\mathrm{hf}^\mathrm{h} = \frac{v_0}{2} \sum_j \frac{A_j^\mathrm{h}}{\sqrt{1+|\beta_\mathrm{VB}|^2}} \sum_n^{N_j} |\Psi(\boldsymbol{r}_n)|^2 \left(2 I_{n,\mathrm{z}} S_{\mathrm{h,z}} + \frac{2|\beta_\mathrm{VB}|}{\sqrt{3}} \left[I_n^+ S_\mathrm{h}^- + I_n^- S_\mathrm{h}^+ \right] \right), \tag{3.6}$$

with the valence band mixing parameter β_VB. More recent experiments have revealed that this picture is still incomplete: NMR data shows that the sign of the hole hyperfine constant depends on the lattice sites, with $A^\mathrm{h} > 0$ for anionic sites and $A^\mathrm{h} < 0$ for cations. This feature cannot be explained by pure p-shell VB mixing. Instead, a more extensive model including d-orbital contributions to the VB can account for the sign changes[120]. These contributions reduce the Ising nature of the hole hyperfine interaction further, setting an intrinsic limit to the extent to which hole decoherence can be suppressed by preparing the nuclear spin bath.

3.1.1 Overhauser and Knight Fields

The hyperfine interaction manifests itself experimentally in the form of reciprocal effective magnetic fields that act on the charge carrier (*Overhauser field*, [127]) and on the nuclear spins (*Knight field*, [128]). In the following discussion, we will focus only on the effective fields arising from electron-nuclear interaction. Similar expressions can be derived for the hole-nuclear interaction. However, since $A^\mathrm{h} \approx 0.1 \cdot A^\mathrm{e}$ the associated fields are considerably smaller and hence usually neglected.

In a mean field approach, the flip-flop term in equation (3.3) averages to zero and the Overhauser field can be approximated as arising from a mean nuclear spin

polarisation $\langle I_\mathrm{z}\rangle$[112, 121]

$$B_\mathrm{hf} = \frac{2}{\mu_\mathrm{B} g_\mathrm{e}} \sum_j c_j A_j^\mathrm{e} \left\langle I_\mathrm{z}^j \right\rangle . \tag{3.7}$$

Here, c_j denotes the relative concentration of the j-th isotope in the quantum dot. For a typical $In_{0.2}Ga_{0.8}As$ dot with $g_\mathrm{e} \approx 0.4$, the maximum Overhauser field induced by a fully polarised nuclear spin bath would be ~ 7.3 T, corresponding to a change in the measured exciton Zeeman splitting $E_\mathrm{hf} = \mu_\mathrm{B} g_\mathrm{e} B_\mathrm{hf} \approx 170\ \mu$eV.

In the next section, we will see how the nuclear spin bath can be polarised effectively. In thermal equilibrium, the bath polarisation ρ is negligibly small even at liquid helium temperatures and external magnetic fields of several tesla. For the $In_{0.2}Ga_{0.8}As$ system at $T = 4$ K and $B_{0,\mathrm{z}} = 8$ T, we can estimate $\rho < 0.1\%$ corresponding to an Overhauser field $B_\mathrm{hf} \approx 5 - 10$ mT from the Boltzmann distribution

$$p_{m,j} = \exp\left[\frac{m_\mathrm{I} \hbar \gamma_j B_{0,\mathrm{z}}}{k_\mathrm{B} T}\right] \Big/ \sum_{m_\mathrm{I}=-I}^{I} \exp\left[\frac{m_\mathrm{I} \hbar \gamma_j B_{0,\mathrm{z}}}{k_\mathrm{B} T}\right], \tag{3.8}$$

with Boltzmann constant k_B and describing the population probabilities $p_{m,j}$ of the $m_\mathrm{I} = -I, -I+1, \ldots I$ states for the j-th isotope. This weak equilibrium polarisation can be understood when taking into account that the nuclear magneton is very small ($\mu_\mathrm{n} \approx \mu_\mathrm{B}/2000$), resulting in correspondingly small Zeeman splittings $\Delta E_\mathrm{Z,n} \ll k_\mathrm{B} T$[129]. However, the hyperfine interaction still leads to a fluctuating Overhauser field with magnitude and direction described by a Gaussian distribution[29, 130]

$$\begin{aligned} f(\boldsymbol{B}_\mathrm{hf}) &= \frac{1}{(2\pi)^{3/2}\sigma_\mathrm{hf}^3} \exp\left(-\frac{|\boldsymbol{B}_\mathrm{hf}|^2}{2\sigma_\mathrm{hf}^2}\right), \\ \sigma_\mathrm{hf}^2 &= \frac{2}{3\mu_\mathrm{B}^2 g_\mathrm{e}^2} \frac{\sum_j c_j^2 (A_j^\mathrm{e})^2 I^j (I^j+1)}{N}, \end{aligned} \tag{3.9}$$

where the standard deviation σ_hf is found to be on the order of $10 - 30$ mT for an $In_{0.2}Ga_{0.8}As$ dot with $N \approx 10^4 - 10^5$ nuclear spins. Once again the index j denotes the summation over all nuclear species present in the quantum dot. From equation

(3.9) we see that the width of the distribution scales with $1/\sqrt{N}$, indicating that the fluctuations become smaller for larger systems such as electrostatically defined quantum dots[131, 132] or dots in nanowires[133].

The corresponding Knight field which an individual nuclear spin in the quantum dot is exposed to is generally weaker than the Overhauser field. Introducing a filling factor $f_\mathrm{e} \in [0, 1]$ for the electron occupation of the dot, we have[112]

$$B_{\mathrm{K},n} = \frac{f_\mathrm{e} v_0}{\gamma_n} A_n^\mathrm{e} \left|\Psi(\boldsymbol{r}_n)\right|^2 \langle S_\mathrm{z}^\mathrm{e}\rangle \,, \tag{3.10}$$

for a nucleus n at relative position $\boldsymbol{r}_n$. We can roughly estimate the relative field amplitudes as $B_{\mathrm{K},k}/B_\mathrm{hf} \approx (\mu_\mathrm{B} g_\mathrm{e})/(N \mu_\mathrm{n} g_\mathrm{n})$. The magneton ratio $\mu_\mathrm{e}/\mu_\mathrm{n} \approx 2000$ only partially compensates for the fact that the small probability of locating the electron at a specific lattice site ($\propto N^{-1}$) reduces the effective field acting on a given nucleus n[112]. This is in agreement with experimental results: reported Knight field values in InGaAs quantum dots are in the range of $1 - 3$ mT[134, 135].

3.1.2 Spin Flips and Dynamic Nuclear Polarisation

So far we have only analysed the effect of the diagonal or secular hyperfine interaction term $\propto 2 I_{k,\mathrm{z}} S_{\mathrm{e,z}}$ in equation (3.3). However, the off-diagonal or spin-flip term also plays a significant role in the interaction between the electron spin (and to a lesser extent the hole spin) and the nuclear spin bath. As mentioned before, the equilibrium nuclear spin polarisation at $T = 4$ K is very small ($\rho < 0.1\%$) even at large magnetic fields[129]. On the other hand, the nuclear spins in InGaAs are only very weakly coupled to the lattice at low temperatures $T \lesssim 10$ K[136]. In quantum dot systems nuclear spin relaxation times of several minutes and even hours have been reported[85, 114, 115]. By comparison, electron spin relaxation times are found to be on the order of tens of milliseconds[77].

The concept of *dynamic nuclear polarisation* (DNP) is based on an effective trans-

fer of spin polarisation from the electron to the nuclear bath: first a non-equilibrium electron spin polarisation is created optically[137, 138] or electrically[139, 140]. The electron spin then transfers its polarisation to the nuclei via the flip-flop term of the hyperfine interaction. If this two-step process is repeated at a sufficiently high rate a considerable nuclear spin polarisation degree can be reached[127, 141, 142]. In self-assembled quantum dots, DNP is commonly created by optical spin pumping. In the following discussion we only look at electron-nuclear spin flips and neglect the weaker coupling of the hole spin to the nuclear bath.

The established scheme for producing large nuclear polarisation in a quantum dot is based on optical excitation with high powers and circular polarisation. Using this approach, polarisation degrees of up to $\rho \approx 65\%$ were first observed in GaAs quantum dots[121, 137]. Similar nuclear polarisation degrees have since been achieved in InGaAs[138, 143–145] and InP dots[82, 146, 147] under both resonant and non-resonant (wetting layer) optical excitation.

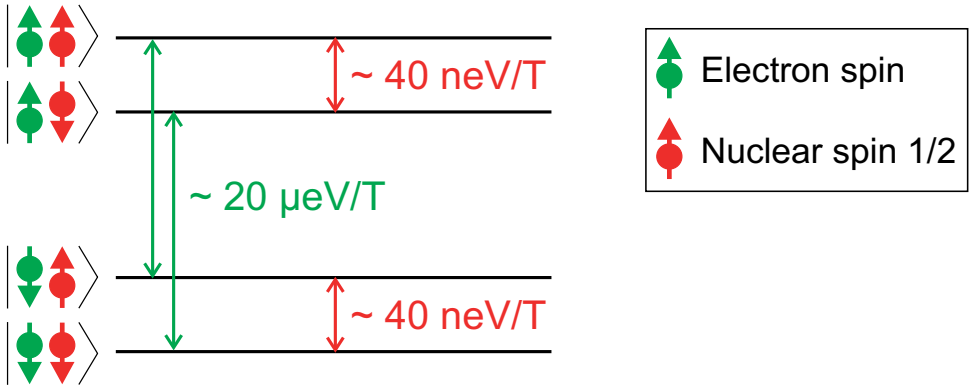

Figure 3.1: Schematic energy level structure of a coupled electron-nuclear spin system. For illustration purposes we assume that $I_n = \frac{1}{2}$. The nuclear Zeeman splitting (red) is three orders of magnitude smaller than the splitting of the electron spin states in a magnetic field (green).

In general, electron-nuclear spin-flips are suppressed in a magnetic field as the nuclear Zeeman splitting $\Delta E_{\mathrm{Z,n}}$ is $\sim 10^3$ times smaller than that of the electron[148] (see figure 3.1). However, there are several ways of achieving significant nuclear polarisation degrees despite this limitation. In quantum dots, two primary DNP

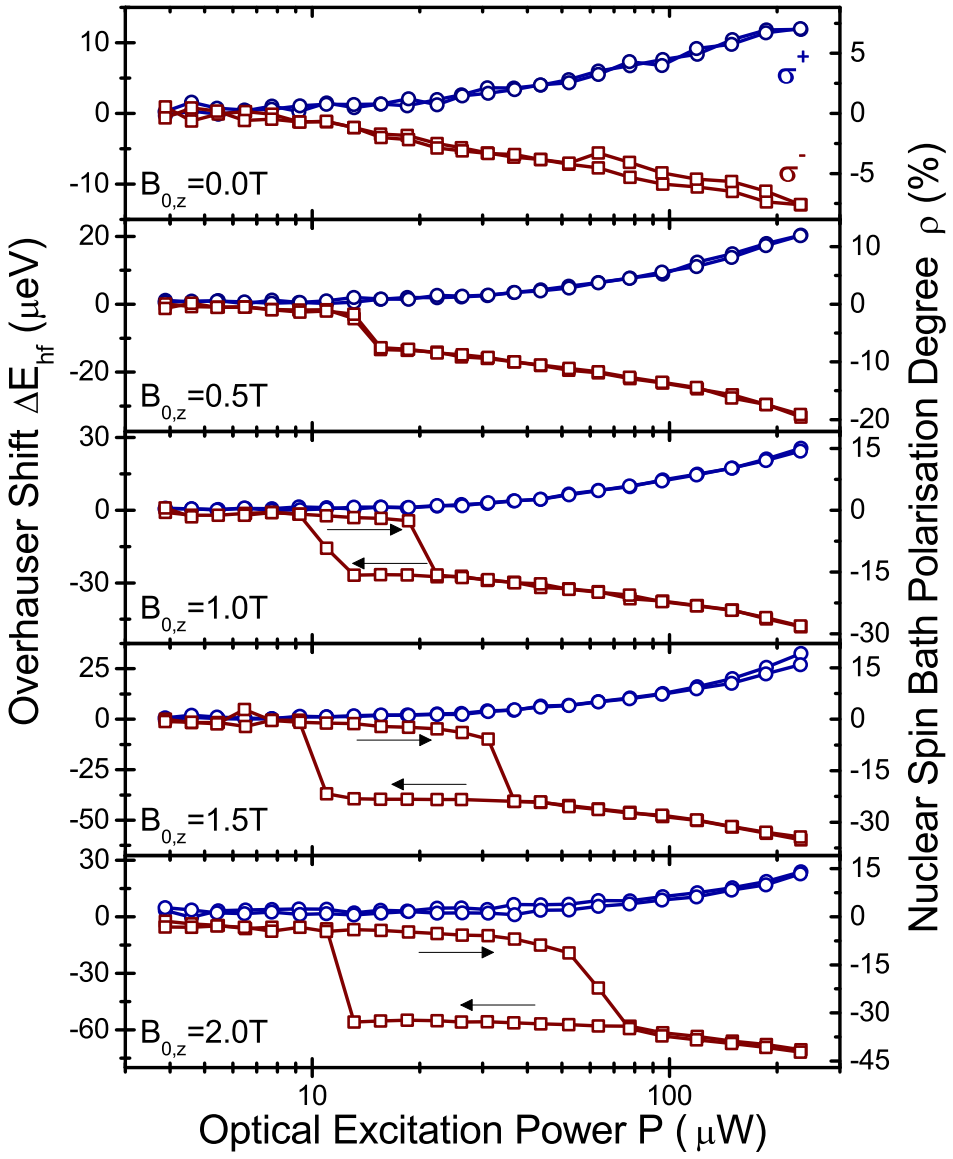

Figure 3.2: Dependence of the Overhauser splitting ΔE_{hf} between the bright X^0 transitions on the non-resonant σ^+ (circles) or σ^- (squares) circularly polarised optical excitation power P at different external magnetic fields $B_{0,z}$. The right axis shows ΔE_{hf} in terms of the spin bath polarisation degree ρ. Black arrows indicate increasing/ decreasing excitation power. Pronounced non-linearities are observed under σ^- polarised excitation for $B_{0,z} \geq 1$ T.

paths have been identified: hyperfine spin-flips in combination with the radiative recombination of dark neutral exciton states, and nuclear polarisation via an electron spin-flip in the initial (final) state of a positive (negative) trion. We note that the first process requires either off-resonant excitation followed by a hole spin-flip during relaxation into the dot or a finite mixing of bright and dark states. Furthermore, the bright and dark states are split by the exchange interaction δ_0, requiring an external magnetic field to tune them into resonance for a commensurable build-up of DNP[149]. Under non-resonant excitation it appears that spin flips of delocalised electrons are responsible for the observed nuclear polarisation as large Overhauser fields are only measured at optical pumping powers beyond the saturation values of X^0 and $2X^0$[82, 83].

The efficiency of the spin-flip process is mainly limited by three factors: a large energy splitting of the electron spin states ΔE_e reduces the spin-flip rate as $w_{ff} \propto \frac{|A^e|^2}{\Delta E_e^2}$ (the nuclear Zeeman splitting is negligible as it is several orders of magnitude smaller, see figure 3.1)[121, 145, 150]. In addition, low electron spin pumping or extraction efficiencies limit the degree of spin bath polarisation that can be achieved. These two parameters depend strongly on the experimental technique used for spin pumping, with the extraction rate generally limited by the radiative exciton lifetime[148]. By contrast, the splitting of the electron spin levels changes dynamically during the DNP build-up. If an external magnetic field $B_{0,z}$ is applied, the Overhauser field can be oriented either parallel or anti-parallel to $B_{0,z}$, thus increasing or decreasing ΔE_e and resulting in a negative or positive feedback on the polarisation rate. This in turn can lead to strong non-linearities in the optical power and magnetic field dependence of the energy shift induced by the Overhauser field. Several groups have reported on such non-linear behaviour characterised by bistabilities and hysteresis effects occurring for anti-parallel orientation of B_{hf} and $B_{0,z}$[143–145].

An example of such a bistability in X^0 under non-resonant ($\sim$ 850 nm) optical excitation in sample A is shown in figure 3.2. The Overhauser shift is measured

as a function of the excitation power at different external magnetic fields $B_{0,z}$. For $B_{0,z} \geq 1$ T, a pronounced hysteresis loop starts to appear under σ^--excitation (red) as an efficient positive feedback facilitates the DNP build-up. This mechanism remains efficient either until the external field is fully compensated ($B_{hf} = -B_{0,z}$) or an equilibrium with competing depolarisation processes is reached[121, 148].

However, even under optimal conditions the highest polarisation degrees reported to date are limited to values of $\rho \approx 65\%$[121, 145, 147, 151], seemingly independent of the type of quantum dot and chosen DNP technique. It has been concluded that, in addition to limitations due to the finite radiative exciton lifetime and electron Zeeman energy, a nuclear hyperfine dark state fundamentally limits the extent to which the spin bath can be polarised[147, 152].

3.2 Spin Relaxation in a Quantum Dot

The spin of a single confined electron or hole is the centrepiece of the prevalent scheme for the implementation of qubits in quantum dots[14]. The most important requirement for quantum computation is the isolation of the qubit from its environment[18]. It is intuitive that information encoded in a single electron or hole spin can get lost if this spin is exposed to a fluctuating spin or charge environment. Here we will first discuss how this "loss" of information can be quantified before looking at the relevant spin-environment interactions in a quantum dot in more detail.

The lifetime of a given spin state is characterised by two timescales. The *longitudinal* or *spin-lattice relaxation time* T_1 is a time constant characterising the likelihood of a spin-flip along the quantisation axis (in our case the optical excitation axis $\hat{e}_z$). For a spin ensemble or for the average over many single-spin measurements it describes the timescale over which the initial polarisation along $\hat{e}_z$ decays back to its equilibrium value (see figure 3.3a). The *transverse relaxation* or *decoherence time*

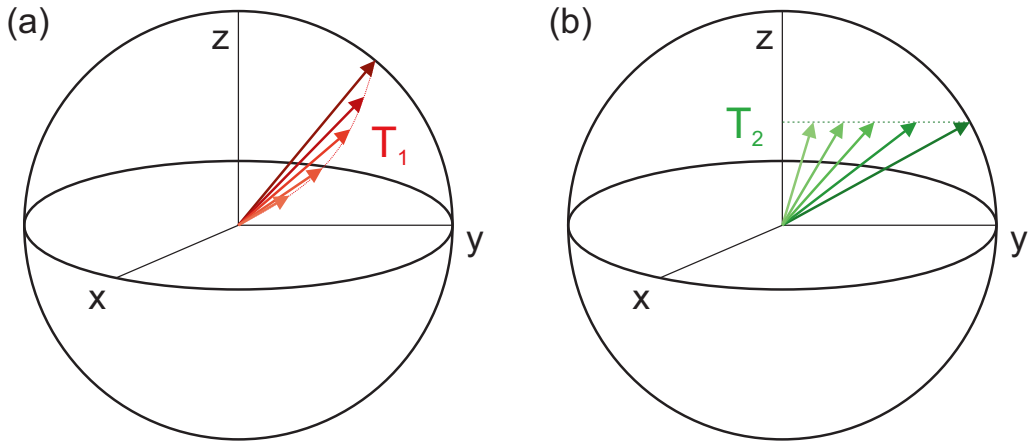

Figure 3.3: Spin relaxation is characterised by the longitudinal and transverse decay times. (a) The longitudinal relaxation time T_1 describes the decay of the spin polarisation along the quantisation axis $\hat{e}_z$. (b) The decoherence time T_2 is a measure of the transverse decay and does not change the polarisation along $\hat{e}_z$.

T_2 is illustrated in figure 3.3b. It describes how quickly a spin loses its phase coherence, i.e. the timescale over which spin-environment interactions change the phase of the spin precession about $\hat{e}_z$. In an ensemble measurement, we have to take into account additional contributions: even if the spins are not interacting with each other, variations in the local precession frequency of each spin can lead to a much faster ensemble dephasing, described by the *dephasing time* T_2^*[18, 153]. The phase information is not necessarily irretrievably lost in T_2^* processes and can be recovered under certain circumstances. All three relaxation timescales are linked by the expression

$$\frac{1}{T_2} = \frac{1}{2T_1} + \frac{1}{T_2^*} \,, \tag{3.11}$$

where we see that $T_2 \leq 2T_1$. In the course of this work we will also use a fourth decay time constant, the phase memory time T_M. In nuclear magnetic resonance, we probe and manipulate ensembles of up to $\sim 10^5$ nuclear spins. In this context, we refer to T_M as the bath decoherence timescale for a spin ensemble decoupled from its environment and T_2 as the single spin decoherence time obtained when intrinsic couplings of the ensemble are also suppressed.

3.2.1 Electron and Hole Spin Relaxation and Decoherence

In this section, we will only review the mechanisms and timescales of charge spin relaxation and decoherence in self-assembled quantum dots. The experimental methods for obtaining these quantities are similar to the techniques used for measuring the corresponding nuclear spin lifetimes which will be discussed in greater detail in chapters 5.3 and 5.5.

In bulk semiconductors and quantum wells, the electron spin relaxation time $T_{1,\mathrm{e}}$ is usually limited by various spin-orbit mediated relaxation mechanisms. Most of these couplings are suppressed in a quantum dot due to the strong confinement of the electron wavefunction[154]. Instead, the electron-nuclear hyperfine flip-flop discussed in the previous section dominates spin relaxation in the absence of magnetic fields[131]. This mechanism can be quenched effectively by applying a small external field $B_{0,\mathrm{z}}$ as the nuclear Zeeman splitting is much smaller than that of the electron ($\mu_\mathrm{n} \approx \mu_\mathrm{B}/2000$).

At larger magnetic fields a phonon-assisted relaxation process becomes dominant. This mechanism is not very efficient and experiments have found $T_{1,\mathrm{e}} \geq 20$ ms at $B_{0,\mathrm{z}} \leq 4$ T in self-assembled quantum dots[77] as well as $T_{1,\mathrm{e}} \geq 1$ s at $B_{0,\mathrm{z}} \leq 1$ T in electrostatically defined dots[155]. In both cases a proportionality $T_{1,\mathrm{e}} \propto \omega_0^4 B_{0,\mathrm{z}}^{-5}$ was observed, with ω_0 denoting the shell spacing introduced in chapter 2.2.1[156]. This behaviour can be understood when taking into account a finite spin-orbit coupling between s- and p-shell states of opposite spin which depends on the level spacing[154, 157]. The discrepancy between the findings in self-assembled and electrostatically defined quantum dots can be explained to some extent by an additional temperature dependence $T_{1,\mathrm{e}} \propto T^{-1}$[109, 158] as the results of [155] were obtained at $T \sim 120$ mK compared to $T = 1$ K in the experiments on self-assembled quantum dots[77].

For holes in semiconductors, spin-orbit mixing of heavy and light hole bands typically results in spin relaxation over sub-picosecond timescales[159]. Experiments

in self-assembled quantum dots have shown that this mechanism is quenched by the strong confinement. Instead, $T_{1,\mathrm{h}}$ is limited by the same phonon-mediated relaxation process as $T_{1,\mathrm{e}}$ with the longest reported values of up to $T_{1,\mathrm{h}} = 1$ ms at small $B_{0,\mathrm{z}} \approx 20$ mT ($T = 4.2$ K) being slightly shorter than the corresponding electron values[110]. With increasing $B_{0,\mathrm{z}}$ and T, a strong decrease of the relaxation time down to $T_{1,\mathrm{h}} \lesssim 10$ μs is observed[109].

While longitudinal relaxation does ultimately restrict the decoherence time of a charge carrier spin in a quantum dot (see equation (3.11)), $T_{2,\mathrm{e/h}}$ is normally limited by pure dephasing mechanisms unrelated to spin-orbit coupling[29, 160]. For electron spins, time- or ensemble-averaged dephasing times $T^*_{2,\mathrm{e}}$ in the range of a few nanoseconds have been reported by several groups[161–165]. As we saw in section 3.1.1, the nuclear spin bath polarisation of a quantum dot typically fluctuates on a scale of $\sigma_{\mathrm{hf}} \sim 10 - 30$ mT in excellent agreement with these timescales ($T^*_{2,\mathrm{e}} \approx \frac{\hbar}{\mu_{\mathrm{B}} g_{\mathrm{e}} \sigma_{\mathrm{hf}}} \sim 1 - 3$ ns). Although the spin bath is frozen at $T^*_{2,\mathrm{e}}$ timescales, it still induces a randomly oriented static Overhauser field about which the electron spin precesses[29, 30, 166]. In this respect, the strong confinement of the quantum dot is disadvantageous as the fluctuation amplitude scales as $\propto 1/\sqrt{N}$ (see equation (3.9)). However, using electron *Hahn echo* techniques, this ensemble dephasing can be refocused and $T_{2,\mathrm{e}}$ values of ~ 1 μs have been reported[164, 167, 168].

A second source of decoherence particular to self-assembled quantum dots has been identified recently: the intrinsic strain in the system induces an electric field gradient to which the nuclear quadrupole moment couples (see chapter 5, [39, 41, 169]). This causes a coherent evolution of the spin bath which in turn affects the electron spin coherence on a timescale of ~ 750 ns[170, 171]. Along with dephasing arising from equally coherent nuclear Larmor precession, this can also be refocused by a Hahn echo sequence. However, a Hahn echo can by its nature only refocus dephasing processes occurring on sufficiently long timescales. Longer $T_{2,\mathrm{e/h}}$ times can be achieved using *dynamical decoupling sequences*[172, 173] which will be discussed

in more detail in the context of nuclear spin dephasing in chapter 6. Using one such sequence, values of up $T_{2,e} \approx 0.87$ ms have been demonstrated recently in electrostatically defined quantum dots[174].

Several alternative approaches have been put forward for suppressing the inhomogeneous hyperfine dephasing[15]. The most straight-forward of these is based on applying magnetic fields and polarising the nuclear spin bath[148, 175]. Although hitherto unachievable polarisation degrees of $\rho > 99\%$ would be required for a substantial increase of $T_{2,e}$[15, 37], extended electron spin dephasing times $T^*_{2,e}$ have already been observed experimentally for much smaller nuclear polarisation degrees[38, 135, 176].

Generally, the single spin decoherence time is limited by spectral diffusion due to nuclear-nuclear dipolar flip-flops[29, 30, 177]. For GaAs quantum dots, this timescale agrees well with the sub-millisecond decoherence times measured in dynamical decoupling experiments[174, 178]. As we will see in chapter 5, the strain in an InGaAs quantum dot leads to a slow-down of the nuclear spin flip-flop rate. Therefore, the potential limit for central spin decoherence times is considerably longer in this system[41].

Although the hole-nuclear hyperfine coupling is approximately ten times weaker than that with the electron, reported dephasing times are only marginally longer. Several groups have found ensemble dephasing times of $T^*_{2,h} \approx 10 - 20$ ns[20, 122, 179], with Hahn echo decay times of $T_{2,h} = 1.1$ μs similar to those found for electron spins[78]. In stark contrast, a coherent population trapping experiment yielded $T^*_{2,h} > 100$ μs[125]. This discrepancy has been attributed largely to the high sensitivity of hole spins to electric field fluctuations[180, 181].

3.2.2 Nuclear Spin Decoherence

We have seen in the previous section that the coherence of the central spin in a quantum dot is usually limited by hyperfine-induced dephasing[29]. A full under-

standing of the nuclear spin coherence properties is therefore desirable to identify the timescales on which the intrinsic bath dynamics will limit the electron and hole T_2 times. In this section we will only introduce the nuclear spin relaxation mechanisms in a general fashion. A more detailed discussion will be given in chapters 5-7 where these mechanisms and the associated timescales are probed experimentally.

The nuclear spin bath in an empty self-assembled quantum dot is very stable at cryogenic temperatures. Longitudinal spin relaxation times $T_{1,\mathrm{n}}$ of several hours have been measured, indicating extremely weak coupling to the environment[85, 114, 115]. This is because the main relaxation mechanism of spin diffusion out of the dot is quenched by the intrinsic strain in the dot. Furthermore, quadrupolar relaxation is strongly suppressed due to the lack of phonons at temperatures $T \lesssim 10$ K[136]. In chapter 5, we will see that $T_{1,\mathrm{n}}$ depends strongly on the charge occupancy in the dot as cotunnelling and electron-mediated nuclear spin diffusion result in hyperfine-mediated fast relaxation[115, 182].

Nuclear spin dephasing in InGaAs quantum dots is dominated by is isotope-dependent quadrupolar interactions which limit $T^*_{2,\mathrm{n}}$ to $5-20$ μs (for the central spin transition $-\frac{1}{2} \leftrightarrow +\frac{1}{2}$)[39]. This dephasing can be refocused by nuclear Hahn echo sequences and in chapter 5 we will show that the nuclear spin phase memory times $T^{\mathrm{HE}}_{\mathrm{M,n}}$ are within a range of $1-4$ ms, confirming earlier results reported in [41]. In the absence of confined charges, nuclear $T_{\mathrm{M,n}}$ times are limited by dipolar dephasing which is partially suppressed by the quadrupolar interaction in our system. For comparison, decoherence times in unstrained GaAs/AlGaAs quantum dots and wells were found to be about five times shorter[183, 184].

Recent results by Munsch et al.[42] indicate that RKKY-type interactions[185] similar to those limiting $T_{1,\mathrm{n}}$ might reduce the nuclear decoherence time in the presence of an electron down to $20-40$ μs. The implications of this and strategies towards decoupling the central spin from the bath will be discussed in chapters 6 and 8.

3.3 Nuclear Spin Manipulation

A range of experimental techniques have been developed that allow the manipulation of nuclear spin states using radio frequency (rf) excitation in a constant magnetic field. These are collectively referred to as *nuclear magnetic resonance* (NMR) and based on identical theoretical principles. The first experimental demonstration of NMR was reported by I. Rabi in 1939. He showed in a modified version of the Stern-Gerlach experiment that rf excitation at the nuclear transition frequencies of atoms caused additional deflections[186, 187]. Major early contributions that opened the field of NMR to experiments in solids and liquids were made independently by F. Bloch[188, 189] and E. Purcell et al.[190] in 1946. Bloch's technique was based on the realisation that the nuclear spin rotation under rf excitation causes a macroscopic change of the sample magnetisation away from an external magnetic field vector $\boldsymbol{B}_0$. As the tilted nuclear spins precess about $\boldsymbol{B}_0$, they induce a small but measurable current signal at their resonance frequency in a suitably placed copper coil. Purcell et al. detected the NMR signal directly via the rf energy absorbed at resonance.

3.3.1 Spin Resonance in the Rabi Model

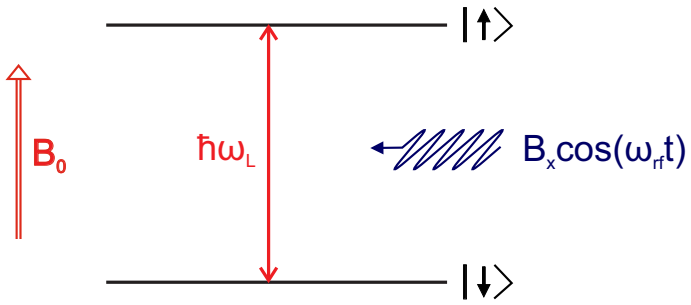

Figure 3.4: NMR is the resonant interaction of a Zeeman split nuclear spin level system with an oscillating magnetic field $\boldsymbol{B}_\mathrm{x} \perp \boldsymbol{B}_0$.

For a theoretical description of NMR we have to consider a nuclear spin system coupled to a static external magnetic field $B_{0,\mathrm{z}}$ and interacting with a weak magnetic field B_x oscillating at radio frequency ω_rf in a plane perpendicular to $B_{0,\mathrm{z}}$ as illus-

trated in figure 3.4. For simplicity, we shall limit the following discussion to a nuclear spin-$\frac{1}{2}$ system, although all of the concepts introduced here can be generalised to systems with $I > \frac{1}{2}$[116, 191].

Without loss of generality, we assume that $\boldsymbol{B}_0 = B_{0,\mathrm{z}}\hat{e}_\mathrm{z}$. Interaction with a given nuclear spin is described by the Zeeman Hamiltonian $\mathcal{H}_0 = -\gamma \boldsymbol{I} \cdot \boldsymbol{B}_0 = -\gamma I_\mathrm{z} B_{0,\mathrm{z}}$ where $I_\mathrm{z} = \frac{\hbar}{2}\sigma_\mathrm{z}$ and σ_z denotes the Pauli matrix with eigenspinors $|\uparrow\rangle$ and $|\downarrow\rangle$. In the absence of further interactions, this system has the well-known Zeeman eigenenergies $E_0 = \pm\frac{\hbar}{2}\gamma B_{0,\mathrm{z}} = \mp\frac{\hbar}{2}\omega_\mathrm{L}$ with $\omega_\mathrm{L} = -\gamma B_{0,\mathrm{z}}$ describing the Larmor precession frequency of the nuclear spin about $\boldsymbol{B}_0$.

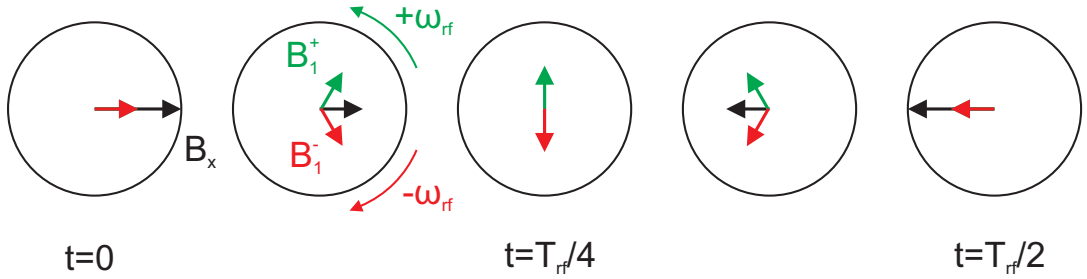

Figure 3.5: The linearly polarised rf field B_x can be split into two counter-rotating circularly polarised fields of amplitude $B_1 = \frac{B_\mathrm{x}}{2}$.

We now consider the effect of a second magnetic field $\boldsymbol{B}_\mathrm{x}$ linearly polarised along $\hat{e}_\mathrm{x}$ and oscillating at frequency ω_rf. For convenience, we split the oscillating field into two counter-rotating fields of equal amplitude as illustrated in figure 3.5.

$$\boldsymbol{B}_\mathrm{x} = B_\mathrm{x}\cos(\omega_\mathrm{rf}t)\hat{e}_\mathrm{x} = \frac{B_\mathrm{x}}{2}\left(\mathrm{e}^{\mathrm{i}\omega_\mathrm{rf}t} + \mathrm{e}^{-\mathrm{i}\omega_\mathrm{rf}t}\right) . \tag{3.12}$$

As we will see shortly, this approach becomes advantageous when $\omega_\mathrm{rf} \approx \omega_\mathrm{L}$. We label the effective field amplitudes of the two counter-rotating components as $B_1 = \frac{B_\mathrm{x}}{2}$ with corresponding Larmor frequencies $\omega_1 = -\gamma B_1$. Unless stated otherwise, these will be the quantities used to characterise the NMR field amplitude throughout this thesis. The full time-dependent Schrödinger equation for the interacting system is

given by

$$\mathrm{i}\hbar\frac{\partial}{\partial t}\left|\Psi\right\rangle = \left(\mathcal{H}_0 + \mathcal{H}_1\right)\left|\Psi\right\rangle = \left(I_\mathrm{z}\omega_\mathrm{L} + I_\mathrm{x}\omega_1\left(\mathrm{e}^{\mathrm{i}\omega_\mathrm{rf}t} + \mathrm{e}^{-\mathrm{i}\omega_\mathrm{rf}t}\right)\right)\left|\Psi\right\rangle \ . \tag{3.13}$$

In order to remove the time dependence of the Hamiltonian, we switch to an interaction frame of reference rotating about $\hat{e}_\mathrm{z}$ at frequency ω_rf. We split $\mathcal{H} = \mathcal{H}_0 + \mathcal{H}_1$ into an interaction Hamiltonian $\mathcal{H}_\mathrm{I} = I_\mathrm{z}\omega_\mathrm{rf}$ and a perturbation Hamiltonian $\mathcal{V} = \mathcal{H} - \mathcal{H}_\mathrm{I}$. The benefits of this choice of reference frame and of the counter-rotating field description of $\boldsymbol{B}_\mathrm{x}$ become clear when we look at $\mathcal{V}$ in the interaction frame. After transformation under the time evolution operator $\mathcal{U} = \mathrm{e}^{-\mathrm{i}\mathcal{H}_\mathrm{I}t/\hbar}$ we obtain

$$\mathcal{V}_\mathrm{I} = \mathcal{U}^\dagger\mathcal{V}\mathcal{U} = \frac{\hbar}{2}\begin{pmatrix} -\Delta & \omega_1\left(1+\mathrm{e}^{2\mathrm{i}\omega_\mathrm{rf}t}\right) \\ \omega_1\left(1+\mathrm{e}^{-2\mathrm{i}\omega_\mathrm{rf}t}\right) & \Delta \end{pmatrix} \ , \tag{3.14}$$

where $\Delta = \omega_\mathrm{rf} - \omega_\mathrm{L}$ is the detuning between the rf excitation and the Zeeman splitting. In the *rotating wave approximation*, we can drop the fast-oscillating time-dependent terms $\propto 2\omega_\mathrm{rf}$. If the rf excitation is resonant ($\Delta = 0$) this leaves us with an effective static in-plane field $\boldsymbol{B}_1 \parallel \hat{e}_{\mathrm{x}'}$ acting on the spin in the rotating frame $\{\hat{e}_{\mathrm{x}'}, \hat{e}_{\mathrm{y}'}, \hat{e}_\mathrm{z}\}$. The approximate Schrödinger equation in the rotating frame (including detuning Δ) is

$$\mathrm{i}\hbar\frac{\partial}{\partial t}\left|\Psi\right\rangle_\mathrm{I} = \left(I_\mathrm{z}\Delta - I_\mathrm{x}\omega_1\right)\left|\Psi\right\rangle_\mathrm{I} \ . \tag{3.15}$$

Using the ansatz $\left|\Psi\right\rangle_\mathrm{I} = c_1(t)\left|\uparrow\right\rangle_\mathrm{z} + c_2(t)\left|\downarrow\right\rangle_\mathrm{z}$ with $|c_1|^2 + |c_2|^2 = 1$, we obtain two coupled linear differential equations with solutions

$$\begin{pmatrix} c_1(t) \\ c_2(t) \end{pmatrix} = \begin{pmatrix} \cos\left(\frac{\Omega t}{2}\right) - \frac{\mathrm{i}\Delta}{\Omega}\sin\left(\frac{\Omega t}{2}\right) \\ \frac{\mathrm{i}\omega_1}{\Omega}\sin\left(\frac{\Omega t}{2}\right) \end{pmatrix} \ , \tag{3.16}$$

where we introduced the *Rabi frequency* $\Omega = \sqrt{\Delta^2 + \omega_1^2}$ and assumed that the spin was initially in state $\left|\uparrow\right\rangle_\mathrm{z}$, i.e. $c_1(0) = 1$ and $c_2(0) = 0$. The time dependent

populations of the two states are described by

$$p_\uparrow = |c_1(t)|^2 = \frac{\Delta^2}{\Omega^2} + \frac{\omega_1^2}{\Omega^2}\cos^2\left(\frac{\Omega t}{2}\right) \tag{3.17}$$

$$p_\downarrow = |c_2(t)|^2 = \frac{\omega_1^2}{\Omega^2}\sin^2\left(\frac{\Omega t}{2}\right) \ , \tag{3.18}$$

Experimentally, we measure the population difference between the two spin states. Our NMR signal is therefore proportional to $p_\uparrow - p_\downarrow = \frac{\Delta^2}{\Omega^2} + \frac{\omega_1^2}{\Omega^2}\cos(\Omega t)$.

We note that the population oscillates between the two spin states, although a full spin rotation is only possible in resonance ($\Delta = 0$). In this case the Rabi frequency corresponds to the Larmor frequency about the static field B_1 in the rotating frame. By applying a resonant rf pulse of duration t_p, we can rotate the nuclear spin about a given in-plane axis. In addition, we can introduce a phase φ in equation (3.12). This does not affect the populations of the states $|\uparrow\rangle_\mathrm{z}$ and $|\downarrow\rangle_\mathrm{z}$. However, it alters the in-plane rotation axis, allowing for rotations over the surface of the entire Bloch sphere:

$$\mathrm{i}\hbar\frac{\partial}{\partial t}\left|\Psi\right\rangle_\mathrm{I} = \left(-I_\mathrm{z}\Delta + \left[I_\mathrm{x}\cos(\varphi) + I_\mathrm{y}\sin(\varphi)\right]\omega_1\right)\left|\Psi\right\rangle_\mathrm{I} \ . \tag{3.19}$$

As we will see in the next section and in chapters 5 and 6 in more detail, this allows us to probe and control the decay dynamics of the nuclear spin bath coherently.

Finally, we look at nuclear spins with $I > \frac{1}{2}$. From table 3.1 we see that the stable isotopes in an InGaAs quantum dot have either nuclear spin $I = \frac{3}{2}$ (gallium, arsenic) or $I = \frac{9}{2}$ (indium). Neglecting higher quantum transitions (e.g. $-\frac{1}{2} \leftrightarrow +\frac{3}{2}$), we can use the same theoretical treatment as above to describe the resonant interaction of a spin transition with an rf field. However, we have to take into account that the

spin operators σ_i change.

$$\sigma_{\mathrm{x}}(\tfrac{1}{2}) = \begin{pmatrix} 0 & 1 \\ 1 & 0 \end{pmatrix} \quad \sigma_{\mathrm{x}}(\tfrac{3}{2}) = \begin{pmatrix} 0 & \sqrt{3} & 0 & 0 \\ \sqrt{3} & 0 & 2 & 0 \\ 0 & 2 & 0 & \sqrt{3} \\ 0 & 0 & \sqrt{3} & 0 \end{pmatrix} , \tag{3.20}$$

This is important for the coupling to the rf field: the Rabi oscillations observed for the central transition (CT) of a spin-$\frac{3}{2}$ nucleus are twice as fast as those for a spin-$\frac{1}{2}$ system at identical rf field $B_1 = -\frac{\omega_1}{\gamma}$. If one of the satellite transitions (ST, $\pm\frac{3}{2} \leftrightarrow \pm\frac{1}{2}$) is driven, the oscillation frequency is still increased by a factor $\sqrt{3}$.

3.3.2 The Bloch Equations of Motion

The results of the previous section can also be derived from purely classical considerations. As we will see, this allows us to introduce the phenomenological relaxation constants from section 3.2. Instead of the spin $\boldsymbol{I}$, we now use the nuclear magnetic moment $\boldsymbol{\mu} = \gamma \boldsymbol{I}$ which we can generalise further as a macroscopic magnetisation $\boldsymbol{M} = \sum_j \boldsymbol{\mu}_j$ arising from j nuclear spins. As before, we consider a static external magnetic field $\boldsymbol{B}_0$ and an orthogonal linearly polarised field $\boldsymbol{B}_{\mathrm{x}}$

$$\begin{aligned} \boldsymbol{B}_0 &= B_{0,\mathrm{z}} \hat{e}_{\mathrm{z}} \, , \\ \boldsymbol{B}_{\mathrm{x}} &= 2B_1 \cos(\omega_{\mathrm{rf}} t) \hat{e}_{\mathrm{x}} \, . \end{aligned} \tag{3.21}$$

The precession of the magnetisation vector about the magnetic field $\boldsymbol{B}_0 + \boldsymbol{B}_{\mathrm{x}}$ is described by the torque formula[192]

$$\frac{\mathrm{d}\boldsymbol{M}}{\mathrm{d}t} = -\gamma(\boldsymbol{B}_0 + \boldsymbol{B}_{\mathrm{x}}) \times \boldsymbol{M} = \boldsymbol{T}_\omega \cdot \boldsymbol{M} \, , \tag{3.22}$$

where we replaced the cross product by a matrix multiplication for convenience and introduced the skew-symmetric transformation matrix

$$\boldsymbol{T}_\omega = \begin{pmatrix} 0 & -\omega_\mathrm{L} & 0 \\ \omega_\mathrm{L} & 0 & -2\omega_1 \cos(\omega_\mathrm{rf} t) \\ 0 & 2\omega_1 \cos(\omega_\mathrm{rf} t) & 0 \end{pmatrix} , \tag{3.23}$$

with $-\boldsymbol{T}_\omega = \boldsymbol{T}_\omega^\mathsf{T}$. Next, we transform the equation of motion (3.22) into the rotating frame of ω_rf. We define a second transformation matrix

$$\boldsymbol{R} = \begin{pmatrix} \cos(\omega_\mathrm{rf} t) & \sin(\omega_\mathrm{rf} t) & 0 \\ -\sin(\omega_\mathrm{rf} t) & \cos(\omega_\mathrm{rf} t) & 0 \\ 0 & 0 & 1 \end{pmatrix} , \tag{3.24}$$

and translate the coordinate system as $\hat{e}_i \mapsto \boldsymbol{R} \cdot \hat{e}_i = \hat{e}_{i'}$. From the left side of equation (3.22) we get

$$\frac{\mathrm{d}\boldsymbol{M}'}{\mathrm{d}t} = \frac{\mathrm{d}(\boldsymbol{R} \cdot \boldsymbol{M})}{\mathrm{d}t} = \boldsymbol{R} \cdot \frac{\mathrm{d}\boldsymbol{M}}{\mathrm{d}t} + \frac{\mathrm{d}\boldsymbol{R}}{\mathrm{d}t} \cdot \boldsymbol{M} . \tag{3.25}$$

Now we can substitute for $\frac{\mathrm{d}\boldsymbol{M}}{\mathrm{d}t}$ from the inertial equation of motion (3.22):

$$\begin{aligned} \frac{\mathrm{d}\boldsymbol{M}'}{\mathrm{d}t} &= \boldsymbol{R} \cdot \boldsymbol{T}_\omega \cdot \boldsymbol{M} + \frac{\mathrm{d}\boldsymbol{R}}{\mathrm{d}t} \cdot \boldsymbol{M} = \left(\boldsymbol{R} \cdot \boldsymbol{T}_\omega + \frac{\mathrm{d}\boldsymbol{R}}{\mathrm{d}t} \right) \cdot \boldsymbol{M} = \\ &= \left(\boldsymbol{R} \cdot \boldsymbol{T}_\omega \cdot \boldsymbol{R}^\mathsf{T} + \frac{\mathrm{d}\boldsymbol{R}}{\mathrm{d}t} \cdot \boldsymbol{R}^\mathsf{T} \right) \cdot \boldsymbol{M}' , \end{aligned} \tag{3.26}$$

where we used $\boldsymbol{M} = \boldsymbol{R}^\mathsf{T} \cdot \boldsymbol{M}'$. Evaluation of the bracketed term gives another skew-symmetric matrix (i.e. a matrix $\boldsymbol{T}'_\omega$ with $-\boldsymbol{T}'_\omega = \boldsymbol{T}'^\mathsf{T}_\omega$) which we can readily

reconvert to obtain the equation of motion in the rotating frame:

$$\frac{\mathrm{d}\boldsymbol{M}'}{\mathrm{d}t} = \boldsymbol{T}'_{\omega} \cdot \boldsymbol{M}' = \begin{pmatrix} \omega_1(1+\cos(2\omega_{\mathrm{rf}}t)) \\ -\omega_1 \sin(2\omega_{\mathrm{rf}}t) \\ -\Delta \end{pmatrix} \times \boldsymbol{M}' \approx \begin{pmatrix} \omega_1 \\ 0 \\ -\Delta \end{pmatrix} \times \boldsymbol{M}' \,. \tag{3.27}$$

The fast-oscillating terms can be neglected once more as they only add a small correction to the resonance frequency, the *Bloch-Siegert shift*. We are left with an angular velocity vector $\boldsymbol{\Omega} = (\omega_1, 0, -\Delta)^{\mathsf{T}}$, the length of which is the Rabi frequency $\Omega = \sqrt{\Delta^2 + \omega_1^2}$ as defined in the previous chapter. Equation (3.27) therefore describes the rotation of the magnetisation about a static axis $\hat{e}_{\Omega}$ at frequency Ω. As all further theoretical analysis will be based in the rotating frame, we will drop the apostrophe from here onwards.

In section 3.2 we introduced the longitudinal and transverse relaxation times T_1 and T_2. These phenomenological decay constants do not appear in the theoretical treatment so far as the physical mechanisms causing the relaxation are not included. Instead, they were introduced by Bloch under the assumption of a general exponential relaxation behaviour at different rates along $\hat{e}_{\mathrm{z}}$ and in the x-y plane. Over time M_{z} will relax back to its equilibrium value M_0 whereas M_{x} and M_{y} will decay to zero. Including the relaxation, we obtain the *Bloch equations of motion*[189]

$$\frac{\mathrm{d}\boldsymbol{M}}{\mathrm{d}t} = \boldsymbol{\Omega} \times \boldsymbol{M} - \boldsymbol{\Gamma} \cdot (\boldsymbol{M} - \boldsymbol{M}_0) \,, \tag{3.28}$$

where $\boldsymbol{M}_0 = M_0 \hat{e}_{\mathrm{z}}$ and $\boldsymbol{\Gamma}$ is a diagonal matrix with generally non-zero entries $\Gamma_{\mathrm{xx}} = \Gamma_{\mathrm{yy}} = T_2^{-1}$ and $\Gamma_{\mathrm{zz}} = T_1^{-1}$. Note that the length of the magnetisation vector is no longer constant over time if $\boldsymbol{\Gamma} \neq \boldsymbol{0}$. This is in contrast to the single spin relaxation illustrated in figure 3.3. Unlike an individual nuclear magnetic moment $\boldsymbol{\mu}$, the magnetisation is a vector sum and can have any magnitude between zero and $N\mu$.

As before, we can introduce a phase φ to the rf excitation in the Bloch picture.

In this case the oscillating in-plane field becomes

$$\boldsymbol{B}_{\mathrm{x}} = 2B_1 \cos(\omega_{\mathrm{rf}} t)(\cos(\varphi)\hat{e}_{\mathrm{x}} + \sin(\varphi)\hat{e}_{\mathrm{y}}) \;, \tag{3.29}$$

and the angular velocity vector in equation (3.28) is altered to the expression $\boldsymbol{\Omega} = (\omega_1 \cos\varphi, \omega_1 \sin\varphi, -\Delta)^{\mathsf{T}}$. We see that the Rabi frequency Ω remains unaffected by the phase. However, it allows us to rotate the magnetisation vector about an arbitrary in-plane axis under resonant driving ($\Delta = 0$).

In a real system the resonance frequency of an ensemble of nuclei is generally broadened by inhomogeneous effects such as local variations in $B_{0,\mathrm{z}}$ or strain gradients. This means that even for "resonant" rf excitation the angular velocity vector $\boldsymbol{\Omega}$ acting on any individual spin typically has a finite detuning $|\Delta| \lesssim \frac{\Delta\omega_{\mathrm{inh}}}{2}$, where $\Delta\omega_{\mathrm{inh}}$ denotes the linewidth of the inhomogeneously broadened resonance frequency. Experimentally, this can be overcome by using sufficiently large rf amplitudes. If $\omega_1 \gg \frac{\Delta\omega_{\mathrm{inh}}}{2}$, the detuning becomes negligible and $\boldsymbol{\Omega} \approx \boldsymbol{\omega}_1$. This is referred to as the *hard pulse* condition under which the spin system is driven coherently.

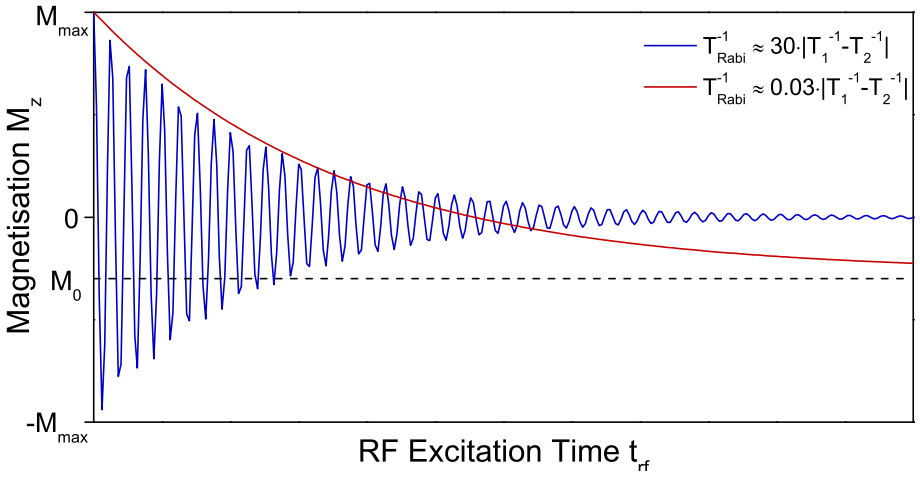

Figure 3.6: Simulations of the magnetisation decay along $\hat{e}_{\mathrm{z}}$ as a function of the resonant rf excitation time t_{rf} as described by the Bloch equations of motion. We choose parameters $M_{0,\mathrm{z}} = -0.3$ and $T_{1,\mathrm{n}} = 100 \cdot T_{2,\mathrm{n}}$. Under weak resonant driving M_{z} decays exponentially to M_0 ($T_{\mathrm{Rabi}}^{-1} \approx 0.03 \cdot |T_1^{-1} - T_2^{-1}|$, red). By contrast, the magnetisation shows an oscillatory decay to zero under strong rf excitation ($T_{\mathrm{Rabi}}^{-1} \approx 30 \cdot |T_1^{-1} - T_2^{-1}|$, blue).

A second aspect deserving consideration in NMR experiments are the relative time scales of the *Rabi period* $T_{\mathrm{Rabi}} = \frac{2\pi}{\Omega}$ and the nuclear spin relaxation times $T_{1,\mathrm{n}}$ and $T_{2,\mathrm{n}}$. Under continuous resonant driving, the magnetisation will always eventually decay to a steady-state value. Figure 3.6 shows simulations of the magnetisation decay along M_{z} as described by equation (3.28) for an equilibrium magnetisation $M_{0,\mathrm{z}} = -0.3$ and $T_{1,\mathrm{n}} = 100 \cdot T_{2,\mathrm{n}}$. These values are chosen for illustration purposes only. In a real quantum dot nuclear spin bath, the equilibrium polarisation is typically close to zero and $T_{1,\mathrm{n}}$ can be more than 10^6 times larger than $T_{2,\mathrm{n}}$[41, 114].

If $T_{\mathrm{Rabi}}^{-1} \ll |T_{1,\mathrm{n}}^{-1} - T_{2,\mathrm{n}}^{-1}|$, a (bi)exponential decay of the magnetisation along the quantisation axis M_{z} to its equilibrium value M_0 is observed, similar to an overdamped classical oscillator (red line in figure 3.6). By contrast, the magnetisation shows an exponentially damped oscillating behaviour if $T_{\mathrm{Rabi}}^{-1} \gg |T_{1,\mathrm{n}}^{-1} - T_{2,\mathrm{n}}^{-1}|$ (blue line). In this case, the steady state value is $M_{\mathrm{z}}(t_{\mathrm{rf}} \to \infty) = 0$[193]. This is, irrespective of the magnitude of the driving field, the furthest the magnetisation can be driven from its equilibrium under continuous wave (cw) NMR.

3.4 Summary

In an InGaAs quantum dot, the hyperfine interaction between the nuclear spin bath and a central electron or hole spin is the main source of relaxation and decoherence for the central spin at low temperatures. While the relaxation mechanism can be suppressed easily by a small magnetic field, the dephasing can only be partly refocused using electron spin echo techniques. The hyperfine interaction can also be used to polarise the nuclear spin bath very efficiently, with polarisation degrees up to $\rho = 70\%$ reported. Nuclear spins in an InGaAs quantum dot dephase rapidly due to strong inhomogeneous quadrupolar interactions. However, the nuclear spin phase memory time $T_{\mathrm{M,n}}$ is on the order of milliseconds and limited by nuclear dipolar interactions.

In a strong external magnetic field, the nuclear spin bath can be manipulated by applying an oscillating in-plane magnetic field that is resonant with the nuclear Larmor frequency. This NMR technique allows the resonant driving of a nuclear two-level system. As we will show in the following chapters, NMR can be used to probe the longitudinal and transverse decay timescales of the nuclear spin bath.

4 Experimental Methods and Samples

We saw in chapter 2.1 that a typical epitaxially grown quantum dot sample contains a large number of randomly distributed nanoscale dots ($\sim 1-3\ \frac{\text{dots}}{\mu\text{m}^2}$ in the samples used in this work) embedded in a GaAs matrix. Thus it is beyond the capabilities of conventional NMR techniques to isolate the NMR signature of an individual dot from that of its vicinity. However, we also saw in chapter 3.1 that the nuclear spin bath of a quantum dot interacts strongly with a localised charge spin. The hyperfine interaction allows us to both polarise nuclear spins efficiently and probe any existing nuclear polarisation indirectly via the Overhauser field acting on the confined charge. By combining optical techniques that utilise these properties with NMR driving fields we are able to overcome the limitations of conventional spin resonance methods and probe the NMR signal of an individual quantum dot.

In this chapter, we look at the experimental implementation of *optically detected nuclear magnetic resonance* (ODNMR). Section 4.1 describes the bath cryostat system used to keep the sample at cryogenic temperatures and to provide an external magnetic field $\boldsymbol{B}_0$ of up to 8 T. In section 4.2, the optical setup used for confocal *photoluminescence spectroscopy* (PL) is introduced. Section 4.3 discusses in greater detail how rf excitation fields are coupled to the sample and detected optically in our setup. Finally, the two samples on which the experimental work of this project was performed are described in section 4.4.

4.1 Cryogenic System

The shell splittings $\omega_{0,e/h} \gtrsim 10$ meV[70, 72] of the electron and hole energy states in a quantum dot are of the same order as the thermal energy at room temperature. Therefore, experiments are commonly performed at cryogenic temperatures $T < 50$ K. In our experiments this was achieved by using an *Attocube LTSys-He* liquid helium bath cryostat.

The system is shown in the schematic of figure 4.1. The sample itself is not in direct contact with the liquid helium but is contained inside a stainless steel tube. Thermal exchange with the cryogen is facilitated by a low-pressure (< 1 mbar) helium atmosphere inside the insert tube. This has a number of benefits over alternative methods of cryogenic cooling. In immersion cryostats, the helium bath needs to be cooled below the λ-point for optical measurements due to the strong scattering in the boiling He I phase. By contrast, the optical beam path (red in figure 4.1) does not pass through the helium bath in our system, making optical excitation and detection feasible without additional pumping. Unlike flow cryostat systems, the bath cryostat also does not require continuous pumping for a constant temperature of $T = 4.2$ K, which increases the mechanical stability of the system and enables us to run day-long experiments with only minor sample drift corrections. In addition, exchange gas cooling prevents condensation of residual contaminants on the sample surface as the insert tube itself is cooled down at a faster rate than the sample.

The cryostat also contains a superconducting magnet (orange in figure 4.1) which provides static magnetic fields of up to $B_{0,\mathrm{max}} = 8$ T along the optical axis $\hat{e}_z$. Unless stated otherwise, all experimental results presented in chapters 5-7 were obtained at a persistent field of $B_{0,\mathrm{max}} = 8$ T.

The sample is mounted on a non-magnetic aluminium holder with conductive silver paint to ensure good thermal contact and the holder is glued onto a stack of *Attocube* piezo-actuators. These piezoelectrically driven stages allow movement of the sample with sub-μm accuracy over a range of ~ 5 mm in all three spatial dimen-

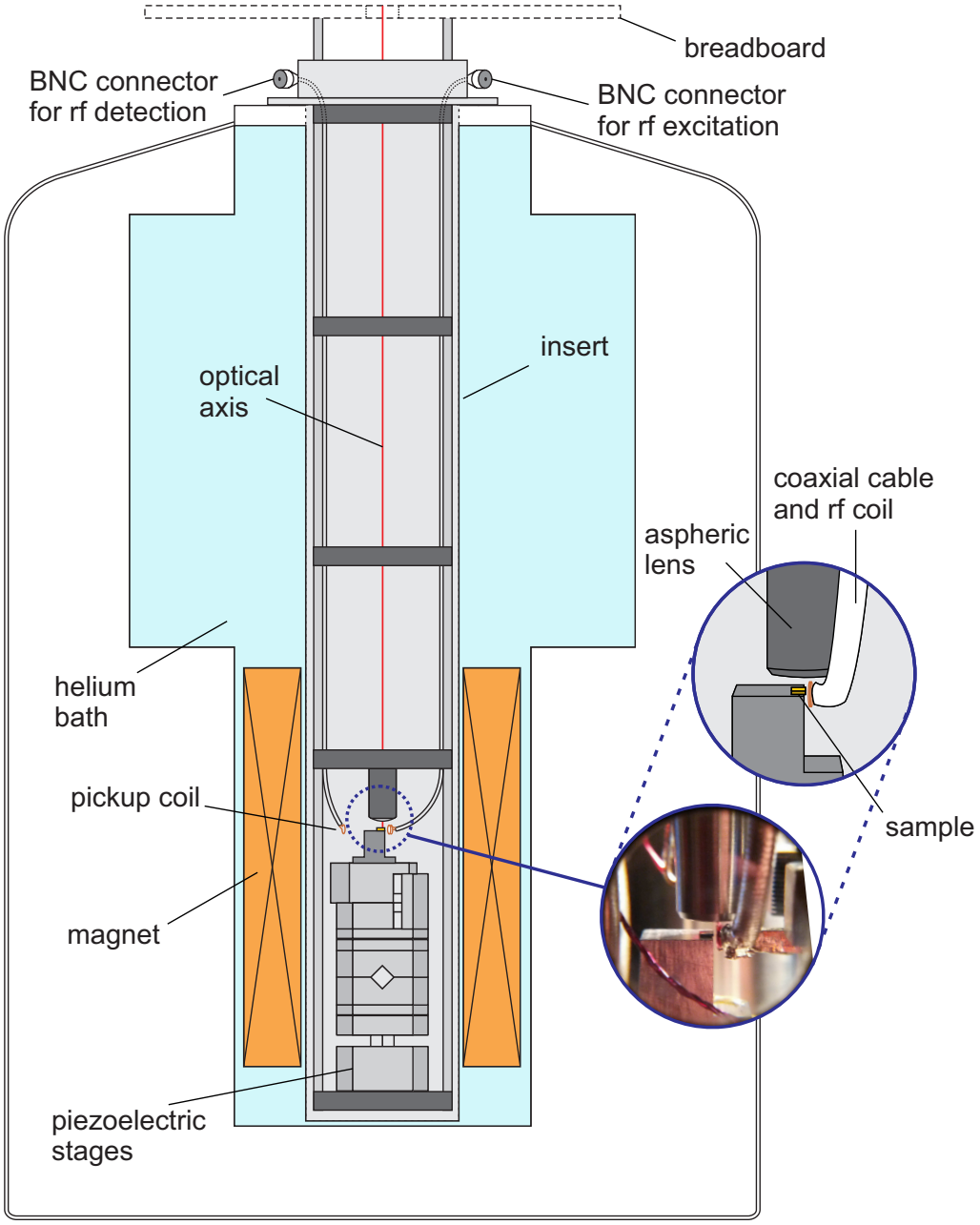

Figure 4.1: Schematic of the bath cryostat (not to scale): The sample is mounted on an aluminium pedestal and can be moved in all three spatial dimensions by a set of piezoelectrically driven stages. A multi-layer copper coil soldered to a coaxial cable is placed close to the sample to provide the rf excitation in NMR experiments (insets). The setup is contained within an insert and cooled by the liquid helium bath via a low-pressure helium atmosphere that serves as an exchange gas. The cryostat also hosts a superconducting magnet providing static fields along the optical axis. A breadboard containing optical components for PL experiments is mounted on top of the insert.

sions, allowing the precise focusing of an optical excitation beam to any position on the sample surface. The stages are attached to an optical cage system formed by four stainless steel rods and a series of cage plates that are inserted at regular intervals for stability. An aspheric lens mounted in the cage system above the sample surface acts as an objective, focusing the incoming laser light and the emitted PL signal along the confocal beam path.

The cage system is fixed to the neck of the insert which contains a number of plug sockets. Two of these are used for the control of the piezo-actuators and for the readout of a resistive temperature sensor mounted below the sample. Additional twisted wire pairs are used to provide bias voltages in experiments involving diode structures such as sample B (see section 4.4.2). Finally, two semirigid low-loss coaxial cables are interfaced at the insert neck. The first of these is terminated by a multi-layer multi-winding copper coil which is located close to the sample edge and provides the rf driving fields required in NMR experiments (see insets in figure 4.1). The second coaxial cable ends in a single copper loop which is placed sufficiently far from the rf coil to avoid inductive feedback. This loop serves as a pickup antenna and allows us to monitor the rf magnetic field in both time and frequency domain using an oscilloscope and a signal analyser.

4.2 Photoluminescence Spectroscopy

The NMR experiments discussed in this work are conducted employing a pump-rf-probe scheme for the optical preparation and detection of the nuclear spin bath polarisation[39, 41]. This is implemented using the confocal spectroscopy setup shown schematically in figure 4.2: two diode lasers emitting at ∼850 nm are used as high power pump and low power probe sources (1a, 1b). Each laser beam passes through a mechanical shutter and a neutral density filter (2) before it is coupled into a single mode fibre (3) and guided to a breadboard (4) mounted on top of the insert

(see figure 4.1). The pump laser light subsequently passes a half-wave plate and a polariser (5a) which are set up such that the excitation beam becomes fully linearly polarised parallel to the breadboard plane. Here, the half-wave plate ensures that the major polarisation axis of the laser light coupled out of the fibre coincides with the axis of the polariser, ensuring a maximum intensity throughput.

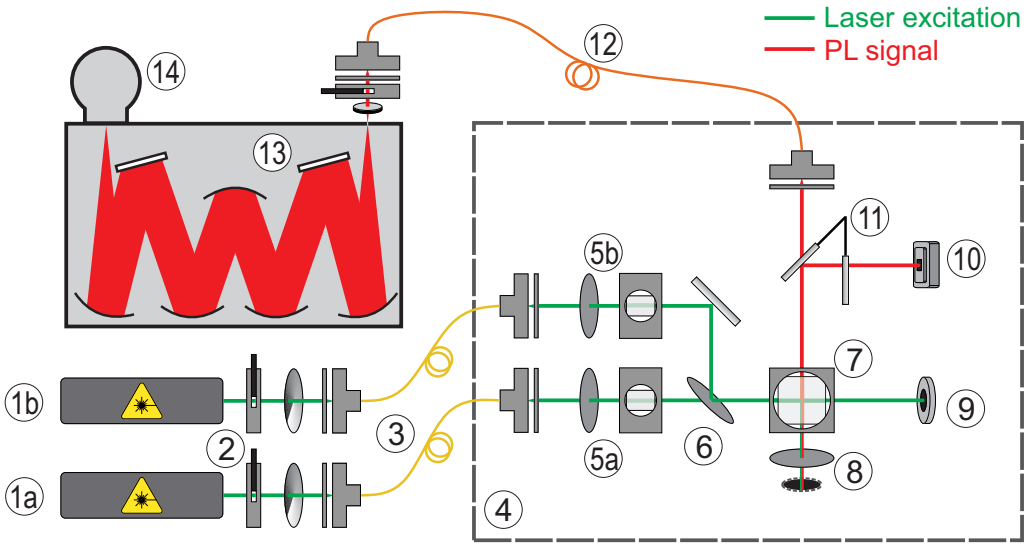

Figure 4.2: Schematic of the optical setup: light from the pump (1a) and probe laser (1b) passes a mechanical shutter and a variable ND filter (2) and is coupled into a single mode fibre (3). Both laser beams are guided to a breadboard (4) on top of the insert tube. After passing polarisation optics (5a, 5b) the beam paths are combined using a pellicle beamsplitter (6). A second beamsplitter (7) deflects the pump and probe beam towards the sample inside the insert and a quarter-wave plate (8) is used to convert the pump beam polarisation from linear to circular. Pump and probe excitation powers are monitored via a power meter (9). The PL signal (red) can either be directed towards a camera (10) for visual alignment on the sample surface with a flip-mirror (11) or coupled into a multi-mode fibre (12) and sent to a Raman spectrometer (13) with an attached LN_2 cooled CCD (14) for PL measurements.

A nominally non-polarising beamsplitter (7) is used to deflect the excitation beam towards the insert. The horizontal polarisation of the incoming pump beam is required because the beamsplitter still introduces a slight ellipticity if the polarisation axis does not coincide with the axis of the beamsplitter. Finally, a calibrated quarter-wave plate (8) mounted on a motorised stage converts the excitation beam to circular polarisation before it is sent into the insert. Inside the insert, the beam

passes along the optical axis marked in figure 4.1 in free space before reaching an aspheric lens with focal length $f = 2.75$ mm, which serves as an objective and focuses the beam onto a spot of $\sim 1\ \mu\text{m}^2$ on the sample surface.

The probe beam follows a similar path and is coupled into the pump beam path by an additional pellicle beamsplitter (6). However, the polarisation optics for the probe laser (5b) set its polarisation axis to coincide approximately with one of the two optical axes of the quarter-wave plate instead. In this way, the probe beam remains linearly polarised until it reaches the sample.

Both laser wavelengths have been selected to coincide with the optical transition energy in the InAs wetting layer. The excited electron-hole pairs relax into the energetically lower bound states of the quantum dot before recombining under emission of a photon at the intershell transition energy. This process is known as *non-resonant photoluminescence* (PL).

Using the mechanical shutters, we can switch the two laser excitation paths on or off separately. The circularly polarised pump laser beam is only used for preparation of the nuclear spin bath and the emitted PL signal is omitted from the spectral analysis by keeping the shutter in the detection path (red) closed. By contrast, the probe laser induced PL emission is collected by the objective lens and sent back towards the beamsplitter. From there it is coupled into a multi-mode fibre (12) and directed to a *Ramanor U1000* double spectrometer (13) with nitrogen-cooled charged coupled device (CCD) camera (14) for spectral analysis. As the probe laser excitation is linearly polarised, both of the circularly polarised Zeeman split optical transitions (see chapter 2.2.2) are visible in the PL spectrum. The emission spectra obtained from the CCD are typically integrated over ~ 1 s. For this reason the optical detection technique we employ is commonly referred to as *time-averaged* PL spectroscopy, reflecting the ensemble-broadened nature of the excitonic transition lines measured by these means.

The breadboard contains two additional elements that allow us to monitor the

experimental conditions: firstly, a power meter (9) is used to record the laser excitation powers continuously. In addition, the alignment of the laser beam on the sample surface is checked via a camera (10) which can be switched into the detection path via a flip-mirror (11) and which is connected to a TV screen. Our sample surfaces contain gold markers or shadow masks which scatter the incident laser light stronger than the GaAs surface. The scattered light is detected by the camera and, in combination with the piezostages, can be used to image the sample surface in order to locate quantum dots relative to the marker positions. In addition, we can use the image to optimise the focusing of the excitation beam on the sample surface.

4.3 Nuclear Magnetic Resonance

We already studied the theoretical concepts of NMR in chapter 3.3. Here, we discuss the experimental implementation of NMR excitation in our setup in more detail and look at the optical detection of the NMR signal within an experiment cycle.

4.3.1 NMR Setup

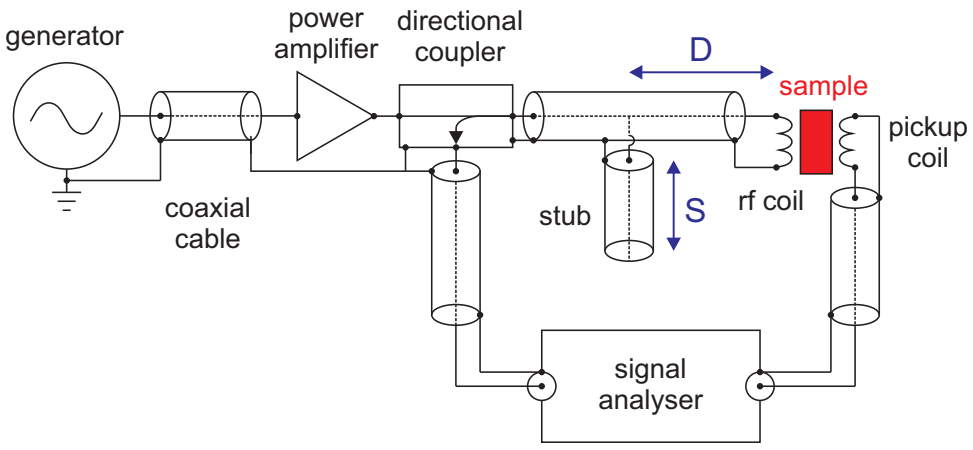

Figure 4.3: Circuit diagram of the NMR setup. The rf signal is amplified and fed to the rf coil via coaxial cables. A shunt stub of length S at a distance D from the coil provides impedance matching for strong rf transmission to the sample (red). The reflection (transmission) characteristics of the coil are probed with a directional coupler (pickup coil) and measured with a signal analyser.

The basic NMR setup is shown in figure 4.3. An rf input signal from the generator is amplified and sent to the rf coil inside the insert via coaxial cables. The rf coil is placed at a fixed distance $d \approx 300$ μm from the focal point of the objective (see figure 4.4 below). It consists of three layers of two windings each with a wire diameter $\varnothing_w = 0.3$ mm and an inner coil diameter $\varnothing_c \approx 0.8$ mm ($\varnothing_c \approx 0.4$ mm for the measurements in chapter 7.5). The quantum dots studied in this work are all located within 100 μm of the sample edge, allowing simultaneous optical and rf access.

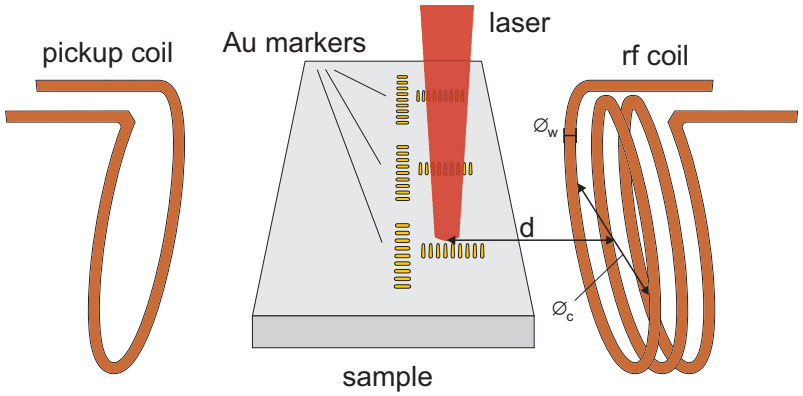

Figure 4.4: Schematic of the relative placement of rf coil and sample (not to scale). The rf coil is placed at a distance $d \approx 300$ μm from the optical focal point on the sample. A second pickup coil is placed ~ 1 cm from the rf coil to monitor the rf transmission amplitude.

The rf amplitude at the dot location depends on several parameters including the coil geometry and the distance d between coil and dot. The most important parameter, however, is the transmission coefficient T_{rf}, characterising the ratio of the rf input power which is transmitted by the rf coil. The transmission and reflection (Γ_{rf}) coefficients are linked by the formula $T_{rf}^2 + \Gamma_{rf}^2 = 1$ and both depend strongly on the load impedance $Z_L \approx i\omega L_c$ of the coil (with inductance L_c). We see that Z_L is frequency-dependent and almost purely reactive. It is therefore generally not equal to the characteristic impedance $Z_0 = 50\ \Omega$ of the coaxial cables, amplifier and generator. In this case, the coil is *mismatched* and a proportion $\Gamma_{rf} = \frac{Z_L - Z_0}{Z_L + Z_0}$ of the rf signal is reflected back to the source. This strongly reduces the rf magnetic field

amplitude transmitted to the sample and can damage the source.

In order to match the coil and reduce reflections for a given frequency ω, we added a *shunt stub* to the rf circuit. This is a coaxial cable of length S in parallel to the effective load consisting of the coil and a cable length D (see figure 4.3). The input impedance of the effective load at the connection point is given by the transmission line impedance equation[194]

$$Z_{\mathrm{i}}(\mathrm{D}) = Z_0 \frac{Z_{\mathrm{L}} + \mathrm{i}Z_0 \tan(\beta_{\mathrm{p}}\mathrm{D})}{Z_0 + \mathrm{i}Z_{\mathrm{L}} \tan(\beta_{\mathrm{p}}\mathrm{D})} \,, \tag{4.1}$$

where $\beta_{\mathrm{p}} = \frac{\omega\sqrt{\epsilon_{\mathrm{r}}}}{c}$ is the phase constant and ϵ_{r} is the relative permittivity of the cable dielectric. The same expression can also be used to obtain the input impedance of the stub Z_{S}. As there is no load connected, we have an open circuit corresponding to $Z_{\mathrm{L}} \to \infty$, which gives $Z_{\mathrm{S}}(\mathrm{S}) = -\mathrm{i}Z_0 \cot(\beta_{\mathrm{p}}\mathrm{S})$. The load is matched if the equivalent resistance of the parallel stub-coil circuit is equal to Z_0, i.e.

$$\frac{1}{Z_0} = \frac{1}{Z_{\mathrm{S}}(\mathrm{S})} + \frac{1}{Z_{\mathrm{i}}(\mathrm{D})} \,. \tag{4.2}$$

Since the stub impedance $Z_{\mathrm{S}}(S)$ is always imaginary, this corresponds to matching criteria $\mathrm{Re}(Z_{\mathrm{i}}(\mathrm{D})^{-1}) = Z_0^{-1} = (50\ \Omega)^{-1}$ and $\mathrm{Im}(Z_{\mathrm{i}}(\mathrm{D})^{-1}) = -Z_{\mathrm{S}}(\mathrm{S})^{-1}$. In this case the system forms a resonant parallel RLC circuit with $\omega = \frac{1}{\sqrt{L_{\mathrm{c}}' C}}$ and quality factor $\mathrm{Q} = Z_0\sqrt{C/L_{\mathrm{c}}'}$.

While periodic solutions for the lengths S and D can be derived analytically for a given set of parameters, we obtained good matching conditions using a purely empirical approach: If the stub-coil circuit is fed with broadband rf noise (100 MHz bandwidth), it will only absorb at the resonance frequency ω and reflect all other excitation frequencies. We can measure the reflected spectrum using a directional coupler and a signal analyser (see figure 4.3). Figure 4.5a shows the reflected rf spectrum for a matched circuit at $\nu = \frac{\omega}{2\pi} = 58.8$ MHz. Under fully impedance matched conditions we achieve rf field amplitudes of up to $B_1 \approx 7$ mT in the rotating

frame at an rf input power of $P_{\mathrm{rf}} \approx 200$ W for the NMR resonance frequencies of ^{75}As ($\nu_{\mathrm{L}} \approx 58.8$ MHz) and ^{71}Ga ($\nu_{\mathrm{L}} \approx 104.8$ MHz) at $B_{0,\mathrm{z}} = 8$ T. Although the amplifier can in principle provide pulse powers of up to 1kW we find that excitation levels > 200 W inevitably lead to strong heating of the sample.

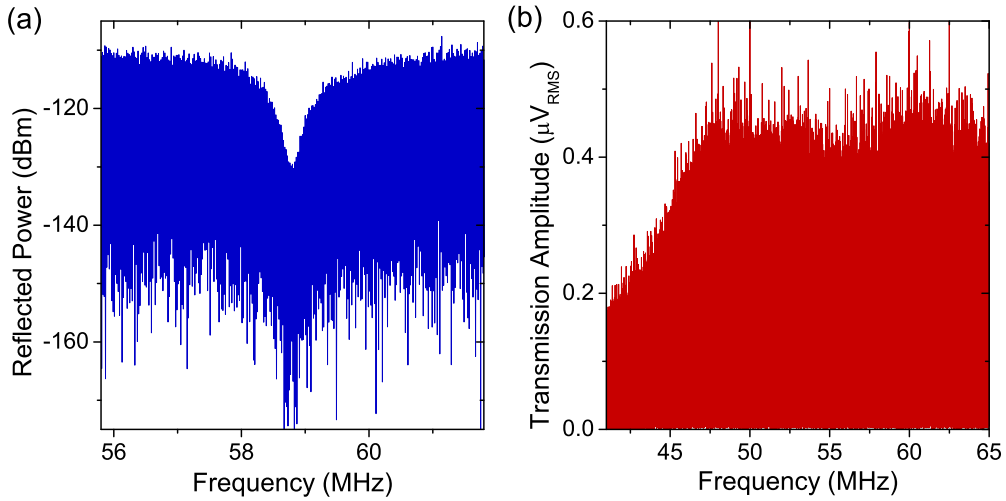

Figure 4.5: Reflection and transmission spectra of the impedance matched NMR circuit. (a) Reflected power spectrum for good matching at the ^{75}As resonance frequency of $\nu_{\mathrm{L}}(^{75}\mathrm{As}) = 58.8$ MHz at $B_{0,\mathrm{z}} = 8$ T. (b) Transmitted signal amplitude under broadband matching conditions. The rf excitation amplitude is flat over a bandwidth $\nu_{\mathrm{L}}(^{75}\mathrm{As}) \pm 12.5$ MHz.

The single stub technique can only provide impedance matching for one resonance frequency. This is sufficient for hard pulse excitation where we coherently drive a single NMR transition. However, matching the coil to a broad band of excitation frequencies generally requires a more complex circuit design. Instead, we tune the circuit to a position where the transmission spectrum measured by the pickup coil is approximately flat over the desired bandwidth (figure 4.5b). Since this still causes non-negligible reflections we use a 30W class A amplifier capable of handling full signal reflection in experiments requiring broadband rf excitation.

4.3.2 Optical Detection of NMR

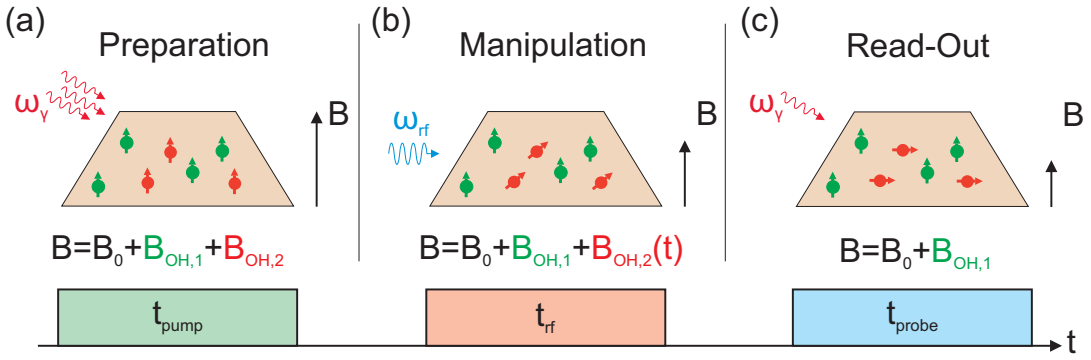

Figure 4.6: The ODNMR pump-probe scheme for a depolarisation experiment. (a) The nuclear spin bath is polarised under high-power circularly polarised optical pumping. (b) Isotopes are depolarised selectively by the rf excitation. (c) Changes in the nuclear polarisation are probed in low-power PL.

The experiment cycle of an ODNMR measurement is illustrated in figures 4.6a-c and consists of three distinct steps: optical preparation of the nuclear spin bath, rf manipulation and optical read-out. This scheme was used in all of our NMR experiments and makes use of the strong hyperfine interaction in a quantum dot.

In the first step, the spin bath is prepared using dynamic nuclear polarisation (see chapter 3.1.2): under circularly polarised optical excitation at ~ 850 nm, polarised electron-hole pairs are created in the wetting layer and relax into the quantum dot. As we saw before, the flip-flop term of the electron-nuclear hyperfine interaction (equation (3.3)) can lead to an efficient polarisation transfer to the nuclear spin bath under certain conditions. Using optical excitation powers at least an order of magnitude above the saturation level of a single neutral exciton $P_{\mathrm{Sat}}(\mathrm{X}^0)$, we can reach nuclear polarisation degrees of up to $\rho \approx 70\%$ in the dot[82, 120]. The strongly polarised spin bath creates a net Overhauser magnetic field B_{hf} which is aligned either parallel or anti-parallel to an applied external field $B_{0,\mathrm{z}}$. This additional magnetic field manifests itself in PL as a change of the Zeeman splitting between optical transitions as shown in figure 4.7 for a dot in sample A: under σ^+/σ^- polarised excitation the splitting shifts by ± 125 μeV compared to the pure Zeeman

splitting $\Delta E_{\mathrm{Z},0} \approx 1.125$ meV at $B_{0,\mathrm{z}} = 8$ T, corresponding to an Overhauser field $B_{\mathrm{hf}} \approx 5$ T.

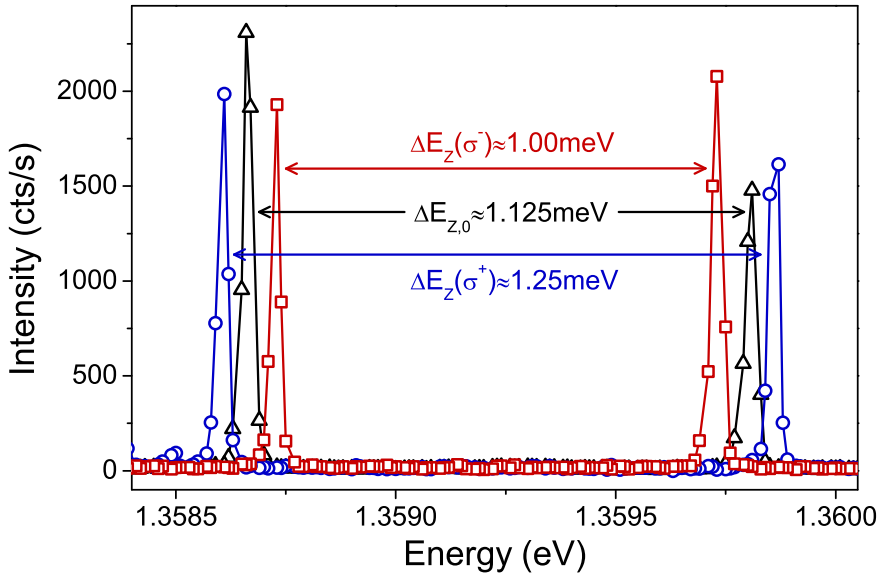

Figure 4.7: Pump-probe PL spectra of the Zeeman split X^0 transitions of a quantum dot at $B_{0,\mathrm{z}} = 8$ T. After the dot has been optically pumped for several seconds with high-power σ^+ (σ^-) circularly polarised light, the splitting is increased (reduced) by an Overhauser shift $E_{\mathrm{hf}} \approx \pm 125$ μeV, corresponding to an Overhauser field of $B_{\mathrm{hf}} \approx 5$ T and a nuclear polarisation degree of $\rho \approx 70\%$ for an $In_{0.2}Ga_{0.8}As$ quantum dot.

Next, one or more rf excitation pulses are applied to the system via the rf coil. Depending on the experimental requirements these rf pulses can be designed to drive a given spin transition coherently, to swap the populations of two spin energy levels adiabatically or to depolarise all spins of a selected isotope. Any changes induced in the polarisation of the nuclear spin bath are reflected in a change of the Overhauser field B_{hf}.

Finally, the probe laser pulse is applied to the sample. The probe beam is linearly polarised to obtain a strong PL signal from both Zeeman split transition lines. Excitation power and pulse length are kept at a level that is low enough to prevent the probe pulse from affecting the Overhauser splitting noticeably while providing sufficient PL intensity for short data acquisition times. The experiment cycle is repeated $10 - 20$ times for each data point to obtain a PL signal strength of ~ 1000 counts

and the signal-to-noise ratio is further improved by averaging over $2-3$ spectral frames.

In addition to measurements with varying rf parameters we perform control measurements under fixed conditions, e.g. without the rf field or under hard pulse excitation at a fixed pulse length. These serve both as a reference to extract the induced change of the nuclear spin bath polarisation and as a baseline to filter out small time-dependent drifts induced by changing environmental parameters during a day-long experiment (e.g. laboratory temperature).

4.4 Quantum Dot Samples

The experimental results obtained in this project are measured on two samples. The first, subsequently referred to as sample A, is an undoped and ungated InGaAs quantum dot sample with a GaAs/AlGaAs cavity. Sample B is a p-i-n diode with an InGaAs quantum dot layer embedded in its intrinsic region.

4.4.1 Ungated Sample A

Sample A was grown in MBE at the National Centre for III-V Technologies in Sheffield and consists of a single InGaAs quantum dot layer in a microcavity. The InAs layer thickness of 1.85 ML was chosen just above the nucleation threshold, giving a very low, homogeneous dot density of $1-3\ \frac{\text{dots}}{\mu\text{m}^2}$. Previous ODNMR studies on samples from the same wafer have shown a relatively low indium content of $\sim 20\%$ within the dot volume probed by the electron wavefunction of a confined neutral exciton[39].

The microcavity is formed by several pairs of distributed Bragg reflectors (DBRs) embracing a λ/n GaAs cavity. The TEM image in figure 4.8a shows the 17 bottom and 6 top DBR pairs formed by alternating GaAs (dark) and $Al_{0.8}Ga_{0.2}As$ (light) layers of thickness $\lambda/(4n)$. The quantum dot layer (red arrow) is centred in the

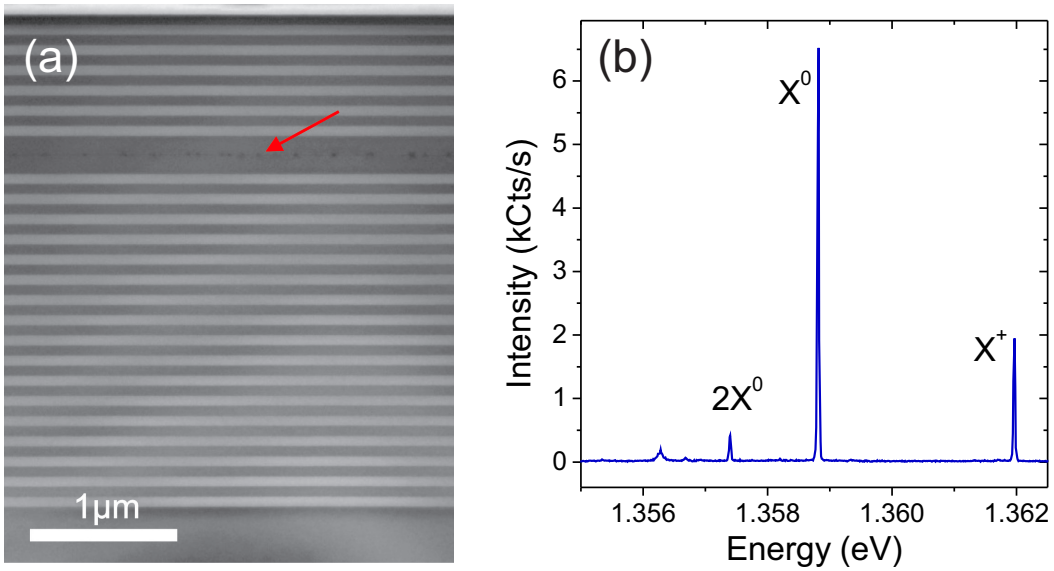

Figure 4.8: (a) TEM image of sample A. The dot layer (red arrow) is embedded in a cavity formed by GaAs/$Al_{0.8}Ga_{0.2}As$ DBR pairs. (b) PL spectrum of a quantum dot in sample A at $B_0 = 0$ T and at optical excitation power 1 μW. Apart from the dominant neutral exciton line X^0 we can distinguish a weak biexciton $2X^0$ at lower energy and a blue-shifted transition line associated with the positive trion X^+.

cavity and has a large inhomogeneous distribution of optical transition energies. The resonant wavelength of the cavity at $T = 4.2$ K lies at $\lambda = 920$ nm with a Q factor of ~ 250[120]. The light extraction efficiency is further enhanced by a short-period GaAs/AlGaAs superlattice in which the quantum dot layer is embedded (see figure 2.1b). In saturation, we obtain PL intensities of up to $100,000\frac{\text{cts}}{\text{s}}$ using the setup introduced in section 4.2.

A representative PL spectrum of a single dot in Sample A is shown in figure 4.8b. Although the sample is nominally undoped, a weak positive trion transition is observed for most dots. However, long nuclear spin relaxation times $T_{1,\text{n}}$ have been found for several dots in sample A, indicating the absence of free charge carriers. Therefore, the appearance of X^+ might be caused mainly by the non-resonant optical excitation. Spectral transition linewidths vary from dot to dot, but are typically close to or below the resolution limit of the spectrometer (~ 15 μeV).

4.4.2 PIN Diode Sample B

The p-i-n diode sample was provided by the Toshiba Cambridge Research Laboratory and grown in MBE at the University of Cambridge. A detailed description of the sample structure is given in [96, 101, 195]. As illustrated in figure 4.9, the quantum dot layer is centred in a thin 10 nm GaAs quantum well which is bracketed by $Al_{0.75}Ga_{0.25}As$ tunnel barriers of 71.8 nm thickness. The structure is embedded in a planar microcavity consisting of 14 GaAs/$Al_{0.98}Ga_{0.02}As$ bilayers below and 4 bilayers above the dot layer. The intrinsic region is 140 nm thick and centred on the dot layer with n- and p-doped regions extending into the tunnel barriers. The cavity resonance at 4.2 K is found at $\sim$ 940 nm where excitonic PL intensities in our setup reach up to $50,000\frac{\text{cts}}{\text{s}}$ in saturation. Electric gates above and below the dot layer allow control of the exciton charge state.

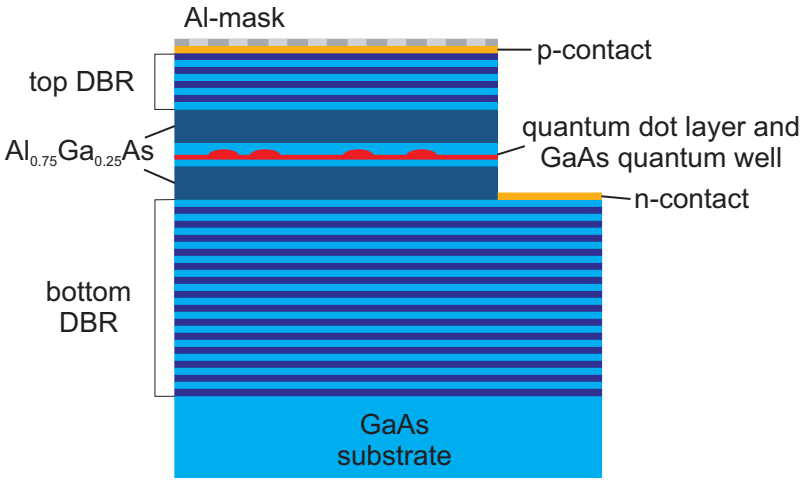

Figure 4.9: Structure of the p-i-n diode sample (after [195]). The quantum dot layer is embedded in a thin GaAs quantum well. Two $Al_{0.75}Ga_{0.25}As$ tunnel barriers ensure optical recombination over a large bias range. GaAs/$Al_{0.98}Ga_{0.02}As$ DBRs above and below the dot layer form a planar cavity and increase the PL collection efficiency.

A schematic band diagram of the p-i-n structure is depicted in figure 4.10a. The energy bands are tilted in the intrinsic region even without an applied voltage as the Fermi level E_F (dashed line) is pinned close to the valence (conduction) band edge in the p- (n-)doped region. As indicated by the arrows, the intrinsic region

becomes fully depleted of charge carriers under large reverse biases. The I-V curve in figure 4.10b shows the characteristic diode behaviour with a sudden increase of the current under large forward biases.

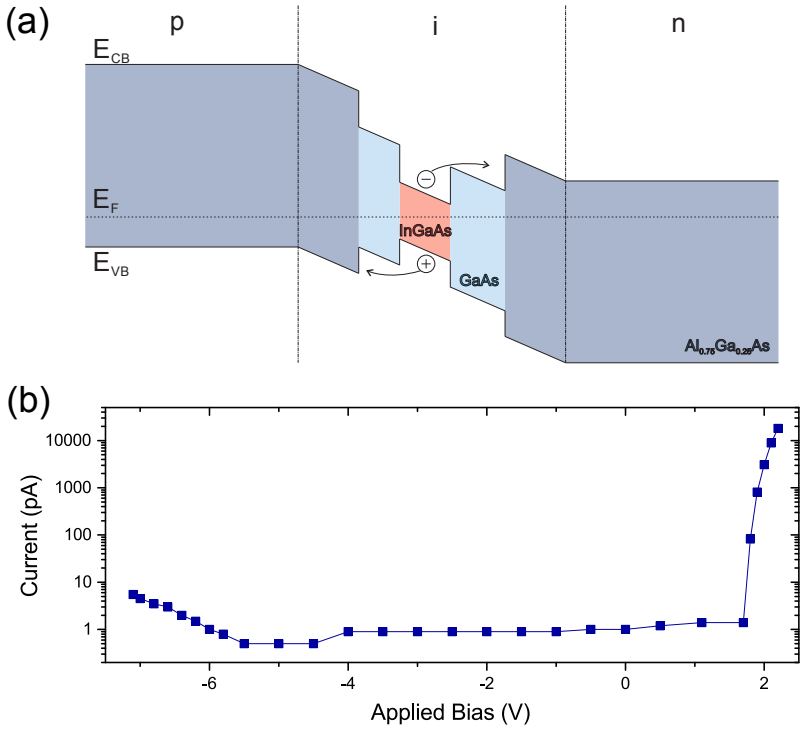

Figure 4.10: (a) Schematic band diagram of the p-i-n diode structure. The InGaAs quantum dot layer (red) is embedded in the intrinsic region. Under a large reverse bias the intrinsic region becomes fully depleted of charge carriers (indicated by arrows). (b) Dark I-V characteristics of the p-i-n diode sample at $T = 4$ K. A strong increase of the measured current is observed under forward biases exceeding the built-in voltage $V_{\mathrm{bi}} = 1.8$ V.

As shown in figure 2.5, PL emission can be observed over a wide bias range of $\gtrsim 6$ V with large transition energy Stark shifts of up to 25 meV. This is due to the $Al_{0.75}Ga_{0.25}As$ barriers which prevent charge carrier escape and increase the charge tunnelling times. PL linewidths vary depending on the bias region but are found to be narrowest ($\gtrsim 20$ μeV) at small reverse biases in the transition region between X^0 and X^+. We will examine the bias dependent characteristics of sample B in detail in chapter 5.3 where we will see that the gated structure allows us to empty dots reliably of all charges under large reverse biases.

4.5 Summary

We can perform optically detected NMR experiments by making use of the hyperfine interaction between the nuclear spin bath and a confined charge in a quantum dot. Using a confocal spectroscopy setup in combination with a cryostat system, we can strongly polarise the nuclear spins using optical dynamic nuclear polarisation. Nuclear spin level splittings are on the order of $10 - 100$ MHz in an external magnetic field of several tesla and can be driven resonantly via a copper rf coil in close proximity to the quantum dot sample. NMR induced changes of the nuclear spin polarisation are reflected in PL as changes in the Overhauser shift of the Zeeman splitting between the bright neutral exciton transitions.

Experiments are performed on two InGaAs quantum dot samples with similar optical properties. In both structures a planar microcavity is used to enhance the PL intensity of individual dots. While sample A is ungated and undoped, the p-i-n diode structure of sample B allows us to tune over a large bias range and to empty the studied dot controllably of all charges.

5 Strain-Induced Nuclear Spin Freezing in InGaAs Quantum Dots

5.1 Introduction

The decoherence of an electron spin confined in a self-assembled quantum dot is dominated by the influence of the nuclear spin bath. Since all constituent nuclei have non-zero spin, hyperfine interaction leads to dephasing within nanoseconds (see chapter 3.2.1 and e.g. [29, 30]). The hyperfine induced electron spin dephasing can be suppressed to a considerable extent by applying an external magnetic field and using electron spin echo techniques[167, 168, 178]. However, *spectral diffusion* arising from nuclear-nuclear dipolar interactions still ultimately limits the electron spin decoherence time $T_{2,e}$[196, 197]: since the electron wave function overlaps with a finite number of nuclei, nuclear spin flip-flops eventually lead to irreversible changes in the effective Overhauser field that acts on the electron spin. Therefore, the timescale of such flip-flop processes is of great interest as it presents an upper limit to the theoretically achievable electron spin coherence time in the presence of the nuclear spin bath environment.

The nuclear dipolar coupling strengths are reflected by the homogeneous NMR linewidths of the constituent isotopes[116, 198]. However, these values are not easily obtained experimentally due to the particular properties of our system. The strong lattice mismatch driving the self-assembled formation of InGaAs quantum dots on a

GaAs substrate gives rise to considerable strain gradients within each dot[169]. This strain in turn causes electric field gradients that nuclei with spin $I \geq 1$ couple to via their quadrupolar moment[116]. Previous work has shown that the NMR spectra in InGaAs quantum dots are strongly inhomogeneously broadened as a result of the quadrupolar interaction: linewidths of $10 - 50$ kHz were found for the central spin transitions (CTs, $-1/2 \leftrightarrow +1/2$) of all isotopes at $B_{0,\mathrm{z}} = 5.3$ T and even stronger broadening of $2 - 10$ MHz was measured for satellite transitions (STs, e.g. $+1/2 \leftrightarrow +3/2$)[39].

While it is not possible to measure homogeneous linewidths in this system using conventional cw NMR techniques, the inhomogeneous broadening can be refocused under coherent pulsed NMR schemes such as the $\frac{\pi}{2} - \tau - \pi - \tau$ Hahn echo sequence[192, 199]. Recently, such experiments were performed in our group on a sample from the same wafer as sample A, revealing unexpectedly long nuclear phase memory times $T_{\mathrm{M,n}}^{\mathrm{HE}} \approx 1.2 - 4.5$ ms[41]. This was attributed to quenching of the nuclear dipolar flip-flops due to the strong inhomogeneous quadrupolar interactions in the quantum dot, a mechanism which had previously been described by Dzhioev et al.[200]

However, it was not clear how universal the findings of [41] were. The wafer of sample A was not designed for the fabrication of electrically gated devices. Hence the studied sample did not possess any degree of charge control beyond the intrinsic (nominally neutral) dopant levels. It was therefore difficult to determine the charge occupancy of the studied quantum dots accurately. While it was surmised that the dots were empty of trapped charge carriers during rf excitation, the presence of a weak positive trion transition in PL spectra (see figure 4.8b) indicated that this might not necessarily be the case. Consequently, charge fluctuations may have contributed to the nuclear spin bath decoherence via electron- or hole-mediated nuclear spin interactions[182, 201] and could affect multiple pulse NMR sequences beyond the Hahn echo.

In this chapter, we perform pulsed NMR experiments on sample B, a gated p-i-n structure with very long nuclear spin relaxation times $T_{1,\mathrm{n}}$ and with bias control over the charge occupancy of an individual quantum dot. Most importantly, this device allows us to empty a dot of charges under large reverse biases. We discuss in detail how key parameters for pulsed ODNMR in a quantum dot are calibrated and present the results of Hahn echo experiments in an empty InGaAs dot. Our findings strongly support the interpretation given in [41]: we find the measured phase memory times in sample B to be in very good agreement with the reported values, confirming that direct dipolar interactions in the nuclear spin bath are limiting $T_{\mathrm{M,n}}^{\mathrm{HE}}$ at millisecond timescales.

The chapter is structured as follows: after a brief general overview of nuclear dipolar interactions in a quantum dot in section 5.2.1, we discuss the origin of inhomogeneous quadrupolar interactions in strained InGaAs dots and their impact on the nuclear spin bath dynamics in sections 5.2.2 and 5.2.3. The nuclear spin relaxation timescales and optical pump and probe parameters for stable preparation and readout of the spin bath magnetisation in sample B are measured in section 5.3. The experiment cycle of a pulsed ODNMR measurement is discussed in detail in section 5.4, where we also show how experimental parameters are calibrated to obtain maximised spin echo signal amplitudes. Finally, we present the results of our Hahn echo experiments in sample B and compare them to the findings from sample A in section 5.5, proving conclusively that the reported $T_{\mathrm{M,n}}^{\mathrm{HE}}$ times are limited by dipolar interactions within the spin bath.

5.2 Nuclear Spin Bath Dynamics in a Quantum Dot

In this section, we first discuss the various forms in which nuclear-nuclear dipolar interactions can result in nuclear spin decoherence. The self-assembled InGaAs quantum dots are subject to considerable intrinsic strain fields, which give rise to additional quadrupolar couplings[39, 169]. In the second and third part of this section we look at how quadrupolar interactions broaden the NMR spectra inhomogeneously and suppress nuclear dipolar interactions in the quantum dot[41, 200].

5.2.1 Nuclear Dipolar Interactions

The magnetic interaction between two nuclear spins $\boldsymbol{I}$ and $\boldsymbol{J}$ is described in the same way as the dipolar term of the hyperfine coupling between a nuclear spin $\boldsymbol{I}$ and a charge spin $\boldsymbol{S}$ discussed in chapter 3.1. With nuclear gyromagnetic ratios γ_I, γ_J and introducing a vector $\boldsymbol{r}_{ij}$ denoting the spatial separation between the two spins, we can write[116]

$$\mathcal{H}_{\mathrm{dd}} = \frac{\mu_0}{4\pi}\gamma_I\gamma_J\frac{\hbar}{r_{ij}^3}\left(\boldsymbol{I}\cdot\boldsymbol{J} - 3\frac{(\boldsymbol{I}\cdot\boldsymbol{r}_{ij})(\boldsymbol{J}\cdot\boldsymbol{r}_{ij})}{r_{ij}^2}\right) . \tag{5.1}$$

This equation can be rewritten in terms of the *dipolar alphabet* (see appendix 9.1). The terms C-F in equation (9.4) are responsible for one or two quantum transitions, i.e. induce spin flips ($\uparrow\downarrow\leftrightarrow\uparrow\uparrow$), ($\uparrow\downarrow\leftrightarrow\downarrow\downarrow$) and ($\uparrow\uparrow\leftrightarrow\downarrow\downarrow$). As they do not commute with the Zeeman Hamiltonian $\mathcal{H}_{\mathrm{Z}} = -\hbar B_{0,\mathrm{z}}\sum_n^N \gamma_n I_{n,\mathrm{z}}$ for N spins $\boldsymbol{I}_n$, we can drop them if $B_{0,\mathrm{z}}$ is sufficiently large and are left with the secular dipolar Hamiltonian

$$\begin{aligned}\mathcal{H}_{\mathrm{D}} &= \omega_{\mathrm{D}}\left(I_{\mathrm{z}}J_{\mathrm{z}} - \frac{1}{2}\left[I_{\mathrm{x}}J_{\mathrm{x}} + I_{\mathrm{y}}J_{\mathrm{y}}\right]\right) ,\\ \omega_{\mathrm{D}} &= \frac{\hbar\mu_0}{4\pi}\gamma_I\gamma_J\frac{1-3\cos^2\theta}{r_{ij}^3} ,\end{aligned} \tag{5.2}$$

where θ is the angle between $\boldsymbol{r}_{ij}$ and $\boldsymbol{B}_0 = B_{0,\mathrm{z}}\hat{e}_{\mathrm{z}}$. Analogous to the discussion of the hyperfine interaction in chapter 3.1, we look at the *static* term ($\propto I_{\mathrm{z}}J_{\mathrm{z}}$) and the

flip-flop term $\propto [I_\mathrm{x}J_\mathrm{x} + I_\mathrm{y}J_\mathrm{y}]$ separately. The dipolar coupling strength ω_D depends strongly on the spatial separation and decays as $\propto r_{ij}^{-3}$. Hence the unmediated coupling between distant nuclear spins is extremely weak.

While equation (5.2) describes the mutual interaction between any two nuclear spins, we generally distinguish the *homonuclear* interaction between spins $\boldsymbol{I}_n$ and $\boldsymbol{I}_m$ of the same isotope from the *heteronuclear* interaction between unlike spins $\boldsymbol{I}_n$ and $\boldsymbol{J}_m$.

Heteronuclear Dipolar Dephasing of Nuclear Spin Magnetisation

The effect of heteronuclear interactions between $\boldsymbol{I}$ and $\boldsymbol{J}$ spins on the coherence time of $\boldsymbol{I}$ spins is similar to that of an additional, time-dependent external magnetic field. The heteronuclear flip-flop term can be ignored at large magnetic fields $B_{0,\mathrm{z}}$ as the different nuclear Zeeman splittings for $\boldsymbol{I}$ and $\boldsymbol{J}$ spins strongly suppress this process[202]. We can view this in the lab frame as the in-plane components of the $\boldsymbol{I}$ and $\boldsymbol{J}$ spins precessing about $\boldsymbol{B}_0 = B_{0,\mathrm{z}}\hat{e}_\mathrm{z}$ at their respective Larmor frequencies $\omega_\mathrm{L}^{I/J}$. In the rotating frame of $\boldsymbol{I}$, the in-plane magnetisation vector of $\boldsymbol{J}$ appears to rotate at $\omega_\mathrm{L}^J - \omega_\mathrm{L}^I$ and we can safely discard its influence on $\boldsymbol{I}$ in analogy to the treatment of the counter-rotating rf field in chapter 3.3.1.

For this reason, the heteronuclear dipolar interaction is commonly treated as a pure Ising Hamiltonian $\mathcal{H}_\mathrm{D}^{IJ}(t) = \omega_\mathrm{D}^{IJ} I_\mathrm{z} J_\mathrm{z}(t)$ with the time-dependence of J_z arising from homonuclear spin flip-flops among the $\boldsymbol{J}$ spins. This fluctuating offset to the Larmor frequency of $\boldsymbol{I}$ is responsible for the spin dephasing process of *spectral diffusion*. Similar to static resonance offsets, it can be refocused partially by π pulses. This approach requires the refocusing to take place on a timescale at which the effective field of $\boldsymbol{J}$ appears static, which can be achieved by using a series of π pulses and is the basis of *dynamic decoupling*[203, 204]. We will discuss this concept in greater detail in chapter 6.

Homonuclear Dipolar Dephasing of Nuclear Spins Magnetisation

The dipolar interaction between like spins $\boldsymbol{I}_n$ and $\boldsymbol{I}_m$ is the source of two more echo decay mechanisms. Once again, we can consider the Ising term $\propto I_{n,\mathrm{z}} I_{m,\mathrm{z}}$ as an additional external field which shifts the NMR resonance frequency of spin $\boldsymbol{I}_n$ by $\delta\omega_{\mathrm{L},m} \propto \mu_0 \gamma_I^2 I_{m,\mathrm{z}}$. When a coherent rf pulse is applied to the spin ensemble, both $\boldsymbol{I}_n$ and $\boldsymbol{I}_m$ are rotated by the same angle. Consequently, for a π pulse the resonance frequency of $\boldsymbol{I}_n$ is instantaneously shifted by $2\delta\omega_{\mathrm{L},m}$. Not only are we unable to decouple the two spins with a π pulse sequence, but the application of the rf pulse strongly accelerates the decoherence arising from homonuclear coupling. This parasitic effect is referred to as *instantaneous diffusion*[196, 205, 206]. Unfortunately, it can only be suppressed partially by reducing the rotation angle of the rf pulses, which in turn reduces the echo signal amplitude[207–209]. However, it is actively used in a separate class of *solid echo* sequences which partially refocus homonuclear dipolar dephasing (see chapter 6 and e.g. [210–212]).

Unlike their heteronuclear counterparts, homonuclear spin flip-flops are generally not suppressed by a magnetic field and can limit the Hahn echo decay time. Since all spins $\boldsymbol{I}$ have approximately the same Larmor precession frequency, the in-plane component of $\boldsymbol{I}_m$ in the rotating frame produces a quasi-static in-plane magnetic field at the site of $\boldsymbol{I}_n$. In this way, it corresponds to a resonant weak rf field and due to the mutual nature of the interaction, can lead to effective flip-flops between the two spins. This mechanism is commonly labelled *direct flip-flop*.

We can therefore conclude that the nuclear spin dynamics in solids in a strong magnetic field are commonly governed either directly or indirectly by the respective homonuclear flip-flops amongst spin ensembles $\boldsymbol{I}, \boldsymbol{J}, \ldots$ for an otherwise unperturbed system. By contrast, instantaneous diffusion as an additional decoherence mechanism only arises under rf excitation.

5.2.2 Quadrupolar Coupling in a Strained System

As mentioned in the introduction, self-assembled InGaAs quantum dots are subject to considerable intrinsic strain gradients due to their strain-driven formation process. The elastic strain tensor ϵ_{ij} is in turn linked to an electric field gradient V_{ij} by the gradient-elastic tensor S_{ijkl}[39, 169]:

$$V_{ij} = \sum_{k,l=x,y,z} S_{ijkl}\epsilon_{kl} \ . \tag{5.3}$$

Both GaAs and InGaAs are zincblende structures with cubic symmetry. For this case, the gradient-elastic tensor in Voigt notation has only three non-zero components S_{11}, S_{12} and S_{44}, two of which are further linked by the symmetry property $S_{12} = -S_{11}/2$[213, 214]. Any anisotropic strain will result in a finite electric field gradient in these structures and V_{ij} only vanishes for hydrostatic strain ($\epsilon_{\mathrm{xx}} = \epsilon_{\mathrm{yy}} = \epsilon_{\mathrm{zz}}$ and $\epsilon_{ij} = 0$ for $i \neq j$)[39].

All stable nuclei in InGaAs quantum dots have magnetic moments $I > \frac{1}{2}$ and therefore possess a non-vanishing quadrupolar moment Q which will couple to the electric field gradient as[116, 192]

$$\begin{aligned} \mathcal{H}_{\mathrm{Q}} &= \frac{\hbar\omega_{\mathrm{Q}}}{6}\left(3I_{\mathrm{z}'}^2 - I^2 + \eta(I_{\mathrm{x}'}^2 - I_{\mathrm{y}'}^2)\right) \ , \\ \omega_{\mathrm{Q}} &= \frac{3eQV_{\mathrm{z}'\mathrm{z}'}}{\hbar 2I(2I-1)} \ , \qquad \eta = \frac{V_{\mathrm{x}'\mathrm{x}'} - V_{\mathrm{y}'\mathrm{y}'}}{V_{\mathrm{z}'\mathrm{z}'}} \ , \end{aligned} \tag{5.4}$$

where ω_{Q} denotes the quadrupolar coupling strength, η is the asymmetry parameter, and $\{\hat{e}_{\mathrm{x}'}, \hat{e}_{\mathrm{y}'}, \hat{e}_{\mathrm{z}'}\}$ are the principal axes of V_{ij}.

The intrinsic strain in self-assembled quantum dots gives rise to strong quadrupolar interactions. Here, we assume cylindrical symmetry of the electric field ($\eta = 0$) and an angle θ between the principal axis $\hat{e}_{\mathrm{z}'}$ and the magnetic field axis $\hat{e}_{\mathrm{z}}$ (a more general discussion is given in [39, 116]). At high magnetic fields $B_{0,\mathrm{z}}$, the quadrupolar Hamiltonian of equation (5.4) can be treated as a perturbation and causes first

and second order energy shifts[116]

$$\omega_{\mathrm{Q}}^{(1)}(I_{\mathrm{z}} \rightarrow I_{\mathrm{z}}+1) = \tfrac{1}{2}\omega_{\mathrm{Q}}\left(3\cos^2\theta - 1\right)\left(I_{\mathrm{z}} + \tfrac{1}{2}\right) \ , \tag{5.5}$$

$$\begin{aligned}\omega_{\mathrm{Q}}^{(2)}(I_{\mathrm{z}} \rightarrow I_{\mathrm{z}}+1) = &\frac{\omega_{\mathrm{Q}}^2}{32\omega_{\mathrm{L}}}\sin^2\theta(6I_{\mathrm{z}}(I_{\mathrm{z}}+1)(1-17\cos^2\theta) - \\ &- 2I(I+1)(1-9\cos^2\theta+3(1-13\cos^2\theta)) \ .\end{aligned} \tag{5.6}$$

We see that the first order term is zero for the central transition (CT). The second order contribution vanishes if the electric field gradient is parallel to the magnetic field ($\theta = 0$) and can generally be neglected for the STs as $\omega_{\mathrm{Q}}^{(2)} \ll \omega_{\mathrm{Q}}^{(1)}$. A schematic level diagram for the ^{75}As and ^{71}Ga spin-$\frac{3}{2}$ system is shown in figure 5.1a.

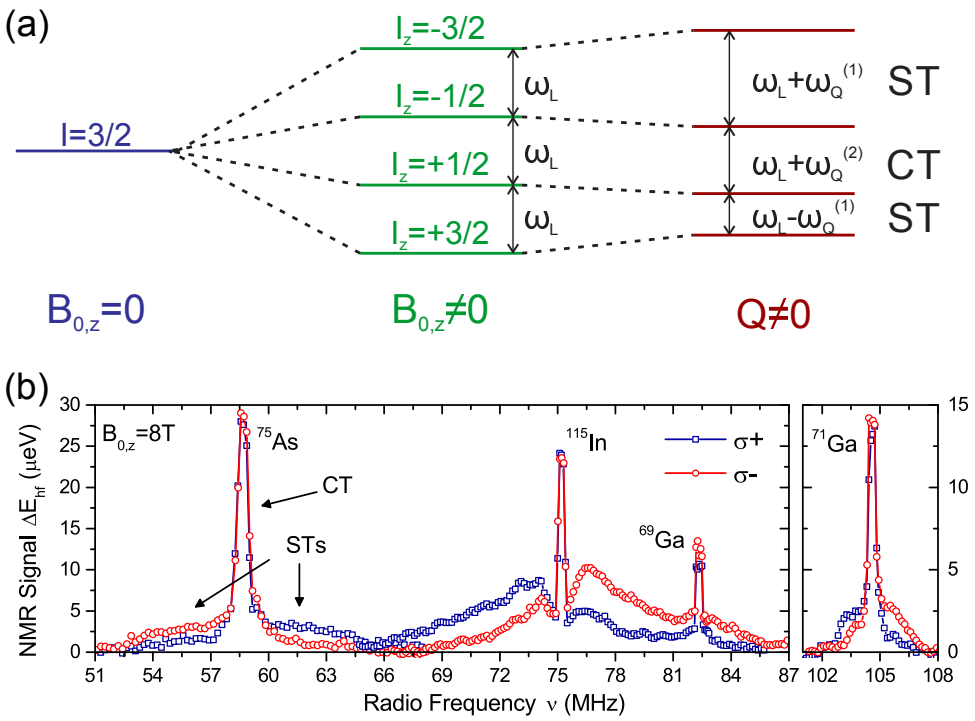

Figure 5.1: (a) Energy levels of an $I = \frac{3}{2}$ nuclear spin. NMR transitions in a magnetic field $B_{0,\mathrm{z}}$ are given by the Larmor frequency ω_{L} (centre). Additional quadrupolar shifts lift the degeneracy (right). While the CT is only shifted by a leading second order term $\omega_{\mathrm{Q}}^{(2)}$, the STs are also affected by the larger first order term $\omega_{\mathrm{Q}}^{(1)}$. (b) Full NMR spectrum of an InGaAs quantum dot at $B_{0,\mathrm{z}} = 8$ T under σ^+ (blue) and σ^- (red) circularly polarised excitation. The stronger broadening of the STs is clearly distinguishable. Experimental data courtesy of Evgeny Chekhovich. Full experimental details are given in section 5.4.1 and in [39].

Representative experimental data for all stable isotopes in an InGaAs quantum dot is plotted in figure 5.1b and is in excellent agreement with this theoretical description. The weak second order shift $\omega_{\mathrm{Q}}^{(2)}$ of the CT is found to be much smaller ($10 - 30$ kHz at $B_{0,\mathrm{z}} = 8$ T, also see figure 5.7 in section 5.4.1) than the first order shift $\pm\omega_{\mathrm{Q}}^{(1)}$ of several MHz observed for the satellite transitions (STs). As the strain gradually changes throughout the dot, the resulting quadrupolar shifts are highly inhomogeneous, leading to strong inhomogeneous broadening in cw NMR measurements.

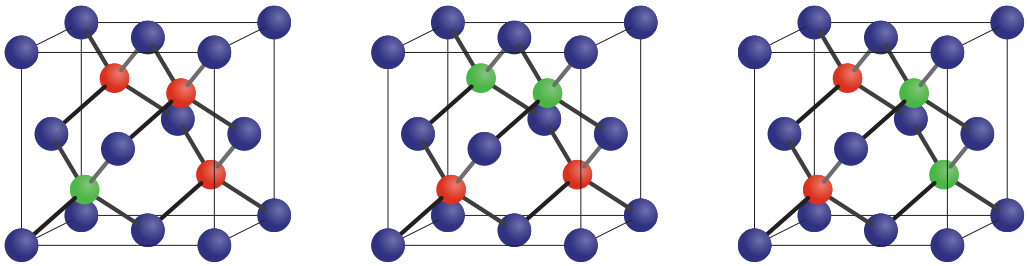

Figure 5.2: InGaAs unit cell with zincblende crystal structure. The three examples illustrate different tetrahedrally closest neighbour configurations for the arsenic sites (blue). Each of the four neighbouring sites can be occupied by an indium (red) or gallium (green) atom.

Experiments have shown that the quadrupolar broadening observed for ^{75}As is considerably stronger than that for ^{71}Ga[39]. This is due to a second source of nuclear displacement on the atomic scale. The quantum dot is formed by an InGaAs alloy with zincblende crystal structure. This means that every indium and gallium atom has four anionic nearest neighbours of arsenic in a tetrahedral configuration. By contrast the tetrahedral nearest neighbours of arsenic consists of a random combination of indium and gallium atoms (see figure 5.2). Consequently, the arsenic atoms are subject to an additional local strain and show stronger quadrupolar shifts[41, 215].

5.2.3 Quadrupolar Suppression of Dipolar Flip-Flops

We have seen in section 5.2.1 that the nuclear Hahn echo decay time in solids is commonly limited by spectral diffusion mediated by homonuclear spin flip-flops as well as instantaneous diffusion due to incomplete reversal of the local field under the π refocusing pulse. Strong inhomogeneous quadrupolar interactions directly affect the spectral diffusion mechanism. Even a second order quadrupolar shift $\omega_{\mathrm{Q}}^{(2)}$ changes the resonance frequencies of adjacent spins of the same isotope sufficiently to exceed the dipolar coupling strength ω_{D}. Consequently, the spins become "unlike" and the direct flip-flop term becomes suppressed analogously to the suppression of heteronuclear spin flip-flops in a magnetic field. In this case, the effect of spectral diffusion is also quenched as the heteronuclear static term can only introduce a fixed frequency shift in the absence of flip-flops and is refocused by the Hahn echo. The remaining dephasing is dominated by instantaneous diffusion.

In self-assembled InGaAs quantum dots, considerable biaxial strain of up to $|\epsilon_{\mathrm{b}}| \lesssim 7\%$ has been measured in x-ray[216, 217] and NMR studies[39]. As we discussed in section 5.2.2, this results in strong inhomogeneous broadening of the NMR transition lines, with additional local strain acting on ^{75}As due to compositional disorder. As a consequence, the homonuclear dipolar flip-flop term is suppressed and the nuclear spin bath dynamics are slowed down noticeably compared to similar lattice matched structures[183, 184].

This quadrupole-induced nuclear spin freezing in self-assembled quantum dots has been observed indirectly via its effect on the electron spin lifetime[200] and nuclear spin relaxation times[114, 115]. A direct demonstration of the effect of strain on nuclear phase memory times in a GaAs quantum well structure was made by Ono et al.[218] Most recently, Hahn echo measurements in InGaAs quantum dots revealed long nuclear phase memory times of up to ~ 4 ms in excellent agreement with these previous findings, confirming that the spin bath dynamics in the system are indeed strongly suppressed[41].

5.3 Optical and Spin Bath Properties of Sample B

As mentioned in the introduction, the sample used in the work of [41] was not gated and the absence of charges in the studied dots throughout the duration of the rf pulse sequence could not be fully ascertained. In this chapter, we study the nuclear Hahn echo decay in InGaAs quantum dots embedded in the intrinsic region of the p-i-n diode sample B. Here, we show how the charge occupancy of a dot is reflected in its bias dependent characteristics and discuss how the parameters for the optical preparation and detection of the nuclear spin bath polarisation are calibrated.

5.3.1 Bias Dependence of Quantum Dot Properties

As described in chapter 4.3.2, our experiments consist of three distinct stages: optical preparation of the nuclear spin bath, rf manipulation, and weak optical probing of the final bath polarisation. In principle, this does not impose major limitations on the properties required of the studied quantum dot. However, a number of dot and bias specific characteristics influence the quality and accuracy of the measurement: a high PL count rate is desirable to minimise the necessary measurement time. In addition, narrow optical transition linewidths and large hyperfine fields increase the fitting accuracy and amplitude of the NMR signal derived from changes of the Overhauser splitting. Finally, a long nuclear spin relaxation time $T_{1,\mathrm{n}}$ is favourable as it is indicative of the absence of charges in the dot and saves us from having to correct for the T_1 decay of the Overhauser splitting.

In order to identify suitable quantum dot candidates for NMR experiments, we perform bias dependent PL measurements as illustrated in figure 2.5 on a large number of dots in sample B. Since all of our NMR experiments are done at $B_{0,\mathrm{z}} = 8$ T, we use the same field in our characterisation and calibration measurements. The combined PL intensity profile of these ~ 50 measurements is shown as a dashed grey curve in figure 5.3a together with representative PL curves for the neutral (blue) and

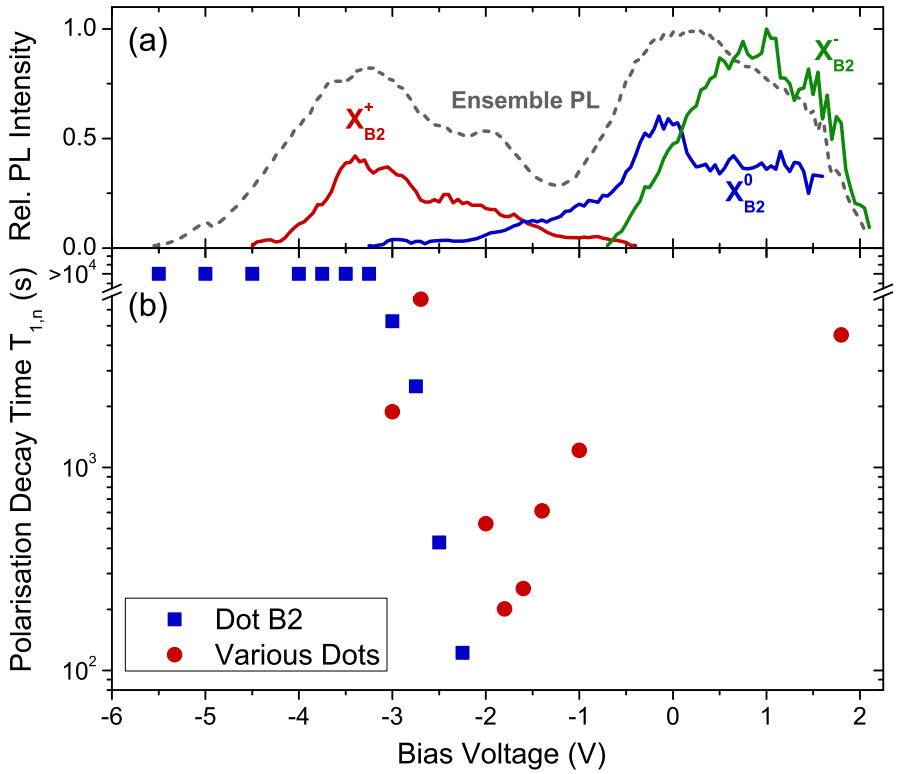

Figure 5.3: Bias dependence of quantum dot parameters in sample B at $B_{0,z}$ = 8 T. (a) Normalised combined PL intensity of $\sim$ 50 quantum dots as a function of the applied diode bias (dashed grey line). Individual intensity profiles for the X^+ (red), X^0 (blue) and X^- (green) transitions in dot B2 are shown as an example. (b) Nuclear spin relaxation time $T_{1,n}$ at different bias voltages. Blue data points were obtained from dot B2 and red data points from several other dots.

singly charged (red and green) exciton transitions in an individual dot (B2). The PL intensities vary from dot to dot due to the narrow cavity resonance of sample B. Highest intensities are typically found for the negative trion X^-, although the optical transition lines in this bias region are slightly broader than in the X^0 region ($\gtrsim$ 30 μeV compared to $\gtrsim$ 20 μeV). Since a similar tendency is observed for the positive trion, we focus on identifying dots with a particularly strong X^0 PL signal for our experiments.

As we saw in chapter 3.1.2, there are several effective DNP channels under high power circularly polarised optical excitation. Both charged and neutral exciton states can be used for nuclear spin pumping. While we detect Overhauser shifts of

$E_{\mathrm{hf}} \gtrsim 50\ \mu\mathrm{eV}$ throughout the bias range of the diode, the highest spin bath polarisations ($E_{\mathrm{hf}} \sim 90\ \mu\mathrm{eV}$) are measured under forward biases where charge extraction is fastest.

Due to the p-i-n diode structure of our sample, we can empty the intrinsic region in which the dot layer is located of all charges under large reverse biases. In order to verify that this is indeed the case, we study the nuclear spin polarisation decay at various diode biases. As we saw in chapter 3.2.2, nuclear spin relaxation dynamics are largely governed by hyperfine-induced processes. Therefore, the presence of charge carriers in a quantum dot strongly reduces $T_{1,\mathrm{n}}$.

Experimentally, we measure the spin bath polarisation decay by adopting the pump-probe scheme introduced in chapter 4.3.2. However, instead of applying an rf field to the sample we use a variable delay between pump and probe pulse during which the bath polarisation evolves in the dark without rf excitation. Our results, shown in figure 5.3b, are in good agreement with the bias dependent behaviour reported by other groups. We observe fast decay on the order of $T_{1,\mathrm{n}} \approx 100 - 200$ s in the X^+ to X^0 transition region where fast charge cotunnelling can depolarise the spin bath quickly via the hyperfine flip-flop process[115, 182]. Extremely long spin relaxation times of $T_{1,\mathrm{n}} \geq 1$ h under large reverse biases $V_{\mathrm{bias}} \leq -3$ V confirm our expectation that the dot is free of charges.

To summarise, we find that different bias regions offer favourable properties for each of the three stages in the experiment cycle. Accordingly, we switch the diode bias during the experiment cycle in the NMR measurements presented in this chapter. We choose a forward bias $V_{\mathrm{pump}} = 1.5$ V for strong nuclear polarisation build-up during the pump stage. Rf excitation is performed at a large reverse bias $V_{\mathrm{rf}} = -4.5$ V where no measurable T_1 decay is detected and the dot is free of charge carriers. Finally, a probe bias in the region $V_{\mathrm{probe}} = -1.5 \ldots 0$ V is selected dot-specifically for optimal signal intensity and PL transition linewidth.

5.3.2 Pump and Probe Pulse Calibration

In addition to the applied voltage bias, several other pump and probe parameters need to be considered. In chapter 3.1.2, we discussed how the feedback of nuclear spin alignment on the polarisation rate can lead to bistable regions in the Overhauser splitting[143–145]. Under non-resonant optical pumping, this behaviour is observed for the σ^- excitation branch in InGaAs quantum dots (see figure 3.2). While this bistability leads to large Overhauser splittings at comparatively low optical pumping powers, it can equally cause a sudden large-scale depolarisation of the spin bath under optical excitation with the linearly polarised probe pulse if the negative DNP feedback is triggered. Therefore, we avoid the bistability in the NMR measurements by preparing the spin bath under σ^+ excitation.

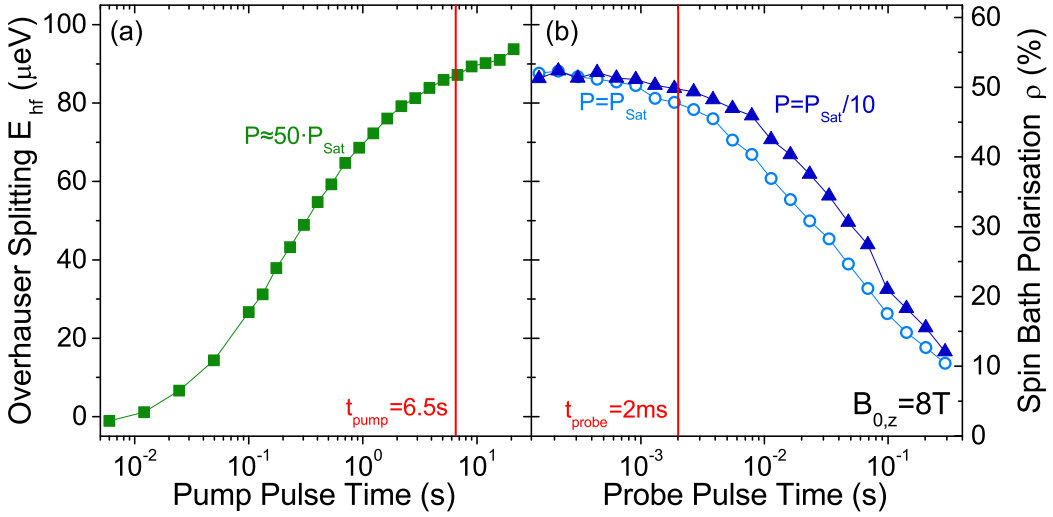

Figure 5.4: Dependence of the Overhauser field induced exciton transition energy splitting E_{hf} at $B_{0,\mathrm{z}} = 8$ T on the optical excitation pulse time. (a) Increase of E_{hf} under strong σ^+ polarised excitation for an initially unpolarised spin bath ($E_{\mathrm{hf}}(0) = 0$). (b) Decrease of E_{hf} under weak, linearly polarised optical excitation for an initially polarised spin bath ($E_{\mathrm{hf}}(0) \approx E_{\mathrm{hf,max}}$). Red lines mark the chosen pump and probe times for NMR experiments.

The build-up of DNP is not an instantaneous process. To characterise the rise time under σ^+ excitation at $B_{0,\mathrm{z}} = 8$ T, we perform a series of pump-probe experiments as described in chapter 4.3.2 with varying pump pulse duration and without rf ex-

citation. Figure 5.4a shows the result of a typical nuclear spin polarisation build-up measurement. The X^0 hyperfine splitting E_{hf} is depicted as a function of the pump pulse excitation time. Using non-resonant optical excitation powers far beyond the saturation level $P_{\mathrm{Sat}} \approx 20\ \mu$W of a neutral exciton ($P \approx 50 \cdot P_{\mathrm{Sat}}$), we observe an increase of the Overhauser splitting with increasing pump time from $E_{\mathrm{hf}}(0) = 0$ up to a saturation value $E_{\mathrm{hf,max}} \sim 90\ \mu$eV (polarisation degree $\rho \sim 53\%$). For NMR experiments we choose a pump pulse time $t_{\mathrm{pump}} = 6.5$ s just beyond the onset of saturation. Longer pump times would slightly increase the stability of the measurement against alignment drifts. However, we have to take into account that t_{pump} dominates the measurement time: doubling the pump time would nearly double the experiment cycle time t_{cycle} as well.

The probe pulse duration is calibrated in a similar fashion, again using the familiar pump-probe scheme without rf excitation. The low power, linearly polarised optical probe pulse depolarises the spin bath over time. Therefore, we have to find a probe pulse power and duration which does not influence the NMR signal, i.e. the rf induced change in the Overhauser splitting ΔE_{hf}, noticeably. Figure 5.4b shows the probe time dependent decay of the Overhauser splitting for probe pulses at X^0 saturation power P_{Sat} (open circles) and at $P = P_{\mathrm{Sat}}/10$ (triangles). As expected, faster decay occurs at the higher probe pulse power. On the other hand, the stronger PL signal also reduces the required CCD exposure time for intensities comparable to those obtained at lower probe power. From a more detailed study we conclude that the lower probe power provides a slightly stronger signal for pulse durations where no measurable decay was observed. We therefore choose $P_{\mathrm{probe}} = P_{\mathrm{Sat}}/10$ and $t_{\mathrm{probe}} = 2$ ms for the experiments.

5.4 Calibration of the Pulsed NMR Experimental Parameters

Figure 5.5a shows the full experiment cycle for pulsed ODNMR measurements. As described in chapter 4.3.2, it follows a pump-rf-probe scheme. In the previous section we discussed the calibration of the optical pump and probe parameters. Here, we focus on the additional calibration steps required for the rf excitation stage.

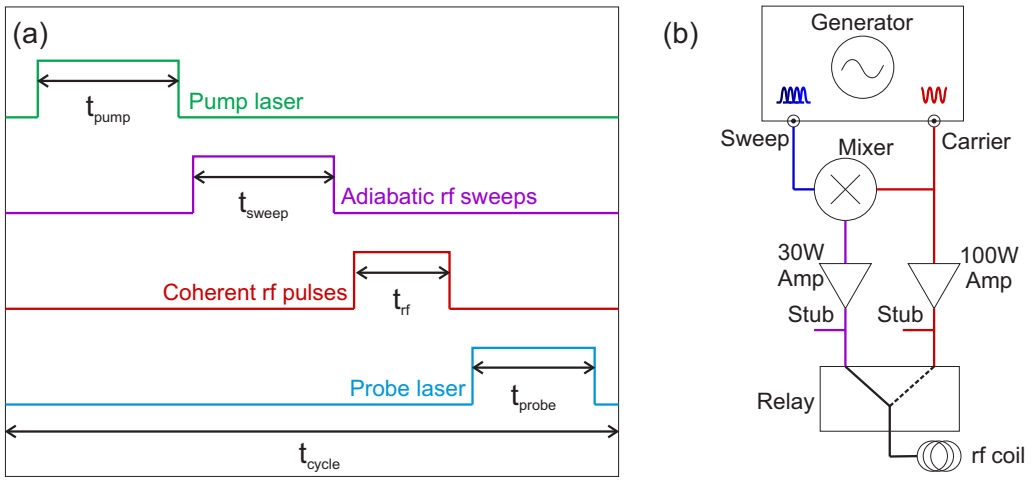

Figure 5.5: (a) The experiment cycle t_{cycle} for pulsed NMR experiments: The spin bath is polarised by a pump laser for a time t_{pump} before the CT population difference is enhanced by adiabatic rf sweeps during t_{sweep}. After coherent rf excitation of the CT for a time t_{rf}, a probe laser pulse is applied for t_{probe}. (b) Setup for the two-stage rf excitation. The adiabatic sweep is formed by mixing the carrier frequency ν_{rf} with a sweep signal. The coherent pulse at ν_{rf} is sent directly to a high power amplifier. Both excitation paths are stub matched and a mechanical relay is used to select which signal is sent to the rf coil.

All coherent NMR experiments are done on CTs as the inhomogeneous NMR linewidths of the STs are far too broad for resonant driving(see figure 5.1b and [39]). However, after the pump pulse, the spin bath is strongly polarised and the populations of the $I_z = \pm\frac{1}{2}$ levels are quite small. This can easily be seen when considering a fully polarised spin bath. In this case, all spins of the ^{75}As and ^{71}Ga isotopes studied in this work would be in the $I_z = +\frac{3}{2}$ state and the population of the $I_z = \pm\frac{1}{2}$ states would be zero. Consequently, no change in the respective

populations would be induced under resonant rf excitation of the CT.

In order to increase the CT population difference and NMR signal amplitude, we use an adiabatic population transfer technique prior to application of the resonant hard pulse sequence[41, 219]. In this section we will first discuss how we determine the NMR resonance frequency and inhomogeneous linewidth of a given isotope before introducing the adiabatic inversion technique. We will conclude with the demonstration of Rabi oscillations of the Overhauser splitting which are used to calibrate the rf pulse durations for coherent spin rotations.

5.4.1 Resonance Frequency Calibration with Inverse NMR

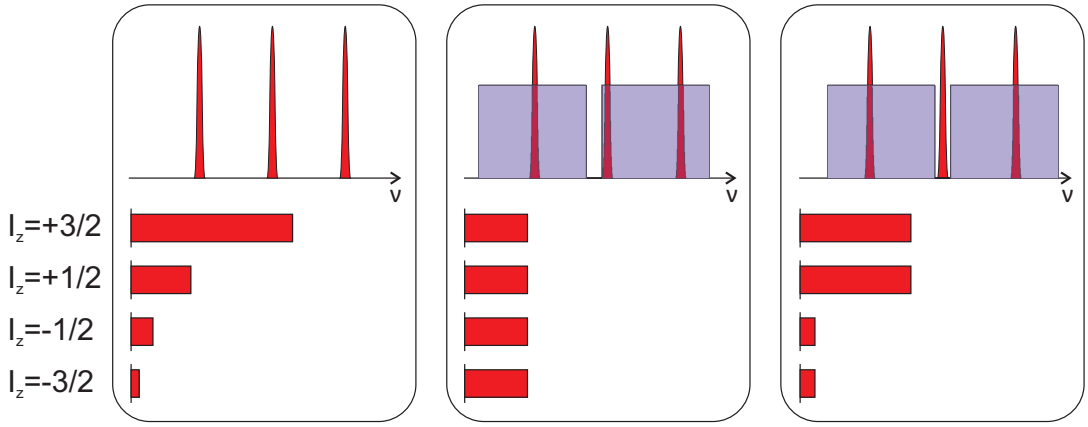

Figure 5.6: Schematic of the inverse NMR technique for a spin-$\frac{3}{2}$ system. Optical excitation creates a strong spin bath polarisation $\rho \sim 65\%$ (left panel). Next, a broad rf excitation spectrum with gap $\delta\nu$ is applied (blue). If the gap does not overlap with any nuclear spin transition, all spin state populations are equalised in saturation ($\rho = 0\%$, centre panel). If the gap overlaps with a transition, two decoupled systems are saturated instead, resulting in a non-zero final nuclear polarisation $\rho > 0\%$ (right panel).

The gyromagnetic ratios γ^* of the nuclear isotopes in InGaAs quantum dots are well-known (see table 3.1) and it is easy to determine the Larmor frequency $\nu_\mathrm{L} = \gamma^* B_{0,\mathrm{z}}$ for a given magnetic field. However, as the sample position is generally slightly offset from the centre of the superconducting magnet (see setup in figure 4.1), the exact magnetic field at the dot location is unknown. In addition, we want to measure the inhomogeneous linewidth $\Delta\nu_\mathrm{inh}$ of the nuclear transition that we

intend to drive resonantly to ensure that the coherent rf excitation pulse will have sufficient bandwidth to fulfil the hard pulse condition $\omega_1 \gg \frac{\Delta\nu_{\mathrm{inh}}}{2}$ (see section 3.3.2).

We determine the nuclear resonance frequencies ν_{L} using a broadband cw NMR technique dubbed *inverse NMR* which was recently introduced by Chekhovich et al.[39] The technique is illustrated in figure 5.6. In contrast to the conventional saturation NMR approach of depolarisation at a fixed frequency or within a narrow frequency band[116, 220], we depolarise all spins within a broad band covering the entire inhomogeneous NMR resonance of a given isotope except for a narrow gap of width $\delta\nu = 8$ kHz (for ^{71}Ga) or $\delta\nu = 24$ kHz (for ^{75}As). Under this excitation scheme, the isotope is fully depolarised if none of the NMR transitions overlap with the gap. By contrast, whenever the gap is in resonance with a transition $m_{\mathrm{I}} \leftrightarrow m_{\mathrm{I}} + 1$, the populations of states $I_{\mathrm{z}} = -I \ldots m_{\mathrm{I}}$ and $I_{\mathrm{z}} = m_{\mathrm{I}} + 1 \ldots I$ are

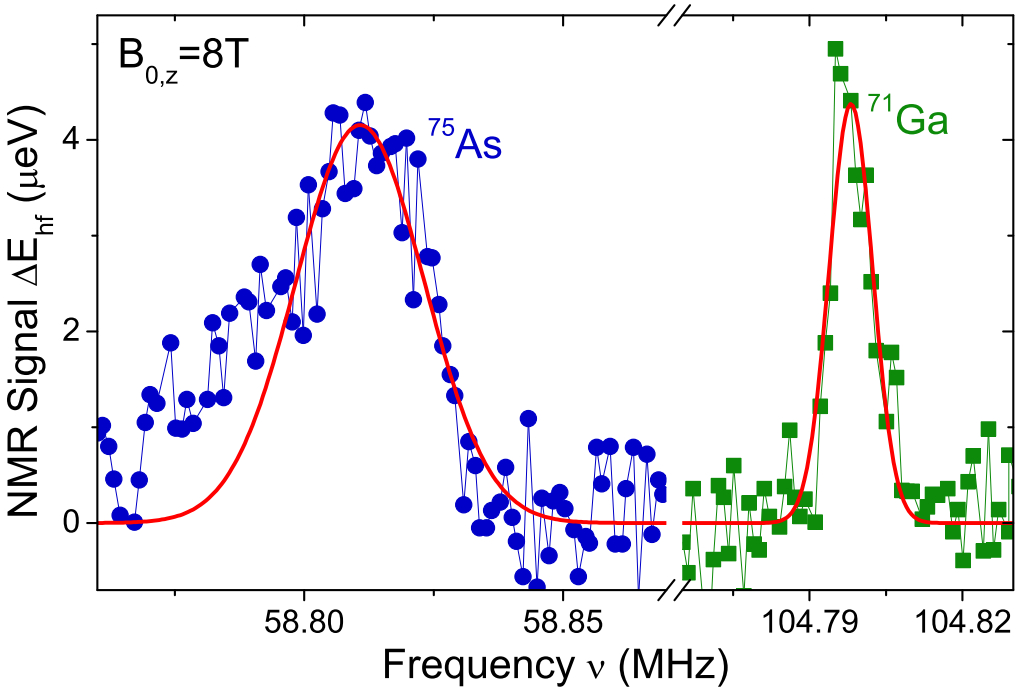

Figure 5.7: Measured hyperfine shift ΔE_{hf} as a function of the inverse NMR gap central frequency ν at $B_{0,\mathrm{z}} = 8$ T. ΔE_{hf} is given relative to full depolarisation of the respective isotope. Data for the CTs of ^{75}As (circles) and ^{71}Ga (squares) is fitted with Gaussian functions (red lines) to obtain the inhomogeneous NMR linewidths $\Delta\nu_{\mathrm{inh}}$.

equalised independently, leading to an enhancement of the NMR signal by up to $(I + 1/2)^3$ compared to standard saturation techniques[39].

Figure 5.7 shows the change in the measured hyperfine shift ΔE_{hf} in an inverse NMR experiment as a function of the rf gap central frequency ν for the ^{75}As (circles) and ^{71}Ga (squares) CTs at $B_{0,\mathrm{z}} = 8$ T. Fitting with a Gaussian function (red lines) gives an NMR resonance frequency $\nu_{\mathrm{L}}(^{75}\mathrm{As}) = 58.81$ MHz and an inhomogeneously broadened linewidth $\Delta\nu_{\mathrm{inh}}(^{75}\mathrm{As}) \approx 24$ kHz for ^{75}As. The corresponding ^{71}Ga resonance linewidth at $\nu_{\mathrm{L}}(^{71}\mathrm{Ga}) = 104.80$ MHz is resolution limited with $\Delta\nu_{\mathrm{inh}}(^{71}\mathrm{Ga}) \approx 8$ kHz. We can calculate the respective ensemble dephasing times from $T^*_{2,\mathrm{n}} = (2\pi\Delta\nu_{\mathrm{inh}})^{-1}$, obtaining $T^*_{2,\mathrm{n}}(^{75}\mathrm{As}) \gtrsim 6.5$ μs and $T^*_{2,\mathrm{n}}(^{71}\mathrm{Ga}) \gtrsim 19.0$ μs in good agreement with previous findings[39, 41]. For both isotopes the inhomogeneous broadening is caused by inhomogeneous second order quadrupolar interactions. The broader ^{75}As NMR linewidth $\Delta\nu_{\mathrm{inh}}$ can be explained by the influence of additional compositional disorder as discussed in section 5.2.2[41].

5.4.2 Adiabatic Population Transfer

Since we perform all pulsed experiments on the CT, we are interested in a large population difference between the $I_{\mathrm{z}} = \pm\frac{1}{2}$ states. Unfortunately, this population difference is small for a strongly polarised spin bath with $I \geq \frac{3}{2}$ and would be zero for a fully polarised spin bath where neither state would be populated. Instead, the largest and smallest populations are generally those of the outermost states ($I_{\mathrm{z}} = \pm\frac{3}{2}$ for ^{75}As and ^{71}Ga, see left panel of figure 5.6). However, we can transfer these populations to the $I_{\mathrm{z}} = \pm\frac{1}{2}$ states by *adiabatic inversion*.

Following the optical pumping, the nuclear spin bath is polarised along $\hat{e}_{\mathrm{z}}$. We saw in chapter 3.3.2 that the time evolution of the magnetisation in the rotating frame in the presence of an rf field with amplitude ω_1 is described by a precession about the vector $\mathbf{\Omega} = (\omega_1, 0, -\Delta)^{\mathsf{T}}$. At large detuning $\Delta = \omega_{\mathrm{rf}} - \omega_{\mathrm{L}}$ from the resonance frequency, the Bloch equation (3.28) approximately describes a rotation

about $\hat{e}_z$. If we keep the rf field amplitude constant and vary the detuning slowly at a rate $\dot{\nu}$, the magnetisation vector will follow the motion of $\mathbf{\Omega}$ adiabatically. In this way, we can invert the population of a two-level system by scanning across the resonance from $-\Delta$ to $+\Delta$[192]. The probability that the population remains in its initial state after the sweep is described by the Landau-Zener tunnelling formula

$$p_{\mathrm{diab}} = \mathrm{e}^{-\omega_1^2/\dot{\nu}} \,. \tag{5.7}$$

If $p_{\mathrm{diab}} \ll 1$, adiabatic inversion occurs and the populations are swapped. We see that this is the case for large rf amplitudes ω_1 and slow sweep rates $\dot{\nu}$[221]. This technique has recently been used on its own for the detection of NMR in InGaAs quantum dots by fully inverting the nuclear bath polarisation[40].

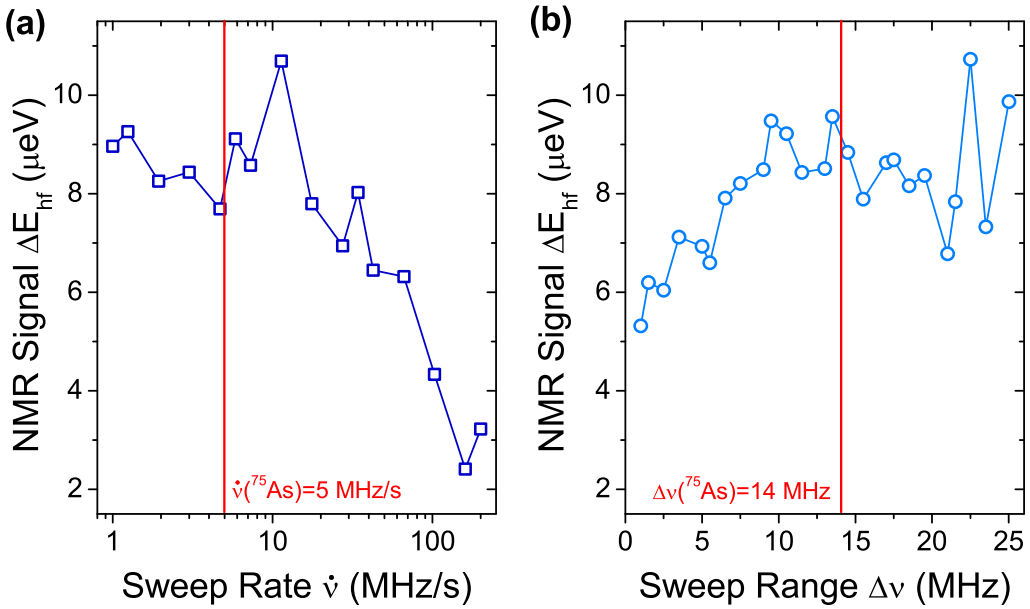

Figure 5.8: Adiabatic sweep calibration for ^{75}As at $B_{0,z} = 8$ T. (a) Dependence of the $I_z = \pm\frac{1}{2}$ population contrast ΔE_{hf} on the rf pulse sweep rate $\dot{\nu}$ for a fixed sweep range $\Delta\nu \approx 8.5$ MHz. (b) Population contrast ΔE_{hf} as a function of the sweep range $\Delta\nu = \nu_{\mathrm{f}} - \nu_{\mathrm{i}}$ for a fixed sweep rate $\dot{\nu} = 5$ MHz/s.

Figure 5.5b illustrates how the chirped rf pulses for adiabatic inversion of the ST transitions are formed in our NMR setup: a sweep envelope (blue) with initial frequency ν_{i}, final frequency ν_{f} and sweep rate $\dot{\nu}$ is mixed with a carrier frequency

ν_{rf} (red)[41]. We use broadband matching (see chapter 4.3.1) for the amplified sweep signal as it covers a range of several MHz. The rf amplitudes of the swept pulses in the rotating frame are on the order of $B_1 \approx 0.1$ mT.

For calibration of the sweep rate we performed pump-rf-probe experiments using adiabatic sweeps with fixed sweep range $\Delta\nu = \nu_{\mathrm{f}} - \nu_{\mathrm{i}}$ and with and without a subsequent coherent π pulse applied to the CT. The difference between the two curves is depicted in figure 5.8a for ^{75}As and corresponds to the full NMR signal amplitude ΔE_{hf} for a given sweep rate. We can clearly see the decreasing signal contrast at higher sweep rates where the adiabatic condition is no longer fulfilled. For adiabatic preparation in pulsed NMR experiments we choose $\dot{\nu}(^{75}\mathrm{As}) = 5$ MHz/s and $\dot{\nu}(^{71}\mathrm{Ga}) = 6$ MHz/s. From analogous measurements with fixed sweep rate and varying range, we determine the maximum width of the STs (see figure 5.8b for ^{75}As). Based on such calibration measurements, we choose $\Delta\nu(^{75}\mathrm{As}) = 14$ MHz and $\Delta\nu(^{71}\mathrm{Ga}) = 3.5$ MHz for sample B. We note that the coherent π pulse had already been calibrated prior to the experiments shown in figure 5.8. However, qualitative results can also be obtained with a hard pulse that is not exactly a π pulse, albeit with smaller signal contrast.

5.4.3 Hard Pulse Calibration

Once the populations of $I_{\mathrm{z}} = \pm\frac{1}{2}$ have been maximised and minimised respectively, the isotope is fully prepared for coherent rf experiments. In chapter 3.3.2, we saw that the magnetisation along the magnetic field axis $\hat{e}_{\mathrm{z}}$ shows an exponentially damped oscillating behaviour under resonant driving if the rf amplitude is sufficiently large. For InGaAs quantum dots with extremely long nuclear spin relaxation times $T_{1,\mathrm{n}}$ (see section 5.3.1), this condition is met when the oscillation period is much shorter than the nuclear spin phase memory time $T_{\mathrm{Rabi}} \ll T_{\mathrm{M,n}}$.

We are able to observe these Rabi oscillations by using the full experiment cycle of figure 5.5a with varying hard pulse times t_{rf}. The resonant rf excitation and the

chirped pulse are provided by the same generator (see figure 5.5b). However, we use a 100 W class AB amplifier for hard pulse excitation and the circuit is stub matched for the rf driving frequency ν_{rf} as described in chapter 4.3.1. A mechanical relay selects the rf path connected to the feeding coil.

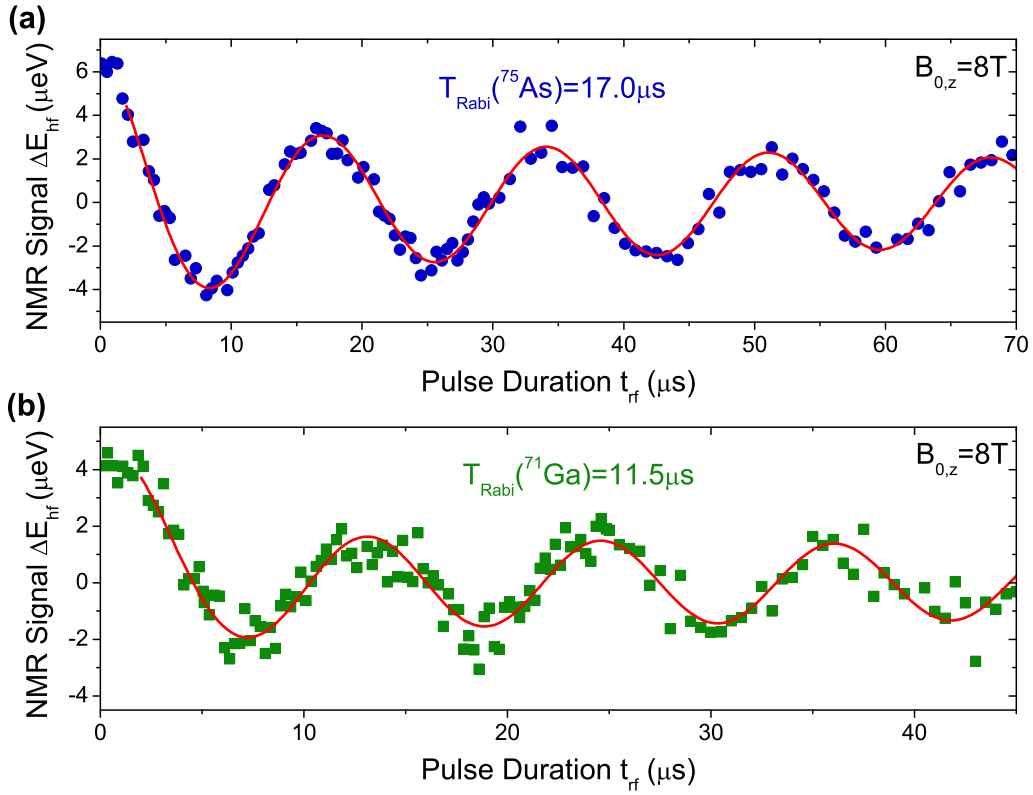

Figure 5.9: Hard pulse rf calibration measurements. The hyperfine shift ΔE_{hf} is shown as a function of the duration t_{rf} of a coherent rf pulse applied to the CT of (a) ^{75}As (blue circles) and (b) ^{71}Ga (green squares) at $B_{0,\mathrm{z}} = 8$ T. Rabi periods T_{Rabi} and corresponding rf fields B_1 are extracted from fitting with an exponentially decaying cosine function (solid red lines).

The results of the Rabi oscillation experiments for ^{75}As and ^{71}Ga are shown in figures 5.9a and b, respectively. From the fitting with an exponentially decaying cosine function (solid red lines), we obtain Rabi periods $T_{\mathrm{Rabi}}(^{75}\mathrm{As}) = 17.0\ \mu$s and $T_{\mathrm{Rabi}}(^{71}\mathrm{Ga}) = 11.5\ \mu$s, which correspond to rf fields $B_1(^{75}\mathrm{As}) = 4.0$ mT and $B_1(^{71}\mathrm{Ga}) = 3.3$ mT in the rotating frame with $B_1 = \frac{1}{2\gamma^* T_{\mathrm{Rabi}}}$. Here we take into account that the Rabi oscillation frequency of the CT for a spin-$\frac{3}{2}$ is twice the frequency ω_1 due to the dipolar transition matrix element (see equation (3.20)).

We note that the fits used to extract the Rabi period (red lines) are slightly phase shifted, corresponding to a 2 μs delay. This is because the fitting implicitly assumes that the pulse area is linearly proportional to the pulse time t_{rf}. While this assumption is justified for long pulses, it fails at short timescales where the rise time of the amplifier gating circuit ($t_{\mathrm{rise}} \approx 440$ ns) dominates the pulse profile. We extract the required pulse duration for a π pulse t_π from the location of the first Rabi oscillation minimum and set $t_{\pi/2} = t_\pi/2$. This calibration proves to be sufficiently accurate for Hahn echo experiments where small pulse errors affect the echo signal amplitude only marginally. In chapter 6, we will introduce a more accurate calibration method which is required for longer NMR pulse sequences.

5.5 Long Nuclear Spin Phase Memory Times in Hahn Echo Experiments

We saw in the inverse NMR calibration measurements that the inhomogeneously broadened CT linewidths of the nuclear spins in InGaAs quantum dots are on the order of $\Delta\nu_{\mathrm{inh}} \approx 10 - 30$ kHz, corresponding to ensemble dephasing times of $T^*_{2,\mathrm{n}} \approx 5 - 20$ μs. A widespread NMR technique used to remove inhomogeneous broadening and recover the homogeneous linewidth is the Hahn echo sequence $\frac{\pi}{2} - \tau - \pi - \tau \left(-\frac{\pi}{2}\right)$ consisting of a coherent initialisation pulse $\frac{\pi}{2}$ and a refocusing π pulse separated by a delay time τ, with detection of the NMR signal after another time interval τ[199]. The final $\frac{\pi}{2}$ pulse is not strictly part of the sequence but is required in the optically detected NMR scheme as our measurement is only sensitive to changes in the magnetisation along the magnetic field axis $\hat{e}_{\mathrm{z}}$.

Figure 5.10 illustrates the effect of the Hahn echo pulse sequence on a nuclear spin ensemble in the rotating frame. Starting with a strongly polarised ensemble with magnetisation oriented along the axis $\hat{e}_{\mathrm{z}}$ of the external magnetic field, a $\frac{\pi}{2}$ pulse rotates the magnetisation vector into the x-y plane. During the first delay τ,

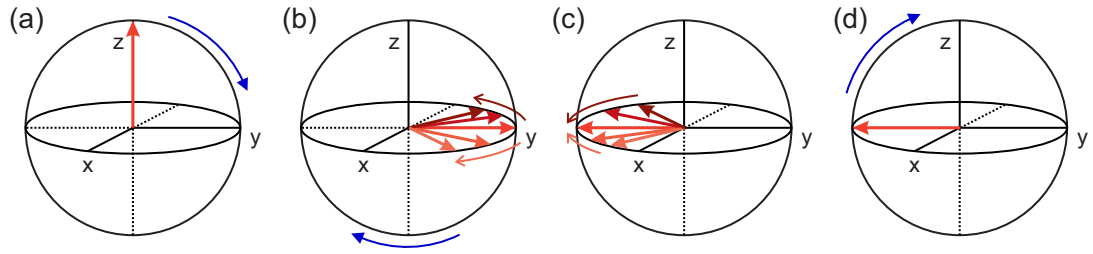

Figure 5.10: The Hahn echo sequence in an ODNMR measurement consists of three coherent pulses separated by delays τ: (a) An initial $\frac{\pi}{2}$ pulse rotates the $\hat{e}_z$ polarised nuclear spins into the x-y plane. (b) After a delay τ during which the spin ensemble has been subject to homogeneous and inhomogeneous dephasing, a π pulse is applied. (c) The inhomogeneous dephasing is refocused over another time period τ. (d) A final $\frac{\pi}{2}$ pulse realigns the refocused magnetisation vector with the $\hat{e}_z$ axis for optical read-out.

the spin ensemble dephases with a time constant $T^*_{2,n}$ due to magnetic field inhomogeneities. Neglecting homogeneous decoherence sources, a spin with resonance frequency $\omega_L = \omega_{rf}$ will remain static in the rotating frame. By contrast, any spin with resonance frequency $\omega_{rf} \pm \Delta\omega$ will begin to precess about the $\hat{e}_z$ axis in a clockwise or anticlockwise fashion. If we were to probe the ensemble polarisation at this point by applying a $-\frac{\pi}{2}$ pulse we would measure the free induction decay described by $T^*_{2,n}$. Instead, we apply a π pulse which flips the dephased spin ensemble about the rotation axis. Crucially, spins with a resonance offset will continue to precess in the same direction as before. Therefore, after another delay τ, the ensemble has refocused itself and upon application of the second $\frac{\pi}{2}$ pulse we can detect the remaining magnetisation optically. With varying delay τ, a magnetisation decay over the timescale $T^{HE}_{M,n} > T^*_{2,n}$ is observed, arising from homogeneous decoherence sources that affect the entire ensemble in the same way.

We apply the Hahn echo sequence to the CTs of the ^{75}As and ^{71}Ga spin ensembles in an InGaAs quantum dot on sample B. As before, we use a static external magnetic field $B_{0,z} = 8$ T and employ the pump-rf-probe scheme introduced in figure 5.5a with the experimental parameters determined in the previous sections. For each data point with fixed delay τ, we also take a reference measurement with a single

$\frac{\pi}{2}$ rf pulse, corresponding to full depolarisation of the probed ensemble. As this measurement is independent of τ, it allows us to correct for small drifts of the Zeeman splitting during the measurement time of up to 24 h.

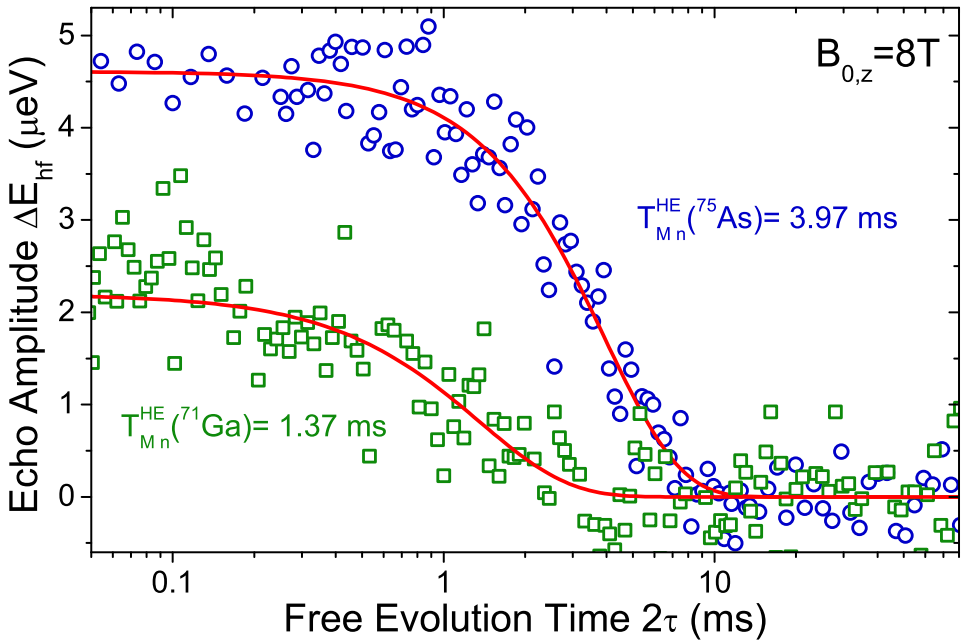

Figure 5.11: Nuclear Hahn echo amplitude ΔE_{hf} at $B_{0,\mathrm{z}} = 8$ T for ^{75}As (blue circles) and ^{71}Ga (green squares) as a function of the total free evolution time 2τ before and after the π refocusing pulse. Phase memory times $T^{\mathrm{HE}}_{\mathrm{M,n}}$ are obtained from compressed exponential fits $\propto \mathrm{e}^{-(2\tau/T^{\mathrm{HE}}_{\mathrm{M,n}})^{\beta}}$ (solid red lines).

Figure 5.11 shows representative results from ^{75}As (circles) and ^{71}Ga (squares) Hahn echo measurements at $B_{0,\mathrm{z}} = 8$ T with varying pulse delays τ. The echo amplitude ΔE_{hf} is given as the difference between the X^0 optical transition energy splittings in the Hahn echo and reference measurements. Solid red lines show the fitting with a compressed exponential function (CEF)[222, 223]

$$\Delta E_{\mathrm{hf}}(2\tau) = \Delta E_{\mathrm{hf}}(0)\mathrm{e}^{-(2\tau/T^{\mathrm{HE}}_{\mathrm{M,n}})^{\beta}} , \tag{5.8}$$

with nuclear phase memory time $T^{\mathrm{HE}}_{\mathrm{M,n}}$ and compression factor β. We extract the respective phase memory times $T^{\mathrm{HE}}_{\mathrm{M,n}}(^{75}\mathrm{As}) = 3.97 \pm 0.25$ ms and $T^{\mathrm{HE}}_{\mathrm{M,n}}(^{71}\mathrm{Ga}) = 1.37 \pm$

0.23 ms. These values exceed the ensemble dephasing times $T^*_{2,n}$ derived from the inhomogeneous linewidth by more than two orders of magnitude. The errors stated correspond to 90% confidence intervals and the compression factors for the best fits are $\beta(^{75}\mathrm{As}) = 1.57 \pm 0.19$ and $\beta(^{71}\mathrm{Ga}) = 1.33 \pm 0.28$. The compression factors indicate that the underlying spin bath dynamics limiting $T^{HE}_{M,n}$ contain contributions with both quadratic ($\beta = 2$, Gaussian) and single ($\beta = 1$, Lorentzian) exponential decay behaviours[209, 222]. However, we refrain from a more detailed discussion of β as the error margins for this parameter are too large to justify a physical interpretation and similar $T^{HE}_{M,n}$ can be obtained for a fixed $\beta = 1$ or $\beta = 2$. We note that the weaker NMR signal amplitude $\Delta E_{hf}(0)$ of ^{71}Ga is expected as the stoichiometric ratio of ^{71}Ga in the dot is considerably lower than that of ^{75}As.

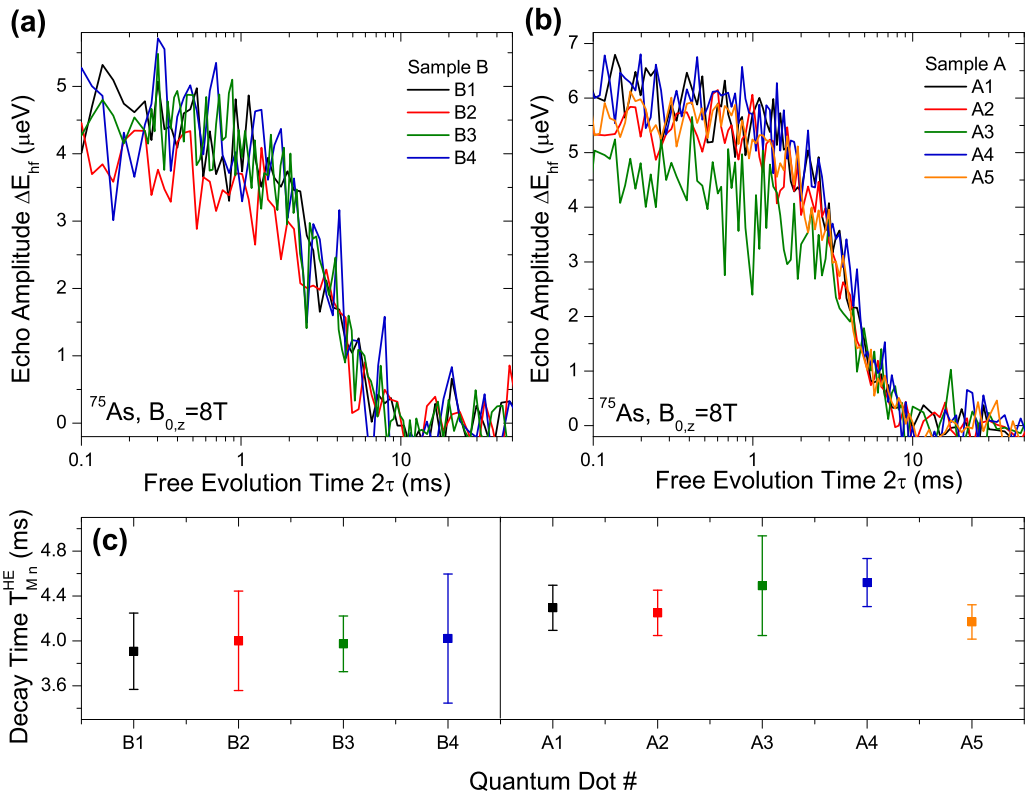

Figure 5.12: Comparison of ^{75}As Hahn echo decay measurements in samples A and B at $B_{0,z} = 8$ T. (a,b) Dependence of the nuclear spin echo amplitude ΔE_{hf} on the free evolution time 2τ for (a) dots B1-B4 in the p-i-n sample B and (b) dots A1-A5 in the ungated sample A. (c) Hahn echo phase memory times $T^{HE}_{M,n}$ obtained from fitting to the data shown in (a) and (b) with compressed exponential functions.

The results of additional ^{75}As Hahn echo decay measurements on different quantum dots in sample B are shown in figure 5.12a. The phase memory times $T_{\mathrm{M,n}}^{\mathrm{HE}}$ extracted from fitting with equation (5.8) are shown in the left half of figure 5.12c. We find that the results presented in figure 5.11 (dot B3) are well reproducible within the error margins.

For comparison, we also perform Hahn echo measurements on the ^{75}As CT of quantum dots in the gate-free sample A. This sample originates from the same wafer as the sample from which the results reported in [41] were obtained. Figure 5.12b shows the nuclear echo decay curves for five dots A1-A5, with fitted phase memory times $T_{\mathrm{M,n}}^{\mathrm{HE}}$ displayed in the right half of figure 5.12c. We note that thanks to the larger amplitude $\Delta E_{\mathrm{hf}}(0)$ in sample A, we can obtain more accurate fits for the decay times. The phase memory times in sample A are in very good agreement with the reported values from [41] and only marginally longer than those in the p-i-n diode sample. The small difference between the two samples can be attributed to different indium to gallium ratios, which will affect the dynamics of the system-environment coupling between the probed ^{75}As ensemble and the other isotopes in the dot as the relative sizes of the ^{115}In, ^{69}Ga and ^{71}Ga ensembles are different.

To summarise, Hahn echo experiments on ^{75}As and ^{71}Ga in empty quantum dots on sample B reveal nuclear phase memory times $T_{\mathrm{M,n}}^{\mathrm{HE}}$ which are in very good agreement with the values presented in [41] for a gate-free sample. We can therefore confirm the previous assumption that the quantum dots in these experiments were indeed free of charge carriers and the observed millisecond $T_{\mathrm{M,n}}^{\mathrm{HE}}$ timescales were not limited by charge-mediated nuclear spin interactions.

For both isotopes, $T_{\mathrm{M,n}}^{\mathrm{HE}}$ is noticeably longer than in similar strain-free structures such as GaAs/AlGaAs interface quantum dots, where CT Hahn echo experiments on ^{71}Ga gave decay times of $T_{\mathrm{M,n}}^{\mathrm{HE}}(^{71}\mathrm{Ga}) = 360 \pm 40$ μs at $B_{0,\mathrm{z}} = 3.55$ T[184], or GaAs/AlGaAs quantum wells, where ^{75}As CT phase memory times of $T_{\mathrm{M,n}}^{\mathrm{HE}}(^{75}\mathrm{As}) \lesssim 800$ μs were found at $B_{0,\mathrm{z}} \leq 2$ T[183]. As discussed in section 5.2.3, this is due

to the presence of strong inhomogeneous quadrupolar shifts which suppress the homonuclear dipolar flip-flop mechanism[41, 169, 200].

5.6 Conclusions

Self-assembled InGaAs quantum dots are strongly strained systems and are therefore subject to significant electric field gradients. As all isotopes in the dot have magnetic moments $I > \frac{1}{2}$, their cw NMR spectra are strongly inhomogeneously broadened by quadrupolar interactions. For the CTs of ^{75}As and ^{71}Ga we measured $\Delta\nu_{\mathrm{inh}}(^{75}\mathrm{As}) \approx 24$ kHz and $\Delta\nu_{\mathrm{inh}}(^{71}\mathrm{Ga}) \approx 8$ kHz in charge-free quantum dots at $B_{0,\mathrm{z}} = 8$ T. Using pulsed NMR and applying Hahn echo sequences we were able to refocus the inhomogeneous quadrupolar broadening and measure nuclear spin phase memory times $T^{\mathrm{HE}}_{\mathrm{M,n}}(^{75}\mathrm{As}) = 3.97 \pm 0.23$ ms and $T^{\mathrm{HE}}_{\mathrm{M,n}}(^{71}\mathrm{Ga}) = 1.37 \pm 0.25$ ms.

These results are in very good agreement with the previous findings reported in [41] for measurements in a gate-free sample. We can therefore conclude that the latter results were also obtained under charge-free conditions and not affected by charge-mediated nuclear spin interactions. The measured decay times are ~ 5 times longer than comparable $T^{\mathrm{HE}}_{\mathrm{M,n}}$ obtained in strain-free structures, which can be explained by a partial suppression of the dominant nuclear decoherence mechanism of spectral diffusion. This process is governed by homonuclear spin flip-flops within the spin environment, which in an unstrained structure occur between neighbouring spins with identical Zeeman splitting. In an InGaAs quantum dot, the process is quenched as the different quadrupolar shifts of neighbouring spins make spin flip-flops energetically forbidden. The measured phase memory times are therefore limited by a combination of instantaneous diffusion and possibly spectral diffusion due to residual direct nuclear spin flip-flops.

6 Suppression of Spin Bath Decoherence under Multiple Pulse NMR

6.1 Introduction

We saw in the previous chapter that the nuclear spin phase memory times $T_{\mathrm{M,n}}^{\mathrm{HE}} \gtrsim 1$ ms in self-assembled InGaAs quantum dots under Hahn echo pulse sequences are ~ 5 times longer than in comparable lattice-matched nanostructures[183, 184]. This is due to strongly inhomogeneous strain-induced quadrupolar interactions which quench the homonuclear dipolar flip-flop term[41, 200]. Consequently, spectral diffusion as a source of electron spin decoherence is suppressed[171] - a notable potential advantage over strain-free systems. However, the remaining interactions with the nuclear spin bath are still expected to limit the central spin coherence on much shorter timescales than those observed for qubit systems in a nuclear-spin-free environment, such as defect centres in isotopically pure diamond[13] or donors in ^{28}Si[11, 224].

Our approach towards increasing the $T_{2,\mathrm{e}}$ in InGaAs quantum dots directly targets the nuclear spin bath as a source of decoherence. In this chapter, we are exploring multiple pulse NMR techniques which allow us to control and suppress the nuclear spin bath decoherence and thus to create a predictably evolving environment for a confined electron spin. We consider the spin bath as consisting of two "sub-baths".

The spin ensemble of the probed isotope is denoted as $\boldsymbol{I}_n$ whereas the remaining nuclear spins of the other isotopes in the dot are considered as $\boldsymbol{J}_m$. The Hahn echo decay of $\boldsymbol{I}_n$ is limited by a combination of several contributions including the nuclear spin relaxation time $T_{1,\mathrm{n}}$, dipolar coupling to the $\boldsymbol{J}_m$ sub-bath and nearby charge spins, instantaneous diffusion introduced by the rf pulses $\mathcal{H}_{\mathrm{rf}}(t)$ and arising from the diagonal homonuclear interaction term, and the remaining homonuclear dipolar flip-flops. In a strong external magnetic field $B_{0,\mathrm{z}}$ we can summarise the dynamics of a nuclear spin sub-ensemble $\boldsymbol{I}_n$ in the rotating frame with a Hamiltonian

$$\mathcal{H}_{\mathrm{total}} = \mathcal{H}_{\mathrm{Q}} + \mathcal{H}_{\mathrm{dd}}^{\mathrm{hom}} + \mathcal{H}_{IJ}(t) + \mathcal{H}_{I-\mathrm{env}}(t) + \mathcal{H}_{\mathrm{rf}}(t) \ , \tag{6.1}$$

where $\mathcal{H}_{\mathrm{Q}}$ denotes the Larmor resonance offsets due to the inhomogeneous quadrupolar interaction, $\mathcal{H}_{\mathrm{dd}}^{\mathrm{hom}}$ is the homonuclear dipolar coupling Hamiltonian, $\mathcal{H}_{IJ}(t)$ describes the time-dependent heteronuclear dipolar interaction and $\mathcal{H}_{I-\mathrm{env}}(t)$ contains additional terms including $T_{1,\mathrm{n}}$ processes and coupling to charge spins.

Different experimental techniques exist to selectively remove each of the contributions to the spin bath decoherence of $\boldsymbol{I}_n$. Because of the strong suppression of the nuclear spin diffusion in a strained quantum dot, the nuclear spin relaxation time $T_{1,\mathrm{n}} \gtrsim 1$ h is much slower than the pure dephasing processes[85, 115]. Its contribution on the few-millisecond timescales of the Hahn echo decay is therefore negligible (see chapter 5.3.1). Similarly, we saw in the previous chapter that we have a stable, charge-free environment in both of the samples studied in this work. While the dephasing due to the static resonance offset of the quadrupolar Hamiltonian $\mathcal{H}_{\mathrm{Q}}$ is eliminated by a Hahn echo, the presence of the second nuclear spin sub-bath $\boldsymbol{J}_m$ gives rise to an additional, fluctuating resonance offset. We note that the time-dependence of $\mathcal{H}_{IJ}(t)$ can be removed if we describe the evolution of the sub-bath $\boldsymbol{J}_m$ in equation (6.1) explicitly by a Hamiltonian $\mathcal{H}_J$[225].

The problem of refocusing spin dephasing arising from interaction of a central spin with its "noisy" environment has attracted a lot of attention in recent years and has been addressed successfully with the design of robust *dynamical decoupling* (DD) sequences[203, 204]. DD is based on the principle that a π pulse can refocus any dephasing due to interactions which couple linearly to the spin operator $\boldsymbol{I}$ as long as the dephasing is slow compared to time intervals τ before and after the pulse. Purely static resonance offsets are refocused fully by a Hahn echo. By contrast, the suppression of decay due to coupling to the slowly evolving environment can be improved by applying a series of π pulses with shorter pulse spacings 2τ. Here, we are adopting this approach using *Carr-Purcell (-Meiboom-Gill)* sequences[226, 227] with constant pulse separation to eliminate the decoherence of nuclear spins due to $\mathcal{H}_{IJ}(t)$ in equation (6.1) and to "decouple" the nuclear spin sub-ensemble $\boldsymbol{I}_n$ from the remaining nuclear spins $\boldsymbol{J}_m$ in the dot.

Nuclear spin dephasing due to instantaneous diffusion is an artefact of the pulsed NMR measurement technique used to obtain $T_{\mathrm{M,n}}$: the static term $\propto I_{n,\mathrm{z}} I_{m,\mathrm{z}}$ of the homonuclear dipolar interaction $\mathcal{H}_{\mathrm{dd}}^{\mathrm{hom}}$ contributes to $T_{\mathrm{M,n}}$ as the magnitude of the local field of each spin $\boldsymbol{I}_n$ in the rotating frame is altered when the ensemble is resonantly driven (described by the rf Hamiltonian $\mathcal{H}_{\mathrm{rf}}(t)$ in equation (6.1)). Together with the direct (homonuclear) dipolar flip-flop term, this contribution can be suppressed by reducing the pulse rotation angles, which unfortunately comes at the cost of a reduced echo amplitude[209, 228].

A different class of so-called *solid echo* sequences consisting of a series of $\frac{\pi}{2}$ pulses with phase shifted carriers is very effective at refocusing dephasing due to the homonuclear dipolar Hamiltonian $\mathcal{H}_{\mathrm{dd}}^{\mathrm{hom}}$[210, 229]. Generally, these sequences suppress the homonuclear dipolar broadening selectively and only rescale the coupling strength of terms that are linear in $\boldsymbol{I}$, such as $\mathcal{H}_{\mathrm{Q}}$ and $\mathcal{H}_{IJ}(t)$. This is a desirable property for NMR spectroscopy in systems where dominant dipolar broadening masks a weak inhomogeneous contribution (e.g. chemical shifts)[230, 231].

In this chapter, we aim to bring together the respective advantages of dynamical decoupling sequences and solid echoes in a new class of NMR pulse sequences under which the nuclear spin bath evolves in a predictable way. Although addition of π pulses to solid echo sequences has been used before to refocus both dipolar and inhomogeneous dephasing in Si:P[232] and NV centres[13], no systematic analysis of such combined sequences has been reported to date. Based on established solid echo sequences such as WAHUHA[210], MREV8[211, 212] and BR24[233], we use *average Hamiltonian theory* (AHT)[210, 230] calculations to design a set of combined echo sequences incorporating π pulses. Under these new sequences we observe an increase of the measured nuclear spin coherence time by a factor of $\gtrsim 2.5 - 3$ compared to the Hahn echo decay for ^{75}As and ^{71}Ga nuclear spins.

After an introduction to the concepts of dynamical decoupling and average Hamiltonian theory in sections 6.2.1 and 6.2.2, we develop several new combined echo sequences in section 6.2.3. Although the measurements in this chapter are conceptually similar to the previous Hahn echo experiments, the multiple pulse sequences require a far more accurate calibration of pulse durations and carrier phases. This is discussed in section 6.3. The results of our decoupling experiments and a theoretical interpretation of the observed significantly extended phase memory times are presented in section 6.4. Finally, we demonstrate the capability of combined echo sequences to increase the nuclear spin bath coherence experimentally and discuss possible origins of performance limitations for these sequences in section 6.5.

6.2 Theory of Multiple Pulse NMR

In this section we first briefly review the principle of dynamical decoupling (DD) and illustrate how multiple pulse sequences can decouple a spin or spin ensemble from its environment by refocusing the dephasing introduced by the system-environment interaction. We then review average Hamiltonian theory (AHT), a powerful analysis

tool which allows the expected system evolution under an rf pulse cycle to be examined. In the last part, we use AHT to design and characterise a novel set of multiple pulse NMR sequences which eliminate both dipolar and inhomogeneous dephasing in the nuclear spin bath.

6.2.1 Dynamical Decoupling

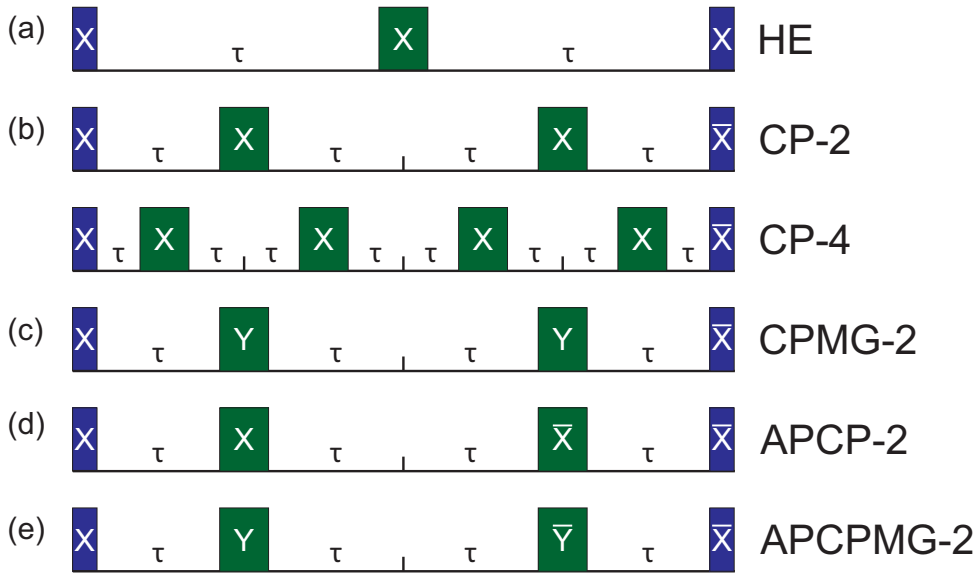

Figure 6.1: Illustration of the Hahn echo (HE) sequence (a) and the multiple pulse Carr-Purcell(-Meiboom-Gill) CP(MG) decoupling sequences (b) and (c). In the experiments presented in section 6.4, we use sequences with alternating π pulse carrier phases. Two-pulse versions of these alternating-phase sequences APCP(MG) are shown in (d) and (e), respectively. Initial and final $\frac{\pi}{2}$ pulses are marked in blue and π pulses are shown in green. X, Y, $\bar{\text{X}}$ and $\bar{\text{Y}}$ indicate the in-plane rotation axes corresponding to a carrier phase $\varphi(\text{X}) = 0°$, $\varphi(\text{Y}) = 90°$, $\varphi(\bar{\text{X}}) = 180°$ or $\varphi(\bar{\text{Y}}) = 270.0°$ of the respective pulse.

In chapter 5, we demonstrated how the dephasing of a nuclear spin ensemble $\boldsymbol{I}_n$ due to a *static* inhomogeneous strain field can be refocused by a Hahn echo sequence (figure 6.1a). Interactions such as the heteronuclear coupling with different spin species $\boldsymbol{J}_m$ or coupling to charge spins in the dot environment can give rise to additional time-dependent local fields $B_{\text{loc}}(t)$ acting on the spins $\boldsymbol{I}_n$. In such cases, the efficiency of a Hahn echo in recovering the phase memory depends on

the correlation time τ_c associated with the dephasing process. If τ_c exceeds the free evolution time during the sequence $\tau_{evol} = 2\tau$, the local field appears quasistatic and its effect on the spin bath dephasing is refocused. For shorter $\tau_c < \tau_{evol}$, the local field is dynamic and the refocusing becomes incomplete[203, 204].

Consequently, the timescale on which we can eliminate the effects of $B_{loc}(t)$ with a Hahn echo sequence is limited by the time intervals τ before and after the π pulse. However, it is possible to increase the refocusing efficiency by adding more control pulse cycles $\tau - \pi - \tau$ to the sequence. Even with just two pulses, the *control period* 2τ is already halved compared to a Hahn echo sequence and we can eliminate dephasing over timescales $\tau_c > \tau_{evol}/2$. With increasing control pulse number n_π, the sequence is capable of decoupling noise with shorter correlation time $\tau_c \gtrsim \tau_{evol}/n_\pi$. This approach towards increasing the phase memory time is referred to as *dynamical decoupling* (DD). Its efficiency depends strongly on the spectral profiles of the time-dependent sources of dephasing.

The oldest and best-known DD sequence was originally developed to reduce the acquisition time of Hahn echo experiments and is formed by a series of equally spaced π pulses. Rotations of the nuclear magnetisation about the in-plane axes $\hat{e}_x$ and $\hat{e}_y$ in the rotating frame are implemented experimentally by relative phase shifts of the rf pulse carriers. If the carriers of the initial and final $\frac{\pi}{2}$ pulses are in phase with those of the π pulses, we refer to the pulse series as a *Carr-Purcell* (CP) sequence (figure 6.1b)[226]. By contrast, if the π pulse carrier phases are orthogonal to those of the $\frac{\pi}{2}$ pulses, it is labelled as a *Carr-Purcell-Meiboom-Gill* (CPMG) sequence (figure 6.1c)[227].

In recent years, several tailored DD sequences with varied pulse separations have been developed to increase the decoupling efficiency for specific noise spectra[204, 234]. Seminal contributions were made by Khodjasteh and Lidar, who described the recursively defined *concatenated dynamical decoupling* sequence (CDD)[235] and by Uhrig, whose optimised dynamical decoupling (UDD) sequence modulates the

pulse separation sinusoidally[236, 237]. The latter in particular has been shown to be optimal for suppressing low-frequency noise and is highly robust against pulse errors[238, 239].

While other DD sequences are more effective if the initial spin state is not known and more suitable for noise spectroscopy purposes, theoretical and experimental work has shown that CP-type sequences are best-suited for increasing the phase memory time T_{M}[204, 225]. CPMG in particular has been applied in various systems including diamond NV centres and Si:P donors with great success[224, 240]. In electrostatically defined GaAs/AlGaAs quantum dots, Malinowski et al.[174] recently demonstrated electron spin coherence times of $T_{2,\mathrm{e}}^{\mathrm{CPMG}} \sim 0.87$ ms compared to Hahn echo results of $T_{2,\mathrm{e}}^{\mathrm{HE}} \gtrsim 1\ \mu$s[164, 167] by using a CPMG sequence with optimal pulse spacing 2τ.

In the decoupling experiments of this chapter we will use CP(MG) sequences with alternating phase (AP), i.e. the carrier phases of consecutive π pulses are shifted by 180°, corresponding to rotations about anti-parallel axes. We denote the phase φ as a capital letter subscript where $\varphi(\mathrm{X}) = 0°$, $\varphi(\mathrm{Y}) = 90°$, $\varphi(\bar{\mathrm{X}}) = 180°$ and $\varphi(\bar{\mathrm{Y}}) = 270°$. Using this notation, the APCP-2 and APCPMG-2 sequences of figures 6.1d and 6.1e are described as

$$\left(\tfrac{\pi}{2}\right)_{\mathrm{X}} - \tau - \pi_{\mathrm{X}} - 2\tau - \pi_{\bar{\mathrm{X}}} - \tau - \left(\tfrac{\pi}{2}\right)_{\bar{\mathrm{X}}} \qquad \text{(APCP-2)}$$

$$\left(\tfrac{\pi}{2}\right)_{\mathrm{X}} - \tau - \pi_{\mathrm{Y}} - 2\tau - \pi_{\bar{\mathrm{Y}}} - \tau - \left(\tfrac{\pi}{2}\right)_{\bar{\mathrm{X}}} \qquad \text{(APCPMG-2).}$$

6.2.2 Review of Average Hamiltonian Theory

Average Hamiltonian theory (AHT) is a powerful theoretical tool used in the design and analysis of multiple pulse sequences and was first introduced by Haeberlen and Waugh[230], extending a similar method proposed earlier by Evans[241]. The AHT approach is based on a transformation of the spin system Hamiltonian into an interaction representation in which the time-dependent rf excitation $\mathcal{H}_{\mathrm{rf}}(t)$ no

longer appears explicitly.

We begin by considering a spin Hamiltonian

$$\mathcal{H}_{\text{total}}(t) = \mathcal{H}_0 + \mathcal{H}_{\text{D}}^{\text{zz}} + \mathcal{H}_{\text{rf}}(t) \,, \tag{6.2}$$

describing a nuclear sub-bath of N spins $\boldsymbol{I}_n$ interacting with a time-dependent rf field in the rotating frame of an external magnetic field $B_{0,\text{z}}$. Here, the resonance offset Hamiltonian is denoted by $\mathcal{H}_0 = \mathcal{H}_{\text{Q}} + \mathcal{H}_{IJ} = \sum_{n=1}^{N} \Omega_{\text{z},n} I_{n,\text{z}}$. The frequency shift $\Omega_{\text{z},n} = \omega_{\text{Q},n} + \sum_m \omega_{mn} J_{m,\text{z}}$ of the n-th nucleus is dominated by the quadrupolar shift. For the purpose of this discussion, we assume that the heteronuclear coupling $\mathcal{H}_{IJ}$ is static, i.e. that the $\boldsymbol{J}_m$ sub-bath does not evolve over time. The homonuclear dipolar interactions between the n-th and m-th spin are described by the secular term $\mathcal{H}_{\text{D}}^{\text{zz}} = \sum_{m=1}^{N} \sum_{n>m}^{N} \omega_{mn} \left(3 I_{\text{z},n} I_{\text{z},m} - \boldsymbol{I}_n \cdot \boldsymbol{I}_m\right)$ with dipolar coupling ω_{mn}. We can drop all other dipolar interaction terms since we are working at large magnetic fields where these terms average to zero[116, 242]. The rf field is described by a time-dependent step function Hamiltonian with $\mathcal{H}_{\text{rf}}(t) = -\hbar\omega_1 I_\phi$ during each pulse and $\mathcal{H}_{\text{rf}}(t) = 0$ otherwise. I_ϕ denotes the rotation axis of the pulse in the rotating frame.

Three conditions (i)-(iii) must be fulfilled for AHT to be applicable[230, 242]:

(i) All individual Hamiltonians must be periodic over a cycle time t_{c}. This is primarily a constraint on the pulse sequence $\mathcal{H}_{\text{rf}}(t)$. In principle, this condition also applies to $\mathcal{H}_0$ and $\mathcal{H}_{\text{D}}^{\text{zz}}$, e.g. in magic angle spinning (MAS) experiments where explicit time dependences are introduced by sample rotation[230, 243]. However, in the context of this work, the resonance offset and truncated heteronuclear dipolar terms have been assumed static. For the analysis of DD sequences decoupling a noisy environment $\mathcal{H}_{I-\text{env}}(t)$, this condition is also fulfilled as the time dependence of $\mathcal{H}_{I-\text{env}}$ only arises in the interaction representation of the environment Hamiltonian $\mathcal{H}_{\text{env}}$ and can be removed by including $\mathcal{H}_{\text{env}}$ explicitly in $\mathcal{H}_{\text{total}}$[225].

(ii) The net rotation after a full rf cycle is zero or a multiple of 2π. Again, this is a condition on the pulse cycle design. It implies that the spin states at the start and end of a cycle are identical. However, we note that the latter is not equivalent to the initial statement as there are infinitely many paths over the Bloch sphere that start and end in the same point with a finite net rotation.

(iii) The cycle time t_c is short enough that the spin state is not strongly altered under free evolution within each cycle. This is the case if $|\mathcal{H}_0|t_c \ll 1$ and $|\mathcal{H}_D^{zz}|t_c \ll 1$. As AHT is a perturbation method in terms of t_c/T_2, this condition must be fulfilled for the average Hamiltonian to converge quickly.

In order to use AHT, we first have to switch to the interaction picture with respect to the rf Hamiltonian, the so-called *toggling frame*. For this, we split $\mathcal{H}_{\text{total}}(t)$ into a static (or t_c-periodic) internal Hamiltonian $\mathcal{H}_{\text{int}} = \mathcal{H}_0 + \mathcal{H}_D^{zz}$ and a time-dependent external term $\mathcal{H}_{\text{ext}}(t) = \mathcal{H}_{\text{rf}}(t)$. In this case, the propagator (time evolution operator) for the total Hamiltonian is given by

$$\mathcal{U}(t) = \mathcal{T}\exp\left[-\frac{\mathrm{i}}{\hbar}\int_0^t dt'\mathcal{H}_{\text{total}}(t')\right] = \mathcal{U}_{\text{rf}}(t)\mathcal{U}_{\text{int}}(t)\ , \tag{6.3}$$

with the Dyson time-ordering operator $\mathcal{T}$ and

$$\mathcal{U}_{\text{rf}}(t) = \mathcal{T}\exp\left[-\frac{\mathrm{i}}{\hbar}\int_0^t dt'\mathcal{H}_{\text{rf}}(t')\right]\ , \tag{6.4}$$

$$\mathcal{U}_{\text{int}}(t) = \mathcal{T}\exp\left[-\frac{\mathrm{i}}{\hbar}\int_0^t dt'\tilde{\mathcal{H}}_{\text{int}}(t')\right]\ , \tag{6.5}$$

where the toggling frame Hamiltonian $\tilde{\mathcal{H}}_{\text{int}}(t)$ is given by[230, 244]

$$\tilde{\mathcal{H}}_{\text{int}}(t) = \mathcal{U}_{\text{rf}}^{-1}(t)\mathcal{H}_{\text{int}}\mathcal{U}_{\text{rf}}(t)\ . \tag{6.6}$$

While equation (6.5) formally describes the time evolution in the toggling frame, the problem of calculating the propagator remains a challenging task. However, under the three conditions mentioned above, we can find an approximate description of

the spin bath system at times $t = n_c \cdot t_c$ (with cycle number $n_c \in \mathbb{N}$).

The cycle condition (ii) corresponds to $\mathcal{U}_{rf}(n_c t_c) = 1$ and together with the periodicity condition (i) ensures that the toggling frame Hamiltonian is also periodic over t_c, i.e. $\tilde{\mathcal{H}}_{int}(t + n_c t_c) = \tilde{\mathcal{H}}_{int}(t)$. As a consequence, it is sufficient to determine the propagator of the system over a single cycle. The time evolution after n_c cycles is then given by $\mathcal{U}_{int}(n_c t_c) = (\mathcal{U}_{int}(t_c))^{n_c}$[242]. Next, we apply a *Magnus expansion*[245] to the toggling frame propagator: instead of trying to solve equation (6.5) for the time-dependent Hamiltonian $\tilde{\mathcal{H}}_{int}(t)$, we introduce an effective *average Hamiltonian* such that

$$\mathcal{U}_{int}(t_c) = \exp\left[-\frac{i}{\hbar} t_c \bar{\mathcal{H}}\right] = \exp\left[-\frac{i}{\hbar} t_c \left(\bar{\mathcal{H}}^{(0)} + \bar{\mathcal{H}}^{(1)} + \dots\right)\right] , \tag{6.7}$$

where the leading terms $\bar{\mathcal{H}}^{(i)}$ are given by

$$\bar{\mathcal{H}}^{(0)} = \frac{1}{t_c} \int_0^{t_c} \tilde{\mathcal{H}}(t) \mathrm{d}t , \tag{6.8}$$

$$\bar{\mathcal{H}}^{(1)} = \frac{-i}{2t_c} \int_0^{t_c} \mathrm{d}t_2 \int_0^{t_2} \mathrm{d}t_1 \left[\tilde{\mathcal{H}}(t_2), \tilde{\mathcal{H}}(t_1)\right] , \tag{6.9}$$

$$\begin{aligned} \bar{\mathcal{H}}^{(2)} = \frac{1}{6t_c} \int_0^{t_c} \mathrm{d}t_3 \int_0^{t_3} \mathrm{d}t_2 \int_0^{t_2} \mathrm{d}t_1 \Big(&\left[\tilde{\mathcal{H}}(t_1), \left[\tilde{\mathcal{H}}(t_2), \tilde{\mathcal{H}}(t_3)\right]\right] + \\ &+ \left[\tilde{\mathcal{H}}(t_3), \left[\tilde{\mathcal{H}}(t_2), \tilde{\mathcal{H}}(t_1)\right]\right] \Big) . \end{aligned} \tag{6.10}$$

The expansion converges quickly only if condition (iii) is satisfied and $\tilde{\mathcal{H}}_{int} t_c \ll 1$. For any t_c, the decay of the nuclear magnetisation due to the m-th order average Hamiltonian is expected to be of the order of $T_2(T_2/t_c)^m$, where $T_2^{-1} \sim |\mathcal{H}_{int}|$. Hence higher order terms become negligible for small ratios t_c/T_2[230].

We can use this technique to predict the evolution of the nuclear spin bath $\mathcal{H}_{int}$ under any given cyclic pulse series. As an example, AHT correctly describes the refocusing of the static inhomogeneous broadening term $\mathcal{H}_0$ under a Carr-Purcell sequence and gives $\bar{\mathcal{H}}_{CP} = \mathcal{H}_D^{zz}$, i.e. the decay is governed by homonuclear dipolar interaction. For DD experiments where a dynamic environment $\mathcal{H}_{env}$ is taken into

account, only the zeroth order offset term $\bar{\mathcal{H}}_0^{(0)}$ vanishes and the refocusing of higher order terms depends on the structure of the DD sequence[204, 239, 246]. In the context of this work, we aim towards full suppression of the spin bath decoherence. To this end, we will have to design a multiple pulse sequence under which $\bar{\mathcal{H}} = 0$ and $\mathcal{U}_{\text{int}}(t_c) = 1$. In this case the nuclear spin bath evolution would be fully coherent and predictable, making longer electron spin qubit coherence times feasible using electron spin manipulation schemes.

6.2.3 Design of NMR Sequences for Increased Spin Bath Coherence

In the NMR experiments of this project, we are studying the coherence properties of a sub-ensemble $\boldsymbol{I}_n$ of the nuclear spin bath in an InGaAs quantum dot. DD sequences such as CP(MG) are well-suited for decoupling this sub-ensemble from the remaining nuclear spins $\boldsymbol{J}_m$. However, a sequence consisting only of π pulses does not affect the intrinsic evolution of the sub-bath under homonuclear dipolar coupling.

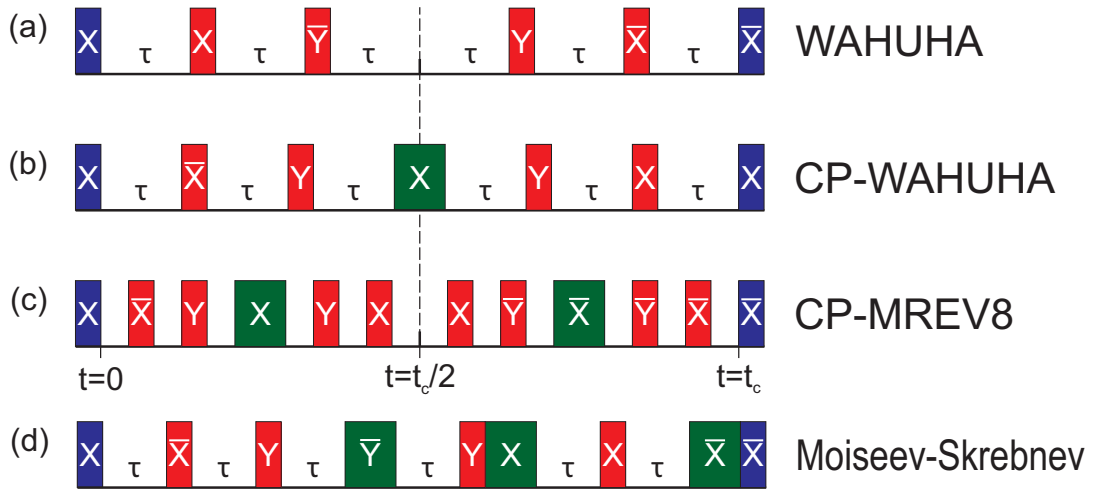

Figure 6.2: Illustration of the WAHUHA sequence (a) and the two modified combined multiple pulse sequences CP-WAHUHA (b) and CP-MREV8 (c). The Moiseev-Skrebnev sequence[247] (d) is shown for comparison. Initial and final $\frac{\pi}{2}$ pulses are marked in blue, refocusing $\frac{\pi}{2}$ pulses in red and π pulses in green. The dashed line marks the half-cycle $t = t_c/2$.

NMR pulse sequences for the selective suppression of homonuclear dipolar interactions, so-called *solid echo* sequences, have been known for a long time. Based on the four pulse WAHUHA sequence[210] (see figure 6.2a), longer sequences such as MREV8 and BR24 were designed using AHT to eliminate higher order terms of the average dipolar Hamiltonian $\bar{\mathcal{H}}_{\mathrm{D}}$ and to increase robustness against finite pulse durations t_{p}[233, 248]. However, just as DD sequences are designed specifically to decouple the spin (bath) from its environment, solid echo sequences aim to preserve these couplings selectively. In many systems probed by solid echo NMR, dominant dipolar interactions mask small resonance offsets arising from e.g. chemical shifts which are of interest in the analysis of molecular structures and which can only be detected if the dipolar coupling term is suppressed[230, 231].

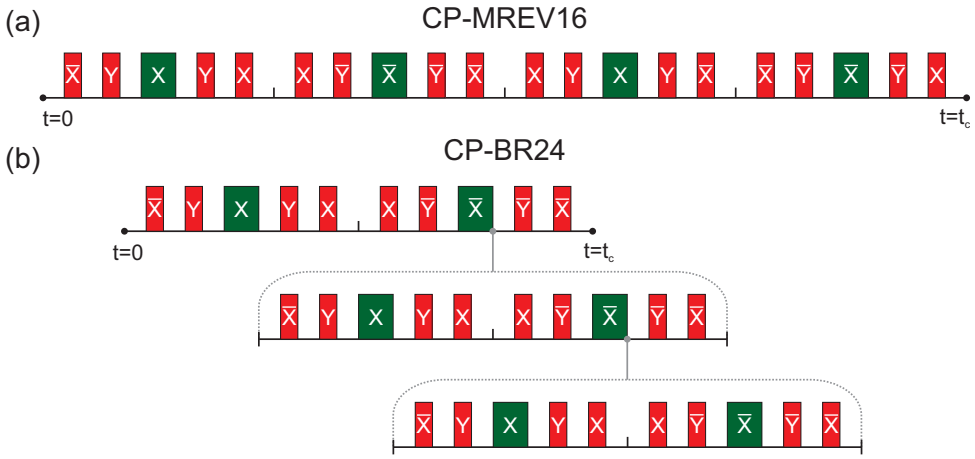

Figure 6.3: Schematic of the robust CP-MREV16 sequence (a) and the CP-BR24 sequence (b) which is formed by repeated nesting of CP-MREV8 as illustrated. $\frac{\pi}{2}$ pulses are marked in red and π pulses in green.

Here, we will combine the features of both types of NMR sequences and design a set of new multiple pulse sequences (figures 6.2b and c as well as 6.3a and b) which are capable of suppressing the full spin bath Hamiltonian $\mathcal{H}_{\mathrm{int}} = \mathcal{H}_0 + \mathcal{H}_{\mathrm{D}}^{\mathrm{zz}}$ in leading orders of AHT. Similar sequences have been used in spin resonance experiments on Si:P[232] and NV centres[13] where MREV8 cycles were interspersed with π pulses. However, neither paper offers a theoretical analysis of the combined sequences. An alternative 7-pulse sequence has recently been proposed by Moiseev and

Skrebnev[247] (figure 6.2d). However, it requires composite pulses (two contiguous pulses with different phases) which are difficult to implement experimentally (see discussion in section 6.3.2). Furthermore, AHT shows its performance to be identical with that of the 5-pulse sequence of equal cycle time t_c proposed by us which is shown in figure 6.2b and discussed below.

Starting from the WAHUHA sequence shown in figure 6.2a it is an intuitive approach to add a π pulse after 3τ to the cycle as illustrated in figure 6.2b. If the pulse carrier phases are adjusted correctly, this does indeed fully remove the zeroth order AHT term $\bar{\mathcal{H}}_{\text{int}}^{(0)} = 0$ under the assumption of infinitely strong pulses (pulse duration $t_p \to 0$). However, the dipolar refocusing efficiency in higher order AHT terms is reduced compared to the original WAHUHA sequence. A fundamental property of AHT is the symmetry criterion: if the toggling frame Hamiltonian is symmetric under time reversal ($\tilde{\mathcal{H}}_{\text{int}}(t) = \tilde{\mathcal{H}}_{\text{int}}(t_c - t)$), all odd-order terms of the average Hamiltonian vanish[242]: $\bar{\mathcal{H}}^{(1)} = \bar{\mathcal{H}}^{(3)} = \ldots = 0$. For the pulse sequences illustrated in figure 6.2, this corresponds to antisymmetry with respect to $t_c/2$ (dashed line).

Clearly, this is the case for WAHUHA (figure 6.2a), where for example the $(\frac{\pi}{2})_{\bar{Y}}$ pulse at $t_c/2 - \tau$ is "reversed" by a $(\frac{\pi}{2})_{Y}$ pulse at $t_c/2 + \tau$. The addition of the π_X pulse after 3τ makes it impossible to preserve this symmetry for a CP-WAHUHA sequence (figure 6.2b). Consequently, the first non-vanishing average Hamiltonian term is a first-order cross term $\bar{\mathcal{H}}_{D0}^{(1)}$ between $\mathcal{H}_0$ and $\mathcal{H}_D$:

$$\bar{\mathcal{H}}_{\text{CP-WAHUHA}} = \frac{i\tau}{3}[\mathcal{H}_D^{zz} - \mathcal{H}_D^{xx}, \mathcal{H}_0^{y}] + \mathcal{O}(t_c^{-2}) \,, \tag{6.11}$$

where $\mathcal{H}_D^{xx}$, $\mathcal{H}_D^{yy}$ and $\mathcal{H}_D^{zz}$ are the transformed secular dipolar Hamiltonians along $\hat{e}_x$, $\hat{e}_y$ and $\hat{e}_z$, respectively, and $\mathcal{H}_0^{x}$, $\mathcal{H}_0^{y}$, $\mathcal{H}_0^{z}$ are the corresponding frequency offset Hamiltonians. A full list of the non-vanishing terms of $\bar{\mathcal{H}}_{\text{CP-WAHUHA}}$ up to second order AHT including zeroth order contributions for finite pulse duration t_p is given in table 6.1. We note that an AHT analysis of the Moiseev-Skrebnev sequence[247]

AHT term	CP-WAHUHA	CP-MREV8
$\bar{\mathcal{H}}_0^{(0)\dagger}$	$\frac{4t_\mathrm{p}}{\pi t_c}\mathcal{H}_0^\mathrm{z}$	0
$\bar{\mathcal{H}}_\mathrm{D}^{(0)\dagger}$	$-\frac{\mathrm{i}2t_\mathrm{p}}{\pi t_c}\{[\mathcal{H}_\mathrm{D}^{\mathrm{xx}}-\mathcal{H}_\mathrm{D}^{\mathrm{yy}},\mathcal{H}_0^\mathrm{z}]+[\mathcal{H}_\mathrm{D}^{\mathrm{yy}}-\mathcal{H}_\mathrm{D}^{\mathrm{zz}},\mathcal{H}_0^\mathrm{x}]\}$	0
$\bar{\mathcal{H}}_0^{(1)}$	0	0
$\bar{\mathcal{H}}_\mathrm{D}^{(1)}$	0	0
$\bar{\mathcal{H}}_\mathrm{D0}^{(1)}$	$\frac{\mathrm{i}\tau}{3}[\mathcal{H}_\mathrm{D}^{\mathrm{zz}}-\mathcal{H}_\mathrm{D}^{\mathrm{xx}},\mathcal{H}_0^\mathrm{y}]$	$\frac{\mathrm{i}\tau}{3}[\mathcal{H}_\mathrm{D}^{\mathrm{zz}}-\mathcal{H}_\mathrm{D}^{\mathrm{xx}},\mathcal{H}_0^\mathrm{y}]$
$\bar{\mathcal{H}}_0^{(2)}$	0	0
$\bar{\mathcal{H}}_\mathrm{D}^{(2)}$	$\frac{\tau^2}{18}[\mathcal{H}_\mathrm{D}^{\mathrm{zz}}-\mathcal{H}_\mathrm{D}^{\mathrm{xx}},[\mathcal{H}_\mathrm{D}^{\mathrm{zz}},\mathcal{H}_\mathrm{D}^{\mathrm{yy}}]]$	$\frac{\tau^2}{18}[\mathcal{H}_\mathrm{D}^{\mathrm{zz}}-\mathcal{H}_\mathrm{D}^{\mathrm{xx}},[\mathcal{H}_\mathrm{D}^{\mathrm{zz}},\mathcal{H}_\mathrm{D}^{\mathrm{yy}}]]$
$\bar{\mathcal{H}}_\mathrm{D0}^{(2)}$	$\frac{\tau^2}{3}\{[\mathcal{H}_0^\mathrm{y},[\mathcal{H}_0^\mathrm{y},\mathcal{H}_\mathrm{D}^{\mathrm{xx}}-\mathcal{H}_\mathrm{D}^{\mathrm{zz}}]]+[\mathcal{H}_\mathrm{D}^{\mathrm{zz}}-\mathcal{H}_\mathrm{D}^{\mathrm{yy}},[\mathcal{H}_0^\mathrm{z},\mathcal{H}_0^\mathrm{y}]]\}$	$\frac{\tau^2}{3}[\mathcal{H}_0^\mathrm{y},[\mathcal{H}_0^\mathrm{y},\mathcal{H}_\mathrm{D}^{\mathrm{xx}}-\mathcal{H}_\mathrm{D}^{\mathrm{zz}}]]$

AHT term	CP-MREV16	CP-BR24
$\bar{\mathcal{H}}_0^{(0)\dagger}$	0	0
$\bar{\mathcal{H}}_\mathrm{D}^{(0)\dagger}$	0	0
$\bar{\mathcal{H}}_0^{(1)}$	0	0
$\bar{\mathcal{H}}_\mathrm{D}^{(1)}$	0	0
$\bar{\mathcal{H}}_\mathrm{D0}^{(1)}$	0	$\frac{\mathrm{i}\tau}{9}\{[\mathcal{H}_\mathrm{D}^{\mathrm{zz}}-\mathcal{H}_\mathrm{D}^{\mathrm{xx}},\mathcal{H}_0^\mathrm{y}]+[\mathcal{H}_\mathrm{D}^{\mathrm{yy}}-\mathcal{H}_\mathrm{D}^{\mathrm{zz}},\mathcal{H}_0^\mathrm{x}]+[\mathcal{H}_\mathrm{D}^{\mathrm{xx}}-\mathcal{H}_\mathrm{D}^{\mathrm{yy}},\mathcal{H}_0^\mathrm{z}]\}$
$\bar{\mathcal{H}}_0^{(2)}$	0	0
$\bar{\mathcal{H}}_\mathrm{D}^{(2)}$	$\frac{\tau^2}{18}[\mathcal{H}_\mathrm{D}^{\mathrm{zz}}-\mathcal{H}_\mathrm{D}^{\mathrm{xx}},[\mathcal{H}_\mathrm{D}^{\mathrm{zz}},\mathcal{H}_\mathrm{D}^{\mathrm{yy}}]]$	0
$\bar{\mathcal{H}}_\mathrm{D0}^{(2)}$	$\frac{\tau^2}{3}[\mathcal{H}_0^\mathrm{y},[\mathcal{H}_0^\mathrm{y},\mathcal{H}_\mathrm{D}^{\mathrm{xx}}-\mathcal{H}_\mathrm{D}^{\mathrm{zz}}]]$	$\frac{\tau^2}{9}\{3[\mathcal{H}_0^\mathrm{x}+\mathcal{H}_0^\mathrm{y}+\mathcal{H}_0^\mathrm{z},[\mathcal{H}_\mathrm{D}^{\mathrm{zz}},\mathcal{H}_0^\mathrm{x}+\mathcal{H}_0^\mathrm{y}+\mathcal{H}_0^\mathrm{z}]]+3[\mathcal{H}_\mathrm{D}^{\mathrm{zz}}-\mathcal{H}_\mathrm{D}^{\mathrm{yy}},[\mathcal{H}_0^\mathrm{x},\mathcal{H}_0^\mathrm{z}]]+$ $+3[\mathcal{H}_\mathrm{D}^{\mathrm{zz}}-\mathcal{H}_\mathrm{D}^{\mathrm{xx}},[\mathcal{H}_0^\mathrm{y},\mathcal{H}_0^\mathrm{z}]]-[\mathcal{H}_\mathrm{D}^{\mathrm{yy}}-\mathcal{H}_\mathrm{D}^{\mathrm{xx}},[\mathcal{H}_0^\mathrm{x},\mathcal{H}_0^\mathrm{y}]]\}$

Table 6.1: Zeroth, first and second order average Hamiltonian terms for the combined echo sequences CP-WAHUHA, CP-MREV8, CP-MREV16 and CP-BR24. Here, we adopt the notation introduced by Rhim et al.[233, 248, 249] where $\bar{\mathcal{H}}_0^{(i)}$ denotes the frequency offset average Hamiltonian, $\bar{\mathcal{H}}_\mathrm{D}^{(i)}$ is the dipolar average Hamiltonian and $\bar{\mathcal{H}}_\mathrm{D0}^{(i)}$ are higher order cross terms between $\mathcal{H}_0$ and $\mathcal{H}_\mathrm{D}$. The zeroth order terms (marked by †) are calculated taking into account finite pulse durations t_p, whereas the δ-pulse approximation ($t_\mathrm{p}\to 0$) is used for the first and second order terms.

gives identical non-vanishing average Hamiltonian terms in the $t_\mathrm{p} \to 0$ limit. Its zeroth order AHT contributions for finite t_p are in fact larger than those under CP-WAHUHA.

A major improvement of the MREV8 sequence over WAHUHA is its robustness against finite pulse durations[249]. Likewise, we find that for a modified sequence CP-MREV8 as illustrated in figure 6.2c the zeroth order average Hamiltonian vanishes even for pulses of finite duration t_p. The limiting term in the δ-pulse approximation $\bar{\mathcal{H}}^{(1)}_{\mathrm{D0}}$ is identical to that of the CP-WAHUHA sequence. However, the additional robustness is an important improvement as our experimental rf pulse times are on the order of microseconds and generally not negligible in multiple pulse experiments.

We can eliminate the first order AHT term by symmetrising the sequence: we combine CP-MREV8 with a mirror flipped cycle with reversed phases ($\mathrm{X} \to \bar{\mathrm{X}}$, etc.) to obtain a sequence CP-MREV16 (see figure 6.3a) which meets the symmetry criterion $\tilde{\mathcal{H}}_\mathrm{int}(t) = \tilde{\mathcal{H}}_\mathrm{int}(t_\mathrm{c} - t)$. The first non-zero contributions to the average Hamiltonian of this sequence are given by $\bar{\mathcal{H}}^{(2)}_{\mathrm{D}}$ and $\bar{\mathcal{H}}^{(2)}_{\mathrm{D0}}$ (see table 6.1).

Finally, we design a sequence analogous to BR24[233], which refocuses both dipolar and inhomogeneous broadening up to second order and is only limited by the first and second order cross terms listed in table 6.1. This CP-BR24 sequence, shown in figure 6.3b, can also be symmetrised, resulting in a 60-pulse series with average Hamiltonian

$$\bar{\mathcal{H}}_{\mathrm{CP-BR48}} = \bar{\mathcal{H}}^{(2)}_{\mathrm{D0}} + \mathcal{O}(t_\mathrm{c}^{-4}) \,. \tag{6.12}$$

As we will see in section 6.5.1, the CP-BR24 sequence suffers from a small spin echo amplitude in our experiments. This is at least in part owing to its sensitivity to frequency offsets, which we will examine in more detail in section 6.5.3. Similar issues are known for solid echo sequences where the less complex MREV8 cycle remains far more widespread than BR24 and the related 52-pulse cycle BR52 in practice[13, 232].

6.3 Methodology

The multiple pulse NMR experiments presented in the following sections are an extension of the Hahn echo measurements discussed in the previous chapter. Hence most of the experimental techniques and calibration methods are identical to those introduced in chapter 5.4. Having established the consistency between the Hahn echo results of sample A and sample B under charge-free conditions, we perform most of the measurements in this chapter on sample A. This choice is solely based on the larger NMR signal amplitudes (see figure 5.12) and stronger PL signals found in sample A. While our results on sample B are in qualitative agreement with those in sample A, the experimental accuracy is noticeably lower. This is particularly the case in the combined echo experiments where the echo amplitudes are further reduced compared to the Hahn echo due to the finite resonance offset tolerance of these sequences.

As before, we adopt the pump-rf-probe measurement cycle which was introduced in chapter 4.3.2 with a two-step NMR scheme consisting of adiabatic state preparation and coherent pulsed driving of the CT of the studied isotope. The external magnetic field is kept at $B_{0,\mathrm{z}} = 8$ T for all experiments and the sample temperature is $T \approx 4.2$ K. Two measurement parameters require particular attention for multiple pulse experiments: the pulse durations and the relative phases of the pulses.

6.3.1 Rotation Angle Calibration

As we apply sequences of up to 120 pulses to the sample, it is no longer sufficient to extract the required pulse durations for $\frac{\pi}{2}$ and π rotations from a Rabi oscillation measurement. To prevent the accumulation of pulse errors we use a $\left[\left(\frac{\pi}{2}\right)_{\mathrm{X}} - \left(\frac{\pi}{2}\right)_{\mathrm{X}} - \left(\frac{\pi}{2}\right)_{\mathrm{X}} - \left(\frac{\pi}{2}\right)_{\mathrm{X}}\right]_{n_\mathrm{c}}$ *tune up cycle* as illustrated in figure 6.4a for rotation angle calibration[248, 250]. In this measurement, we apply $4n_\mathrm{c}$ pulses with fixed separation τ and identical varying pulse time t_p. The magnetisation along the

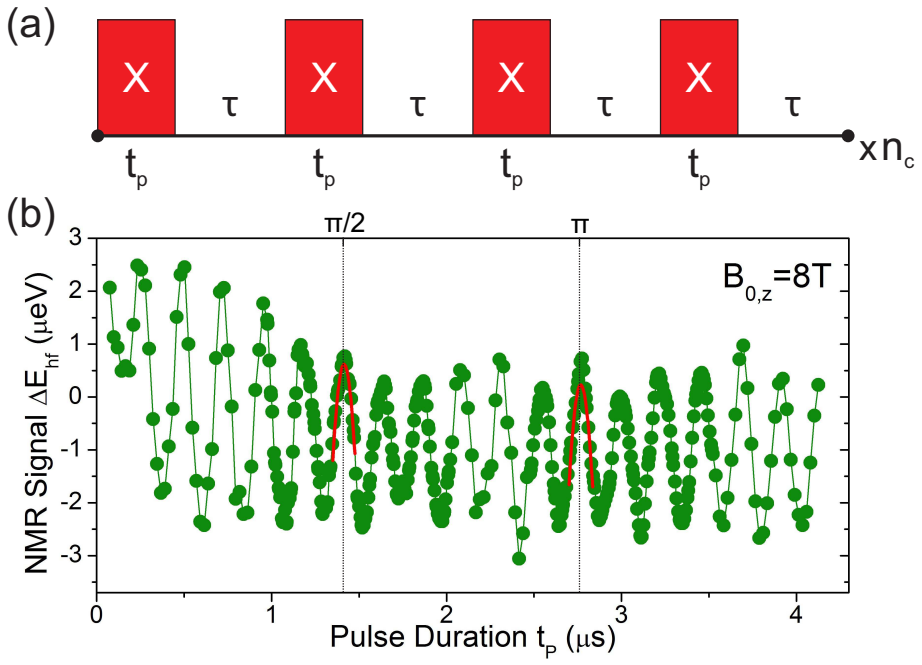

Figure 6.4: Calibration of the rotation angles for multiple pulse NMR. (a) The 4-pulse tune up cycle consisting of four pulses of equal duration t_p, carrier phase $\varphi = 0°$ and spacing τ. (b) Measurement on ^{71}Ga with $n_\mathrm{c} = 6$. The hyperfine shift ΔE_hf as a function of rf pulse duration t_p shows periodic revivals. From parabolic fits (red) to the 6th and 12th maxima of the NMR signal we extract pulse durations $t_{\pi/2} = 1.42$ μs and $t_\pi = 2.77$ μs at an rf input power of $P_\mathrm{rf} = 200$ W.

polarisation axis $\hat{e}_\mathrm{z}$ is restored whenever the net rotation of the $4n_\mathrm{c}$ rf pulses adds up to a multiple of 2π. As a consequence, the measured Overhauser splitting shows oscillatory behaviour as the polarisation of the driven spin ensemble is periodically inverted and restored with increasing t_p. The n_c-th oscillation maximum corresponds to a set of $4n_\mathrm{c}$ $\frac{\pi}{2}$ rotations and the $2n_\mathrm{c}$-th maximum analogously gives the required duration for a π pulse. The accuracy of this calibration method increases with n_c as the oscillation period becomes shorter, although the signal amplitude is reduced due to dephasing over the increasing evolution time $(4n_\mathrm{c} - 1)\tau$.

A representative rotation angle calibration measurement for ^{71}Ga with $n_\mathrm{c} = 6$ repetitions of the tune up cycle and pulse separation $\tau = 6$ μs is shown in figure 6.4b. We obtain pulse durations $t_{\pi/2} = 1.42$ μs and $t_\pi = 2.77$ μs from parabolic fits to the 6th and 12th oscillation maximum. The deviation from the ideal case of

$t_{\pi/2} = t_\pi/2$ is due to the finite pulse rise time in the rf circuit which distorts the ideal square pulse shape.

In the experiments presented in this chapter, we use a 1 kW class AB amplifier for hard pulse excitation. Due to the long rise time of the in-built amplifier gating circuit, the pulse rise time in the rf circuit $t_{\text{rise}} \approx 580$ ns becomes comparable to $t_{\pi/2}$. We reduce the distortion of the pulse shape by pre-gating the amplifier and gating the rf pulses externally with an absorptive switch. As the rise time of the switch is on the order of $5 - 10$ ns, the resulting pulse rise time $t_{\text{rise}} \approx 180$ ns is limited by the Q factor of the matching circuit.

6.3.2 Phase Calibration

In the Hahn echo sequence used in chapter 5 the carriers of all three rf pulses are in phase. As we saw in section 6.2.3, this is generally not the case for multiple pulse NMR sequences where the carriers of consecutive rf pulses often have alternating or orthogonal phases. We implement rotations of the nuclear magnetisation about the in-plane axes $\hat{e}_\text{x}$ and $\hat{e}_\text{y}$ in the rotating frame by a relative carrier phase shift of $\Delta\varphi = 90°$. Here, we note that the choice of $\hat{e}_\text{x}$ is arbitrary and defined as $\varphi = 0°$ in our measurements. Following the notation introduced in the previous section, we continue to denote the rotation axes in pulse sequences as capital letters, i.e. $\varphi(\text{X}) = 0°$ ($\hat{e}_\text{x}$), $\varphi(\text{Y}) = 90°$ ($\hat{e}_\text{y}$), $\varphi(\bar{\text{X}}) = 180°$ ($-\hat{e}_\text{x}$) and $\varphi(\bar{\text{Y}}) = 270.0°$ ($-\hat{e}_\text{y}$).

Experimentally, the phase is controlled by gating the modulation input of the rf generator. We calibrate the relative phase shifts between consecutive pulses by applying a test rf sequence of six pulses with duration $t_\text{p} = 15$ μs, pulse spacing $\tau = 1.2$ μs and phase relation $\text{X}-\bar{\text{Y}}-\bar{\text{X}}-\text{Y}-\text{X}-\bar{\text{Y}}$, and detecting the transmitted rf signal with a weakly inductively coupled pickup coil connected to an oscilloscope. The recorded rf pulse trace of such a calibration measurement is shown in green in figure 6.5. By fitting a set of local cosine functions with linked phase relations to the oscillogram we extract the relative calibration error for all four phases. By

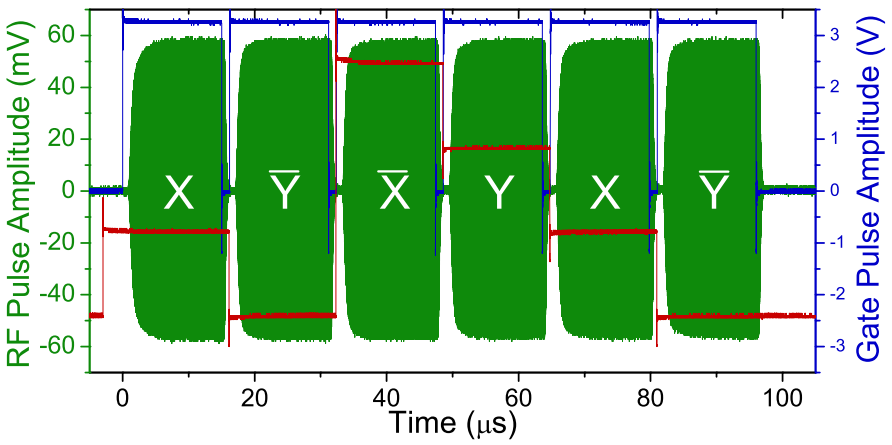

Figure 6.5: Oscillogram of the pulse phase calibration. The pulse and phase gating voltages as a function of time are marked in blue and red, respectively. The rf pulse amplitude over time (green) was detected in transmission with a pickup coil. Fitting of the pulses with phase shifted cosine functions gives the required phases for orthogonal rotation axes: $\varphi_{\mathrm{X}} = -0.5°$, $\varphi_{\mathrm{Y}} = 89.8°$, $\varphi_{\bar{\mathrm{X}}} = 181.1°$ and $\varphi_{\bar{\mathrm{Y}}} = -91.0°$.

adjusting the phase gating voltages and repeating the calibration cycle, we are able to reduce the phase error to $\delta\varphi \leq 0.4°$.

The class AB amplifier is very sensitive to phase shifted reflected signals. In order to avoid damage to the amplifier as well as to ensure a stable phase during each individual rf pulse, we always use a minimum delay ≥ 1 μs between consecutive pulses. The rf phase is changed during the interpulse delay time. Further protection against damage by reflected signals is added in the form of a 6 dB attenuator after the amplifier output.

6.4 Long-Lived Spin Echoes under Carr-Purcell Sequences

In this section we study the nuclear spin dephasing of the ^{75}As and ^{71}Ga CTs in a single neutral quantum dot under π pulse trains. We expect only a moderate increase of the measured nuclear phase memory time $T_{\mathrm{M,n}}$ since the bath coherence of the probed isotope is limited by homonuclear dipolar interactions which are

not refocused under such sequences. However, dephasing due to time-dependent heteronuclear dipolar coupling to the remaining slowly-evolving nuclear spin bath should be removed by a small number of π pulses.

Due to their robustness against pulse errors, we use sequences with alternating carrier phase: an APCP sequence with cycles $\tau - \pi_{\mathrm{X}} - 2\tau - \pi_{\bar{\mathrm{X}}} - \tau$ (see figure 6.1d) and an APCPMG sequence with $\tau - \pi_{\mathrm{Y}} - 2\tau - \pi_{\bar{\mathrm{Y}}} - \tau$ (figure 6.1e). Both sequences have an initialisation pulse $\left(\frac{\pi}{2}\right)_{\mathrm{X}}$ and a final readout pulse $\left(\frac{\pi}{2}\right)_{\bar{\mathrm{X}}}$.

6.4.1 Experimental Results

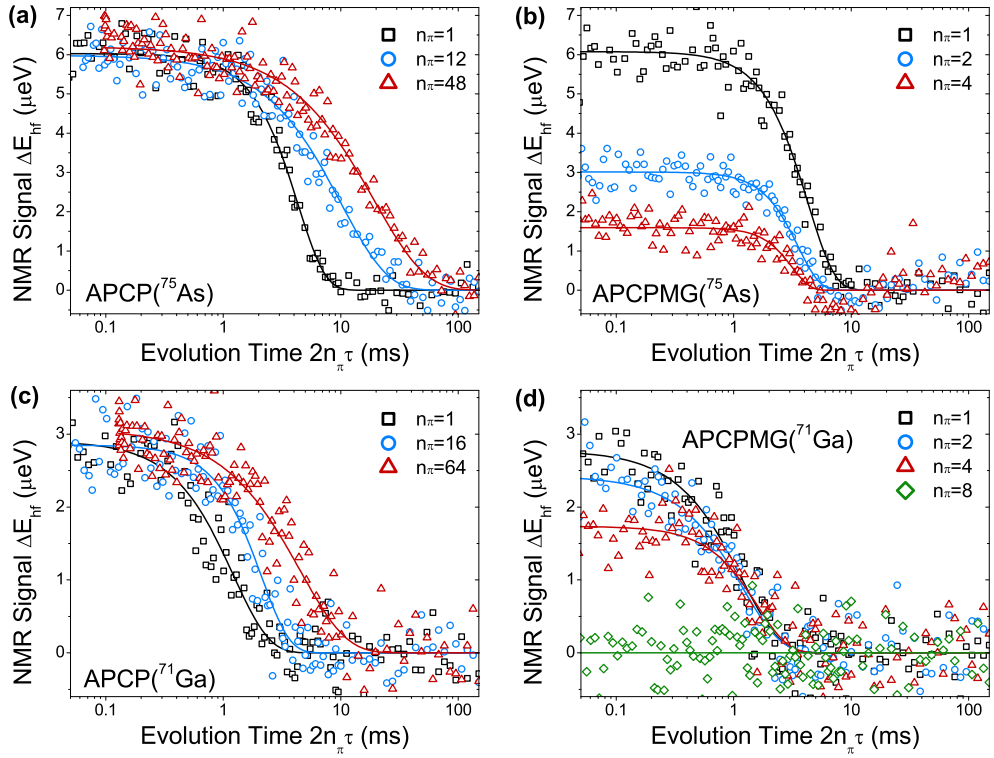

Figure 6.6: Dependence of the ^{75}As (a,b) and ^{71}Ga (c,d) nuclear spin echo amplitude ΔE_{hf} on the total evolution time $2n_\pi\tau$ under APCP and APCPMG. Square symbols show Hahn echo data with only one π pulse. Representative data for pulse numbers $n_\pi > 1$ is marked with different symbols. Solid lines show compressed exponential fits $\propto \exp[-(2n_\pi\tau/T_{\mathrm{M,n}})^\beta]$ from which nuclear spin decay times $T_{\mathrm{M,n}}$ are extracted.

Figures 6.6 show representative results of the APCP and APCPMG experiments on ^{75}As (6.6a and 6.6b, respectively) and on ^{71}Ga (6.6c and 6.6d) for different π pulse

numbers n_π. We note that each APCP(MG) cycle actually consists of two pulses, i.e. the corresponding number of cycles is given by $n_c = n_\pi/2$. Each dataset shows the nuclear spin echo signal ΔE_{hf} as a function of the total free evolution $2n_\pi\tau$ during the pulse sequence for a fixed n_π. For comparison, all four panels also include Hahn echo decay data with only one refocusing pulse (squares). Nuclear phase memory decay times $T_{M,n}$ are extracted using a fit with a compressed exponential function (solid lines)

$$\Delta E_{hf}(2n_\pi\tau) = \Delta E_{hf}(0)e^{-(2n_\pi\tau/T_{M,n})^\beta}\ , \tag{6.13}$$

where $\Delta E_{hf}(0)$ is the initial hyperfine shift for a maximally polarised nuclear spin ensemble and $\beta \in [1,2]$ is a compression factor as introduced in chapter 5.5.

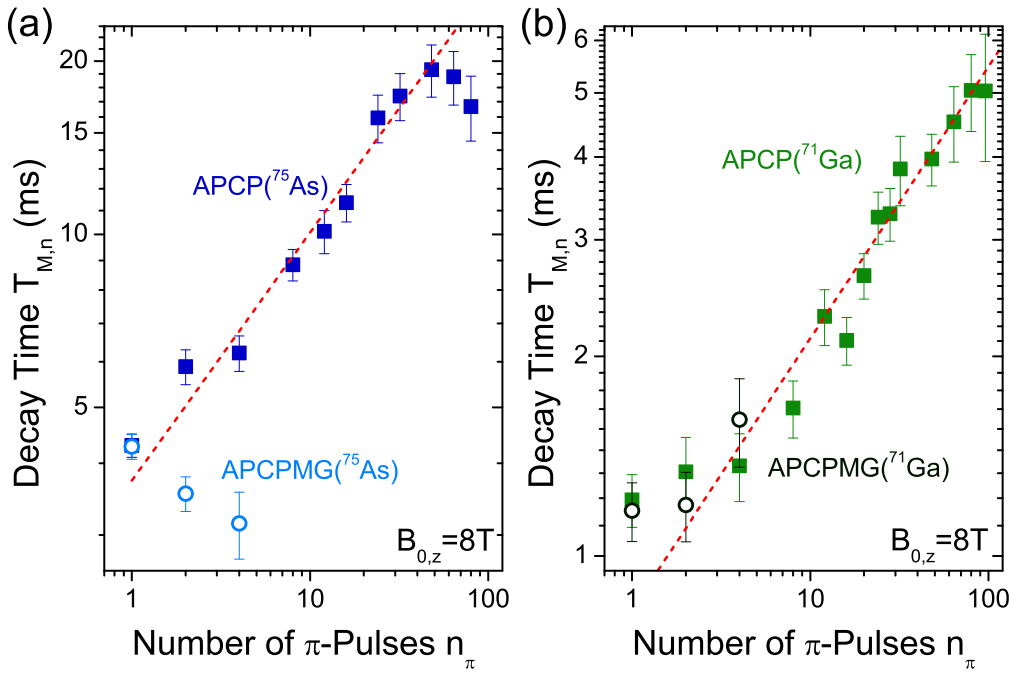

Figure 6.7: Fitted nuclear spin echo decay time $T_{M,n}$ as a function of pulse number n_π for (a) ^{75}As and (b) ^{71}Ga. Solid squares show the APCP decay times obtained from compressed exponential fits to the experimental data and open circles mark the corresponding APCPMG decay times. The error bars correspond to 90% confidence intervals. Dashed red lines show power law fits $\propto n_\pi^\kappa$ to the APCP data.

The nuclear spin echo decay under APCP shows a pronounced slow-down with increasing refocusing pulse number n_π for both isotopes. By contrast, no noticeable

increase of the echo decay time is observed under APCPMG. Instead, the echo amplitude $\Delta E_{\mathrm{hf}}(0)$ drops significantly even for small n_π and vanishes entirely for $n_\pi \geq 8$.

Nuclear phase memory times extracted from fits to the experimental data are shown in figures 6.7a and b as a function of the π pulse number n_π. For the APCP sequence, the ^{75}As decay time reaches a maximum value of $T_{\mathrm{M,n}}^{\mathrm{APCP}}(^{75}\mathrm{As}) = 19.3 \pm 2.0$ ms for $n_\pi = 48$ before decreasing again at higher pulse numbers. The dependence up to the maximum value can be described by a power law $T_{\mathrm{M,n}}(n_\pi) \propto n_\pi^\kappa$ (dashed red line) where $\kappa(^{75}\mathrm{As}) = 0.43 \pm 0.06$ is a scaling exponent. Analogously, we observe a maximum $T_{\mathrm{M,n}}^{\mathrm{APCP}}(^{71}\mathrm{Ga}) = 5.04 \pm 0.67$ ms with a fitted scaling exponent $\kappa(^{71}\mathrm{Ga}) = 0.41 \pm 0.06$ for ^{71}Ga (dashed red line in figure 6.7). At pulse numbers $n_\pi > 64$ the error bars of $T_{\mathrm{M,n}}^{\mathrm{APCP}}(^{71}\mathrm{Ga})$ are very large. This is due to a reduced spin echo amplitude $\Delta E_{\mathrm{hf}}(0)$, which we attribute to the accumulation of pulse imperfections and of frequency offset errors arising from the broad inhomogeneous NMR linewidths $\Delta\nu_{\mathrm{inh}} \sim 10-40$ kHz. A decrease of the echo amplitude is also observed in the APCP measurements on ^{75}As with $n_\pi = 64$ and $n_\pi = 80$. The shorter decay times for these pulse numbers are therefore also attributed to these effects.

Even under a single cycle ($n_\pi = 2$) of APCPMG (open circles in figure 6.7a) the nuclear spin decay time for ^{75}As is reduced compared to $T_{\mathrm{M,n}}^{\mathrm{HE}}(^{75}\mathrm{As})$. While an increase of $T_{\mathrm{M,n}}(n_\pi)$ is observed for ^{71}Ga under APCPMG, the associated error bars are larger than for the corresponding APCP values. As we saw in figures 6.6b and 6.6d, the echo amplitude $\Delta E_{\mathrm{hf}}(0)$ drops quickly with increasing n_π for both isotopes. This indicates that APCPMG is extremely sensitive to pulse errors and resonance offsets, a conclusion which we will see confirmed in section 6.4.3, where we will analyse the offset-dependent performance of both sequences and show that the inhomogeneous broadening of the ^{75}As and ^{71}Ga CTs is too large for the respective full spin ensembles to be driven resonantly under APCPMG.

The power law scaling of the phase memory time under the APCP decoupling se-

quence up to large n_π would ordinarily imply that we have decoupled the $\boldsymbol{I}_n$ sub-bath from a strongly fluctuating environment. The scaling exponents κ for both isotopes are comparatively small, although the values $\kappa \approx 0.5 - 0.75$ reported for similar DD experiments on electrons in InAs nanowires[251], NV centres[252] and electrostatically defined GaAs quantum dot systems[253] are close to our experimental error margins. The associated noise spectrum of the system-environment coupling would be expected to scale as $S(\omega) \propto \omega^{-\zeta}$ with $\zeta = \kappa/(1-\kappa) \approx 2/3$[224, 253, 254] in our system. The presence of such a strong, broadband noise source is in stark contrast to our understanding of the spin bath dynamics in a quantum dot. The static inhomogeneous dephasing due to quadrupolar interactions is already fully refocused in Hahn echo and hence cannot be suppressed any further. While we expect APCP sequences to suppress decoherence arising from heteronuclear coupling, the associated local field fluctuates on the timescale of homonuclear dipolar flip-flops among the environment nuclear spins, which are strongly suppressed by the inhomogeneous quadrupolar interaction (see chapter 5 and [41]). Since previous measurements on sample A gave no indications for strong charge fluctuations in the dot environment either, we conclude that the increased nuclear spin decay times under APCP are in fact not linked to the decoupling of the fluctuating sub-bath environment.

6.4.2 Spin-Locking under π Pulses of Finite Duration

We find that similar unexpectedly long-lived spin echo decay times under π pulse trains have been reported for other solid state systems in the past. Experiments on ^{29}Si in Si:P revealed a slow decay tail in CPMG which exceeded the Hahn echo phase memory time $T_{\mathrm{M,n}}^{\mathrm{HE}}(^{29}\mathrm{Si}) \approx 5.6$ ms by more than an order of magnitude[255, 256]. Subsequent work showed similar behaviour in a wide range of materials from fullerenes and yttria[257, 258] to adamantene and ferrocene[259]. Three competing theoretical models have been put forward to explain this deviation from the expected behaviour.

Franzoni et al. argue that the extended decay times arise due to stimulated echoes[257]. In a system with strong field inhomogeneities, imperfect π pulses can lead to partial storage of the coherence along the $\hat{e}_z$ axis where it decays with the spin relaxation time T_1. As the authors demonstrate, a subsequent second imperfect π pulse can lead to a stimulated echo which coincides with the normal spin echo and interferes either constructively or destructively depending on the phase relation between the two pulse carriers. Consequently, long-lived spin echoes are observed under APCP and CPMG pulse trains while the echo decays with T_M^{HE} under CP and APCPMG as the authors verify experimentally in NMR measurements on ^{13}C in fullerenes.

A second explanation provided by Li et al. is based on an AHT analysis of π pulse trains[260]. The authors show that spin locking effects can arise under a series of π pulses depending on the phase relation between consecutive pulses when finite pulse durations t_p are taken into account. The theoretically derived and experimentally observed behaviour of the spin echo is identical to that predicted by Franzoni et al., i.e. extended phase memory times only occur under APCP and CPMG sequences. However, as Ridge et al. point out[259], long-lived echoes are observed by all groups even for conditions where the evolution time between pulses 2τ strongly exceeds the pulse time t_p.

The most recent proposal was made by Ridge et al.[259] Like Franzoni and collaborators, they attribute the extended decay time to π pulse imperfections. Using AHT, they demonstrate that a combination of resonance offsets and rotation angle errors can lead to pulsed spin locking, i.e. an effective static in-plane magnetic field that can preserve the magnetisation along either $\hat{e}_x$ or $\hat{e}_y$. In agreement with the other two models, persistent echoes are only predicted for APCP and CPMG pulse sequences.

In order to determine which theory describes our experimental results best, we must identify features that are unique to each model. The Franzoni and Ridge pro-

posals could be distinguished easily by a separate stimulated echo experiment[199, 261]. The presence or absence of a stimulated echo would provide strong evidence in favour of the respective model. The theoretical frameworks of both proposals share the assumption that a δ-pulse approach is justified, i.e. that the pulse spacing 2τ is much larger than the pulse duration t_p. This is in contrast to the Li proposal, where we would expect a dependence of the spin locking effect on the relative timescales of 2τ and t_p.

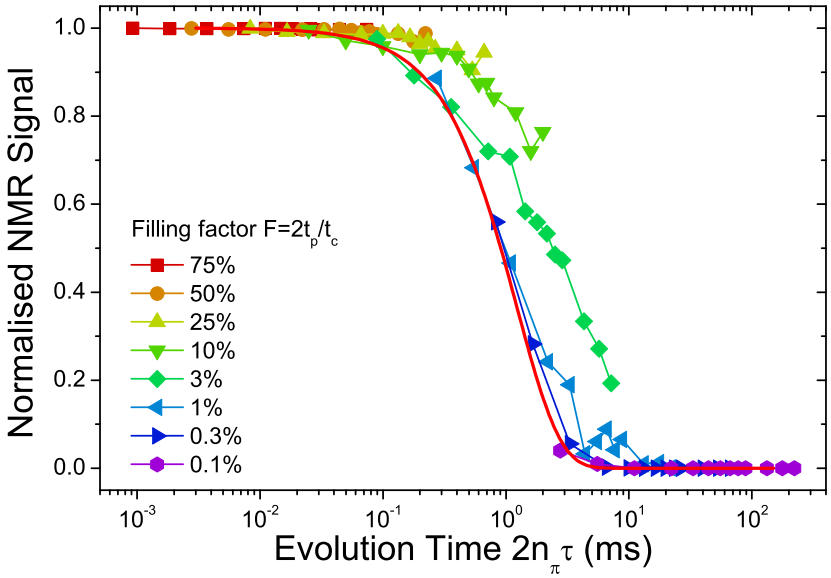

Figure 6.8: Dependence of the normalised ^{71}Ga nuclear spin echo amplitude on the total evolution time $2n_\pi\tau$ under APCP. Each trace shows values with fixed filling factor $\mathrm{F} = 2t_\mathrm{p}/t_\mathrm{c}$ and varying pulse number n_π. Values are extracted from exponential fits to the experimental data shown in figure 6.6c. The Hahn echo decay fit is shown as a solid red line.

We can examine this dependence using the results of the previous section. To this end, we quantify the time $2t_\mathrm{p}$ during which rf pulses are applied in an APCP cycle $t_\mathrm{c} = 4\tau + 2t_\mathrm{p}$ by a *filling factor* F, which we define as

$$\mathrm{F} = \frac{2t_\mathrm{p}}{t_\mathrm{c}} = \frac{2t_\mathrm{p}}{4\tau + 2t_\mathrm{p}} \quad , \quad \mathrm{F} \in [0, 1] \; . \tag{6.14}$$

Figure 6.8 shows the normalised ^{71}Ga nuclear spin echo amplitude as a function of the total evolution time $2n_\pi\tau$ for fixed F and varying pulse number n_π, i.e. the first

data point of each trace corresponds to a Hahn echo, the second point to a single APCP cycle, etc. with fixed π pulse spacing 2τ. Since different pulse spacings were used in each of the measured data sets with fixed pulse number n_π (as shown in figure 6.6), the values shown in figure 6.8 are obtained using equation (6.13) with fixed τ and with parameters $T_{\mathrm{M,n}}$ and β determined from fitting to the experimental data for each n_π.

We observe a strong dependence of the nuclear spin echo decay on the filling factor F. While a pronounced slow-down of the decay dynamics occurs at large F, the spin echo amplitude for F $< 1\%$ follows the Hahn echo decay curve (solid red line in figure 6.8). This is in strong contrast to the observations of long-lived echoes in other systems where the Hahn echo amplitude for a given τ is recovered under subsequent pulses even for timescales $\tau > T_{\mathrm{M,n}}^{\mathrm{HE}} \gg t_{\mathrm{p}}$. Therefore, we conclude that the models of Franzoni et al.[257] and Ridge et al.[259], which both predict such a *decay tail* behaviour, do not describe the mechanism responsible for the extended spin echo decay times in our system.

Instead, we find that our results are in good agreement with the model presented by Li et al.[260] As we mentioned in section 6.2.2, an AHT analysis of the ideal Carr-Purcell sequence without pulse errors and under the assumption of δ-pulses shows that inhomogeneous broadening is fully refocused whereas the homonuclear dipolar term remains unaltered, i.e. $\bar{\mathcal{H}}_{\mathrm{CP}} = \mathcal{H}_{\mathrm{D}}^{\mathrm{zz}}$. This is a general result for all CP- and CPMG-type sequences. By contrast, the average Hamiltonians of the four (AP)CP(MG) sequences are no longer identical if finite pulse durations t_{p} are taken into account. In particular, we obtain[260]

$$\bar{\mathcal{H}}_{\mathrm{APCP}}^{(0)} = \frac{1}{t_{\mathrm{c}}}\left(-\frac{4t_{\mathrm{p}}\Omega_{\mathrm{z}}}{\pi}I_{\mathrm{y}} + 4\tau\mathcal{H}_{\mathrm{D}}^{\mathrm{zz}} - t_{\mathrm{p}}\mathcal{H}_{\mathrm{D}}^{\mathrm{xx}}\right) , \tag{6.15}$$

for the zeroth order average Hamiltonian under an APCP cycle. The first order term $\bar{\mathcal{H}}_{\mathrm{APCP}}^{(1)}$ vanishes due to the symmetry properties of the sequence. A full derivation of

equation (6.15) is given in [260] and in appendix 9.2.1. The term $\propto I_y$ corresponds to an effective static in-plane magnetic field. By transforming $\bar{\mathcal{H}}^{(0)}_{\mathrm{APCP}}$ into a second toggling frame with respect to the transverse field (derivation given in appendix 9.2.2) and time-averaging over one Rabi cycle in the effective field, we obtain a twice averaged Hamiltonian

$$\bar{\bar{\mathcal{H}}}^{(0)}_{\mathrm{APCP}} = -\frac{1}{t_c}\left(2\tau - \frac{t_p}{2}\right)\mathcal{H}^{yy}_{D} \ . \tag{6.16}$$

This expression is very similar to the average Hamiltonian under the Mansfield-Waugh *pulsed spin locking* sequence (MW4). This sequence consists of four $\left(\frac{\pi}{2}\right)_Y$ pulses with equal pulse spacing τ and has a zeroth order average Hamiltonian $\bar{\mathcal{H}}^{(0)}_{\mathrm{MW4}} = -\frac{1}{2}\mathcal{H}^{yy}_{D}$, leading to spin echo decay times orders of magnitude longer than T^{HE}_{M}[262, 263]. We can understand this behaviour when taking into account that the initial rf pulse $\left(\frac{\pi}{2}\right)_X$ applied before either sequence prepares the nuclear spin $\boldsymbol{I}$ in a state $-I_y$. In both the APCP and MW4 sequences the average Hamiltonian is proportional to the secular dipolar Hamiltonian $\mathcal{H}^{yy}_{D}$ along $\hat{e}_y$ which commutes with the observable. Consequently, the magnetisation along this axis is preserved or "locked" under both sequences and no echo decay is predicted in zeroth order AHT. While an expression similar to equation (6.16) can be derived for CPMG, AHT does not predict any spin locking effects for CP and APCPMG[260].

We note that the spin locking mechanism under π pulse trains relies fundamentally on the dipolar evolution during t_p and is not expected to persist for small filling factors F. This can be seen when we look at the Rabi frequency of the transverse field in equation (6.15), $\Omega' = \frac{4t_p\Omega_z}{\pi t_c} \propto \mathrm{F}$. As the second averaging is based on a perturbation approach which assumes slow evolution of the spin bath under the dipolar terms in equation (6.15) over a timescale $T'_{\mathrm{Rabi}} = \frac{2\pi}{\Omega'} \propto \mathrm{F}^{-1}$, $\bar{\bar{\mathcal{H}}}_{\mathrm{APCP}}$ is no longer expected to converge for small F[259]. In this limit, the δ-pulse approximation is justified and equation (6.15) is reduced to $\bar{\mathcal{H}}^{(0)}_{\mathrm{APCP}} = \mathcal{H}^{zz}_{D}$. This is in agreement

with our experimental observation that the spin locking effect vanishes and the decay time is reduced to $T_{\mathrm{M,n}}^{\mathrm{HE}}$ for $\mathrm{F} < 1\%$ (red line in figure 6.8).

In conclusion, we can attribute the long-lived nuclear spin echoes of ^{75}As and ^{71}Ga under APCP to a form of pulsed spin locking arising from homonuclear dipolar evolution during the finite pulse duration t_{p}. Such effects are not expected under APCPMG, although we were not able to verify this experimentally for pulse numbers $n_\pi \gtrsim 8$ due to the rapid drop of the echo amplitude with increasing pulse number under this sequence.

6.4.3 Effect of Resonance Offsets on Carr-Purcell Sequences

As we will now show, this behaviour of the APCPMG sequence can be explained by its high sensitivity to resonance offsets. The CTs of ^{75}As and ^{71}Ga are both inhomogeneously broadened to $\sim 10 - 40$ kHz by the second order contributions of quadrupolar interactions in the quantum dot. In chapter 3.3.2, we introduced a hard pulse condition $\omega_1 \gg \frac{\Delta\nu_{\mathrm{inh}}}{2}$ for coherent pulse rotations. We assumed that under this condition the full CT is driven by an rf pulse of field amplitude $B_1 = -\frac{\omega_1}{\gamma}$. This can become infeasible for strongly inhomogeneously broadened transitions such as the ^{75}As STs ($\Delta\nu_{\mathrm{inh}} \sim 10$ MHz), where a Hahn echo experiment would require rf field amplitudes of $B_1 > 0.5$ T.

While we can easily meet the hard pulse condition for nuclear Hahn echo experiments on the ^{75}As and ^{71}Ga CTs, this can become insufficient for coherent manipulation under longer pulse sequences. Depending on the robustness of a sequence against resonance offsets, errors due to incomplete refocusing can rapidly add up with increasing cycle number and reduce the echo amplitude $\Delta E_{\mathrm{hf}}(0)$.

In order to quantify the effect of resonance offsets on the relative performance of the APCP and APCPMG sequences, we simulate the evolution of a magnetisation vector $\boldsymbol{M} = M_z\hat{e}_z$ under a given pulse sequence as described by the Bloch equations of motion. The rotation axis for each pulse with carrier phase φ is set to

$\hat{e}_\Omega = (1+\delta^2)^{-1/2}(\cos\varphi, \sin\varphi, -\delta)^\mathsf{T}$, where δ denotes the resonance offset in terms of the inverse resonant Rabi period T_{Rabi}^{-1}. We then study the offset dependence of the magnetisation along the polarisation axis $\hat{e}_\mathrm{z}$ after a full sequence including initialisation and readout pulse. In these simulations no spin relaxation or spin dephasing mechanisms are considered, i.e. we set $T_1 = T_2 = \infty$. We further assume that all pulses have the same frequency offsets δ and do not take into account carrier phase errors.

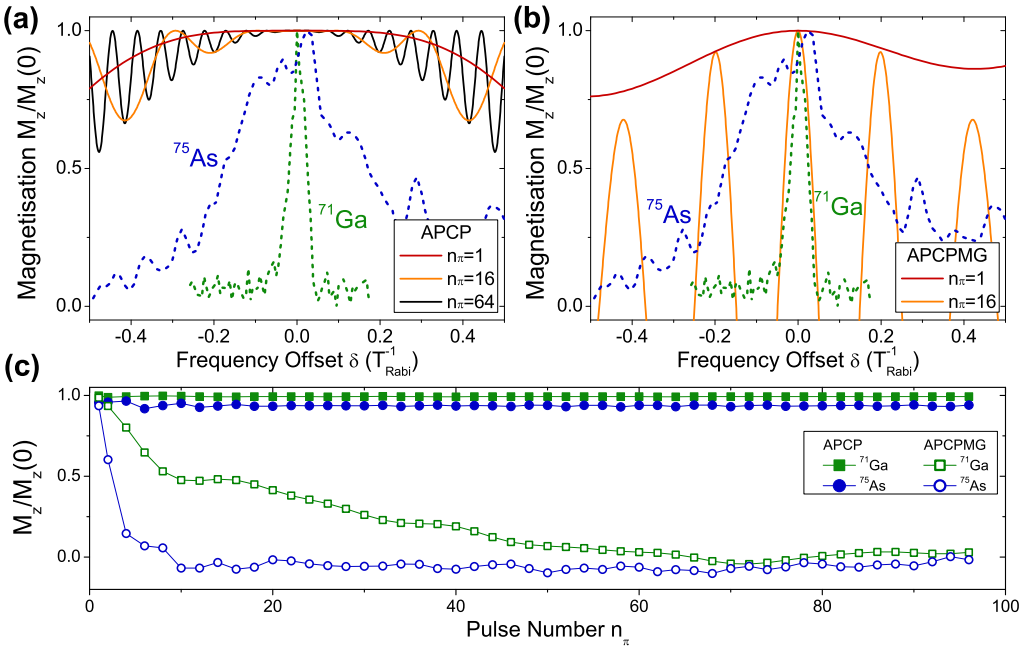

Figure 6.9: (a,b) Normalised magnetisation along $\hat{e}_\mathrm{z}$ after evolution under a series of non-resonant rf pulses as a function of the resonance frequency offset δ for (a) APCP and (b) APCPMG. Solid curves show simulated data for different π pulse numbers n_π. Dashed lines show normalised ^{75}As (blue) and ^{71}Ga (green) CT NMR spectra with frequency axes rescaled by T_{Rabi} at $P_{\mathrm{rf}} = 200$ W. (c) Weighted average of the normalised magnetisation over the ^{75}As (circles) and ^{71}Ga (squares) CT resonance after an APCP (solid symbols) or APCPMG (empty symbols) sequence as a function of refocusing pulse number n_π.

The results of our simulations for the two decoupling sequences are shown in figures 6.9a (APCP) and 6.9b (APCPMG). The recovered normalised magnetisation after evolution under a Hahn echo sequence (red) and sequences with $n_\pi = 16$ (orange) and $n_\pi = 64$ (black) refocusing pulses is shown as a function of the normalised

resonance offset δ. Normalised NMR spectra of the ^{75}As and ^{71}Ga CTs are shown as blue and green dashed lines with the frequency axis rescaled for the respective Rabi period derived at $P_{\mathrm{rf}} = 200$ W in our experiments.

Several features of the simulated curves are distinguishable. Firstly, we notice offset-dependent oscillations in the normalised magnetisation. These periodic magnetisation revivals arise from the effect of the offset δ in the rotating frame: the pulse rotation axis $\hat{e}_\Omega$ is tilted towards $\pm\hat{e}_\mathrm{z}$ with increasing δ, while the pulse duration t_p stays constant. As a consequence, depending on the initial conditions, the magnetisation vector can precess about $\hat{e}_\Omega$ multiple times within t_p, an effect which is amplified for large n_π. At very large offsets $|\delta| \gg T_{\mathrm{Rabi}}^{-1}$ the initial magnetisation $M_\mathrm{z}(0)$ remains entirely unaltered as the pulse rotation axis $\hat{e}_\Omega$ is parallel to $\hat{e}_\mathrm{z}$ in this limit (not shown). Secondly, we note that the curve for $n_\pi = 1$ in figure 6.9b is asymmetric. This is a recurring effect which we only observe for sequences which contain pulses with rotation axes along both $\hat{e}_\mathrm{x}$ and $\hat{e}_\mathrm{y}$, and which lack antisymmetry with respect to $t_\mathrm{c}/2$ (i.e. a pulse at $t_\mathrm{c}/2 - t$ is not compensated by a pulse in antiphase at $t_\mathrm{c}/2 + t$).

Most importantly, however, our simulations show that the APCP sequence is remarkably robust against frequency offsets. By contrast, the offset interval within which APCPMG can fully restore the initial magnetisation narrows rapidly with increasing cycle number. This is shown more clearly in figure 6.9c: here, we show the weighted average of the normalised magnetisation over the CT resonances of ^{75}As and ^{71}Ga after n_π pulses for both sequences. The simulations are in excellent agreement with our experimental observations: while the initial magnetisation is fully recovered under APCP even for large pulse numbers $n_\pi > 50$ (solid symbols), it is strongly reduced even for $2 - 4$ pulses under APCPMG.

We can therefore conclude that the APCPMG sequence is extremely sensitive to offset errors and hence unsuitable for application to the inhomogeneously broadened transitions in self-assembled quantum dots even for the moderate broadening of the

CTs. Although the sequence should be able to decouple our nuclear spin sub-bath from its environment without spin locking, we would require significantly stronger rf fields to drive the full transition coherently for several cycles n_c. This is in contrast to the APCP sequence, which is very robust against frequency offsets but is affected by pronounced spin locking effects.

6.5 Nuclear Spin Bath Control under Combined Echo Sequences

In section 6.2.3, we introduced a set of multiple pulse sequences based on well-known solid echo cycles with additional π refocusing pulses. We showed that it is possible to find sequences which suppress dephasing due to both inhomogeneous broadening and homonuclear dipolar interactions in leading orders of AHT (see table 6.1). Here, we apply these sequences to the CTs of the ^{75}As and ^{71}Ga spin ensembles in a neutral InGaAs quantum dot.

Although none of the zeroth and first order AHT terms we obtained for the combine echo sequences are expected to lead to spin locking, previous experiments in Si:P by Ladd et al. have reportedly shown such effects under similar sequences[232]. Taking into account the findings from the CP(MG) experiments of the previous section, we aim to avoid this by testing the sequences not only in the CP-like configuration where the carriers of the initial and final $\left(\frac{\pi}{2}\right)_{\mathrm{X}/\bar{\mathrm{X}}}$ pulses are in (anti-)phase with those of the π pulses (see e.g. figures 6.2b and c), but also in a CPMG-like configuration with initial and final pulse carrier phases $\left(\frac{\pi}{2}\right)_{\mathrm{Y}/\bar{\mathrm{Y}}}$ orthogonal to those of the π refocusing pulses. In order to test how sensitive the combined echo sequences are to the initial in-plane spin state, we also perform several measurements with initial and final pulses $\left(\frac{\pi}{2}\right)_{\mathrm{D}/\bar{\mathrm{D}}}$ about diagonal axes $\varphi_{\mathrm{D}} = 45°$ and $\varphi_{\bar{\mathrm{D}}} = 225°$, which we will denote as *dCP-like*. As we will show, spin locking effects do indeed appear under CP-like sequences and distort the measured decay time. This effect is reduced under

the diagonal initialisation pulse conditions and vanishes for CPMG-like sequences.

In contrast to the nuclear phase memory times $T_{\mathrm{M,n}}$ which we obtained from Hahn echo and CP(MG) experiments, we will label the measured decay times under combined echo sequences in this section as decoherence times $T_{2,\mathrm{n}}$. This is to illustrate that full suppression of the intrinsic homonuclear dipolar coupling will give us the decoherence time of a non-interacting nuclear spin sub-ensemble.

6.5.1 Performance Comparison of Combined Echo Sequences

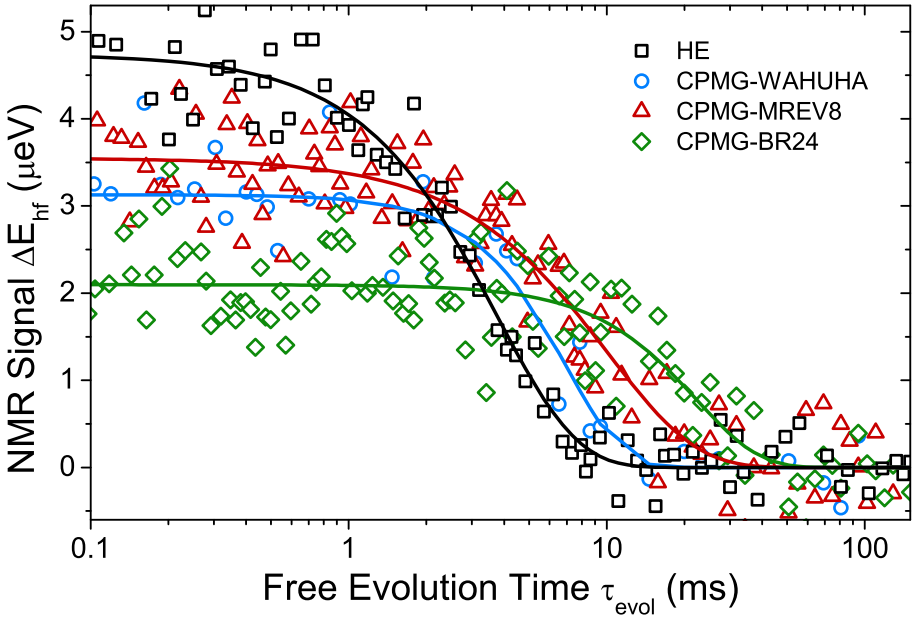

Figure 6.10: Experimental performance comparison for the combined echo sequences at $B_{0,\mathrm{z}} = 8$ T. The ^{75}As nuclear spin echo amplitude ΔE_{hf} is shown as a function of the total free spin evolution time τ_{evol} during the duration of the pulse sequence. Solid lines show compressed exponential fits $\propto \exp[-(\tau_{\mathrm{evol}}/T_{2,\mathrm{n}})^{\beta}]$ to the data for different pulse sequences.

In a first set of experiments, we compare the performance of the combined echo sequences introduced in section 6.2.3. As in all previous experiments, we study the nuclear spin dynamics of a neutral, i.e. charge-free quantum dot in a large external magnetic field $B_{0,\mathrm{z}} = 8$ T. Here, we probe the ^{75}As spin dynamics in a dot in the gated diode sample B. Figure 6.10 shows the decay of the ^{75}As nuclear spin echo amplitude over the total free evolution time τ_{evol} during a cycle of CPMG-WAHUHA

(circles), CPMG-MREV8 (triangles) and CPMG-BR24 (diamonds). A Hahn echo decay curve with $T_{\mathrm{M,n}}^{\mathrm{HE}}(^{75}\mathrm{As}) = 3.8 \pm 0.4$ ms is also depicted for comparison (squares). Fits with a compressed exponential

$$\Delta E_{\mathrm{hf}}(\tau_{\mathrm{evol}}) = \Delta E_{\mathrm{hf}}(0) \mathrm{e}^{-(\tau_{\mathrm{evol}}/T_{2,\mathrm{n}})^{\beta}} , \tag{6.17}$$

are shown as solid lines.

We note that the initial echo amplitude $\Delta E_{\mathrm{hf}}(0)$ for all three combined echo sequences is reduced compared to the Hahn echo amplitude. In section 6.5.3, we will show that this is not unexpected and can be partly attributed to the limited robustness of these sequences against resonance offsets, similar to the behaviour observed for the APCPMG sequence in the previous section. Due to the strong inhomogeneous broadening of the ^{75}As CT ($\Delta\nu_{\mathrm{inh}}(^{75}\mathrm{As}) \approx 24$ kHz, see chapter 5.4.1), we are unable to drive the full spin ensemble resonantly. The amplitude reduction is particularly pronounced for CPMG-BR24. For this reason, we focus on the shorter CPMG-MREV-type sequences in subsequent measurements despite the strongly enhanced decoherence time $T_{2,\mathrm{n}}^{\mathrm{BR24}} = 22.4 \pm 4.5$ ms obtained for CPMG-BR24 from the exponential fit.

The initial echo amplitudes of the CPMG-WAHUHA and CPMG-MREV8 sequences are both reduced by $\sim 30\%$ compared to the Hahn echo signal. Fitting with equation (6.17) gives decay times of $T_{2,\mathrm{n}}^{\mathrm{WHH}} = 7.0 \pm 1.1$ ms and $T_{2,\mathrm{n}}^{\mathrm{MREV8}} = 10.1 \pm 1.3$ ms, respectively. Taking into account these results as well as the additional robustness of CPMG-MREV8 against finite pulse widths which we derived in section 6.2.3 using AHT, we conclude that CPMG-MREV8 (and by extension the symmetrised CPMG-MREV16 version) is the most suitable sequence for suppressing the nuclear spin bath decoherence in the InGaAs quantum dot system.

6.5.2 Suppressed Homonuclear Dipolar Interactions under CPMG-MREV Combined Echo Sequences

Having established the capability of combined echo sequences to extend the nuclear spin bath coherence beyond the Hahn echo dephasing time $T_{\mathrm{M,n}}^{\mathrm{HE}}$, we investigate how far $T_{2,\mathrm{n}}$ can be increased under repeated cycles of CP(MG)-MREV16. Figures 6.11 show the results of such measurements on ^{75}As (a and b) and ^{71}Ga (c and d) in a neutral quantum dot on sample A. The spin echo amplitude ΔE_{hf} under a Hahn echo (squares), CP(MG)-MREV8 (circles) and (CP(MG)-MREV16)$_{n_{\mathrm{c}}}$ sequence (triangles) is shown as a function of the total free evolution time during the respective sequence.

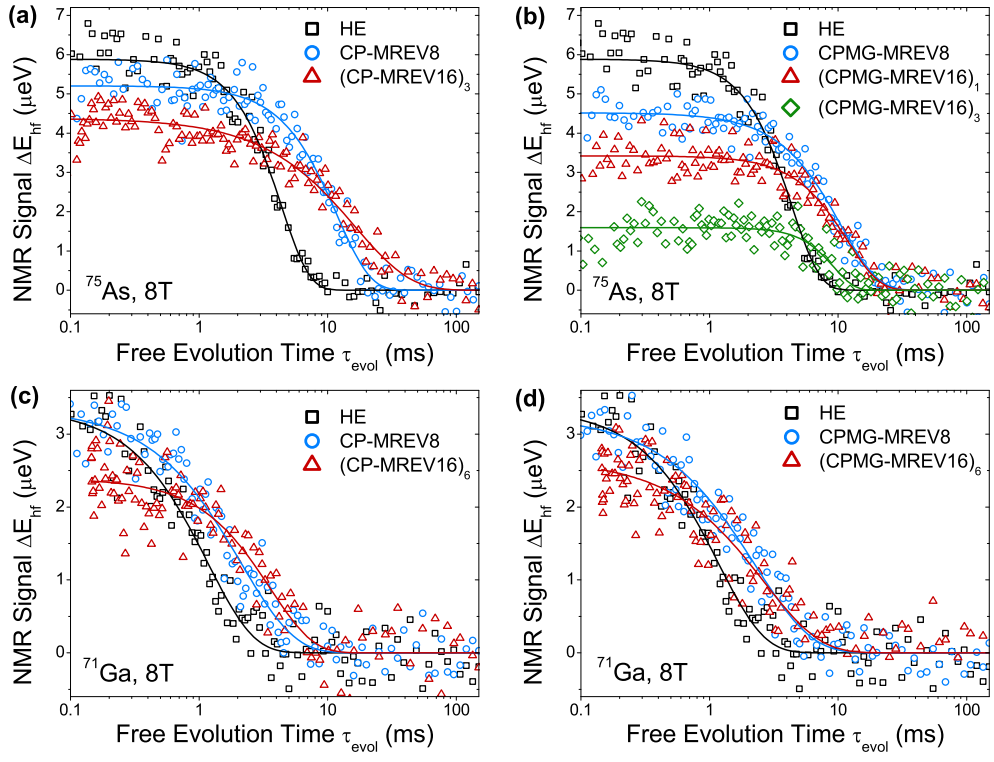

Figure 6.11: Dependence of the ^{75}As (a,b) and ^{71}Ga (c,d) spin echo amplitude ΔE_{hf} on the total free evolution time τ_{evol} under CP-MREV8/16 (a,c) and CPMG-MREV8/16 (b,d). Hahn echo data is shown for comparison (squares). Exponential fits are used to extract decay times (solid lines).

We note that the initial ^{75}As echo amplitude under CP(MG)-MREV8 is reduced by $\sim 15-20\%$ compared to the Hahn echo amplitude. A further decrease in

amplitude is observed under the symmetrised CP(MG)-MREV16 sequence, which in the case of CPMG-MREV16 makes cycle numbers $n_c > 3$ infeasible for ^{75}As. By contrast, in the ^{71}Ga measurements we only see a small change in $\Delta E_{hf}(0)$ after $n_c = 6$ cycles of CP(MG)-MREV16 (corresponding to 120 individual pulses). This is in agreement with our interpretation that the reduced echo amplitudes are due to the sensitivity of the sequence to resonance offsets, as the ^{71}Ga CT is narrower than that of ^{75}As ($\Delta\nu_{inh}(^{71}\text{Ga}) \approx 8$ kHz).

Nuclear spin decoherence times $T_{2,n}$ for different cycle numbers n_c are extracted from compressed exponential fits to the data with equation (6.17) (shown as solid lines in figures 6.11).

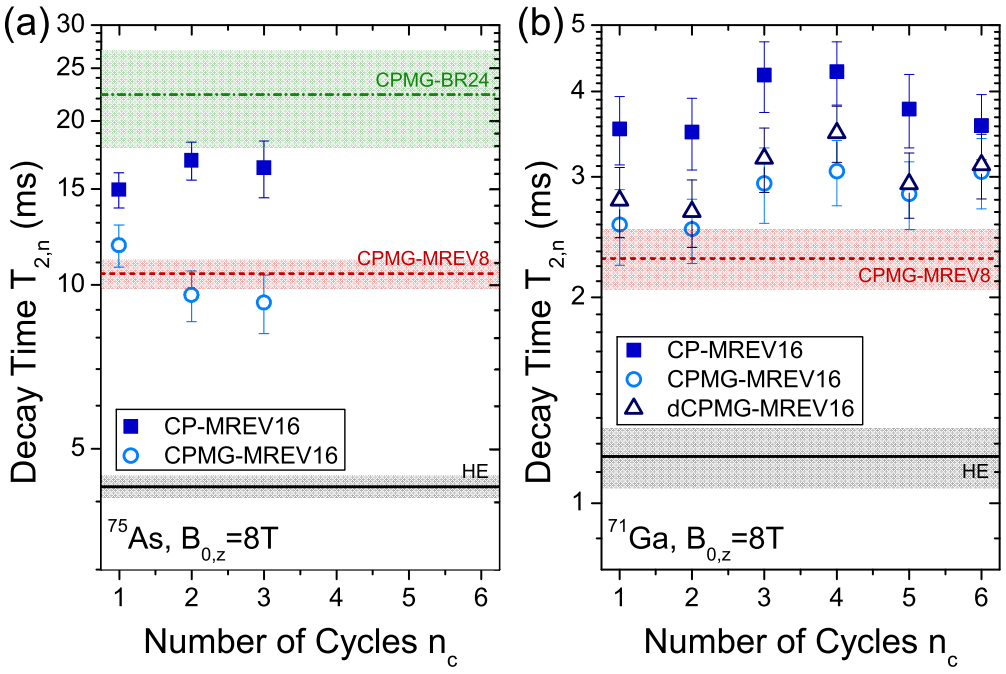

Figure 6.12: Dependence of the fitted exponential decay time $T_{2,n}$ on the cycle number n_c for ^{75}As (a) and ^{71}Ga (b) under CP-MREV16 (solid squares) and CPMG-MREV16 (open circles). Additional results for ^{71}Ga under dCP-MREV16 are marked by triangles in (b). Horizontal lines show decay times under Hahn echo (solid), CPMG-MREV8 (dashed) and CPMG-BR24 (dash-dotted) for comparison. Error bars and shaded areas indicate 90% confidence intervals.

Figures 6.12a and b show the respective extracted ^{75}As and ^{71}Ga decoherence times $T_{2,n}$ as a function of the CP(MG)-MREV16 cycle number n_c. Solid and dashed

lines show the respective Hahn echo and CPMG-MREV8 decoherence times for both isotopes for comparison, with shaded areas marking the associated 90% confidence intervals. Figure 6.12a also shows the ^{75}As decoherence time under CPMG-BR24 (dash-dotted line). An analogous experiment on ^{71}Ga was inconclusive due to the strong reduction of the echo amplitude.

As discussed for ^{75}As in the previous section, we observe a continuous increase of the measured decoherence time $T_{2,n}$ as the combined echo sequences become longer and more complex. By contrast, multiple repetitions of the CP(MG)-MREV16 cycle do not have a noticeable effect on the measured $T_{2,n}$. However, we note that for both isotopes the echo decay times under CP-MREV16 (squares) are consistently longer than those under CPMG-MREV16 (circles). Additional results for ^{71}Ga under dCP-MREV16 (triangles) are found to lie between these two values for all studied cycle numbers n_c, indicating that the magnitude of the $\hat{e}_\mathrm{x}$ component of the initial pulse rotation axis is linked to this inconsistency.

We find that this is indeed the case as the CP-MREV16 decay time is increased beyond the real $T_{2,\mathrm{n}}$ value by a spin-locking effect. This is demonstrated experimentally by conducting additional $(\text{CP-MREV16})_6$ measurements on ^{71}Ga at different rf input powers. All experiments presented so far were obtained at an rf power $P_\mathrm{rf} = 200$ W corresponding to a ^{71}Ga CT NMR Rabi period $T_\mathrm{Rabi} = 5.54$ μs (see section 6.3.1). We saw in the APCP experiments of the previous section that the pulsed spin locking mechanism leading to prolonged nuclear spin decay times depends on the relative timescales of pulse duration t_p and pulse spacing τ. Therefore, we expect the spin locking effect to become stronger for longer t_p and low power P_rf.

Figure 6.13 shows ^{71}Ga nuclear spin echo decay curves under $(\text{CP-MREV16})_6$ for three different rf powers. In addition to the measurements at $P_\mathrm{rf} = 200$ W ($T_\mathrm{Rabi} = 5.54$ μs, squares) which were already shown in figure 6.11c, we measure decay times at $P_\mathrm{rf} = 80$ W ($T_\mathrm{Rabi} = 8.66$ μs, circles) and $P_\mathrm{rf} = 50$ W ($T_\mathrm{Rabi} = 9.56$ μs, triangles) where the pulse durations t_p are almost twice as long. A pronounced slow-

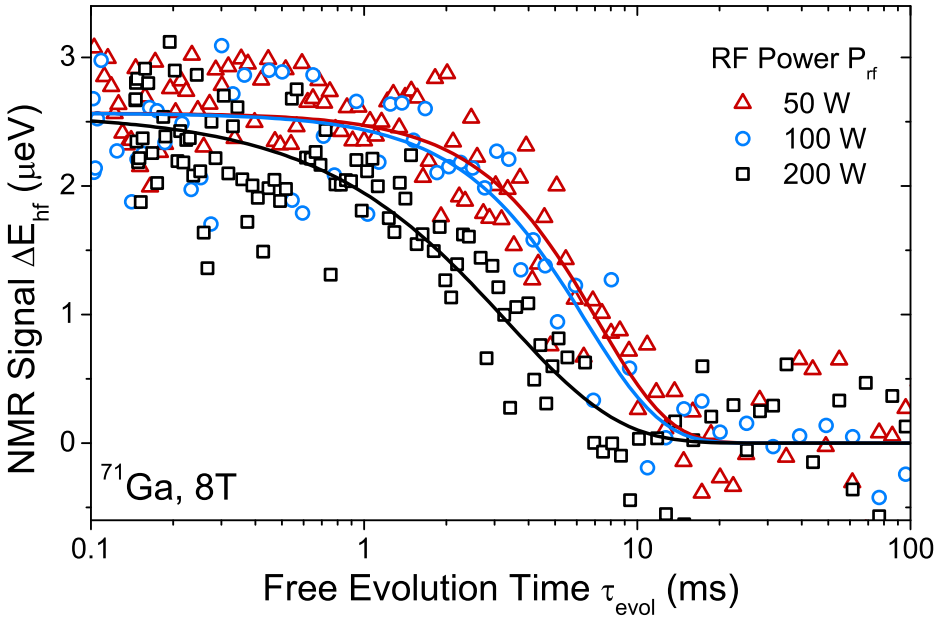

Figure 6.13: Decay of the ^{71}Ga spin echo amplitude under $(\text{CP-MREV16})_6$ as a function of the free evolution time τ_{evol}. Data sets correspond to different fixed rf input powers. Solid lines show exponential fits to the data.

down of the decay from $T_{2,\text{n}}^{200\text{W}}(^{71}\text{Ga}) = 3.34\pm0.39$ ms to $T_{2,\text{n}}^{50\text{W}}(^{71}\text{Ga}) = 7.20\pm0.71$ ms revealed by fitting confirms our earlier interpretation of spin locking due to finite pulse durations.

We therefore focus on the CPMG-MREV16 results for which no such power dependence is observed. The ^{75}As decoherence time under a single cycle of this sequence is $T_{2,\text{n}}^{\text{MREV16}}(^{75}\text{As}) = 11.85 \pm 1.04$ ms, which is a factor of three longer than the Hahn echo phase memory time. Similarly, we observe an increase of the ^{71}Ga decoherence time $T_{2,\text{n}}^{\text{MREV16}}(^{71}\text{Ga}) = 2.79 \pm 0.20$ ms by a factor of 2.5 compared to the corresponding Hahn echo decay time.

We can summarise our experimental results as follows: application of CPMG-MREV16 does lead to a noticeable increase in the measured nuclear spin echo decay time for both of the isotopes studied. However, no further increase of $T_{2,\text{n}}$ is observed upon repetition of the cycle. In addition, although the CPMG-BR24 cycle has a strongly reduced initial spin echo amplitude, it gives ^{75}As spin decoherence times which are twice as along as those observed under CPMG-MREV16.

This leads us to several conclusions. Firstly, the combined echo sequences can indeed suppress the homonuclear dipolar interactions in the quantum dot nuclear spin bath in addition to refocusing the dephasing due to inhomogeneous quadrupolar broadening. Secondly, the absence of further increase of $T_{2,\mathrm{n}}$ at larger cycle numbers n_c implies that the spin bath dynamics do not contain fast-fluctuating components and are fully refocused by CPMG-MREV16 within the cycle times $t_\mathrm{c} \lesssim T_{2,\mathrm{n}}^{\mathrm{MREV16}}$. As discussed in section 6.4.1, the only relevant source of fluctuations in a charge-free quantum dot is heteronuclear coupling, which is quasistatic due to the quenched homonuclear dipolar flip-flop term (see chapter 5 and [41]). Therefore, excluding other unidentified noise sources, we can assume the studied spin sub-ensemble to be effectively decoupled from its environment by the combined echo sequences.

Finally, the continuous increase of the measured $T_{2,\mathrm{n}}$ from CPMG-WAHUHA to CPMG-BR24 shows that the nuclear spin bath decoherence is suppressed further by more complex sequences. This is in agreement with the results of our AHT calculations as the longer sequences eliminate more higher-order terms of the average Hamiltonian (see discussion in section 6.2.3). Unfortunately, this comes at the cost of reduced echo amplitudes due to the higher sensitivity of complex sequences to pulse errors, an effect we will discuss in more detail in the next section.

6.5.3 Offset Sensitivity of Combined Echo Amplitudes

In the combined echo experiments presented in the preceding sections, we noticed repeatedly that the ^{75}As initial echo amplitudes $\Delta E_{\mathrm{hf}}(0)$ were reduced compared to the Hahn echo amplitude. By contrast, these effects were far less pronounced in experiments on ^{71}Ga. To understand this behaviour, we simulate the resonance offset dependent evolution of a magnetisation vector $\boldsymbol{M} = M_\mathrm{z}\hat{e}_\mathrm{z}$ under the combined echo sequences using the same model as in section 6.4.3. We assume once more that the evolution is well described by the Bloch equations of motion and set $T_1 = T_2 = \infty$.

Figures 6.14a and b show the normalised magnetisation $M_\mathrm{z}/M_\mathrm{z}(0)$ after one, three

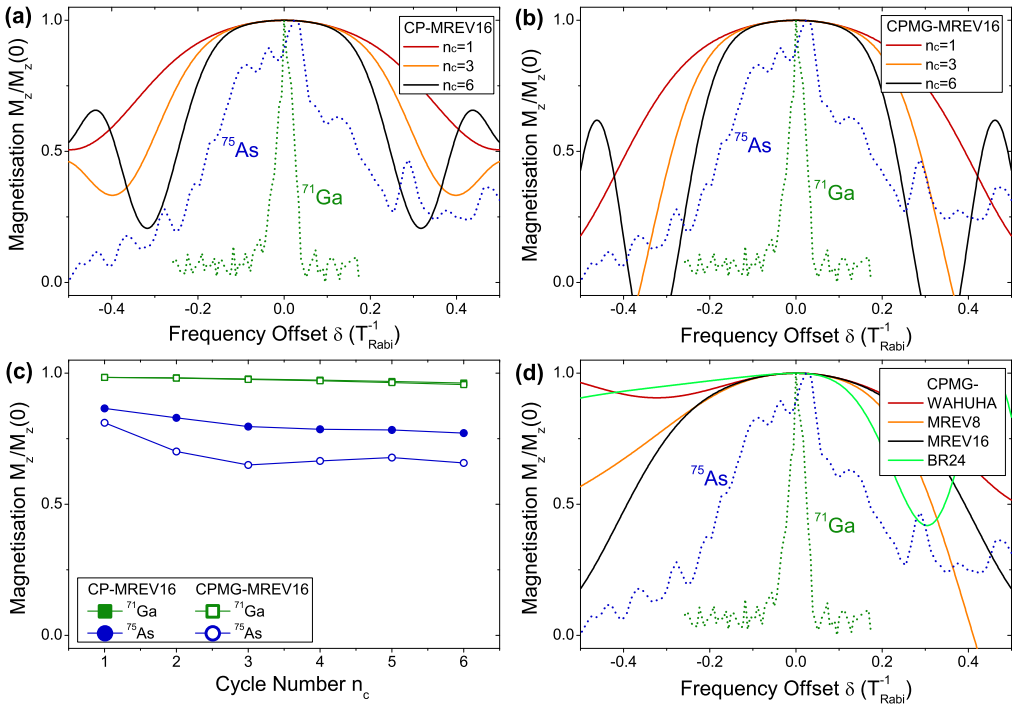

Figure 6.14: (a,b) Dependence of the normalised magnetisation along $\hat{e}_z$ on the resonance frequency offset δ under CP-MREV16 (a) and CPMG-MREV16 (b). Solid curves show simulations for different pulse cycles n_c. Dashed lines show normalised ^{75}As and ^{71}Ga CT spectra with rescaled frequency axes for $P_{rf} = 200$ W. (c) Weighted average of the normalised magnetisation over the ^{75}As (circles) and ^{71}Ga (squares) CT resonance as a function of the CP(MG)-MREV16 cycle number n_c. (d) Simulation of the offset-dependent normalised magnetisation under a single cycle of different combined echo sequences.

and six cycles of CP(MG)-MREV16 as a function of the resonance frequency offset δ. As before, the offset is normalised by the inverse resonant Rabi period T_{Rabi}^{-1}. For comparison, normalised ^{75}As and ^{71}Ga CT NMR spectra are included. Here the resonance offset is rescaled by T_{Rabi}^{-1} at the rf power $P_{rf} = 200$ W used in our experiments (with exception of the spin locking experiments shown in figure 6.13). The simulations show that the offset tolerance under both sequences decreases with increasing cycle number n_c. For a fixed n_c, CPMG-MREV16 is less robust against frequency offsets than CP-MREV16, although the difference is small. Figure 6.14c shows weighted averages of $M_z/M_z(0)$ over the CT resonances of ^{75}As and ^{71}Ga as a function of n_c for both pulse sequences. The simulations are in qualitative agreement

with our experimental observations in figures 6.11: the ^{71}Ga initial echo amplitude is fully restored ($M_z/M_z(0) \approx 1$) even after $n_c = 6$ cycles of either sequence. For ^{75}As, the offset sensitivity of CP(MG)-MREV16 results in a reduced echo amplitude even after a single cycle, with further decrease observed at larger n_c.

In addition, we simulate the offset-dependence of the normalised magnetisation under the CPMG-WAHUHA, CPMG-MREV8 and CPMG-BR24 sequences which we had tested experimentally on ^{75}As (see section 6.5.1). The results of these simulations are shown in figure 6.14d. We note that all sequences except CPMG-MREV16 (black) show an asymmetric offset-dependence. As we remarked in section 6.4.3, this is a feature which we observe for all sequences that are containing pulses with orthogonal carrier phases and without time reversal symmetry. From comparison with the simulated curves for CP(MG)-MREV16, it is not clear why the CPMG-BR24 echo amplitude in section 6.5.1 is strongly reduced compared to those of CPMG-WAHUHA and CPMG-MREV8. In fact, weighted averages of the magnetisation over the ^{75}As CT resonance predict amplitudes $M_z/M_z(0) \approx 0.75 - 0.9$ for all of the sequences displayed in figure 6.10. We therefore conclude that additional factors such as pulse duration and phase errors must have a non-negligible influence on the echo amplitude under CPMG-BR24.

6.6 Conclusions

In conclusion, we have explored two routes towards increasing the nuclear spin bath coherence in an InGaAs quantum dot by using multiple pulse NMR techniques. We used CP and CPMG sequences (π pulse trains) with alternating phases (AP) to decouple a spin sub-ensemble of $\sim 10^4 - 10^5$ nuclei $\boldsymbol{I}_n$ from its environment. Instead of the expected suppression of time-dependent heteronuclear dipolar interactions with the remaining nuclear spin sub-bath $\boldsymbol{J}_m$, we observed a surprisingly strong increase of the measured nuclear spin phase memory time under APCP up

to $T_{\mathrm{M,n}}^{\mathrm{APCP}}(^{75}\mathrm{As}) = 19.3 \pm 2.0$ ms and $T_{\mathrm{M,n}}^{\mathrm{APCP}}(^{71}\mathrm{Ga}) = 5.04 \pm 0.67$ ms for large pulse numbers. We were able to attribute this fourfold to fivefold increase compared to the corresponding Hahn echo decay times to a form of spin locking arising from evolution of the spin bath during the finite rf pulse duration[260]. Such spin locking effects masking the suppression of heteronuclear dynamics are neither predicted nor observed for APCPMG. However, the sensitivity of this sequence to resonance frequency offsets makes further studies of heteronuclear decoupling infeasible within our experimental limits. A promising direction for future experiments could be the use of Uhrig dynamical decoupling sequences[236] which do not share the strict periodicity of the CP and CPMG sequences and which are very robust against pulse errors[238].

A second set of experiments was aimed towards full suppression of the decoherence in a nuclear spin ensemble $\boldsymbol{I}_n$ due to both intrinsic homonuclear interactions and inhomogeneous broadening with a single multiple pulse sequence. We designed several combined Hahn and solid echo sequences which can eliminate both inhomogeneous and homonuclear dipolar dephasing. Experimentally, we observed an increase of the spin bath coherence under all tested combined echo sequences, reaching coherence time values of up to $T_{2,\mathrm{n}}^{\mathrm{BR24}}(^{75}\mathrm{As}) = 22.4 \pm 4.5$ ms for ^{75}As. We saw that $T_{2,\mathrm{n}}$ increases continuously with increasing sequence complexity, which indicates that the real spin bath coherence times are even longer and the observed values are limited by non-vanishing higher-order AHT terms. In principle, it would be possible to design longer and more complex combined echo sequences which will increase the control over the nuclear spin bath evolution even further. However, as we saw for the CPMG-BR24 sequence, longer sequences become increasingly sensitive to pulse and frequency offset errors, making them impractical for realistic experimental conditions.

The CPMG-MREV16 sequence with decoherence times $T_{2,\mathrm{n}}^{\mathrm{MREV16}}(^{75}\mathrm{As}) = 11.85 \pm 1.04$ ms and $T_{2,\mathrm{n}}^{\mathrm{MREV16}}(^{71}\mathrm{Ga}) = 2.79 \pm 0.20$ ms offers a good compromise by increasing

the spin bath coherence considerably without reducing the echo amplitude noticeably. Further improvements may be feasible if the coupling between the spin bath and the rf field can be increased, e.g. with an on-chip antenna. In this case, stronger field amplitudes would lead to shorter Rabi periods, increasing the robustness of the combined echo sequences against frequency offsets due to the inhomogeneous NMR spectral linewidths of $\sim 10 - 40$ kHz.

In experiments using multiple cycles of CPMG-MREV16 we observed no significant change of the measured $T_{2,\mathrm{n}}$. This indicates that the environment sub-bath $\boldsymbol{J}_m$ evolves slowly and the time-dependent heteronuclear dipolar dephasing of the $\boldsymbol{I}_n$ spins is fully refocused within the probed free evolution times.

Summarising, the combined Hahn and solid echo sequences introduced in this chapter can increase the coherence of the nuclear spin bath beyond the Hahn echo limit. We expect that further improvements can be made by optimising the coupling to the rf magnetic field. Furthermore, the use of composite pulses, while difficult to implement in our experimental framework due to the requirement of phase shifts during the pulse duration t_{p}, could improve the robustness against pulse calibration errors[264–266] and make the use of longer sequences such as BR-24 feasible. This opens the way for spin qubits in quantum dots with a coherent, predictably evolving nuclear spin environment which can be decoupled using electron (hole) spin echo techniques[174, 178, 204, 225].

7 Spin Bath Correlation Times in Self-Assembled Quantum Dots

7.1 Introduction

An InGaAs quantum dot system consists of an ensemble of $\sim 10^5$ nuclei with spin $I \geq \frac{3}{2}$. As we saw in chapter 5, strong quadrupolar interactions give rise to inhomogeneous broadening on the order of $10 - 100$ kHz for the nuclear spin CTs in inverse NMR (see figure 5.7). Even broader spectra with inhomogeneous broadening $\Delta\nu_{\text{inh}} \approx 1 - 10$ MHz have been measured for STs using the same technique (see figure 5.1b and [39]). This severely limits the amount of information that can be gained from conventional cw NMR experiments as the homogeneous lineshapes and coherence properties of the system are masked by fast dephasing.

The most common method for removing inhomogeneous NMR lineshape broadening is the use of nuclear spin echo techniques. We have shown in chapter 5 that it is possible to refocus the quadrupolar dephasing of the CT under a Hahn echo sequence[41]. However, we also saw in chapter 6 that pulsed NMR techniques have their own drawbacks: spin locking effects caused by calibration errors[257, 259] or by dipolar evolution during the finite pulse duration[260] can result in long-lived spin echoes unrelated to spin decoherence. Furthermore, the pulse powers required for coherent driving of a full transition can quickly become unattainable for inhomogeneously broadened spin ensembles. We saw in the previous chapter

that the performance of most multiple pulse sequences is limited by their tolerance against frequency offsets even for the ^{75}As and ^{71}Ga CTs at rf input powers of $P_{\mathrm{rf}} \approx 200$ W ($B_1 \approx 7$ mT). For the pulsed manipulation of an ^{75}As ST, we would require magnetic field amplitudes $B_1 \gtrsim 0.5$ T, corresponding to infeasible pulse powers of $\gtrsim 1$ MW. This can be handled to some extent by employing alternative methods of coherent manipulation such as adiabatic plane rotation pulses[267]. However, these techniques require complex composite pulses involving simultaneous amplitude, frequency and phase modulation. In addition, the adiabatic pulses can modify the intrinsic spin-bath interactions in non-trivial ways and directly affect the measured coherence times (see e.g. [268]).

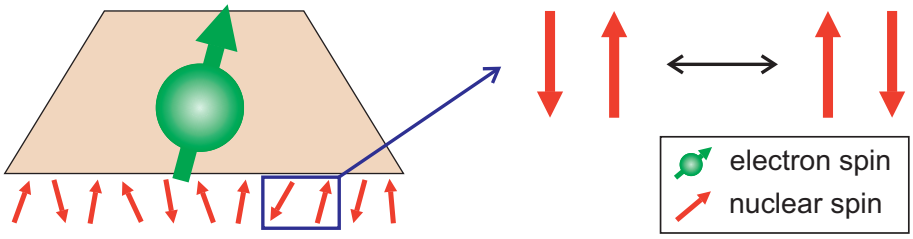

Figure 7.1: The electron spin coherence is only affected by spin bath fluctuations due to the nuclear spin flip-flop term. It is not influenced by the diagonal nuclear-nuclear dipolar term $\propto I_{n,\mathrm{z}} I_{m,\mathrm{z}}$.

In a similar way, the influence of the instantaneous diffusion due to the diagonal term of the homonuclear dipolar interaction ($\propto I_{n,\mathrm{z}} I_{m,\mathrm{z}}$) makes it very difficult to obtain the spin bath correlation times τ_{c} which limit the central spin coherence from a pulsed echo measurement[41, 209]. This is a conceptual drawback of spin echoes: the initial $\frac{\pi}{2}$ pulse prepares the nuclear spin ensemble in a state with large transverse magnetisation which is a superposition of eigenstates with a broad spread of energies. The spin dynamics in this state are characterised by $T_{\mathrm{M,n}}$, with a strong contribution from the instantaneous diffusion term. By contrast, the coherence of a central spin interacting with the nuclear spin bath is only affected by the off-diagonal nuclear spin flip-flop term[29, 177, 197] (see figure 7.1), which is characterised by τ_{c} and which is much longer than $T_{\mathrm{M,n}}$. In short, pulsed NMR is a powerful tool for controlling

the nuclear spin bath and creating a predictable environment for a confined charge spin qubit. However, it is not well suited for non-invasive measurements aimed at characterising the bath fluctuation timescales which limit the central spin coherence.

In this chapter, we introduce a novel cw NMR technique which allows us to probe the coherent dynamics of an inhomogeneously broadened nuclear spin ensemble in a weakly-invasive measurement. We adopt a *frequency comb* rf excitation profile as used in optical metrology[269, 270] to measure the homogeneous NMR lineshapes of ^{75}As and ^{71}Ga. This technique is highly sensitive to intrinsic and artificially induced fluctuations in the spin environment of the probed ensemble, allowing us to measure extremely long nuclear spin correlation times $\tau_c > 1$ s in an empty InGaAs quantum dot[271].

We discuss the experimental implementation of the frequency comb technique in section 7.2. The capability of this technique to extract the homogeneous spectral linewidth and lineshape of an isotope is demonstrated in section 7.3. We then explore the potential of frequency comb NMR by artificially restoring the spin flip-flop mechanism for ^{71}Ga and detecting its influence on the ^{75}As lineshape in section 7.4. This concept is taken further in section 7.5, where we adopt a three-comb NMR scheme to extract the spin bath correlation times τ_c determined by the intrinsic homonuclear dipolar flip-flop timescales.

7.2 Methodology

For the ODNMR experiments presented in this chapter we use the optical pump-rf-probe scheme introduced in chapter 4.3.2. Measurements are performed on individual empty quantum dots in samples A and B in an external magnetic field $B_{0,z} = 8$ T. In this section, we only address those experimental aspects which are unique to the frequency comb experiments. The experimental implementation of rf frequency combs is discussed in section 7.2.1 before we briefly look at the pump-

probe measurement cycle in section 7.2.2. Finally, the calibration of the central frequency comb parameters is discussed in section 7.2.3.

7.2.1 Experimental Implementation of RF Frequency Combs

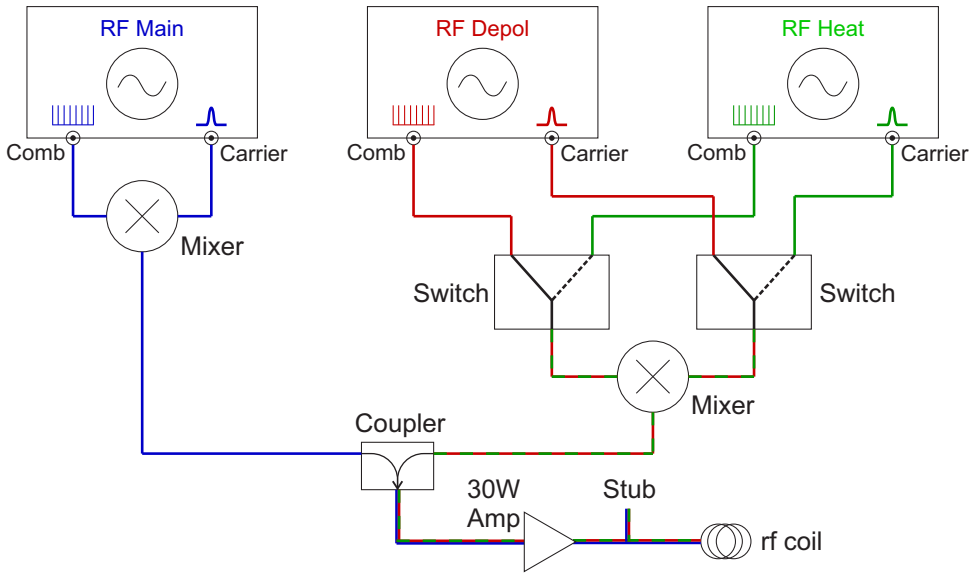

Figure 7.2: Diagram of the frequency comb rf circuit: the primary rf excitation comb (blue) is formed by mixing a carrier with the comb waveform and sent to the broadband matched coil via a 30 W class A amplifier. Additional frequency combs (red and green) are added in later experiments for the rf excitation of more than one isotope.

Each rf frequency comb is characterised by a spectral comb width $\Delta\nu_{\mathrm{comb}}$ and a fixed spectral separation f_{MS} between neighbouring modes. The total number of modes in a frequency comb is therefore given by $N_{\mathrm{m}} = \Delta\nu_{\mathrm{comb}}/f_{\mathrm{MS}} + 1$. In the experiments presented in this chapter, mode spacings in the range of 30 Hz to 21 kHz are used, corresponding to $N_{\mathrm{m}} \sim 330 - 600000$. Each individual mode j is described by its frequency ν_j and phase φ_j and all N_{m} modes have the same amplitude B_1. The phases φ_j are chosen such that the peak-to-average amplitude ratio (crest factor) of the frequency comb waveform is minimised. This is the case for

$$B_{\mathrm{rf}}(t) = B_1 \sum_{j=1}^{N_{\mathrm{m}}} \cos\left(2\pi(\nu_1 + (j-1)f_{\mathrm{MS}})t + \pi\frac{j(j+1)}{N_{\mathrm{m}}}\right) , \tag{7.1}$$

where ν_1 is the frequency of the first comb mode and B_{rf} is the rf amplitude of the full comb. The frequency comb waveforms are created in Mathematica and stored in the memory of an arbitrary waveform generator. Full combs are formed analogous to the implementation of adiabatic sweeps in chapter 5.4: the waveform signal of bandwidth $\Delta\nu_{\mathrm{comb}}/2$ is mixed with a carrier $\nu_{\mathrm{comb},0}$ centred on the CT of the probed isotope, creating a full frequency comb profile overlapping with the inhomogeneously broadened NMR resonance. The rf signal is amplified by a 30 W class A power amplifier and sent to the rf coil. Our rf circuit cannot be matched for the broad frequency bands of the combs used here. However, we can tune the rf circuit such that the (mismatched) transmission over the full comb width is flat within ~ 2 dB (see figure 4.5b).

Figure 7.2 depicts the full rf circuit for application of up to three separate frequency combs. The *RF Main* comb (blue) is used for depolarisation of the probed isotope in all subsequent measurements. For experiments requiring the depolarisation of a second isotope (see section 7.4), the *RF Depol* comb (red) is added. Further experiments involve the additional "heating" of a single NMR transition of the depolarised second isotope (section 7.5). This is achieved by switching between the *RF Depol* and *RF Heat* combs. Details of all waveforms are given in table 7.1 and in the respective experimental sections. The outputs of all three generators and both switches are gated by a master generator which clocks the full experiment cycle.

7.2.2 Optical Pump-Probe Measurement

The pump-rf-probe scheme of chapter 4.3.2 is adopted once more for the frequency comb measurements. A full experiment cycle is depicted in figure 7.3: a high power, σ^- circularly polarised optical pump pulse is applied in resonance with the quantum dot wetting layer ($\sim$ 850 nm) to polarise the nuclear spin bath via DNP at the beginning of each experiment cycle (green trace). As we are studying the same quantum dots as in the previous sections, we use the pump pulse time $t_{\mathrm{pump}} = 6.5$ s

obtained in the calibration measurements of chapter 5.3.2.

In the single comb experiments, rf excitation with the *RF Main* comb follows next (blue trace). The comb is applied continuously for an rf excitation time t_{rf} which is varied over several orders of magnitude ($\sim 10^{-4} - 10^{2}$ s) for each set of measurements. In the two- and three-comb experiments, the *RF Depol* comb is applied to a second isotope. This comb is gated in antiphase to *RF Main* and fully depolarises the second isotope during a time t_{depol} before the *RF Main* comb is switched active (red trace). The *RF Heat* comb is tailored to selectively drive a single transition of the depolarised second isotope during t_{rf} and accordingly is gated synchronously with the primary comb.

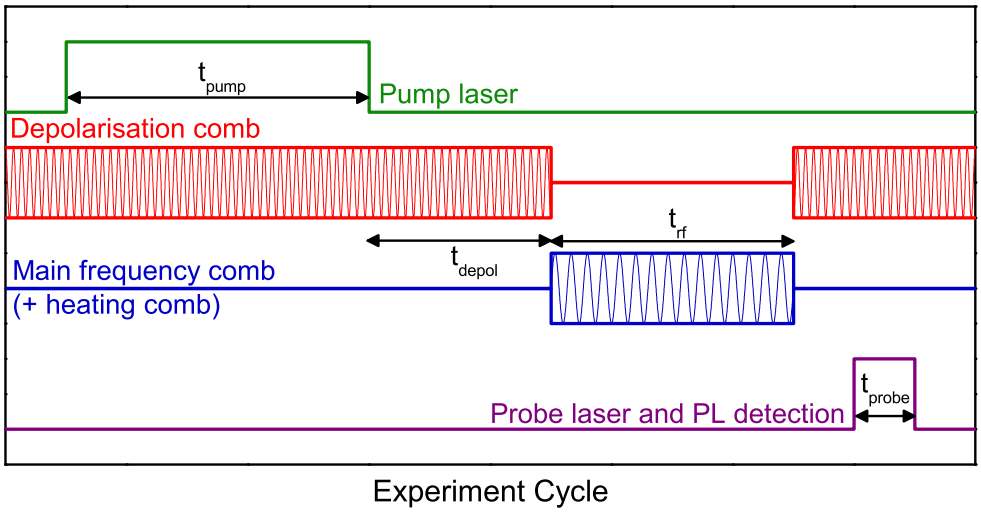

Figure 7.3: The experiment cycle for frequency comb measurements follows the pump-rf-probe scheme of the previous chapters. In two- and three-comb measurements, a second isotope is depolarised using the *RF Depol* for t_{depol} before the main comb and an optional third heating comb are applied.

The remaining magnetisation after rf excitation is probed non-resonantly in PL with a low power, linearly polarised laser for a dot-dependent time t_{probe} (purple trace). As we are interested in the change of the nuclear spin polarisation in the quantum dot induced by the rf frequency comb (change in the Overhauser shift ΔE_{hf}), we perform a second measurement in which the *RF Main* comb (as well as

the *RF Heat* comb in three-comb measurements) is switched off. Then the change in E_{hf} is given by the difference between the respective measured exciton Zeeman splittings where $\Delta E_{\mathrm{hf}} = 0$ corresponds to no rf-induced nuclear spin depolarisation.

7.2.3 Parameter Calibration

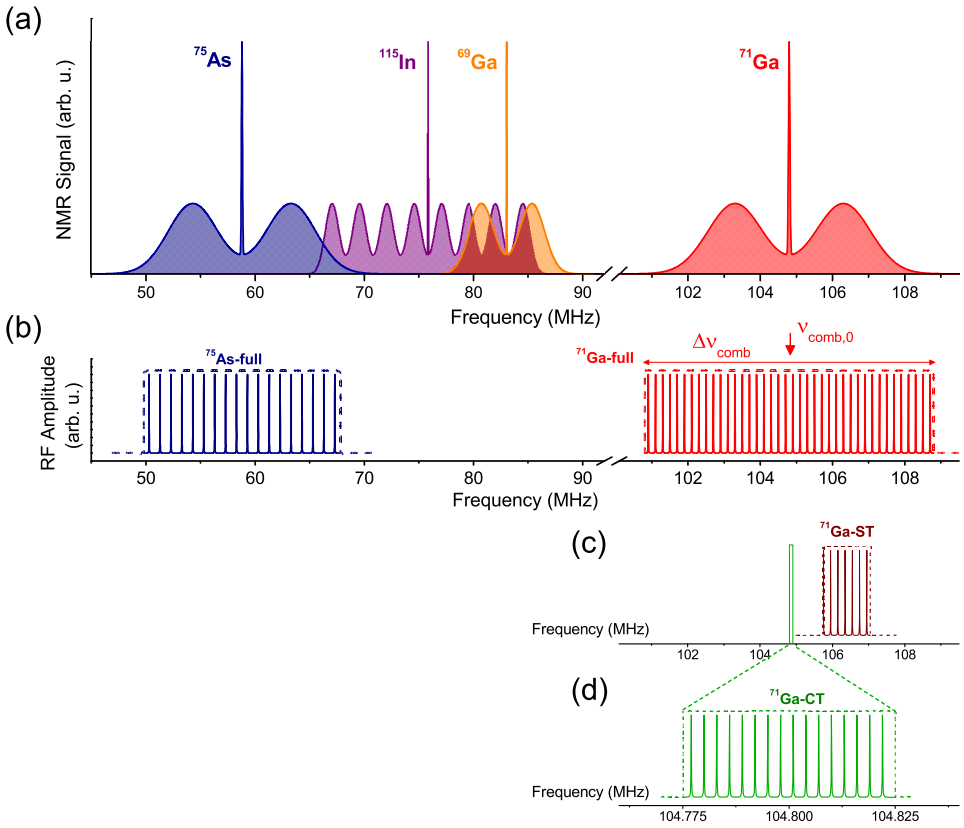

Figure 7.4: Schematic of the frequency combs used in the experiments of sections 7.3-7.5. (a) Sketch of the full NMR spectrum in a self-assembled InGaAs quantum dot at $B_{0,\mathrm{z}} = 8$ T (see figure 5.1b for experimental data). (b)-(d) Frequency combs used in the experiments: the ^{75}As-full and ^{71}Ga-full combs excite the respective full inhomogeneously broadened lineshapes. By contrast, the ^{71}Ga-ST comb selectively excites the $+1/2 \leftrightarrow +3/2$ ^{71}Ga ST and the ^{71}Ga-CT comb overlaps with the $-1/2 \leftrightarrow +1/2$ ^{71}Ga CT. The respective comb parameters are listed in table 7.1 below.

Each frequency comb is tailored to excite either a single CT/ST or the full inhomogeneously broadened NMR spectrum of a given isotope as illustrated in figure 7.4. Hence we have to choose the comb width $\Delta\nu_{\mathrm{comb}}$ and central frequency $\nu_{\mathrm{comb},0}$

accordingly. We already measured the resonance frequencies for the CTs of ^{75}As and ^{71}Ga at $B_{0,z} = 8$ T in chapter 5.4.1 using inverse NMR. In principle, this technique can also be used to measure the full inhomogeneous NMR spectra including the STs as has been shown in [39] (see figure 5.1b).

(a) Homogeneous NMR lineshape experiments (section 7.3, sample B):				
Isotope	^{75}As	^{71}Ga		
Frequency comb	^{75}As-full	^{71}Ga-full		
Central frequency $\nu_{\mathrm{comb},0}$ (MHz)	58.81	104.80		
Comb width $\Delta\nu_{\mathrm{comb}}$ (MHz)	18	9		
Mode spacing f_{MS} (Hz)	varied	varied		
Rf field density β_1 (nT/$\sqrt{\mathrm{Hz}}$)	65.5	39.1		
(b) Line broadening experiments (section 7.4, sample A):				
Isotope	^{75}As	^{71}Ga		
Frequency comb	^{75}As-full	^{71}Ga-full		
Central frequency $\nu_{\mathrm{comb},0}$ (MHz)	58.81	104.80		
Comb width $\Delta\nu_{\mathrm{comb}}$ (MHz)	18	8		
Mode spacing f_{MS} (Hz)	varied	159		
Rf field density β_1 (nT/$\sqrt{\mathrm{Hz}}$)	30.5	27.6		
(c) Extracting spin bath correlation times (section 7.5, sample A):				
Isotope	^{75}As	^{71}Ga	^{71}Ga	^{71}Ga
Frequency comb	^{75}As-full	^{71}Ga-full	^{71}Ga-ST	^{71}Ga-CT
Central frequency $\nu_{\mathrm{comb},0}$ (MHz)	58.81	104.80	106.40	104.80
Comb width $\Delta\nu_{\mathrm{comb}}$ (MHz)	18	8	1.3	0.05
Mode spacing f_{MS} (Hz)	1466	159	150	150
Rf field density β_1 (nT/$\sqrt{\mathrm{Hz}}$)	varied	27.6	varied	varied

Table 7.1: Frequency comb parameters used in the experiments of sections 7.3-7.5.

Here, we use the results of our sweep range calibration measurements instead (see chapter 5.4.2). For sample A, we measure inhomogeneously broadened spectra with $\Delta\nu_{\mathrm{inh}}(^{75}\mathrm{As}) \approx 15$ MHz and $\Delta\nu_{\mathrm{inh}}(^{71}\mathrm{Ga}) \approx 5$ MHz in good quantitative agreement with the findings of inverse NMR studies shown in figure 5.1b and reported in [39] for

another sample from the same wafer. The inhomogeneous NMR spectra in sample B are found to be broader with $\Delta\nu_{\mathrm{inh}}(^{75}\mathrm{As}) \approx 18$ MHz and $\Delta\nu_{\mathrm{inh}}(^{71}\mathrm{Ga}) \approx 7$ MHz. The comb widths $\Delta\nu_{\mathrm{comb}}$ are chosen to cover the ^{75}As and ^{71}Ga spectra fully and are listed in table 7.1. For the three-comb experiments of section 7.5, we also have to choose comb widths and positions for the excitation of individual ^{71}Ga transitions. We choose $\Delta\nu_{\mathrm{inh}}(\mathrm{CT}) = 50$ kHz based on inverse NMR spectra to ensure overlap with the full CT. The ST comb width $\Delta\nu_{\mathrm{inh}}(\mathrm{ST}) = 1.3$ MHz and ST central frequency $\nu_{\mathrm{comb},0} = \nu_{\mathrm{L}}(^{71}\mathrm{Ga}) + 1.6$ MHz are chosen to avoid residual indirect heating of the CT (see detailed discussion in section 7.5.1).

The magnetic field per mode B_1 and corresponding rf field density $\beta_1 = \frac{B_1}{\sqrt{f_{\mathrm{MS}}}}$ are calibrated using a Rabi oscillation measurement on the CT of ^{71}Ga. As we saw in chapter 5.4.3, we can obtain the rf field amplitude from the Rabi period via $B_1 = \frac{1}{2\gamma^* T_{\mathrm{Rabi}}}$. Using a pick-up coil in close proximity to the sample and connected

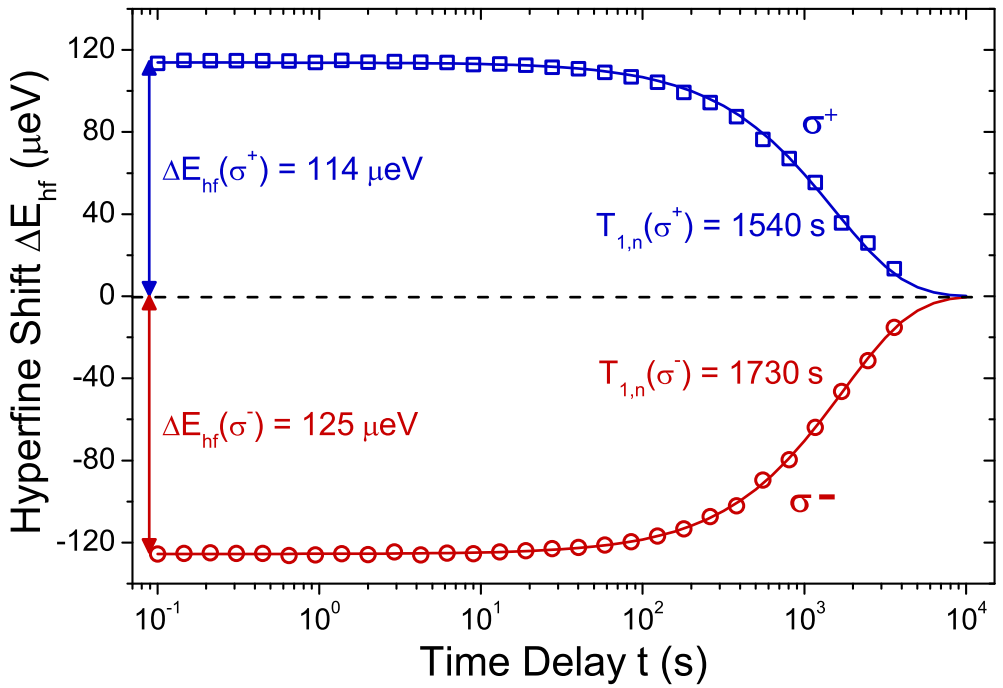

Figure 7.5: Hyperfine shift ΔE_{hf} after maximum negative (circles) or positive (squares) polarisation of the nuclear spin bath as a function of the time delay t. Solid lines show fitting with an exponential decay function with characteristic decay time $T_{1,\mathrm{n}}$.

to a spectrum analyser, we can monitor the transmitted rf fields in all NMR experiments (see chapter 4.3.1). By comparing the voltages induced by the frequency comb modes with the the voltage induced by the coherent rf pulse in the Rabi experiment, we can obtain the corresponding magnetic field amplitude B_1 of each mode.

Finally, we have to take into account that the decay of the hyperfine splitting ΔE_{hf} in our experiments is due to a combination of rf induced depolarisation and intrinsic nuclear spin relaxation. The influence of intrinsic relaxation can be safely ignored for sample B where we have found $T_{1,\mathrm{n}} > 1$ h under large reverse biases (see chapter 5.3.1). While the polarisation in sample A also decays slowly, it becomes non-negligible for long depolarisation times $t_{\mathrm{rf}} \gtrsim 1$ min. Figure 7.5 shows the results of nuclear spin relaxation measurements in sample A at $B_{0,\mathrm{z}} = 8$ T: the nuclear spin bath is maximally polarised with σ^- (circles) and σ^+ (squares) polarised light, respectively, and left to evolve in the dark without rf excitation for a varying time t before a weak optical probe pulse is applied to measure the remaining bath polarisation. From exponential fitting of the hyperfine shift dependence on the time delay t (solid), we obtain nuclear spin relaxation times $T_{1,\mathrm{n}}(\sigma^-) \approx 1730$ s and $T_{1,\mathrm{n}}(\sigma^+) \approx 1540$ s.

7.3 Probing Homogeneous NMR Lineshapes with Frequency Combs

As we will show in this section, the nuclear spin depolarisation times under excitation with rf frequency combs are very sensitive to the mode spacing f_{MS}. In part 7.3.1, we introduce the working principle of frequency comb NMR and illustrate how this technique can extract the narrow homogeneous linewidth $\Delta\nu_{\mathrm{hom}}$ from the strongly inhomogeneously broadened spectrum. We then look at the experimental results of mode spacing and depolarisation time dependent frequency comb measurements (section 7.3.2) before showing how an accurate model of the homogeneous NMR

lineshape can be obtained from these results in section 7.3.3. In the last part 7.3.4 we will discuss the validity of the assumptions made in this model and look at the applicability of the frequency comb technique.

7.3.1 Working Principle of the Frequency Comb Technique

An inhomogeneously broadened NMR spectrum is formed by the sum of a large number of homogeneous spectra with varying frequency offsets from the central resonance frequency ν_L (see figure 7.6a). This can be either the sum over long acquisition times in the NMR measurement of a single spin transition or an ensemble spectrum for the simultaneous probing of a large number of nuclei. In the first case, the homogeneous spectrum can be measured e.g. by reducing the measurement time towards the single-shot limit[272, 273]. The analogous approach to counter-

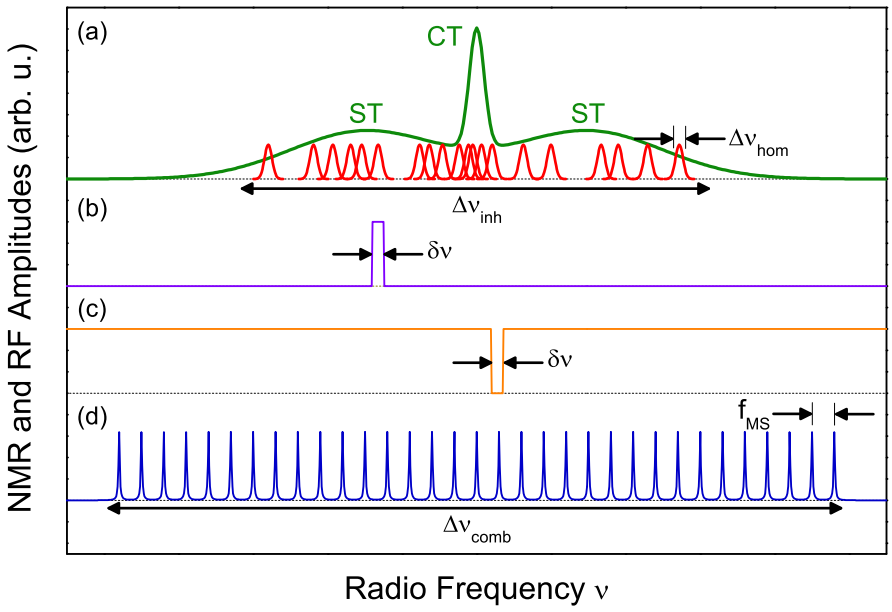

Figure 7.6: (a) The inhomogeneously broadened NMR spectrum (green line, $\Delta\nu_{\mathrm{inh}}$) is formed by a large number of individual nuclear spin transitions with linewidths $\Delta\nu_{\mathrm{hom}}$ (red lines). (b)-(c) RF excitation profiles used for cw NMR techniques: conventional saturation spectroscopy (violet line) with rf excitation window $\delta\nu$ (b), inverse NMR spectroscopy (orange line) with broadband excitation except for a gap $\delta\nu$ (c) and frequency comb NMR (blue line) with comb width $\Delta\nu_{\mathrm{comb}}$ and mode spacing f_{MS} (d).

ing ensemble broadening would be a reduction of the sample volume, which would come at great cost to the detection sensitivity. A more common way for removing inhomogeneous broadening in NMR spectroscopy are spin echoes[41, 199, 226]. However, as mentioned in the introduction and observed in the previous chapters, pulsed NMR techniques are hampered by artefacts which can obscure the intrinsic lineshape[260, 274].

Instead, we use the frequency comb technique which allows us to probe the full homogeneous lineshape of an arbitrarily broadened spin ensemble under weak, non-coherent rf excitation. In conventional saturation cw NMR, the spin sub-ensemble within a finite frequency window $\delta\nu$ (figure 7.6b) or, in the case of inverse NMR[39], a broad frequency band except for an isochrome $\delta\nu$ (figure 7.6c) is depolarised under high power rf excitation. By contrast, we now employ rf excitation in the shape of a frequency comb of width $\Delta\nu_{\mathrm{comb}}$ consisting of N_{m} equidistant modes with amplitudes B_1 and mode spacing f_{MS} (see figure 7.6d).

The working principle of frequency comb spectroscopy is illustrated in figure 7.7. The full inhomogeneous NMR spectrum is excited by a comb (blue line) with comb width $\Delta\nu_{\mathrm{comb}} > \Delta\nu_{\mathrm{inh}}$. This broad excitation bandwidth is only possible due to the low rf power carried in each mode. The mode amplitudes $B_1 \approx 0.1 - 10\ \mu\mathrm{T}$ are several orders of magnitude smaller that the rf amplitudes used in pulsed NMR experiments ($B_{1,\mathrm{pulse}} \approx 3-8$ mT) and are kept constant over the comb width $\Delta\nu_{\mathrm{comb}}$ within the experimental limitations for rf circuit matching ($\pm 20\%$, see figure 4.5b for comparison).

In a typical frequency comb NMR experiment the nuclear spin ensemble is first polarised optically as described in section 7.2.2. Subsequently, we apply an rf comb with mode spacing f_{MS} to the inhomogeneously broadened NMR spectrum of the studied isotope and depolarise the nuclear spins for a time t_{rf}. The observed depolarisation dynamics induced by the comb depend on the relation between the mode spacing f_{MS} and the nuclear homogeneous linewidth $\Delta\nu_{\mathrm{hom}}$. If the mode spacing

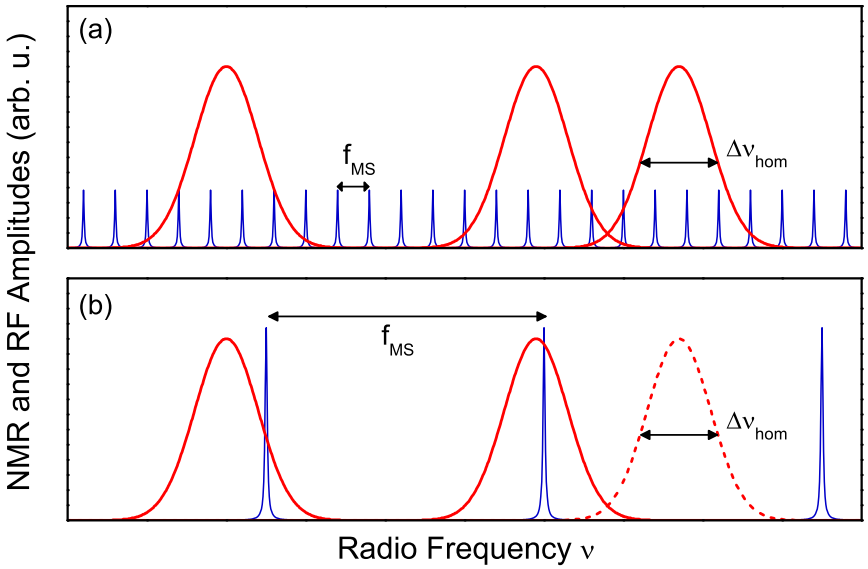

Figure 7.7: Schematic of the frequency comb NMR technique for measuring the homogeneous NMR lineshape (red lines). The rf excitation spectrum (blue) overlaps with the full NMR spectrum as illustrated in figure 7.6, i.e. $\Delta\nu_{\mathrm{comb}} > \Delta\nu_{\mathrm{inh}}$. (a) If the mode spacing f_{MS} is smaller than the homogeneous linewidth $\Delta\nu_{\mathrm{hom}}$, all nuclear transitions get depolarised quickly. (b) For larger mode spacings $f_{\mathrm{MS}} > \Delta\nu_{\mathrm{hom}}$, depolarisation slows down as some transitions (dashed line) no longer get excited by the frequency comb. The rf amplitude per mode is rescaled to keep the power density constant for varying f_{MS}.

is small ($f_{\mathrm{MS}} < \Delta\nu_{\mathrm{hom}}$), each spin transition within $\Delta\nu_{\mathrm{comb}}$ is excited resonantly by several modes as shown in figure 7.7a. As B_1 is small, the induced nuclear spin precession is slower than the phase memory time $T_{\mathrm{M,n}}$ and we expect to observe non-coherent exponential depolarisation with a characteristic decay time τ instead of the Rabi oscillations we observed e.g. in chapter 5.4.3 under strong, coherent rf driving[193].

For the opposite case of large mode spacing $f_{\mathrm{MS}} > \Delta\nu_{\mathrm{hom}}$, we no longer excite every nuclear spin transition resonantly (dashed line in figure 7.7b). As a consequence, the overall depolarisation slows down and becomes non-exponential. Experimentally, we can vary the mode spacing over a wide range (~ 30 Hz $- 20$ kHz) in order to determine the value of f_{MS} at which this slow-down begins. This gives us an estimate of the homogeneous linewidth $\Delta\nu_{\mathrm{hom}}$. The rf field density $\beta_1 = \frac{B_1}{\sqrt{f_{\mathrm{MS}}}}$

is kept constant for different f_{MS} by rescaling the rf amplitude per mode B_1 to keep the depolarisation time τ of resonantly excited spin transitions fixed. As we will show in section 7.3.3, a more detailed analysis of such a dataset allows us to obtain not only $\Delta\nu_{\mathrm{hom}}$ but also to quantify the full homogeneous NMR lineshape.

7.3.2 Experimental Results

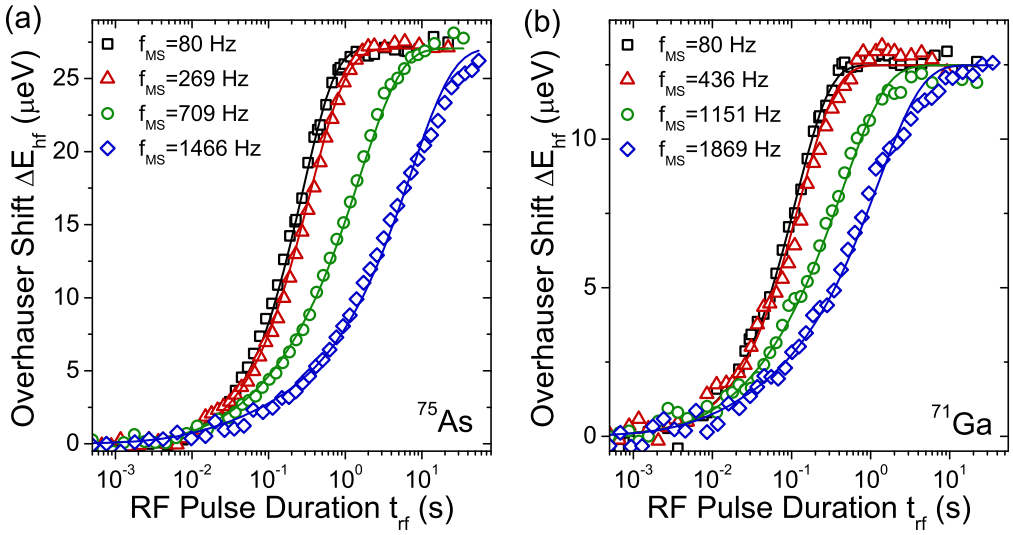

Figure 7.8: Change of the nuclear spin bath polarisation ΔE_{hf} as a function of the duration t_{rf} of an rf frequency comb applied to (a) ^{75}As and (b) ^{71}Ga at $B_{0,\mathrm{z}} = 8$ T and for different mode spacings f_{MS}. Solid lines show fitting with the model discussed in the following section 7.3.3.

Figures 7.8a and b show respective experimental results from frequency comb measurements on ^{75}As and ^{71}Ga in an empty quantum dot on sample B. The polarisation of the nuclear spin ensembles is shown as a function of the frequency comb excitation time t_{rf} at $B_{0,\mathrm{z}} = 8$ T. Each figure shows data obtained with fixed rf field density ($\beta_1(^{75}\mathrm{As}) = 65.5\ \mathrm{nT}/\sqrt{\mathrm{Hz}}$ and $\beta_1(^{71}\mathrm{Ga}) = 39.1\ \mathrm{nT}/\sqrt{\mathrm{Hz}}$) and different mode spacings f_{MS}. While the t_{rf} dependence at small mode spacing is well described by an exponential decay with respective characteristic decay time $\tau(^{75}\mathrm{As}) \approx 240$ ms and $\tau(^{71}\mathrm{Ga}) \approx 105$ ms, we observe a pronounced slow-down of the depolarisation dynamics for large f_{MS}. Solid lines show fits with the homogeneous lineshape model derived in the next section.

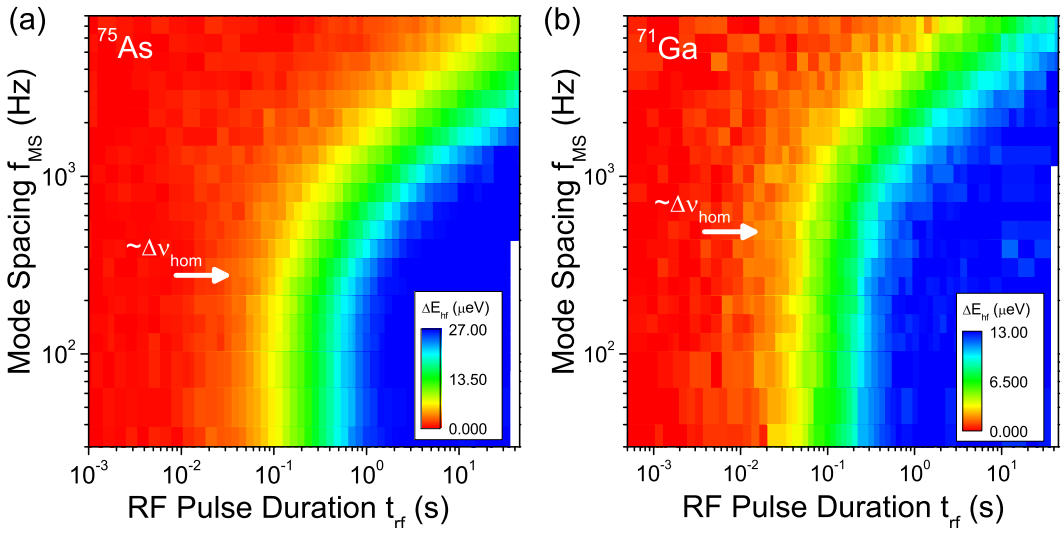

Figure 7.9: Two-dimensional colour plots showing the dependence of the Overhauser shift ΔE_{hf} in (a) ^{75}As and (b) ^{71}Ga on the frequency comb mode spacing f_{MS} and on the depolarisation time t_{rf}. White arrows mark the mode spacings where the depolarisation is beginning to slow down, giving an estimate for the homogeneous linewidths $\Delta\nu_{\mathrm{hom}}(^{75}\mathrm{As}) \approx 250$ Hz and $\Delta\nu_{\mathrm{hom}}(^{71}\mathrm{Ga}) \approx 450$ Hz.

We performed depolarisation time dependent frequency comb NMR experiments on both isotopes for a large range of mode spacings f_{MS}. The combined results of these measurements are shown in figures 7.9a and b as two-dimensional colour plots. Here, the transition from the fast exponential nuclear spin bath depolarisation to the slowed-down depolarisation regime with increasing mode spacing f_{MS} is clearly discernible for both isotopes. The onset of this slow-down is marked by white arrows and gives an estimate for the homogeneous NMR linewidths $\Delta\nu_{\mathrm{hom}}(^{75}\mathrm{As}) \approx 250$ Hz and $\Delta\nu_{\mathrm{hom}}(^{71}\mathrm{Ga}) \approx 450$ Hz. As we will show in the next section, a rate equation model allows us to improve on this estimate and to determine the full homogeneous spectral lineshapes of the ^{75}As and ^{71}Ga resonances from this data.

7.3.3 Extracting the Homogeneous NMR Lineshape

While the spectral linewidth $\Delta\nu_{\mathrm{hom}}$ is linked to the ensemble phase memory time via $T_{\mathrm{M,n}} \approx 1/(\pi\Delta\nu_{\mathrm{hom}})$, the full homogeneous lineshape contains additional information on the nature of the nuclear spin decoherence processes limiting $T_{\mathrm{M,n}}$[275, 276]. Here

we discuss how the homogeneous NMR lineshape of an isotope can be obtained from a set of mode spacing and depolarisation time dependent frequency comb measurements as shown in figures 7.9.

We begin with an initial assumption that the lineshape is symmetric and can be described by a phenomenological model

$$L(\nu) \propto \left(1 + 4(\sqrt[k]{2} - 1)\frac{\nu^2}{\Delta\nu_{\mathrm{hom}}^2}\right)^{-k}, \tag{7.2}$$

with a roll-off parameter k describing the behaviour of $L(\nu)$ far from the centre of the line $\nu_0 = 0$. Equation (7.2) describes a Lorentzian lineshape if $k = 1$ and becomes Gaussian for $k \to \infty$. We can therefore describe the full lineshape by determining the free parameters ν_{hom} and k.

In order to model the depolarisation under a frequency comb, we consider an ensemble of N nuclear spins $I = \frac{3}{2}$ with identical gyromagnetic ratio γ. The depolarisation is isotope-selective, i.e. we can neglect the polarisation of other isotopes. In an external magnetic field $B_{0,\mathrm{z}}$, we get four Zeeman split nuclear spin states $m_{\mathrm{I}} = -\frac{3}{2}, -\frac{1}{2}, \frac{1}{2}, \frac{3}{2}$ with population probabilities p_m, satisfying $\sum_m p_m(t) = 1$. After optical preparation of the spin bath at $t = 0$, we can describe the initial spin bath polarisation by a Boltzmann distribution

$$p_m(t = 0) = p_{m,0} \propto \exp\left(\frac{m_{\mathrm{I}}\hbar\gamma B_{0,\mathrm{z}}}{k_{\mathrm{B}}T_{\mathrm{nuc}}}\right), \tag{7.3}$$

with Boltzmann constant k_{B} and nuclear spin temperature T_{nuc}. Using the known hyperfine constants A^{e} (see table 3.1) and the experimentally measured hyperfine shift at maximum nuclear polarisation, we can determine the spin temperature to be $T_{\mathrm{nuc,A}}(^{75}\mathrm{As}) \approx 3.9$ mK and $T_{\mathrm{nuc,A}}(^{71}\mathrm{Ga}) \approx 5.2$ mK in sample A as well as $T_{\mathrm{nuc,B}}(^{75}\mathrm{As}) \approx 5.6$ mK and $T_{\mathrm{nuc,B}}(^{71}\mathrm{Ga}) \approx 7.1$ mK in sample B.

Under rf excitation the population probabilities change. Assuming weak rf fields far below the saturation level, i.e. where no Rabi oscillations are occurring, and

taking into account only dipole-allowed transitions ($\Delta m_\mathrm{I} = \pm 1$), we can describe the evolution of the spin ensemble by a set of rate equations:

$$\begin{aligned}
\frac{\mathrm{d}p_{3/2}}{\mathrm{d}t} &= W_{1/2,3/2}(-p_{3/2}(t) + p_{1/2}(t)) \\
\frac{\mathrm{d}p_{1/2}}{\mathrm{d}t} &= -(W_{-1/2,1/2} + W_{1/2,3/2})p_{1/2}(t) + W_{-1/2,1/2}p_{-1/2}(t) + W_{1/2,3/2}p_{3/2}(t) \\
\frac{\mathrm{d}p_{-1/2}}{\mathrm{d}t} &= -(W_{-3/2,-1/2} + W_{-1/2,1/2})p_{-1/2}(t) + W_{-3/2,-1/2}p_{-3/2}(t) + W_{-1/2,1/2}p_{1/2}(t) \\
\frac{\mathrm{d}p_{-3/2}}{\mathrm{d}t} &= W_{-3/2,-1/2}(-p_{-3/2}(t) + p_{-1/2}(t)) \ ,
\end{aligned} \tag{7.4}$$

with symmetric transition rates $W_{m,m+1} = W_{m+1,m}$. Therefore we have a set of four differential equations for three independent variables (the $p_m(t)$ are also linked by the normalisation condition). The depolarisation dynamics of the spin ensemble are fully determined by the rf induced transition rates $W_{m,m+1}$.

Each rate $W_{m,m+1}$ is given by the sum of transition rates for the N_m individual modes in the frequency comb with mode spacing f_MS and field amplitudes B_1. We assume that all nuclear transitions are described by the same unknown homogeneous lineshape function $L(\nu)$ given in equation (7.2) with normalisation $\int_{-\infty}^{\infty} L(\nu)\mathrm{d}\nu = 1$. Using Fermi's golden rule with the dipole transition matrix element $(I - m_\mathrm{I})(I + m_\mathrm{I} + 1)$, the rate for any given NMR transition frequency $\nu_{m,m+1}$ is

$$\begin{aligned}
W_{m,m+1}(\nu_{m,m+1}) = &\frac{(I - m_\mathrm{I})(I + m_\mathrm{I} + 1)\gamma^{*2}B_1^2}{2f_\mathrm{MS}} \\
&\sum_{j=-\infty}^{+\infty} L(\nu_{m,m+1} - \nu_1 - jf_\mathrm{MS})f_\mathrm{MS} \ ,
\end{aligned} \tag{7.5}$$

where we sum over all modes with frequencies $\nu_j = \nu_1 + (j-1)f_\mathrm{MS}$. As the comb width $\Delta\nu_\mathrm{comb}$ is much larger than the mode spacing f_MS and the homogeneous linewidth $\Delta\nu_\mathrm{hom}$, we can extend the sum to $\pm\infty$. We note here that in the limit of small $f_\mathrm{MS} \to 0$, the infinite sum in equation (7.5) tends towards the integral expression $\int_{-\infty}^{\infty} L(\nu)\mathrm{d}\nu = 1$ and the polarisation of a given spin transition $m_\mathrm{I} \leftrightarrow m_\mathrm{I} + 1$

decays exponentially with characteristic time

$$\tau_{m,m+1} = \frac{2f_{\mathrm{MS}}}{(I - m_{\mathrm{I}})(I + m_{\mathrm{I}} + 1)\gamma^{*2}B_{\mathrm{I}}^2} \,. \tag{7.6}$$

The general solution to the set of differential equations in (7.4) is of the form

$$p_m(t) = \frac{1}{4} + \sum_{j=1}^{3} a_{m,j} \exp(-\lambda_j t) \,, \tag{7.7}$$

describing the multi-exponential spin relaxation towards a depolarised state with $p_m = \frac{1}{4}$. The eigenvalues λ_j only depend on the transition rates $W_{m,m+1}$, whereas the coefficients $a_{m,j}$ also depend on the initial probabilities $p_{m,0}$ from equation (7.3).

Experimentally, we measure the hyperfine shift of a Zeeman split doublet of exciton transitions. We can express the time-dependent Overhauser shift for a fixed set of nuclear transition frequencies $\{\nu_{m,m+1}\} = \{\nu_{-3/2,-1/2}, \nu_{-1/2,-1/2}, \nu_{1/2,3/2}\}$ as

$$E_{\mathrm{hf},1}(t_{\mathrm{rf}}, f_{\mathrm{MS}}, B_1, T_{\mathrm{nuc}}, L(\nu), \{\nu_{m,m+1}\}) = A^{\mathrm{e}} \sum_{m=-3/2}^{+3/2} m_{\mathrm{I}} p_m(t) \,, \tag{7.8}$$

where A^{e} is the hyperfine constant of the isotope and t_{rf} is the depolarisation time. The dependence on the lineshape $L(\nu)$ originates from the transition rates (equation (7.5)) and is effectively a dependence on $\Delta\nu_{\mathrm{hom}}$ and the roll-off parameter k for equation (7.8). Since the quantum dot consists of several thousand nuclear spins with highly inhomogeneous quadrupolar shifts we need to average over all $\nu_{m,m+1}$. This can be done over a single period f_{MS} as the rf spectrum is periodic. The full Overhauser shift is given by

$$\begin{aligned} &E_{\mathrm{hf}}(t_{\mathrm{rf}}, f_{\mathrm{MS}}, B_1, T_{\mathrm{nuc}}, L(\nu)) = \\ &\quad f_{\mathrm{MS}}^{-3} \int_0^{f_{\mathrm{MS}}} \mathrm{d}\nu_{-3/2,-1/2} \mathrm{d}\nu_{-1/2,1/2} \mathrm{d}\nu_{1/2,3/2} E_{\mathrm{hf},1}(t_{\mathrm{rf}}, f_{\mathrm{MS}}, B_1, T_{\mathrm{nuc}}, L(\nu), \{\nu_{m,m+1}\}) \end{aligned} \tag{7.9}$$

The rf induced change in the Overhauser shift measured in the experiment is

$$\Delta E_{\mathrm{hf}}(t_{\mathrm{rf}}, f_{\mathrm{MS}}, B_1, T_{\mathrm{nuc}}, L(\nu)) = E_{\mathrm{hf}}(t_{\mathrm{rf}}, f_{\mathrm{MS}}, B_1, T_{\mathrm{nuc}}, L(\nu)) - E_{\mathrm{hf}}(t_{\mathrm{rf}} = 0) \quad (7.10)$$

The mode spacing f_{MS}, the rf amplitude B_1 and the rf excitation time t_{rf} are determined by experimental parameters. Since the nuclear spin temperature T_{nuc} is also known from the total hyperfine shift $\Delta E_{\mathrm{hf}}(t_{\mathrm{rf}} \to \infty)$, we are left with only two free parameters: the homogeneous linewidth $\Delta\nu_{\mathrm{hom}}$ and the roll-off parameter k, which fully determine the model lineshape $L(\nu)$ in equation (7.2).

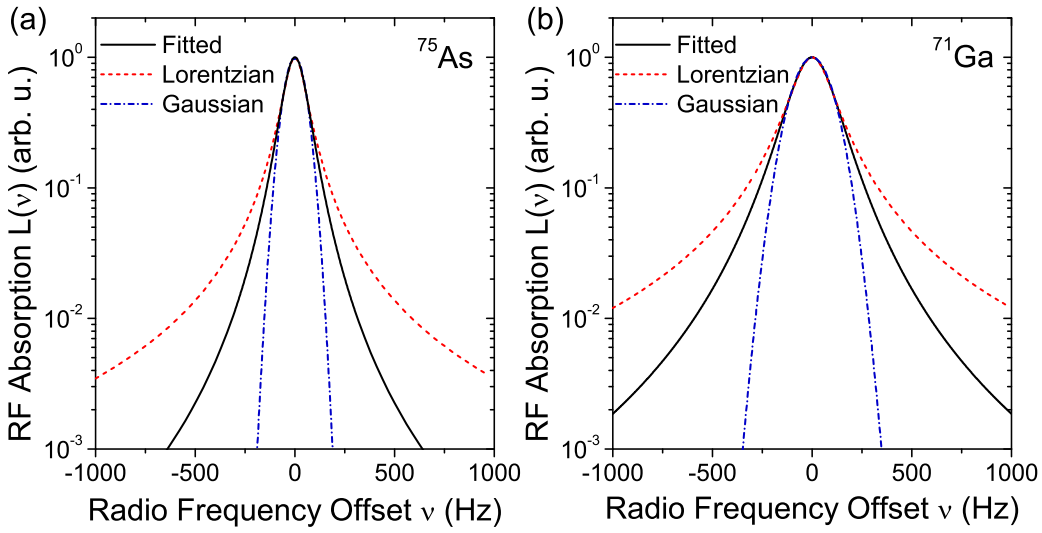

Figure 7.10: Homogeneous NMR lineshape $L(\nu)$ for (a) ^{75}As and (b) ^{71}Ga obtained from fitting of the experimental data shown in figures 7.9 with equation (7.10) (solid lines). Dashed and dash-dotted lines show Lorentzian and Gaussian lineshapes with the same linewidth $\Delta\nu_{\mathrm{hom}}$ for comparison.

Using least-square fitting of the experimental data $\Delta E_{\mathrm{hf}}(t_{\mathrm{rf}}, f_{\mathrm{MS}})$ shown in figures 7.9 with equation (7.10), we obtain best-fit parameters $\Delta\nu_{\mathrm{hom}}(^{75}\mathrm{As}) \approx 118$ Hz and $k(^{75}\mathrm{As}) \approx 1.68$ for ^{75}As, as well as $\Delta\nu_{\mathrm{hom}}(^{71}\mathrm{Ga}) \approx 221$ Hz and $k(^{71}\mathrm{Ga}) \approx 1.67$ for ^{71}Ga. The solid lines in figures 7.10a and b show the best-fit lineshapes together with Lorentzian (dashed lines) and Gaussian lineshapes (dash-dotted lines) with the same homogeneous linewidth $\Delta\nu_{\mathrm{hom}}$. We see a pronounced difference in the tail behaviour at large frequency offsets, indicating a noticeable deviation from the "top-hat"-like

Gaussian lineshape typically expected for a dipolar broadened spin ensemble[275]. The homogeneous linewidths are in good agreement with the Hahn echo results presented in chapter 5: from $T_{\mathrm{M,n}} \approx 1/(\pi\Delta\nu_{\mathrm{hom}})$, we obtain $T^{\mathrm{MS}}_{\mathrm{M,n}}(^{75}\mathrm{As}) \approx 2.7$ ms and $T^{\mathrm{MS}}_{\mathrm{M,n}}(^{71}\mathrm{Ga}) \approx 1.4$ ms compared to $T^{\mathrm{HE}}_{\mathrm{M,n}}(^{75}\mathrm{As}) = 4.3$ ms and $T^{\mathrm{HE}}_{\mathrm{M,n}}(^{71}\mathrm{Ga}) = 1.2$ ms in the Hahn echo measurements.

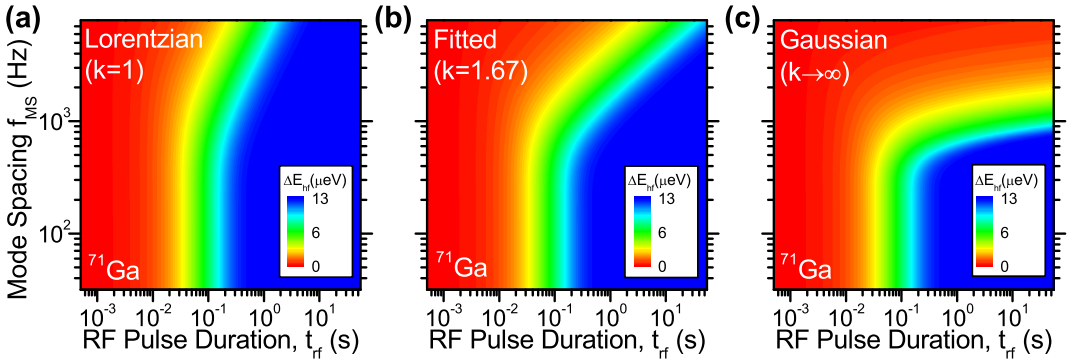

Figure 7.11: Two-dimensional colour plots showing the model dependence of the Overhauser shift ΔE_{hf} on the ^{71}Ga depolarisation time t_{rf} and on the frequency comb mode spacing f_{MS}. The plots show the calculated $\Delta E_{\mathrm{hf}}(t_{\mathrm{rf}}, f_{\mathrm{MS}})$ for (a) Lorentzian, (b) best-fit, and (c) Gaussian lineshape using equation (7.10) with identical parameters (B_1, T_{nuc}, $\Delta\nu_{\mathrm{hom}}$).

The sensitivity of the frequency comb technique to the lineshape can be shown by modelling the full dependence of the hyperfine shift $\Delta E_{\mathrm{hf}}(t_{\mathrm{rf}}, f_{\mathrm{MS}})$ on the depolarisation time t_{rf} and on the mode spacing f_{MS} under the assumption of a Lorentzian or Gaussian lineshape with all other parameters (B_1, T_{nuc}, $\Delta\nu_{\mathrm{hom}}$) kept identical to the best fit. Figures 7.11a, b and c show two-dimensional colour plots of the modelled $\Delta E_{\mathrm{hf}}(t_{\mathrm{rf}}, f_{\mathrm{MS}})$ for ^{71}Ga assuming a Lorentzian, best fit and Gaussian lineshape, respectively. We note that the best fit model is in excellent agreement with the experimental results shown in figure 7.9b whereas the behaviour of the Lorentzian and Gaussian models strongly deviates from the experimental observations at large mode spacings f_{MS}. This demonstrates the high sensitivity of the frequency comb technique to the homogeneous NMR lineshape.

7.3.4 Applicability of the Frequency Comb Technique

Before we further explore the origin of the non-Gaussian homogeneous NMR lineshapes observed for ^{75}As and ^{71}Ga, we consider possible limitations of the applicability of frequency comb NMR by studying the rf amplitude dependent depolarisation behaviour. We saw in chapter 3.3.2 that the evolution of a nuclear spin ensemble under rf excitation can be described by the Bloch equations of motion[189]. If the rf field is resonant with the Larmor frequency of the driven spin ensemble, the solutions to the Bloch equations are fully determined by the rf field amplitude B_1, the spin relaxation time $T_{1,\mathrm{n}}$ and the phase memory time $T_{\mathrm{M,n}}$. Since $T_{1,\mathrm{n}}$ is on the order of hours in empty self-assembled quantum dots (see chapter 5.3.1 and [85, 115]), the nuclear spin dynamics in this system are characterised by B_1 and $T_{\mathrm{M,n}}$ only.

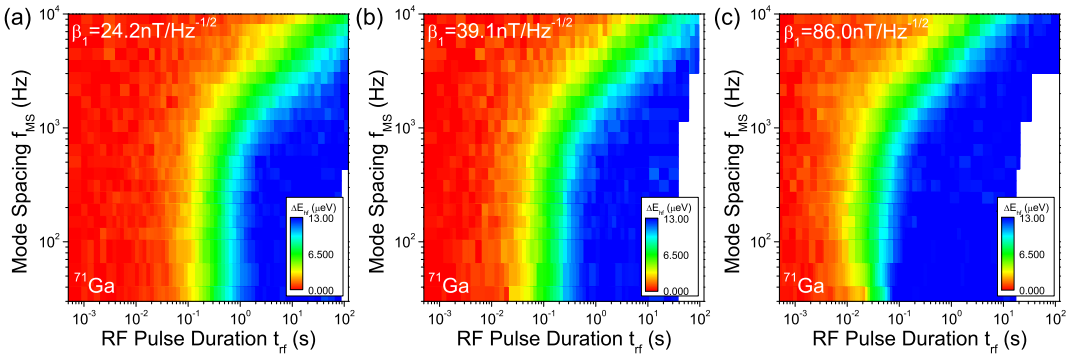

Figure 7.12: Frequency comb NMR on ^{71}Ga at different rf powers. Dependence of the ^{71}Ga Overhauser shift ΔE_{hf} at $B_{0,\mathrm{z}} = 8$ T on the frequency comb excitation time t_{rf} and on the mode spacing f_{MS} at (a) low, (b) medium, and (c) high rf field density β_1.

In the case of strong driving fields ($\gamma B_1 T_{\mathrm{M,n}} \gg 1$), the Bloch equations predict Rabi oscillations for the magnetisation along the $\hat{e}_{\mathrm{z}}$ axis as derived in chapter 3.3. The coherent pulsed NMR experiments discussed in the previous chapters were done in this regime. In the weak rf limit ($\gamma B_1 T_{\mathrm{M,n}} \ll 1$), the magnetisation along $\hat{e}_{\mathrm{z}}$ decays exponentially to its steady state value instead[193]. This regime is much easier to treat theoretically and we assumed its validity implicitly when we described the time evolution of the nuclear spin bath magnetisation by the rate equation model

(7.4). Hence the applicability of the frequency comb technique based on the model introduced in the previous section is limited by the weak rf field assumption.

Figures 7.12a-c show the results of full $\Delta E_{\mathrm{hf}}(t_{\mathrm{rf}}, f_{\mathrm{MS}})$ dependence measurements on ^{71}Ga at three different rf field densities. We find that model fitting yields almost identical lineshape parameters for the low ($\beta_1 = 24.2$ nT/$\sqrt{\mathrm{Hz}}$) and high rf field density ($\beta_1 = 86.0$ nT/$\sqrt{\mathrm{Hz}}$) measurements, in very good agreement with the values obtained for the medium field density $\beta_1 = 39.1$ nT/$\sqrt{\mathrm{Hz}}$ shown in figure 7.9b of the previous section and in figure 7.12b (see table 7.2 below).

Figure 7.12	(a)	(b)	(c)
RF field density β_1 (nT/$\sqrt{\mathrm{Hz}}$)	24.2	39.1	86.0
Exponential decay time τ (ms)	290	105	23
Homogeneous linewidth $\Delta\nu_{\mathrm{hom}}$ (Hz)	223	221	244
Roll-off parameter k	1.68	1.67	1.66

Table 7.2: Fitted lineshape parameters and exponential decay times for the frequency comb measurements at different rf powers shown in figure 7.12.

However, we do notice a pronounced deviation from the single exponential decay behaviour at small mode spacing f_{MS} in the measurement at high rf amplitude. Figure 7.13 shows the ^{71}Ga spin depolarisation dynamics for all three amplitudes at $f_{\mathrm{MS}} = 31.25$ Hz. Solid lines show fitted single exponential decay curves with a time constant τ. While the decay at medium and low rf power is well described by the fit, we see a clear deviation at $\beta_1 = 86.0$ nT/$\sqrt{\mathrm{Hz}}$. This onset of an oscillatory behaviour quickly disappears for larger mode spacings $f_{\mathrm{MS}} \gtrsim 80$ Hz, which explains why the fit to the full data set $\Delta E_{\mathrm{hf}}(t_{\mathrm{rf}}, f_{\mathrm{MS}})$ is still in excellent agreement with the results for lower rf amplitudes.

Taking into account the good agreement of the fitted lineshapes at all three rf field densities (see table 7.2), we can conclude that even at relatively high rf powers the deviation of the nuclear depolarisation dynamics from a pure exponential decay only becomes significant at very small mode spacings. This can be understood if

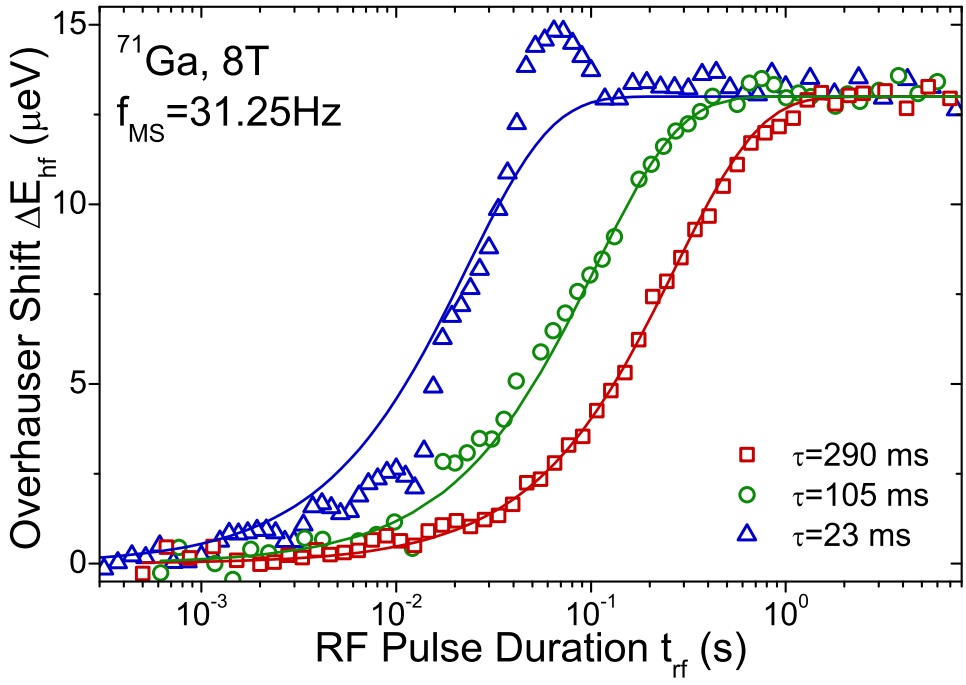

Figure 7.13: ^{71}Ga hyperfine shift ΔE_{hf} dependence on the frequency comb rf depolarisation time t_{rf} for a fixed mode spacing $f_{\mathrm{MS}} = 31.25$ Hz. Data sets show measurements at low (squares), medium (circles) and high (triangles) rf field density β_1. Solid lines show exponential fits $\propto \exp[-t_{\mathrm{rf}}/\tau]$.

we consider that spin depolarisation at high rf powers occurs over a very short timescale τ. If $\tau < 1/f_{\mathrm{MS}}$, we can no longer describe the spectral profile of the rf excitation field as a frequency comb and the rate equation model discussed in the previous section is no longer applicable. In order to obtain the lineshape parameters, we only need mode spacings equal to or larger than the homogeneous linewidth, $f_{\mathrm{MS}} \in \{\Delta\nu_{\mathrm{hom}}, \infty\}$. Combining these two requirements, we can define the following condition for the applicability of the frequency comb technique:

$$\Delta\nu_{\mathrm{hom}} > 1/\tau \; . \tag{7.11}$$

Note that this merely sets an upper limit to the rf amplitude as the condition can always be fulfilled by reducing the rf power sufficiently.

For the weak rf field limit of the Bloch equations (absence of Rabi oscillations) to hold, we also require that the rf induced decay time τ is longer than the nuclear

spin phase memory time $T_{\mathrm{M,n}}$. However, since $T_{\mathrm{M,n}} \sim 1/(\pi\nu_{\mathrm{hom}})$, this leads to the same condition as stated in equation (7.11). In general, a third limitation can arise for short longitudinal relaxation times $T_{1,\mathrm{n}}$. Since the frequency comb technique is based on a measurement of the longitudinal nuclear magnetisation after a time t_{rf}, we require that $\tau < T_{1,\mathrm{n}}$, so that in summary

$$\Delta\nu_{\mathrm{hom}} > 1/\tau > 1/T_{1,\mathrm{n}} \tag{7.12}$$

This expression not only limits the range of rf field amplitudes for which we can perform frequency comb NMR. It also implies a requirement $T_{1,\mathrm{n}} > T_{\mathrm{M,n}}$ for the studied nuclear spin system. Based on the results at different amplitudes discussed in this section, we find that the longitudinal relaxation time $T_{1,\mathrm{n}}$ must be at least $\sim 10-100$ longer than $T_{\mathrm{M,n}}$ for reliable frequency comb NMR measurements. However, this condition is fulfilled for many nuclear spin systems in the solid state with $T_{1,\mathrm{n}} \gg T_{\mathrm{M,n}}$ and does not present a strong limitation to the applicability of the frequency comb technique.

7.4 Detecting Nuclear Spin Flip-Flop Freezing by Frequency Comb NMR

The frequency comb experiments presented and discussed in the previous sections showed that the non-Gaussian homogeneous NMR linewidths $\Delta\nu_{\mathrm{hom}}$ of ^{75}As and ^{71}Ga nuclei in a self-assembled quantum dot are noticeably narrower than in comparable strain-free systems. We already mentioned in chapter 5.2 that Hahn echo decay times of $T_{\mathrm{M,n}}^{\mathrm{HE}}(^{75}\mathrm{As}) \lesssim 800$ μs corresponding to $\Delta\nu_{\mathrm{hom}}(^{75}\mathrm{As}) \approx 400$ Hz have been reported for the CT of ^{75}As in unstrained quantum well structures[183]. NMR studies of ^{75}As in bulk GaAs revealed even broader linewidths of up to ~ 1.5 kHz and a Gaussian homogeneous lineshape[277].

In chapter 5, we attributed the comparatively long nuclear spin decay times in InGaAs quantum dots observed in Hahn echo to the partial suppression of the homonuclear dipolar flip-flop mechanism resulting from strong inhomogeneous broadening of the NMR spectrum[41, 200]. As we will now show, frequency comb NMR allows us to confirm this conclusion in a direct fashion by artificially restoring the dipolar broadening. As before, we depolarise the ^{75}As spins with frequency combs of varying mode spacings f_{MS} to measure their homogeneous lineshape. However, we now apply a second frequency comb (*RF Depol* in figure 7.2) which excites the ^{71}Ga spins. Using a comb with rf field density $\beta_{1,\mathrm{Ga}} = 27.6\ \mathrm{nT}/\sqrt{\mathrm{Hz}}$ corresponding to a decay time of $\tau_{\mathrm{Ga}} = 172$ ms, we depolarise the ^{71}Ga nuclei fully during a time $t_{\mathrm{depol}} = 1.2$ s after the spin bath has been polarised optically and before the ^{75}As nuclei are depolarised for a varying time t_{rf} (see experiment cycle in figure 7.3).

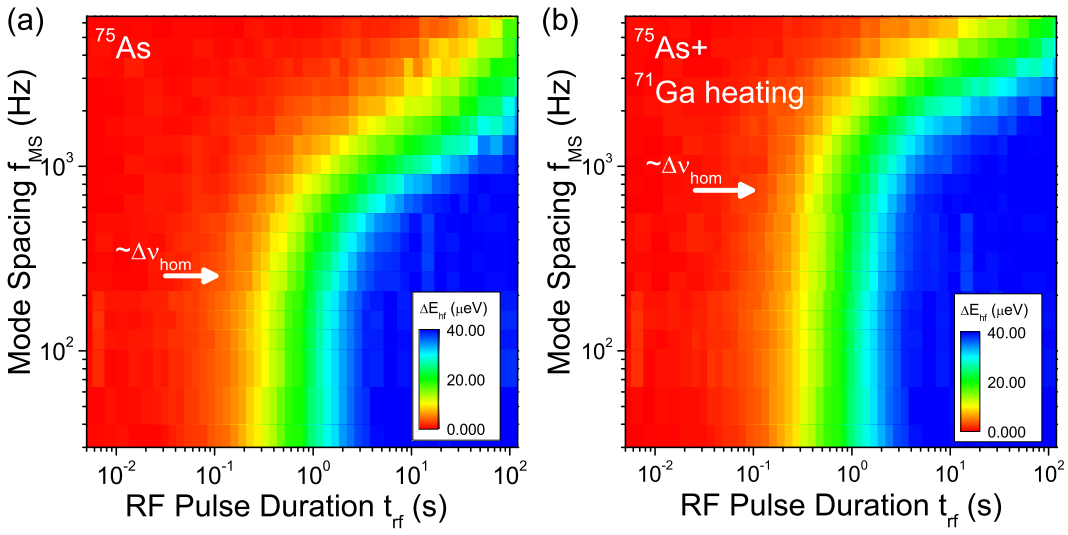

Figure 7.14: Two-dimensional plot of ΔE_{hf} as a function of t_{rf} and f_{MS} in frequency comb NMR measurements on ^{75}As in sample A (a) without and (b) with simultaneous heating of ^{71}Ga. White arrows mark the onset of depolarisation slow-down, giving an estimate of $\Delta\nu_{\mathrm{hom}}$.

If the *RF Depol* comb is switched off during t_{rf}, the ^{71}Ga excitation has no effect on the ^{75}As homogeneous lineshape. This is shown in figure 7.14a for measurements on a dot in sample A. Fitting with equation (7.10) gives lineshape parameters $\Delta\nu_{\mathrm{hom}}(^{75}\mathrm{As}) \approx 117$ Hz and $k(^{75}\mathrm{As}) \approx 1.78$ in excellent agreement with the results

of the single-comb experiment on ^{75}As in sample B (see figure 7.9a).

By contrast, figure 7.14b shows the mode spacing and depolarisation time dependence of the ^{75}As hyperfine shift ΔE_{hf} in a set of experiments where the *RF Depol* comb is kept switched on during t_{rf}. As the ^{71}Ga nuclei have already been depolarised during t_{depol}, the full depolarisation amplitude $\Delta E_{\mathrm{hf},0}$ is identical to that in the previous measurement. However, the continuous "heating" of the ^{71}Ga spins does have an indirect effect on the ^{75}As depolarisation dynamics: the *RF Depol* comb induces additional ^{71}Ga spin-flips and creates a "noisy" spin environment to which the ^{75}As spins couple by heteronuclear dipolar interaction. The resulting spectral line broadening is indicated in figure 7.14b by a white arrow. From fitting, we obtain a two times broader linewidth $\Delta\nu_{\mathrm{hom}}(^{75}\mathrm{As}) \approx 355$ Hz and a noticeable change of the lineshape towards Gaussian ($k(^{75}\mathrm{As}) \approx 2.32$).

These findings are a direct confirmation of the spin freezing mechanism discussed in reference [41] and chapter 5. The strain-induced strongly inhomogeneous broadening of the NMR resonances suppresses homonuclear dipolar flip-flop interactions in the quantum dot. The homogeneous lineshape we measure in frequency comb spectroscopy represents the statistical distribution of frequency shifts each probed nucleus is subject to due to its dipolar interaction with its fluctuating nuclear spin environment. If these fluctuations occur over a timescale exceeding t_{rf}, they are effectively static during the rf probing time. Consequently, their contribution to the homogeneous linewidth is removed and we observe a narrowed, non-Gaussian lineshape. RF heating of the ^{71}Ga spin ensemble reintroduces the suppressed ^{71}Ga spin flip-flop mechanism by inducing additional ^{71}Ga spin-flips and partially restores the ^{75}As dipolar broadening.

If addition depolarisation combs were applied to the remaining isotopes in the dot, we would "thaw" the nuclear spin bath dynamics even further and observe a nearly Gaussian lineshape ($k \gg 1$) for the probed isotope. By contrast, we would observe a non-Lorentzian lineshape $k \gtrsim 1$ even if the spin bath was completely "frozen"

because the frequency comb depolarisation of the studied isotope will always induce a small amount of homonuclear dipolar broadening.

7.5 Extracting Spin Bath Correlation Times

The two-comb experiments presented in the previous section show that the homogeneous NMR lineshape of ^{75}As is very sensitive to changes in the equilibrium spin bath dynamics of ^{71}Ga. This makes it feasible to determine the correlation time τ_c of the intrinsic ^{71}Ga spin flip-flops. The different transition matrix elements of STs and the CT as well as the different extent of inhomogeneous broadening lead us to expect that τ_c is generally not identical for central and satellite transitions. We therefore extend the measurement scheme of the previous section by adding a third frequency comb designed to selectively heat a single ^{71}Ga spin transition during t_{rf}. The resulting depolarisation dynamics observed for ^{75}As depend on three distinct contributions: the pure ^{75}As depolarisation time $\tau_{As}(\beta_{1,As})$ determined by the comb amplitude $\beta_{1,As}$, the characteristic spin flip time of the single ^{71}Ga transition $\tau_{Ga,CT/ST}(\beta_{1,Ga})$ and the ^{71}Ga CT/ST flip-flop correlation time $\tau_{c,CT/ST}$. By varying the amplitudes of the ^{75}As and ^{71}Ga-CT/ST frequency combs we can obtain the unknown spin flip-flop correlation time $\tau_{c,CT/ST}$.

7.5.1 Calibration for Three-Comb Experiments

In the dipolar broadening experiments of the previous section we heated all three NMR transitions of ^{71}Ga during the ^{75}As depolarisation time t_{rf}. Accordingly, the ^{71}Ga frequency comb was chosen to exceed the full inhomogeneous spectral width $\Delta\nu_{inh}(^{71}\text{Ga}) \approx 5$ MHz (in sample A). For selective rf excitation of the CT or of the $(+1/2 \leftrightarrow +3/2)$ ST in ^{71}Ga, we have to choose the comb width and central frequency more carefully to avoid spurious excitation of neighbouring transitions. We choose $\Delta\nu_{comb} = 50$ kHz for the CT to ensure a good overlap with the inhomogeneously

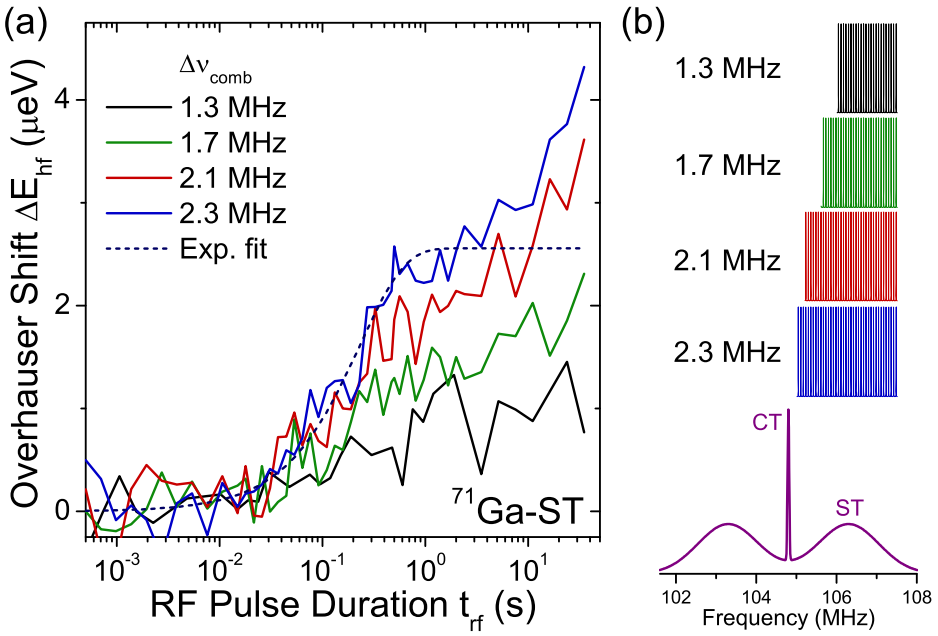

Figure 7.15: Calibration of the ^{71}Ga ST frequency comb width. (a) Change of the hyperfine shift ΔE_{hf} as a function of the depolarisation time t_{rf} under ^{71}Ga ST frequency combs with different comb widths $\Delta\nu_{\mathrm{comb}}$ and fixed mode spacing $f_{\mathrm{MS}} = 150$ Hz (solid lines). The dashed line shows an exponential fit $\propto \exp[-t_{\mathrm{rf}}/\tau_{\mathrm{Ga,ST}}]$ to the data for $\Delta\nu_{\mathrm{comb}} = 2.3$ MHz. (b) Illustration of the relative positions of the frequency combs used in (a) with respect to the full inhomogeneous NMR spectrum of ^{71}Ga (schematic).

broadened NMR spectrum ($\Delta\nu_{\mathrm{inh}}(\mathrm{CT}) \approx 8$ kHz, see chapter 5.4.1).

The optimal ST comb width is determined in a series of single comb experiments measuring the ^{71}Ga ST depolarisation as a function of the rf excitation time t_{rf} with combs of different widths $\Delta\nu_{\mathrm{comb}}$ at a fixed narrow mode spacing $f_{\mathrm{MS}} = 150$ Hz and rf field density $\beta_{1,\mathrm{Ga}} \approx 30.0\ \mathrm{nT}/\sqrt{\mathrm{Hz}}$. The results of these experiments are shown in figure 7.15a. As shown in the right panel (figure 7.15b), we narrow the comb width by increasing the separation from the ^{71}Ga CT resonance and keeping the upper frequency limit of the comb fixed.

From exponential fitting of the polarisation decay at $\Delta\nu_{\mathrm{comb}} = 2.3$ MHz (dashed line), we obtain a characteristic depolarisation time $\tau_{\mathrm{Ga,ST}} \approx 230$ ms. Similar values are obtained for the other comb widths, although the quality of the fit decreases with the amplitude of the Overhauser shift $\Delta E_{\mathrm{hf},0}$ for smaller $\Delta\nu_{\mathrm{comb}}$. We notice that a

second exponential decay occurs at longer time scales $\gtrsim 10$ s for broad frequency combs. This might be caused e.g. by parasitic rf heating in the CT frequency range or by second order depolarisation of the remaining two ^{71}Ga transitions via flip-flops with the heated ST. We see that this secondary decay can be suppressed efficiently by increasing the separation between the ^{71}Ga CT resonance and the ST comb, although this comes at the cost of a reduced number of nuclei excited by the frequency comb. For the subsequent three-comb experiments, we choose $\Delta\nu_{\mathrm{comb}} = 1.3$ MHz where no parasitic effects are observed any more.

The depolarisation amplitude for the ^{71}Ga CT is too small to be measured in ODNMR. Therefore, we cannot calibrate the CT decay time $\tau_{\mathrm{Ga,CT}}$ in the same way. However, we can obtain the CT decay time for a given rf field density $\beta_{1,\mathrm{Ga}}$ from the ST value by taking into account the different transition matrix elements (see chapter 3.3.1 and [116]):

$$\tau_{\mathrm{Ga,CT}} = \frac{3}{4}\tau_{\mathrm{Ga,ST}} \,. \tag{7.13}$$

In order to obtain the ^{71}Ga spin flip-flop correlation times $\tau_{\mathrm{c,CT/ST}}$, we measure the dependence of the ^{75}As nuclear spin depolarisation time $\tau_{\mathrm{As}}(\beta_{1,\mathrm{As}}, \beta_{1,\mathrm{Ga}})$ on the rf field densities of the ^{75}As comb $\beta_{1,\mathrm{As}}$ and of the ^{71}Ga CT/ST heating comb $\beta_{1,\mathrm{Ga}}$. Obtaining a full data set $\Delta E_{\mathrm{hf}}(f_{\mathrm{MS}}, t_{\mathrm{rf}})$ for every pair of rf field densities $(\beta_{1,\mathrm{As}}, \beta_{1,\mathrm{Ga}})$ would be extremely time consuming. For this reason, we select a fixed mode spacing f_{MS} for the ^{75}As frequency comb where the contrast $\Delta\tau_{\mathrm{As}}$ between pure ^{75}As depolarisation and depolarisation with maximum ^{71}Ga CT/ST heating is large.

From comparison of the measurements with and without ^{71}Ga heating in figure 7.9 we notice that the frequency comb is most sensitive to the ^{71}Ga spin dynamics at intermediate mode spacings of $f_{\mathrm{MS}} \approx 0.5 - 2$ kHz. As a measure of the sensitivity of ^{75}As to fluctuations of ^{71}Ga, figure 7.16 shows the ratios $\Delta\tau_{\mathrm{As}}$ of the ^{75}As depolarisation time without and with strong ^{71}Ga CT/ST heating within this range

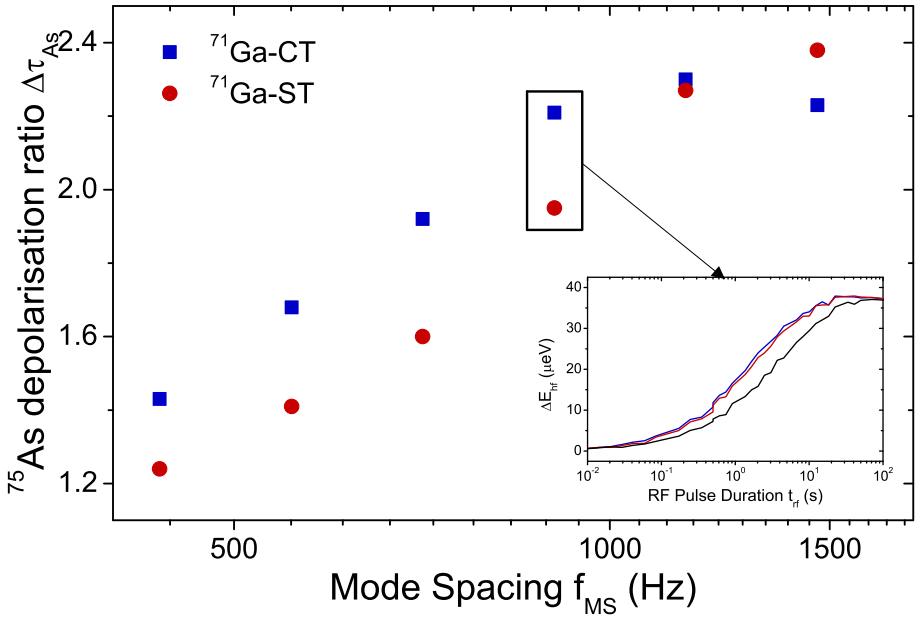

Figure 7.16: Ratio $\Delta\tau_{\mathrm{As}}$ of the ^{75}As depolarisation time without ^{71}Ga heating and with maximum heating $\beta_{1,\mathrm{Ga}} \approx 300\ \mathrm{nT}/\sqrt{\mathrm{Hz}}$ of a single ^{71}Ga transition as a function of the ^{75}As frequency comb mode spacing f_{MS} at a fixed ^{75}As rf field density $\beta_{1,\mathrm{As}} \approx 31\ \mathrm{nT}/\sqrt{\mathrm{Hz}}$ for ^{71}Ga CT (squares) and ST (circles) heating. Inset: $\Delta E_{\mathrm{hf}}(t_{\mathrm{rf}})$ for ^{75}As depolarisation at $f_{\mathrm{MS}} = 903$ Hz without ^{71}Ga heating (black line) and with ^{71}Ga CT (blue) and ST (red) heating, respectively.

of mode spacings for selective heating of the ^{71}Ga CT (squares) and ST (circles). As before, all ^{71}Ga spins are depolarised for a time $t_{\mathrm{depol}} = 1.2$ s before a single ^{71}Ga transition is excited during the ^{75}As depolarisation time t_{rf} (see experiment cycle in figure 7.3). The ^{75}As rf field density is kept fixed at $\beta_{1,\mathrm{As}} \approx 31\ \mathrm{nT}/\sqrt{\mathrm{Hz}}$ and we use $\beta_{1,\mathrm{Ga}} \approx 300\ \mathrm{nT}/\sqrt{\mathrm{Hz}}$ for heating of the ^{71}Ga CT/ST transition.

We observe an increase of the frequency comb sensitivity to ^{71}Ga CT heating with increasing mode spacing up to $f_{\mathrm{MS}} = 1151$ Hz. Under heating of the ST no sensitivity maximum is detected within the measured range of f_{MS}. We select a smaller spacing $f_{\mathrm{MS}} = 903$ Hz for the spin bath correlation measurements as we also have to take into account the spin relaxation time $T_{1,\mathrm{n}} \approx 1730$ s in sample A (see figure 7.5). For larger mode spacings, the pure ^{75}As decay time without ^{71}Ga heating becomes long enough that the $T_{1,\mathrm{n}}$ decay must be taken into account even for high ^{75}As rf field densities $\beta_{1,\mathrm{As}}$ as we can no longer fully depolarise ^{75}As within times $t_{\mathrm{rf}} \ll T_{1,\mathrm{n}}$.

7.5.2 Few-Second-Long Spin Flip-Flop Correlation Times

Having calibrated the heating comb widths $\Delta\nu_{\mathrm{comb,CT}} = 50$ kHz and $\Delta\nu_{\mathrm{comb,ST}} = 1.3$ MHz and the mode spacing $f_{\mathrm{MS}} = 903$ Hz for the ^{75}As frequency comb, we perform three-comb ^{75}As depolarisation measurements at different ^{75}As excitation amplitudes $\beta_{1,\mathrm{As}}$ and varying ^{71}Ga CT and ST heating amplitudes $\beta_{1,\mathrm{Ga}}$.

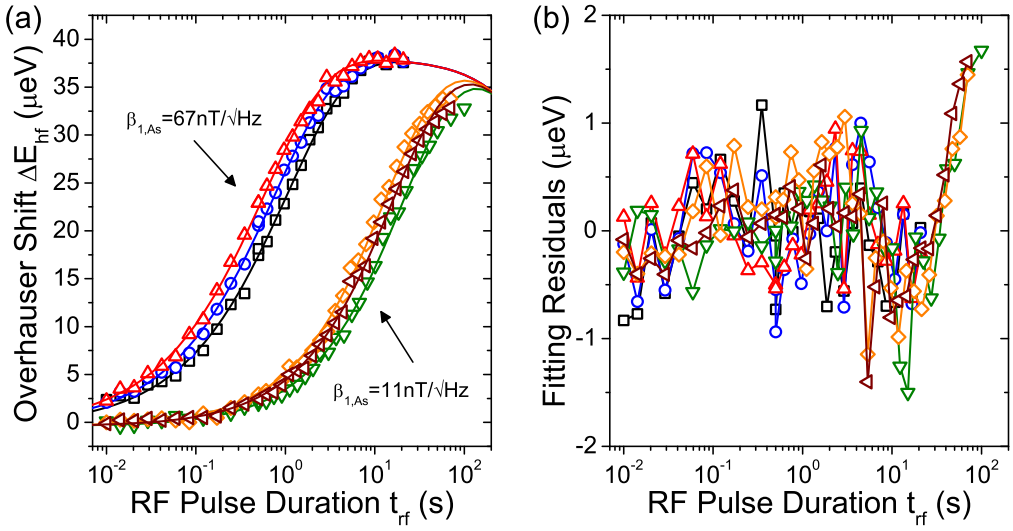

Figure 7.17: (a) Dependence of the ^{75}As depolarisation on the rf pulse duration t_{rf} at ^{75}As comb amplitudes $\beta_{1,\mathrm{As}} \approx 11$ nT/$\sqrt{\mathrm{Hz}}$ and $\beta_{1,\mathrm{As}} \approx 67$ nT/$\sqrt{\mathrm{Hz}}$. Symbols show experimental data for three different ^{71}Ga CT heating comb amplitudes $\beta_{1,\mathrm{Ga}}$. Solid lines show fitting with a stretched exponential function. (b) Respective fitting residuals given by the difference between the experimental and fitted curves.

Representative data for $\beta_{1,\mathrm{As}} \approx 11$ nT/$\sqrt{\mathrm{Hz}}$ and $\beta_{1,\mathrm{As}} \approx 67$ nT/$\sqrt{\mathrm{Hz}}$ at three different ^{71}Ga CT heating amplitudes is shown in figure 7.17a. Solid lines show fitting with a stretched exponential function which takes into account the intrinsic spin relaxation time $T_{1,\mathrm{n}}$:

$$\Delta E_{\mathrm{hf}}(t_{\mathrm{rf}}) = \Delta E_{\mathrm{hf},0}\left(\exp\left[-\frac{t_{\mathrm{rf}}}{T_{1,\mathrm{n}}}\right] - \exp\left[-\left(\frac{t_{\mathrm{rf}}}{\tau_{\mathrm{As}}(\beta_{1,\mathrm{As}},\beta_{1,\mathrm{Ga}})}\right)^{r(\beta_{1,\mathrm{As}})}\right]\right), \quad (7.14)$$

where $r(\beta_{1,\mathrm{As}})$ denotes a dimensionless stretching parameter describing the non-exponential decay at large mode spacings. We keep the total ^{75}As spin polarisation $\Delta E_{\mathrm{hf},0}$ the same for all decay curves and vary r only for different ^{75}As comb ampli-

tudes $\beta_{1,\mathrm{As}}$. The best fits shown in figure 7.17a are obtained for $\Delta E_{\mathrm{hf},0} \approx 39\ \mu$eV and $r \approx 0.6 - 0.9$ depending on $\beta_{1,\mathrm{As}}$. The fitting accuracy is shown in figure 7.17b where the residuals for the curves of figure 7.17a are displayed. We see that all residuals are well within $\pm 2\ \mu$eV, confirming that the depolarisation dynamics are well described by equation (7.14).

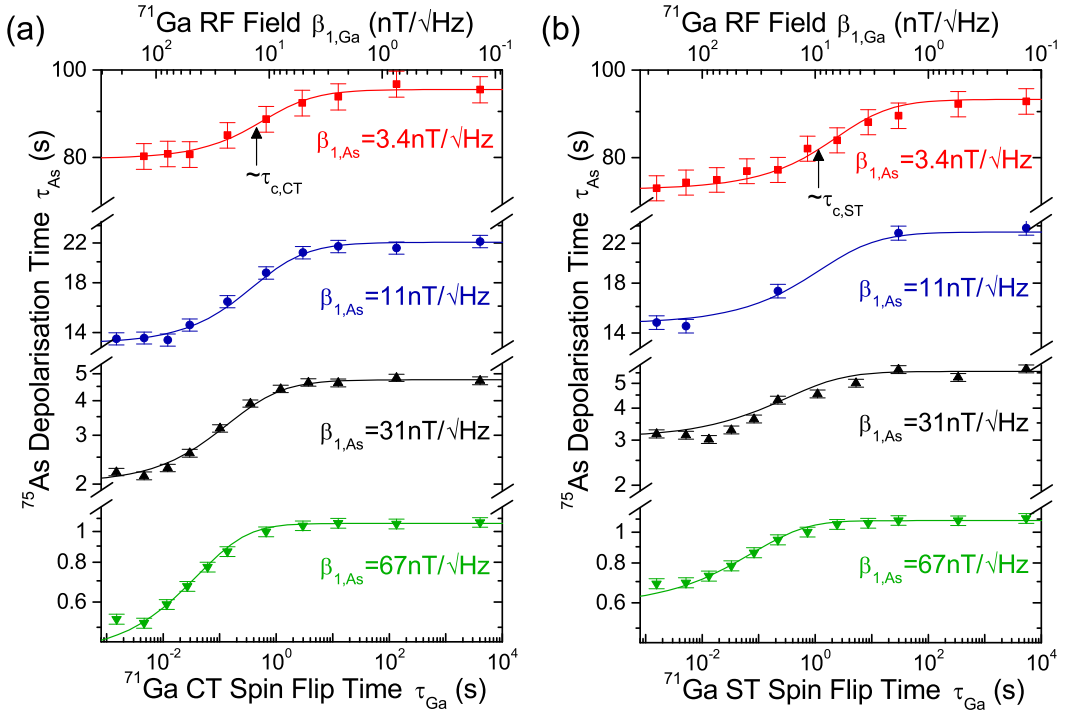

Figure 7.18: ^{75}As depolarisation time τ_{As} as a function of the (a) ^{71}Ga CT and (b) ^{71}Ga ST rf-induced spin-flip time τ_{As} for different ^{75}As comb amplitudes $\beta_{1,\mathrm{As}}$. The top scales show the corresponding ^{71}Ga heating comb amplitudes $\beta_{1,\mathrm{Ga}}$. Error bars mark 95% confidence intervals and solid lines show fitting with the model presented in the text.

Figures 7.18a and b show the central result of this chapter. The ^{75}As depolarisation time τ_{As} is ploted as a function of the ^{71}Ga CT and ST heating amplitude $\beta_{1,\mathrm{Ga}}$, respectively, at four different ^{75}As excitation amplitudes $\beta_{1,\mathrm{As}}$. We also express $\beta_{1,\mathrm{Ga}}$ in terms of the characteristic ^{71}Ga spin flip time $\tau_{\mathrm{Ga}} = 2/(\mathrm{M}_{ij}^2\gamma^2\beta_{1,\mathrm{Ga}}^2)$ with the respective CT and ST transition matrix element M_{ij}.

We observe several key features in the $\tau_{\mathrm{As}}(\beta_{1,\mathrm{As}}, \beta_{1,\mathrm{Ga}})$ dependence which are linked to the intrinsic correlation time τ_{c} of the ^{71}Ga spin flip-flops. Under weak ^{71}Ga heating (small $\beta_{1,\mathrm{Ga}}$), the rf-induced spin-flip time τ_{Ga} is far longer than τ_{c} and the

^{75}As depolarisation time is unaffected by the heating comb. With increasing amplitude $\beta_{1,\mathrm{Ga}}$, we reach a regime where $\tau_{\mathrm{Ga}} < \tau_{\mathrm{c}}$ and the ^{71}Ga spins are "thawed" as discussed in section 7.4. Consequently, the ^{75}As lineshape broadens and τ_{As} is reduced. We further notice that the depolarisation ratio $\Delta\tau_{\mathrm{As}}$ between τ_{As} without ^{71}Ga heating and with strong heating decreases as $\beta_{1,\mathrm{As}}$ is reduced. This is because we probe the ^{71}Ga spin fluctuations over a timescale proportional to the direct ^{75}As spin depolarisation time $\propto \beta_{1,\mathrm{As}}^{-2}$. If the direct ^{75}As depolarisation under the ^{75}As comb is on the order of τ_{c} or slower, the intrinsic ^{71}Ga spin flip-flops also broaden the ^{75}As lineshape and the additional broadening due to ^{71}Ga heating is reduced accordingly.

Taking these considerations into account, we want to find a functional description of $\tau_{\mathrm{As}}(\beta_{1,\mathrm{As}}, \beta_{1,\mathrm{Ga}})$ which allows us to derive the ^{71}Ga spin flip-flop correlation time τ_{c} from the experimental results shown in figures 7.18a and b. We begin by describing the ^{71}Ga spin dynamics by an effective correlation time $(\tau_{\mathrm{Ga}}^{-1} + \tau_{\mathrm{c}}^{-1})^{-1}$. As discussed in the previous paragraph, the ^{75}As lineshape broadening is determined by the ^{71}Ga fluctuations during the characteristic ^{75}As depolarisation time which is on the order of $2/\gamma_{\mathrm{As}}^2\beta_{1,\mathrm{As}}^2$ (compare equation (7.6)). Although we do not know the exact analytical expression linking $\tau_{\mathrm{As}}(\beta_{1,\mathrm{As}}, \beta_{1,\mathrm{Ga}})$ with the ratio $(\tau_{\mathrm{Ga}}^{-1}+\tau_{\mathrm{c}}^{-1})^{-1}/(2/\gamma_{\mathrm{As}}^2\beta_{1,\mathrm{As}}^2)$, we can express it as a Taylor series for which the term linear in $(\tau_{\mathrm{Ga}}^{-1} + \tau_{\mathrm{c}}^{-1})^{-1}$ will be dominant at low ^{75}As comb amplitudes $\beta_{1,\mathrm{As}}$. We note that for varying τ_{Ga} the effective correlation time will always be within the limits $(\tau_{\mathrm{Ga}}^{-1} + \tau_{\mathrm{c}}^{-1})^{-1} \in (0, \tau_{\mathrm{c}})$. Furthermore, we see that $(\tau_{\mathrm{Ga}}^{-1} + \tau_{\mathrm{c}}^{-1})^{-1} = \tau_{\mathrm{c}}/2$ for $\tau_{\mathrm{c}} = \tau_{\mathrm{Ga}}$. Hence, we can obtain an estimate of the ^{71}Ga spin-flip correlation times from the measurements at small $\beta_{1,\mathrm{As}} \approx 3.4\ \mathrm{nT}\sqrt{\mathrm{Hz}}$ (squares in figures 7.18) by determining the induced ^{71}Ga spin-flip time τ_{Ga} for which τ_{As} is the mean of its minimum and maximum values. We get estimated values of $\tau_{\mathrm{c,CT}} \approx 0.5$ s and $\tau_{\mathrm{c,ST}} \approx 1$ s (indicated by black arrows in figures 7.18a and b).

In order to derive τ_{c} more accurately, we have to use an explicit expression which

describes the functional dependence of τ_{As} on $(\tau_{\mathrm{Ga}}^{-1}+\tau_{\mathrm{c}}^{-1})^{-1}/(2/\gamma_{\mathrm{As}}^2\beta_{1,\mathrm{As}}^2)$. We find that a stretched exponential function of the form

$$\tau_{\mathrm{As}}(\beta_{1,\mathrm{As}},\beta_{1,\mathrm{Ga}}) = \tau_{\mathrm{As,min}}(\beta_{1,\mathrm{As}}) \left(\Delta\tau_{\mathrm{As}} + (1-\Delta\tau_{\mathrm{As}})\exp\left[-\left(\frac{1}{\theta}\frac{(\tau_{\mathrm{Ga}}^{-1}+\tau_{\mathrm{c}}^{-1})^{-1}}{2/\gamma_{\mathrm{As}}^2\beta_{1,\mathrm{As}}^2}\right)^{s}\right]\right), \tag{7.15}$$

describes the experimentally observed behaviour well. Here, s and θ are dimensionless parameters characterising the stretched exponential function and $\Delta\tau_{\mathrm{As}}$ is the ratio of the depolarisation times $\tau_{\mathrm{As,max}}(\beta_{1,\mathrm{As}})$ without and $\tau_{\mathrm{As,min}}(\beta_{1,\mathrm{As}})$ with strong ^{71}Ga heating. For fitting of the experimental data, we use the same varied s, θ, $\Delta\tau_{\mathrm{As}}$ and τ_{c} for all $\beta_{1,\mathrm{As}}$ and $\beta_{1,\mathrm{Ga}}$. By contrast, $\tau_{\mathrm{As,min}}(\beta_{1,\mathrm{As}})$ is fitted separately for each set of data with fixed $\beta_{1,\mathrm{As}}$.

The solid lines in figures 7.18a and b show the best fit results for ^{71}Ga CT and ST heating, respectively. We obtain fitting parameters $s \approx 0.62$, $\theta \approx 0.32$, $\Delta\tau_{\mathrm{As}} \approx 2.55$

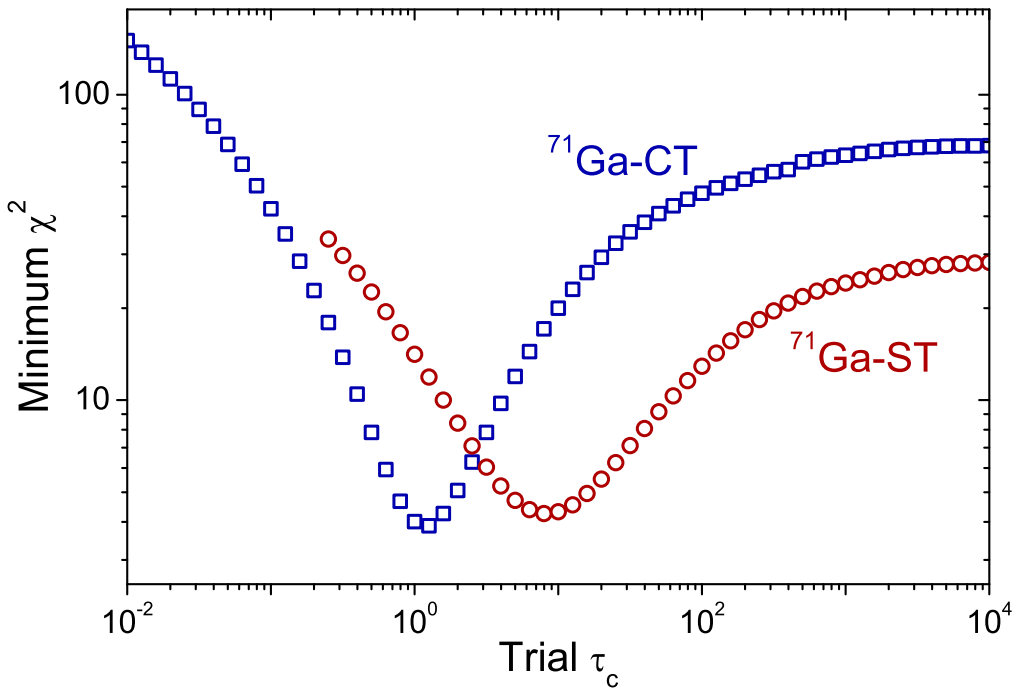

Figure 7.19: Minimum fitting residual χ^2 for fitting of equation (7.15) to the experimental $\tau_{\mathrm{As}}(\beta_{1,\mathrm{As}},\beta_{1,\mathrm{Ga}})$ values as a function of fixed trial τ_{c} values for ^{71}Ga CT (squares) and ST (circles) heating.

and $\tau_{c,CT} \approx 1.2 \pm 0.2$ s for the ^{71}Ga CT measurements and $s \approx 0.51$, $\theta \approx 0.52$, $\Delta\tau_{As} \approx 1.84$ and $\tau_{c,ST} \approx 6.9 \pm 2.7$ s for the ^{71}Ga ST. The errors stated for the spin-flip correlation times τ_c are 95% confidence intervals.

The τ_c values obtained from fitting with equation (7.15) are in reasonable agreement with the estimated correlation times derived from the linear approximation at low ^{75}As comb amplitude. We can examine the quality of the stretched exponential model further by studying the dependence of the fitting residual χ^2 on τ_c: the correlation time τ_c is kept fixed and the remaining fitting parameters are adjusted for a best fit to the experimental data by minimising χ^2. This is done over a wide range of trial τ_c values, with results shown in figure 7.19. Sharp minima for the fit quality of both data sets (^{71}Ga CT and ST heating) demonstrate that equation (7.15) gives a very good description of our experimental results.

The observed homonuclear dipolar spin flip-flop times $\tau_c \gtrsim 1$ s in a self-assembled InGaAs quantum dot are several orders of magnitude longer than the typical values of $\tau_c \sim 100$ μs found in unstrained III-V semiconductor materials[29, 112]. Based on the findings of [41], chapter 5 and section 7.4 we attribute this to the suppression of homonuclear flip-flops under strongly inhomogeneous quadrupolar interactions. The observation of $\tau_{c,ST} > \tau_{c,CT}$ further corroborates this interpretation as the ST is affected by the quadrupolar interaction in first order while the broadening of the CT is dominated by the much smaller second order term[39].

The ^{71}Ga nuclei probed in these experiments have the largest gyromagnetic ratio γ and the smallest quadrupolar moment Q of all stable isotopes in the InGaAs quantum dot. Hence, we expect even longer correlation times for all other isotopes, resulting in $\tau_c \gtrsim 1$ s for the entire nuclear spin bath. As a consequence, we can conclude that electron spin qubit coherence times in the dot will not be limited by the intrinsic nuclear spin bath dynamics up to sub-second timescales in high external magnetic fields[29, 30]. However, additional hyperfine mediated nuclear-nuclear interactions might reduce τ_c noticeably in the presence of an electron.

7.6 Conclusions

Frequency comb NMR allows for the nuclear spin bath dynamics to be probed without limitations such as spin locking, instantaneous diffusion and sensitivity to resonance offsets associated with pulsed NMR techniques. Its low-power, broadband rf excitation profile allows the measurement of the homogeneous lineshape of an isotope with arbitrarily large inhomogeneously broadened NMR spectrum while putting only minimum requirements on the studied system ($T_{1,\mathrm{n}} > 10 - 100 \cdot T_{\mathrm{M,n}}$). From experiments on quadrupolar broadened ^{75}As and ^{71}Ga NMR spectra in self-assembled InGaAs quantum dots we obtained homogeneous linewidths $\Delta\nu_{\mathrm{hom}}(^{75}\mathrm{As}) \approx 118$ Hz and $\Delta\nu_{\mathrm{hom}}(^{71}\mathrm{Ga}) \approx 221$ Hz in good agreement with the phase memory times measured in Hahn echo (see chapter 5).

We further observed that the homogeneous lineshapes of both isotopes were non-Gaussian, a feature which results directly from the strong freezing of homonuclear dipolar spin flip-flops under inhomogeneous quadrupolar interaction. The dipolar broadening can be restored partially by "heating" other isotopes with additional frequency combs during the measurement. We demonstrated this in a two-comb experiment where additional ^{71}Ga spin-flips were induced with a second rf frequency comb while the depolarisation dynamics of ^{75}As were probed. This led to a measurable change of the ^{75}As homogeneous lineshape towards a broader, more Gaussian-like profile.

The sensitivity of frequency comb NMR to the induced and intrinsic spin dynamics of the environment of a probed isotope was used in a subsequent three-comb experiment: from a detailed study of the interplay between the ^{75}As comb amplitude $\beta_{1,\mathrm{As}}$ and the relative effects of rf induced and intrinsic ^{71}Ga CT and ST spin-flip timescales we deduced the ^{71}Ga nuclear spin flip-flop correlation times $\tau_{\mathrm{c,CT}} \approx 1.2 \pm 0.2$ s and $\tau_{\mathrm{c,ST}} \approx 6.9 \pm 2.7$ s. These values are orders of magnitude longer than the corresponding phase memory times $T_{\mathrm{M,n}}$ presented in the previous chapters. We conclude that the intrinsic nuclear spin bath dynamics in a strained

self-assembled quantum dot do not limit the charge spin qubit decoherence times up to sub-second timescales. Instead, the focus of future work aimed at creating a quiescent environment for spin qubits in self-assembled quantum dots should be on the study and control of other sources of charge spin decoherence such as charge fluctuations or indirect electron (hole) mediated nuclear-nuclear interactions.

8 Conclusions and Outlook

The coherence of electron and hole spin qubits in III-V semiconductor quantum dots is ultimately limited by the magnetic interaction with an environment of $\sim 10^4 - 10^6$ non-zero nuclear spins[29, 30]. In order to develop strategies for overcoming this limitation it is essential to gain a comprehensive understanding of the nuclear spin bath dynamics in a quantum dot. The work presented in this thesis was aimed at probing and controlling the spin bath coherence in a single charge-free InGaAs quantum dot. To this end, we developed new multiple pulse NMR protocols and a novel, weakly-invasive frequency comb NMR technique. Using optically detected NMR schemes which exploit the fact that the nuclear spin bath polarisation is reflected in the hyperfine shift of excitonic transition lines, we obtained several key results:

(i) Recent work by Chekhovich et al. revealed unexpectedly long nuclear Hahn echo decay times for the central transitions of ^{75}As and ^{71}Ga in self-assembled InGaAs quantum dots[41]. This was attributed to the strong suppression of homonuclear dipolar flip-flops by strain-induced inhomogeneous quadrupolar interactions. In chapter 5, we presented the results of Hahn echo measurements on quantum dots in a p-i-n diode sample where we were able to ensure charge-free conditions under large reverse bias. The measured phase memory times $T_{\mathrm{M,n}}^{\mathrm{HE}}(^{75}\mathrm{As}) = 3.97 \pm 0.23$ ms and $T_{\mathrm{M,n}}^{\mathrm{HE}}(^{71}\mathrm{Ga}) = 1.37 \pm 0.25$ ms are in excellent agreement with the values reported for a gate-free sample in [41]. We were thus able to establish that these Hahn echo decay timescales are indeed limited by a combination of instantaneous diffusion and

homonuclear spin flip-flops and not by electron- or hole-mediated nuclear-nuclear interactions - an aspect which could not be fully ascertained with the ungated sample structure.

(ii) The central electron/hole spin coherence in a quantum dot is not limited by the mere presence of the nuclear spin bath but by its fluctuations. If the spin bath was evolving in a coherent and predictable way, central spin coherence could be extended noticeably by suitable electron (hole) spin manipulation protocols. In chapter 6, we used average Hamiltonian theory (AHT) to design a set of new combined Hahn and solid echo NMR sequences which are able to suppress both inhomogeneous dephasing and homonuclear dipolar broadening. We measured spin bath decoherence times of up to $T_{2,\mathrm{n}}^{\mathrm{BR24}}(^{75}\mathrm{As}) = 22.4 \pm 4.5$ ms for ^{75}As using the CPMG-BR24 sequence. For practical applications, the shorter and less complex CPMG-MREV16 sequence proved to be more robust against resonance offsets and pulse calibration errors while still increasing the spin bath coherence noticeably beyond the Hahn echo limits with values of $T_{2,\mathrm{n}}^{\mathrm{MREV16}}(^{75}\mathrm{As}) = 11.85 \pm 1.04$ ms and $T_{2,\mathrm{n}}^{\mathrm{MREV16}}(^{71}\mathrm{Ga}) = 2.79 \pm 0.20$ ms obtained experimentally. A general trend of increasing $T_{2,\mathrm{n}}$ under longer and more complex pulse sequences indicates that the decay times are limited by non-vanishing higher-order average Hamiltonian terms and even longer spin bath coherence could be achieved with more advanced pulse sequences.

(iii) Multiple repetitions of the CPMG-MREV16 cycle did not lead to an increase of the measured decoherence times in ^{75}As and ^{71}Ga. This implies that the probed nuclear spin ensemble is not subject to a fast-fluctuating environment and that the heteronuclear coupling with other isotopes is quasistatic over the probed cycle times of up to several milliseconds.

(iv) It is very difficult to measure the characteristic timescales of the nuclear spin bath fluctuations limiting the central spin coherence directly using pulsed NMR. In chapter 7, we introduced a novel frequency comb NMR technique which allowed us to probe the equilibrium spin bath dynamics under low-power rf excitation and to

measure the spin bath fluctuation correlation times τ_c directly. By characterising the relative influence of intrinsic and rf-induced spin-flips within the ^{71}Ga central and satellite transitions on the ^{75}As homogeneous linewidth we derived nuclear spin correlation times $\tau_c \gtrsim 1$ s, exceeding timescales in comparable strain-free structures by four orders of magnitude[29, 112].

These findings not only increase our understanding of the nuclear spin bath dynamics in self-assembled quantum dots considerably, but also give directions to the design of even more stable spin bath environments. We saw that the strong inhomogeneous quadrupolar broadening in the InGaAs dots is a valuable resource for long nuclear phase memory times $T^{\mathrm{HE}}_{\mathrm{M,n}}$ and spin bath correlation times τ_c. As suggested in [41], this effect could be enhanced further by introducing a fourth compound partially substituting the anionic arsenic nuclei. This would extend the additional local strain due to compositional disorder observed for ^{75}As in our system to the cationic nuclei and increase the suppression of homonuclear spin flip-flops within the gallium and indium spin ensembles.

We found that the performance of the multiple pulse combined echo sequences introduced in chapter 6 suffers from some experimental drawbacks. Consequently, the best results were obtained for the 20-pulse CPMG-MREV16 sequence. Further optimisation of the rf matching circuit and of the rf coupling to the quantum dot nuclear spin bath would allow for higher rf magnetic field amplitudes and shorter pulse times. This would in turn increase the robustness of the multiple pulse sequences against frequency offsets arising from the $\sim 10-40$ kHz wide inhomogeneous linewidths of the studied nuclear spin transitions and could be realised by using an on-chip rf antenna as e.g. in [40]. In addition, the use of composite pulses could increase the pulse quality and reduce the effect of pulse calibration errors[264–266]. In this way, it might become experimentally feasible to control the nuclear spin bath evolution under CPMG-BR24 and more elaborate sequences which currently exceed the capability of our setup.

So far, our work has focused on empty quantum dots, i.e. on the evolution of the nuclear spin bath in the absence of localised charge carriers. Having established the outstanding stability of the nuclear spin bath under these conditions, future research efforts should concentrate on the spin bath dynamics in the presence of a confined electron or hole. The effect of the Knight field on the nuclear spin bath in an InGaAs quantum dot has not been studied in much detail yet[134, 135] and electron- or hole-mediated nuclear-nuclear coupling can strongly affect the spin bath coherence. Recent Hahn echo experiments by Munsch et al.[42] have revealed that the nuclear spin phase memory time decreases to tens of microseconds in the presence of a single electron and recovers when a second electron is added. A more detailed study of the homogeneous NMR lineshape and spin bath correlation time under these conditions using frequency comb NMR would be of great interest. Furthermore, the multiple pulse sequences introduced in chapter 6 might provide a ready solution for restoring the nuclear spin bath coherence and suppressing the indirect coupling mechanism, allowing for strongly enhanced electron spin coherence times.

Of course, the applicability of both the combined echo sequences and the frequency comb NMR technique is not limited to InGaAs quantum dots. CPMG-MREV16 NMR sequences could be used e.g. in combination with existing ESR techniques to extend the electron spin coherence time in electrostatically defined GaAs/AlGaAs quantum dots beyond the values of ~ 870 μs obtained by Malinowski et al.[174] Frequency comb NMR, on the other hand, is a tool which performs best in conditions of strong inhomogeneous broadening where conventional pulsed NMR methods are severely handicapped due to their finite resonance offset tolerance. Unlike pulsed NMR, it is also not hampered by instantaneous diffusion, which can mask the spin bath correlation times which are most relevant with regards to spin qubit applications. In conclusion, both techniques could be used in a variety of spin systems and have unique features that can complement existing NMR methods.

9 Appendix

9.1 Dipolar Alphabet

The dipolar coupling Hamiltonian for two interacting spins $\boldsymbol{I}$ and $\boldsymbol{J}$

$$\mathcal{H}_{\mathrm{dd}} = \frac{\mu_0}{4\pi}\gamma_I\gamma_J\frac{\hbar^2}{r_{ij}^3}\left(\boldsymbol{I}\cdot\boldsymbol{J} - 3\frac{(\boldsymbol{I}\cdot\boldsymbol{r}_{ij})(\boldsymbol{J}\cdot\boldsymbol{r}_{ij})}{r_{ij}^2}\right) , \tag{9.1}$$

can be decomposed into six terms describing distinct quantum transitions[116, 192]. We start by expressing the connecting vector $\boldsymbol{r}_{ij}$ of the relative positions of the two spins in spherical coordinates as illustrated in figure 9.1.

$$\begin{aligned}\mathcal{H}_{\mathrm{dd}} = \frac{\mu_0}{4\pi}\gamma_I\gamma_J\frac{\hbar^2}{r_{ij}^3}(\boldsymbol{I}\cdot\boldsymbol{J} - 3(I_{\mathrm{z}}\cos\theta + \sin\theta(I_{\mathrm{x}}\cos\phi + I_{\mathrm{y}}\sin\phi)\cdot \\ \cdot (J_{\mathrm{z}}\cos\theta + \sin\theta(J_{\mathrm{x}}\cos\phi + J_{\mathrm{y}}\sin\phi))) .\end{aligned} \tag{9.2}$$

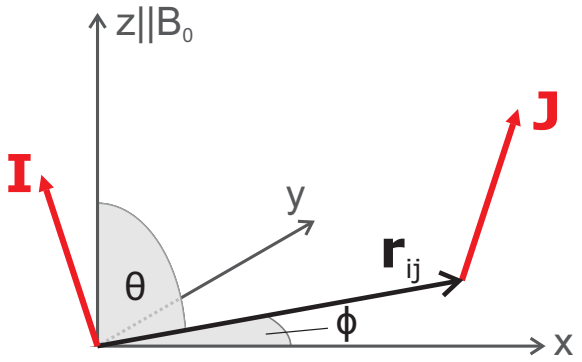

Figure 9.1: The vector $\boldsymbol{r}_{ij}$ describes the relative position of the two dipolar coupled spins $\boldsymbol{I}$ and $\boldsymbol{J}$ and can be expressed as $\boldsymbol{r}_{ij} = r_{ij}(\sin\theta\cos\phi, \sin\theta\sin\phi, \cos\theta)$ in spherical coordinates.

We introduce the raising and lowering operators $I_\pm = I_\mathrm{x} \pm \mathrm{i}I_\mathrm{y}$ and make use of the identity $\mathrm{e}^{\pm\mathrm{i}\phi} = \cos\phi \pm \sin\phi$:

$$\begin{aligned}\mathcal{H}_\mathrm{dd} = \frac{\mu_0}{4\pi}\gamma_I\gamma_J\frac{\hbar^2}{r_{ij}^3}(\boldsymbol{I}\cdot\boldsymbol{J} - 3(I_\mathrm{z}\cos\theta + \tfrac{1}{2}\sin\theta(I_+\mathrm{e}^{-\mathrm{i}\phi} + I_-\mathrm{e}^{\mathrm{i}\phi})\cdot \\ \cdot (J_\mathrm{z}\cos\theta + \tfrac{1}{2}\sin\theta(J_+\mathrm{e}^{-\mathrm{i}\phi} + J_-\mathrm{e}^{\mathrm{i}\phi}))) \qquad (9.3)\\ = \frac{\mu_0}{4\pi}\gamma_I\gamma_J\frac{\hbar^2}{r_{ij}^3}(A+B+C+D+E+F)\ .\end{aligned}$$

These are the terms of the *dipolar alphabet*:

$$\begin{aligned}A &= I_\mathrm{z}J_\mathrm{z}(1-3\cos^2\theta)\\ B &= -\tfrac{1}{2}(\boldsymbol{I}\cdot\boldsymbol{J} - I_\mathrm{z}J_\mathrm{z})(1-3\cos^2\theta)\\ C &= -\tfrac{3}{2}(I_\mathrm{z}J_+ + I_+J_\mathrm{z})\sin\theta\cos\theta\mathrm{e}^{-\mathrm{i}\phi}\\ D &= -\tfrac{3}{2}(I_\mathrm{z}J_- + I_-J_\mathrm{z})\sin\theta\cos\theta\mathrm{e}^{\mathrm{i}\phi} = C^*\\ E &= -\tfrac{3}{4}I_+J_+\sin^2\theta\mathrm{e}^{-2\mathrm{i}\phi}\\ F &= -\tfrac{3}{4}I_-J_-\sin^2\theta\mathrm{e}^{2\mathrm{i}\phi} = E^*\ .\end{aligned} \qquad (9.4)$$

The first term A describes a static interaction between the two spins. Term B can induce mutual spin flip-flops of $\boldsymbol{I}$ and $\boldsymbol{J}$. By contrast, terms C and D induce a single spin flip and the contributions of E and F raise or lower both spins simultaneously. These last four terms represent a weak dipolar mixing of one and two quantum transitions, which can give rise to very weak additional NMR transition lines at frequencies 0, $2\omega_\mathrm{L}$ and $3\omega_\mathrm{L}$.

9.2 Average Hamiltonian Theory Analysis of APCP

9.2.1 Average Hamiltonian of APCP with Finite Pulse Durations

We begin by considering the nuclear spin bath Hamiltonian of equation (6.2)

$$\mathcal{H}_{\text{total}}(t) = \mathcal{H}_0 + \mathcal{H}_{\text{D}}^{\text{zz}} + \mathcal{H}_{\text{rf}}(t) \ , \tag{9.5}$$

The cyclic time-dependent (external) rf Hamiltonian for the APCP sequence ($\tau - \pi_{\text{X}} - 2\tau - \pi_{\bar{\text{X}}} - \tau$) is illustrated in figure 9.2 below.

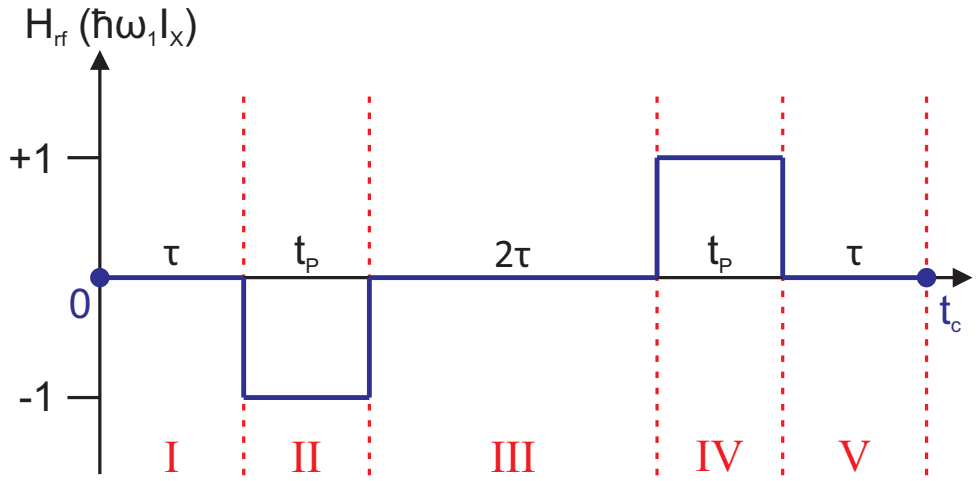

Figure 9.2: Time-dependence of the rf Hamiltonian $\mathcal{H}_{\text{rf}}(t)$ for a cycle of the APCP sequence. Dashed lines mark the intervals I – V, during which $\mathcal{H}_{\text{rf}}(t)$ is constant.

With the rf propagator $\mathcal{U}_{\text{rf}}$ of equation (6.4) and the internal Hamiltonian $\mathcal{H}_{\text{int}} = \mathcal{H}_0 + \mathcal{H}_{\text{D}}^{\text{zz}}$ we can determine the toggling frame Hamiltonian

$$\tilde{\mathcal{H}}_{\text{int}}(t) = \mathcal{U}_{\text{rf}}^{-1}(\text{I})\mathcal{U}_{\text{rf}}^{-1}(\text{II}) \cdots \mathcal{H}_{\text{int}} \cdots \mathcal{U}_{\text{rf}}(\text{II})\mathcal{U}_{\text{rf}}(\text{I}) \ , \tag{9.6}$$

for each of the five time intervals indicated in figure 9.2. We note that the time order of the rf propagators is reversed due to the Dyson operator, i.e. the latest rf pulse within $[0, t]$ is applied to $\mathcal{H}_{\text{int}}$ first. The resulting toggling frame Hamiltonians $\tilde{\mathcal{H}}_0(t)$ and $\tilde{\mathcal{H}}_{\text{D}}(t)$ are listed in table 9.1 (after [260]).

Time Interval	$\tilde{\mathcal{H}}_0$	$\tilde{\mathcal{H}}_\mathrm{D}$
I	$\mathcal{H}_0^\mathrm{z}$	$\mathcal{H}_\mathrm{D}^\mathrm{zz}$
II	$\mathcal{H}_0^\mathrm{z}\cos(\theta(t_\mathrm{II})) - \mathcal{H}_0^\mathrm{y}\sin(\theta(t_\mathrm{II}))$	$-\frac{1}{2}\mathcal{H}_\mathrm{D}^\mathrm{xx} + \mathcal{H}_\mathrm{D}^\mathrm{x,S}\cos(2\theta(t_\mathrm{II})) - \mathcal{H}_\mathrm{D}^\mathrm{x,A}\sin(2\theta(t_\mathrm{II}))$
III	$-\mathcal{H}_0^\mathrm{z}$	$\mathcal{H}_\mathrm{D}^\mathrm{zz}$
IV	$-\mathcal{H}_0^\mathrm{z}\cos(\theta(t_\mathrm{IV})) - \mathcal{H}_0^\mathrm{y}\sin(\theta(t_\mathrm{IV}))$	$-\frac{1}{2}\mathcal{H}_\mathrm{D}^\mathrm{xx} + \mathcal{H}_\mathrm{D}^\mathrm{x,S}\cos(2\theta(t_\mathrm{IV})) + \mathcal{H}_\mathrm{D}^\mathrm{x,A}\sin(2\theta(t_\mathrm{IV}))$
V	$\mathcal{H}_0^\mathrm{z}$	$\mathcal{H}_\mathrm{D}^\mathrm{zz}$

Table 9.1: Toggling frame Hamiltonians for the time intervals of an APCP cycle with finite rf pulse width t_p. $t_\mathrm{II/IV}$ denotes the time within the respective interval, starting from zero.

Here, we have introduced symmetric and asymmetric Hamiltonians as defined in[260]:

$$\begin{aligned}\mathcal{H}_\mathrm{D}^\mathrm{x,A} &= \frac{3}{2}\sum_{m=1}^{N}\sum_{n>m}^{N}\omega_{mn}\left(I_{\mathrm{y},n}I_{\mathrm{z},m} + I_{\mathrm{z},n}I_{\mathrm{y},m}\right)\\ \mathcal{H}_\mathrm{D}^\mathrm{x,S} &= \frac{3}{2}\sum_{m=1}^{N}\sum_{n>m}^{N}\omega_{mn}\left(I_{\mathrm{z},n}I_{\mathrm{z},m} - I_{\mathrm{y},n}I_{\mathrm{y},m}\right)\ .\end{aligned} \tag{9.7}$$

Using equations (6.8) and (6.9), we can now determine the zeroth and first order average Hamiltonian by integrating over the full cycle time $t_\mathrm{c} = 4\tau + 2t_\mathrm{p}$. While the first order term $\bar{\mathcal{H}}^{(1)}$ vanishes due to the symmetry properties of the APCP cycle, we obtain

$$\bar{\mathcal{H}}^{(0)} = \frac{1}{t_\mathrm{c}}\left(-\frac{4t_\mathrm{p}\Omega_\mathrm{z}}{\pi}I_\mathrm{y} + 4\tau\mathcal{H}_\mathrm{D}^\mathrm{zz} - t_\mathrm{p}\mathcal{H}_\mathrm{D}^\mathrm{xx}\right)\ , \tag{9.8}$$

for the zeroth order contribution.

9.2.2 Second Averaging

We treat the term proportional to I_y in equation (9.8) as a static transverse field[260, 278] and define a Rabi angular frequency

$$\Omega' = \frac{4t_\mathrm{p}\Omega_\mathrm{z}}{\pi t_\mathrm{c}}\ . \tag{9.9}$$

Next, we split $\bar{\mathcal{H}}^{(0)}$ into an external Hamiltonian $\bar{\mathcal{H}}_{\text{ext}} = \omega' I_{\text{y}}$ and an internal Hamiltonian $\bar{\mathcal{H}}_{\text{int}}$ containing the two dipolar terms. With $\mathcal{U}_{\text{ext}}(t) = \exp\left(-\frac{\text{i}}{\hbar}\bar{\mathcal{H}}_{\text{ext}}t\right)$, the second toggling frame Hamiltonian is

$$\begin{aligned}\tilde{\bar{\mathcal{H}}}(t) =& \mathcal{U}_{\text{ext}}^{-1}(t)\bar{\mathcal{H}}_{\text{int}}\mathcal{U}_{\text{ext}}(t) = \\ =& \frac{4\tau}{t_{\text{c}}}\left[-\frac{1}{2}\mathcal{H}_{\text{D}}^{\text{yy}} + \cos(2\Omega' t)\mathcal{H}_{\text{D}}^{\text{y,S}} + \sin(2\Omega' t)\mathcal{H}_{\text{D}}^{\text{y,A}}\right] - \\ & - \frac{t_{\text{p}}}{t_{\text{c}}}\left[-\frac{1}{2}\mathcal{H}_{\text{D}}^{\text{yy}} - \cos(2\Omega' t)\mathcal{H}_{\text{D}}^{\text{y,S}} - \sin(2\Omega' t)\mathcal{H}_{\text{D}}^{\text{y,A}}\right] .\end{aligned} \tag{9.10}$$

where we used, in analogy to equations (9.7)[260]:

$$\begin{aligned}\mathcal{H}_{\text{D}}^{\text{y,A}} &= \frac{3}{2}\sum_{m=1}^{N}\sum_{n>m}^{N}\omega_{mn}\left(I_{\text{x},n}I_{\text{z},m} + I_{\text{z},n}I_{\text{x},m}\right) \\ \mathcal{H}_{\text{D}}^{\text{y,S}} &= \frac{3}{2}\sum_{m=1}^{N}\sum_{n>m}^{N}\omega_{mn}\left(I_{\text{z},n}I_{\text{z},m} - I_{\text{x},n}I_{\text{x},m}\right) .\end{aligned} \tag{9.11}$$

The zeroth order second average Hamiltonian is given by time-averaging equation (9.10) over one Rabi cycle $t' = 2\pi/\omega'$ in the transverse field. The oscillating terms average out to zero and we are left with

$$\bar{\tilde{\bar{\mathcal{H}}}}^{(0)} = \frac{1}{t'}\int_0^{t'} \text{d}t\tilde{\bar{\mathcal{H}}}(t) = \frac{1}{t'}\int_0^{t'} \text{d}t\frac{1}{2t_{\text{c}}}(-4\tau + t_{\text{p}})\mathcal{H}_{\text{D}}^{\text{yy}} = -\frac{1}{t_{\text{c}}}\left(2\tau - \frac{t_{\text{p}}}{2}\right)\mathcal{H}_{\text{D}}^{\text{yy}} . \tag{9.12}$$

10 Symbols and Constants

Symbol	Description
∂	Partial derivative
$\boldsymbol{\nabla}$	Nabla operator
$\varnothing_{\mathrm{c}}$	Inner coil diameter
$\varnothing_{\mathrm{w}}$	Wire diameter
a	Lattice constant
a_i	Spin-spin coupling constant
$\boldsymbol{A}$	Vector potential
$A^{\mathrm{e/h}}$	Electron/hole hyperfine constant
b_i	Spin-spin coupling constant
$\boldsymbol{B}_0$, $B_{0,i}$	Magnetic field, with component along direction i
B_1	RF magnetic field in the rotating frame
B_{hf}	Overhauser field
B_{K}	Knight field
B_{loc}	Local magnetic field at lattice site
B_{rf}	Magnetic field amplitude of full frequency comb
c_j	relative concentration of j-th element
d	Height, thickness, separation
D	Length

Symbol	Description
$\hat{e}_i$	Unit vector in direction i
E	Energy
E^{gap}	Band gap energy
E_{B}	Exciton binding energy
E_{hf}	Overhauser/hyperfine energy shift
f	Focal length
f_{e}	Electron filling factor
f_{MS}	Frequency comb mode spacing
F	Pulse filling factor
$\boldsymbol{F}$, F	Electric field
$\boldsymbol{g}_{\mathrm{e/h/ex}}$,	Electron/hole/exciton g factor (tensor)
$g_{\mathrm{e/h/ex},i}$	
$\tilde{\mathcal{H}}$	Toggling frame Hamiltonian
$\bar{\mathcal{H}}$	Average Hamiltonian
$\mathcal{H}_0$	Resonance offset Hamiltonian
$\mathcal{H}_{\mathrm{dd}}$	Dipolar Hamiltonian
$\mathcal{H}_{\mathrm{D}}$	Secular dipolar Hamiltonian
$\mathcal{H}_{\mathrm{D0}}$	Cross term between $\mathcal{H}_{\mathrm{D}}$ and $\mathcal{H}_0$
$\mathcal{H}_{\mathrm{exch}}$	Exchange interaction Hamiltonian
$\mathcal{H}_{\mathrm{hf}}$	Hyperfine interaction Hamiltonian
$\mathcal{H}_{IJ}$	Heteronuclear dipolar Hamiltonian
$\mathcal{H}_{I-\mathrm{env}}$	Spin environment coupling Hamiltonian
$\mathcal{H}_{\mathrm{int}}$	Internal Hamiltonian
$\mathcal{H}_{\mathrm{Q}}$	Quadrupolar Hamiltonian
$\mathcal{H}_{\mathrm{rf}}$	RF coupling Hamiltonian
$\mathcal{H}_{\mathrm{Z}}$	Zeeman Hamiltonian

Symbol	Description
$\boldsymbol{I}$, I, I_i	Probed nuclear spin, with quantum number and projection along i
$\boldsymbol{J}$, J, J_i	Non-probed nuclear spin, with quantum number and projection along i
$\boldsymbol{J}_{\mathrm{ex}}$, J_{ex}, $J_{\mathrm{ex},i}$	Exciton total angular momentum, with quantum number and projection along i
$\boldsymbol{J}_{\mathrm{h}}$, J_{h}, $J_{\mathrm{h},i}$	Hole total angular momentum, with quantum number and projection along i
k	Roll-off parameter
$\boldsymbol{L}$, L, L_i	Orbital angular momentum, with quantum number and projection along i
$L(\nu)$	Lineshape
L_{c}	Coil inductance
m	Mass
m^*	Effective mass
m_{I}	Secondary spin quantum number
$\mathbf{M}$, M_{ij}	Transition matrix
$\boldsymbol{M}$, M_i	Magnetisation, with component along i
$\boldsymbol{M}_0$, M_0	Equilibrium magnetisation
n	Refractive index
n_{c}	RF pulse cycle number
n_π	Number of π pulses
N	Number of spins
N_{m}	Number of modes in a frequency comb
$\boldsymbol{p}$	Momentum operator
$\boldsymbol{p}_{\mathrm{d}}$, p_{d}	Dipole moment
p_{diab}	Diabatic transition probability

Symbol	Description
p_{m}	Population probability of state m_{I}
P	Power
P_{rf}	RF input power
P_{Sat}	Optical saturation power
r	Exponential stretching parameter
$\boldsymbol{r}$, $\boldsymbol{r}_{ij}$, r_{ij}	Connecting vector, displacement vector
q	Charge
Q	Quality factor
Q	Quadrupolar moment
R	Rotation matrix
S	Length
$\boldsymbol{S}$, S, S_i	Charge spin 1/2, with quantum number and projection along i
S_{ijkl}, S_{ij}	Gradient-elastic tensor in matrix and Voigt notation
t	Time
t_{c}	RF pulse cycle time
t_{cycle}	Experiment cycle time
t_{depol}	RF depolarisation comb time
t_{p}	RF pulse duration
t_{probe}	Optical probe time
t_{pump}	Optical pump time
t_{rise}	Pulse rise time
t_{rf}	RF excitation time
$t_{\pi,\pi/2}$	π, $\frac{\pi}{2}$ pulse duration
$\mathcal{T}$	Dyson time-ordering operator
T	Temperature
$T_{1,\mathrm{n/e/h}}$	Longitudinal nuclear/electron/hole spin relaxation time

Symbol	Description
$T_{2,\mathrm{n/e/h}}$	Nuclear/electron/hole spin coherence time
$T^*_{2,\mathrm{n/e/h}}$	Nuclear/electron/hole spin dephasing time
$T_{\mathrm{M,n}}$	Nuclear phase memory time
T_{nuc}	Nuclear spin temperature
T_{rf}	Transmission coefficient
T_{Rabi}	Rabi period
$\boldsymbol{T}_\omega$	Transformation matrix for rotation about $\boldsymbol{\omega}$
u	Bloch function
$\mathcal{U}$	Time evolution operator
v_0	Unit cell volume
$\mathcal{V}$	Perturbation Hamiltonian
V, V_0	Potential
V_{bi}	Built-in bias
V_{bias}	Diode bias voltage
V_{ij}	Electric field gradient tensor
V_{probe}	Diode probe bias voltage
V_{pump}	Diode pump bias voltage
V_{rf}	Diode rf manipulation bias voltage
$W_{m,m+1}$	Transition rate between states m_I and $m_\mathrm{I}+1$
Z_0	Characteristic impedance
Z_i	Input impedance
Z_L	Load impedance
Z_S	Stub impedance

Symbol	Description
α	Polarisability
β	Exponential compression factor
β_1	RF magnetic field density in frequency comb NMR
β_p	Phase constant
β_VB	Valence band mixing parameter
γ, γ_I, γ_J	Nuclear gyromagnetic ratio
γ^*	Nuclear gyromagnetic ratio divided by 2π
γ_2	Diamagnetic coefficient
γ_F	Film surface energy
γ_S	Substrate surface energy
γ_SF	Substrate-film interface energy
$\mathbf{\Gamma}$,Γ_{ij}	Decay rate matrix
Γ_rf	Transmission coefficient
δ	RF resonance offset normalised by T_Rabi^{-1}
δ_0	Bright-dark exciton splitting
δ_b	Bright exciton fine structure splitting
δ_d	Dark exciton fine structure splitting
$\delta\varphi$	Phase error
$\delta\nu$	RF excitation gap in inverse NMR
Δ,$\Delta\omega$	Angular frequency detuning
Δ_so	Spin-orbit splitting
ΔE_hf	Change of hyperfine shift
ΔE_Stark	Stark shift
ΔE_Z	Zeeman splitting
$\Delta\nu$	Sweep range
$\Delta\nu_\mathrm{comb}$	Frequency comb spectral width

Symbol	Description
$\Delta\nu_{\mathrm{hom}}$, $\Delta\omega_{\mathrm{hom}}$	Homogeneous NMR linewidth, times 2π
$\Delta\nu_{\mathrm{inh}}$, $\Delta\omega_{\mathrm{inh}}$	Inhomogeneous NMR linewidth, times 2π
$\Delta\tau$	Depolarisation time ratio
ϵ_{b}	Biaxial strain
ϵ_{ij}	Elastic strain tensor
ϵ_{r}	Relative permittivity
ζ	Scaling exponent
η	Asymmetry parameter
κ	Scaling exponent
λ	Wavelength
$\boldsymbol{\mu}$	Magnetic moment
ν	Frequency
$\dot{\nu}$	Frequency sweep rate
$\nu_{\mathrm{comb,0}}$	Central frequency of frequency comb
ν_{i}, ν_{f}	Initial and final sweep frequency
ν_{L}	Larmor frequency
ν_{rf}	RF frequency
π_{γ}	Photon parity
ρ	Nuclear spin bath polarisation
σ_i	Pauli matrices
τ	Delay time
τ_{c}	Correlation time
τ_{evol}	Free evolution time
τ_j	Depolarisation time of isotope j

Symbol	Description
φ	Phase
Φ	Wavefunction
Ψ	Envelope wavefunction
ω	Angular frequency
ω_0	Energy shell spacing
ω_1	Resonant Rabi angular frequency
ω_D	Dipolar coupling strength
ω_ff	Spin-flip rate
ω_L	Larmor angular frequency
ω_Q	Quadrupolar coupling strength
ω_rf	RF angular frequency
$\boldsymbol{\Omega}$, Ω	Rabi angular frequency

Table 10.1: List of symbols used in this thesis.

Quantity	Symbol	Value
Speed of light in vacuum	c	$2.998 \cdot 10^8$ m/s
Elementary charge	e	$1.602 \cdot 10^{-19}$ C
Boltzmann constant	k_B	$8.617 \cdot 10^{-5}$ eV/K
Free electron mass	$m_{0,\mathrm{e}}$	$9.109 \cdot 10^{-31}$ kg
Reduced Planck constant	$\hbar$	$6.582 \cdot 10^{-16}$ eV s
Vacuum permeability	μ_0	$4\pi \cdot 10^{-7}$ N/A^2
Bohr magneton	μ_B	$5.78 \cdot 10^{-5}$ eV/T
Nuclear magneton	μ_n	$3.15 \cdot 10^{-8}$ eV/T

Table 10.2: List of physical constants used in this thesis.

Bibliography

[1] Y. I. Manin. *Vychislimoe i nevychislimoe [Computable and Uncomputable]*. Sovetskoye Radio, 1980. [in Russian].

[2] P. W. Shor. Introduction to Quantum Algorithms. arXiv:0005003, 2001.

[3] R. P. Feynman. Simulating physics with computers. *International Journal of Theoretical Physics*, 21:467, 1982. doi:10.1007/BF02650179.

[4] R. P. Feynman. Quantum mechanical computers. *Foundations of Physics*, 16: 507, 1986. doi:10.1007/BF01886518.

[5] P. W. Shor. Polynomial-Time Algorithms for Prime Factorization and Discrete Logarithms on a Quantum Computer. *SIAM Journal on Computing*, 26:1484, 1997. doi:10.1137/S0097539795293172.

[6] L. K. Grover. Quantum Mechanics Helps in Searching for a Needle in a Haystack. *Physical Review Letters*, 79:325, 1997. doi:10.1103/PhysRevLett.79.325.

[7] I. Cirac and P. Zoller. Quantum Computations with Cold Trapped Ions. *Physical Review Letters*, 74:4091, 1995. doi:10.1103/PhysRevLett.74.4091.

[8] T. Monz, P. Schindler, J. T. Barreiro, M. Chwalla, D. Nigg, W. A. Coish, M. Harlander, W. Hänsel, M. Hennrich, and R. Blatt. 14-Qubit Entanglement: Creation and Coherence. *Physical Review Letters*, 106:130506, 2011. doi:10.1103/PhysRevLett.106.130506.

[9] M. H. Devoret and R. J. Schoelkopf. Superconducting Circuits for Quantum Information: An Outlook. *Science*, 339:1169, 2013. doi:10.1126/science.1231930.

[10] B. E. Kane. A silicon-based nuclear spin quantum computer. *Nature*, 393:133, 1998. doi:10.1038/30156.

[11] K. Saeedi, S. Simmons, J. Z. Salvail, P. Dluhy, H. Riemann, N. V. Abrosimov, P. Becker, H.-J. Pohl, J. J. L. Morton, and M. L. W. Thewalt. Room-Temperature Quantum Bit Storage Exceeding 39 Minutes Using Ionized Donors in Silicon-28. *Science*, 342:830, 2013. doi:10.1126/science.1239584.

[12] J. O'Gorman, N. H. Nickerson, P. Ross, J. J. L. Morton, and S. C. Benjamin. A silicon-based surface code quantum computer. *npj Quantum Information*, 2:15019, 2016. doi:10.1038/npjqi.2015.19.

[13] P. C. Maurer, G. Kucsko, C. Latta, L. Jiang, N. Y. Yao, S. D. Bennett, F. Pastawski, D. Hunger, N. Chisholm, M. Markham, D. J. Twitchen, J. I. Cirac, and M. D. Lukin. Room-Temperature Quantum Bit Memory Exceeding One Second. *Science*, 336:1283, 2012. doi:10.1126/science.1220513.

[14] D. Loss and D. P. DiVincenzo. Quantum computation with quantum dots. *Physical Review A*, 57:120, 1998. doi:10.1103/PhysRevA.57.120.

[15] C. Kloeffel and D. Loss. Prospects for Spin-Based Quantum Computing in Quantum Dots. *Annual Review of Condensed Matter Physics*, 4:51, 2013. doi:10.1146/annurev-conmatphys-030212-184248.

[16] R. J. Warburton. Single spins in self-assembled quantum dots. *Nature Materials*, 12:483, 2013. doi:10.1038/nmat3585.

[17] D. P. DiVincenzo. The Physical Implementation of Quantum Com-

putation. *Fortschritte der Physik*, 48:771, 2000. doi:10.1002/1521-3978(200009)48:9/11<771::AID-PROP771>3.0.CO;2-E.

[18] T. D. Ladd, F. Jelezko, R. Laflamme, Y. Nakamura, C. Monroe, and J. L. O'Brien. Quantum Computers. *Nature*, 464:45, 2010. doi:10.1038/nature08812.

[19] D. Press, T. D. Ladd, B. Zhang, and Y. Yamamoto. Complete quantum control of a single quantum dot spin using ultrafast optical pulses. *Nature*, 456:218, 2008. doi:10.1038/nature07530.

[20] T. M. Godden, J. H. Quilter, A. J. Ramsay, Y. Wu, P. Brereton, S. J. Boyle, I. J. Luxmoore, J. Puebla-Nunez, A. M. Fox, and M. S. Skolnick. Coherent Optical Control of the Spin of a Single Hole in an InAs/GaAs Quantum Dot. *Physical Review Letters*, 108:017402, 2012. doi:10.1103/PhysRevLett.108.017402.

[21] E. Knill, R. Laflamme, and G. J. Milburn. A scheme for efficient quantum computation with linear optics. *Nature*, 409:46, 2001. doi:10.1038/35051009.

[22] P. Kok, W. J. Munro, K. Nemoto, T. C. Ralph, J. P. Dowling, and G. J. Milburn. Linear optical quantum computing with photonic qubits. *Reviews of Modern Physics*, 79:135, 2007. doi:10.1103/RevModPhys.79.135.

[23] P. Lodahl, S. Mahmoodian, and S. Stobbe. Interfacing single photons and single quantum dots with photonic nanostructures. *Reviews of Modern Physics*, 87:347, 2015. doi:10.1103/RevModPhys.87.347.

[24] O. Gazzano, S. Michaelis de Vasconcellos, C. Arnold, A. Nowak, E. Galopin, I. Sagnes, L. Lanco, A. Lemaître, and P. Senellart. Bright solid-state sources of indistinguishable single photons. *Nature Communications*, 4:1425, 2013. doi:10.1038/ncomms2434.

[25] Y.-M. He, Y. He, Y.-J. Wei, D. Wu, M. Atatüre, C. Schneider, S. Höfling, M. Kamp, C.-Y. Lu, and J.-W. Pan. On-demand semiconductor single-photon source with near-unity indistinguishability. *Nature Nanotechnology*, 8:213, 2013. doi:10.1038/nnano.2012.262.

[26] J. Skiba-Szymanska, A. Jamil, I. Farrer, M. B. Ward, C. A. Nicoll, D. J. P. Ellis, J. P. Griffiths, D. Anderson, G. A. C. Jones, and D. A. Ritchie. Narrow emission linewidths of positioned InAs quantum dots grown on pre-patterned GaAs(100) substrates. *Nanotechnology*, 22:065302, 2011. doi:10.1088/0957-4484/22/6/065302.

[27] G. Juska, V. Dimastrodonato, L. O. Mereni, A. Gocalinska, and E. Pelucchi. Towards quantum-dot arrays of entangled photon emitters. *Nature Photonics*, 7:527, 2013. doi:10.1038/nphoton.2013.128.

[28] A. Delteil, Z. Sun, W. Gao, E. Togan, S. Faelt, and A. Imamoglu. Generation of heralded entanglement between distant hole spins. *Nature Physics*, 12:218, 2016. doi:10.1038/nphys3605.

[29] I. A. Merkulov, A. L. Efros, and M. Rosen. Electron spin relaxation by nuclei in semiconductor quantum dots. *Physical Review B*, 65:205309, 2002. doi:10.1103/PhysRevB.65.205309.

[30] A. V. Khaetskii, D. Loss, and L. Glazman. Electron Spin Decoherence in Quantum Dots due to Interaction with Nuclei. *Physical Review Letters*, 88: 186802, 2002. doi:10.1103/PhysRevLett.88.186802.

[31] M. Veldhorst, J. C. C. Hwang, C. H. Yang, A. W. Leenstra, B. de Ronde, J. P. Dehollain, J. T. Muhonen, F. E. Hudson, K. M. Itoh, A. Morello, and A. S. Dzurak. An addressable quantum dot qubit with fault-tolerant control-fidelity. *Nature Nanotechnology*, 9:981, 2014. doi:10.1038/nnano.2014.216.

[32] M. Veldhorst, C. H. Yang, J. C. C. Hwang, W. Huang, J. P. Dehollain, J. T. Muhonen, S. Simmons, A. Laucht, F. E. Hudson, K. M. Itoh, A. Morello, and A. S. Dzurak. A two-qubit logic gate in silicon. *Nature*, 526:410, 2015. doi:10.1038/nature15263.

[33] E. Kawakami, P. Scarlino, D. R. Ward, F. R. Braakman, D. E. Savage, M. G. Lagally, M. Friesen, S. N. Coppersmith, M. A. Eriksson, and L. M. K. Vandersypen. Electrical control of a long-lived spin qubit in a Si/SiGe quantum dot. *Nature Nanotechnology*, 9:666, 2014. doi:10.1038/nnano.2014.153.

[34] D. Stepanenko, G. Burkard, G. Giedke, and A. Imamoglu. Enhancement of Electron Spin Coherence by Optical Preparation of Nuclear Spins. *Physical Review Letters*, 96:136401, 2006. doi:10.1103/PhysRevLett.96.136401.

[35] D. Klauser, W. A. Coish, and D. Loss. Nuclear spin state narrowing via gate-controlled Rabi oscillations in a double quantum dot. *Physical Review B*, 73: 205302, 2006. doi:10.1103/PhysRevB.73.205302.

[36] X. Xu, W. Yao, B. Sun, D. G. Steel, A. S. Bracker, D. Gammon, and L. J. Sham. Optically controlled locking of the nuclear field via coherent dark-state spectroscopy. *Nature*, 459:1105, 2009. doi:10.1038/nature08120.

[37] W. A. Coish and D. Loss. Hyperfine interaction in a quantum dot: Non-Markovian electron spin dynamics. *Physical Review B*, 70:195340, 2004. doi:10.1103/PhysRevB.70.195340.

[38] R. Oulton, A. Greilich, S. Y. Verbin, R. V. Cherbunin, T. Auer, D. R. Yakovlev, M. Bayer, I. A. Merkulov, V. Stavarache, D. Reuter, and A. D. Wieck. Subsecond Spin Relaxation Times in Quantum Dots at Zero Applied Magnetic Field Due to a Strong Electron-Nuclear Interaction. *Physical Review Letters*, 98:107401, 2007. doi:10.1103/PhysRevLett.98.107401.

[39] E. A. Chekhovich, K. V. Kavokin, J. Puebla, A. B. Krysa, M. Hopkinson, A. D. Andreev, A. M. Sanchez, R. Beanland, M. S. Skolnick, and A. I. Tartakovskii. Structural analysis of strained quantum dots using nuclear magnetic resonance. *Nature Nanotechnology*, 7:646, 2012. doi:10.1038/nnano.2012.142.

[40] M. Munsch, G. Wüst, A. V. Kuhlmann, F. Xue, A. Ludwig, D. Reuter, A. D. Wieck, M. Poggio, and R. J. Warburton. Manipulation of the nuclear spin ensemble in a quantum dot with chirped magnetic resonance pulses. *Nature Nanotechnology*, 9:671, 2014. doi:10.1038/nnano.2014.175.

[41] E. A. Chekhovich, M. Hopkinson, M. S. Skolnick, and A. I. Tartakovskii. Suppression of nuclear spin bath fluctuations in self-assembled quantum dots induced by inhomogeneous strain. *Nature Communications*, 6:6348, 2015. doi:10.1038/ncomms7348.

[42] M. Munsch, G. Wüst, A. V. Kuhlmann, F. Xue, A. Ludwig, A. D. Wieck, D. Reuter, M. Poggio, and R. J. Warburton. Nuclear Magnetic Resonance on a single quantum dot. Talk at MSS-17, Sendai, Japan, 2015. and personal correspondence with the authors.

[43] A. I. Ekimov and A. A. Onushchenko. Quantum size effect in three-dimensional microscopic semiconductor crystals. *Journal of Experimental and Theoretical Physics Letters*, 34:345, 1981.

[44] L. E. Brus. Electron-electron and electron-hole interactions in small semiconductor crystallites: The size dependence of the lowest excited electronic state. *Journal of Chemical Physics*, 80:4403, 1984. doi:10.1063/1.447218.

[45] L. P. Kouwenhoven, A. T. Johnson, N. C. van der Vaart, C. J. P. M. Harmans, and C. T. Foxon. Quantized current in a quantum-dot turnstile using oscillating tunnel barriers. *Physical Review Letters*, 67:1626, 1991. doi:10.1103/PhysRevLett.67.1626.

[46] A. Zrenner, L. V. Butov, M. Hagn, G. Abstreiter, G. Böhm, and G. Weimann. Quantum dots formed by interface fluctuations in AlAs/GaAs coupled quantum well structures. *Physical Review Letters*, 72:3382, 1994. doi:10.1103/PhysRevLett.72.3382.

[47] W. J. Schaffer, M. D. Lind, S. P. Kowalczyk, and R. W. Grant. Nucleation and strain relaxation at the InAs/GaAs(100) heterojunction. *Journal of Vacuum Science and Technology B*, 1:688, 1983. doi:10.1116/1.582579.

[48] E. Bauer. Phänomenologische Theorie der Kristallabscheidung an Oberflächen I. *Zeitschrift für Kristallographie*, 110:372, 1958. doi:10.1524/zkri.1958.110.1-6.372.

[49] S. Adachi. *Physical properties of III-V semiconductor compounds: InP, InAs, GaAs, GaP, InGaAs, and InGaAsP*. Wiley, first edition, 1992.

[50] L. Goldstein, F. Glas, J. Y. Marzin, M. N. Charasse, and G. Le Roux. Growth by molecular beam epitaxy and characterization of InAs/GaAs strained-layer superlattices. *Applied Physics Letters*, 47:1099, 1985. doi:10.1063/1.96342.

[51] D. Leonard, M. Krishnamurthy, C. M. Reaves, S. P. Denbaars, and P. M. Petroff. Direct formation of quantum-sized dots from uniform coherent islands of InGaAs on GaAs surfaces. *Applied Physics Letters*, 63:3203, 1993. doi:10.1063/1.110199.

[52] Y. Sugiyama, Y. Sakuma, S. Muto, and N. Yokoyama. Novel InGaAs/GaAs quantum dot structures formed in tetrahedral-shaped recesses on (111)B GaAs substrate using metalorganic vapor phase epitaxy. *Applied Physics Letters*, 67: 256, 1995. doi:10.1063/1.114685.

[53] S. Jeppesen, M. S. Miller, D. Hessman, B. Kowalski, I. Maximov, and L. Samuelson. Assembling strained InAs islands on patterned GaAs sub-

strates with chemical beam epitaxy. *Applied Physics Letters*, 68:2228, 1996. doi:10.1063/1.115867.

[54] S. M. Thon, M. T. Rakher, K. Hyochul, J. Gudat, W. T. M. Irvine, P. M. Petroff, and D. Bouwmeester. Strong coupling through optical positioning of a quantum dot in a photonic crystal cavity. *Applied Physics Letters*, 94: 111115, 2009. doi:10.1063/1.3103885.

[55] R. J. Coles, D. M. Price, J. E. Dixon, B. Royall, E. Clarke, A. M. Fox, P. Kok, M. S. Skolnick, and M. N. Makhonin. Chirality of nanophotonic waveguide with embedded quantum emitter for unidirectional spin transfer. arXiv:1506.02266, 2015.

[56] A. Wojs, P. Hawrylak, S. Fafard, and L. Jacak. Electronic structure and magneto-optics of self-assembled quantum dots. *Physical Review B*, 54:5604, 1996. doi:10.1103/PhysRevB.54.5604.

[57] A. H. Rodríguez, C. Trallero-Giner, S. E. Ulloa, and J. Marín-Antuña. Electronic states in a quantum lens. *Physical Review B*, 63:125319, 2001. doi:10.1103/PhysRevB.63.125319.

[58] F. M. Peeters and V. A. Schweigert. Two-electron quantum disks. *Physical Review B*, 53:1468, 1996. doi:10.1103/PhysRevB.53.1468.

[59] C. Pryor. Eight-band calculations of strained InAs/GaAs quantum dots compared with one-, four-, and six-band approximations. *Physical Review B*, 57: 7190, 1998. doi:10.1103/PhysRevB.57.7190.

[60] O. Stier, M. Grundmann, and D. Bimberg. Electronic and optical properties of strained quantum dots modeled by 8-band k·p theory. *Physical Review B*, 59:5688, 1999. doi:10.1103/PhysRevB.59.5688.

[61] K.-H. Goetz, D. Bimberg, H. Jürgensen, J. Selders, A. V. Solomonov, G. F. Glinskii, and M. Razeghi. Optical and crystallographic properties and impurity incorporation of $Ga_xIn_{1-x}As$ ($0.44 < x < 0.49$) grown by liquid phase epitaxy, vapor phase epitaxy, and metal organic chemical vapor deposition. *Journal of Applied Physics*, 54:4543, 1983. doi:10.1063/1.332655.

[62] C. P. Kuo, S. K. Vong, R. M. Cohen, and G. B. Stringfellow. Effect of mismatch strain on band gap in III-V semiconductors. *Journal of Applied Physics*, 57: 5428, 1985. doi:10.1063/1.334817.

[63] J. S. Blakemore. Semiconducting and other major properties of gallium arsenide. *Journal of Applied Physics*, 53:R123, 1982. doi:10.1063/1.331665.

[64] J. P. Reithmaier, R. Höger, H. Riechert, A. Heberle, G. Abstreiter, and G. Weimann. Band offset in elastically strained InGaAs/GaAs multiple quantum wells determined by optical absorption and electronic Raman scattering. *Applied Physics Letters*, 56:536, 1990. doi:10.1063/1.102737.

[65] A. P. Zhou and W. D. Sheng. Electron and hole effective masses in self-assembled quantum dots. *European Physical Journal B*, 68:233, 2009. doi:10.1140/epjb/e2009-00098-2.

[66] S. W. da Silva, Y. A. Pusep, J. C. Galzerani, D. I. Lubyshev, P. P. González-Borrero, and P. Basmaji. Photoluminescence study of spin-orbit-split bound electron states in self-assembled InAs and $In_{0.5}Ga_{0.5}As$ quantum dots. *Journal of Physics: Condensed Matter*, 9:L13, 1997. doi:10.1088/0953-8984/9/1/003.

[67] Ioffe Physico-Technical Institute. New Semiconductor Materials. Characteristics and Properties, 2016. http://www.ioffe.ru.

[68] P. W. Fry, I. E. Itskevich, S. R. Parnell, J. J. Finley, L. R. Wilson, K. L. Schumacher, D. J. Mowbray, M. S. Skolnick, M. Al-Khafaji, A. G. Cullis,

M. Hopkinson, J. C. Clark, and G. Hill. Photocurrent spectroscopy of InAs/GaAs self-assembled quantum dots. *Physical Review B*, 62:16784, 2000. doi:10.1103/PhysRevB.62.16784.

[69] R. J. Warburton, B. T. Miller, C. S. Dürr, C. Bödefeld, K. Karrai, J. P. Kotthaus, G. Medeiros-Ribeiro, P. M. Petroff, and S. Huant. Coulomb interactions in small charge-tunable quantum dots: A simple model. *Physical Review B*, 58:16221, 1998. doi:10.1103/PhysRevB.58.16221.

[70] M. Bayer, O. Stern, P. Hawrylak, S. Fafard, and A. Forchel. Hidden symmetries in the energy levels of excitonic 'artificial atoms'. *Nature*, 405:923, 2000. doi:10.1038/35016020.

[71] R. J. Warburton, C. Schäflein, D. Haft, F. Bickel, A. Lorke, K. Karrai, J. M. Garcia, W. Schoenfeld, and P. M. Petroff. Optical emission from a charge-tunable quantum ring. *Nature*, 405:926, 2000. doi:10.1038/35016030.

[72] J. J. Finley, A. D. Ashmore, A. Lemaître, D. J. Mowbray, M. S. Skolnick, I. E. Itskevich, P. A. Maksym, M. Hopkinson, and T. F. Krauss. Charged and neutral exciton complexes in individual self-assembled In(Ga)As quantum dots. *Physical Review B*, 63:073307, 2001. doi:10.1103/PhysRevB.63.073307.

[73] M. Bayer, S. N. Walck, T. L. Reinecke, and A. Forchel. Exciton binding energies and diamagnetic shifts in semiconductor quantum wires and quantum dots. *Physical Review B*, 57:6584, 1998. doi:10.1103/PhysRevB.57.6584.

[74] S. B. Nam, D. C. Reynolds, C. W. Litton, R. J. Almassy, T. C. Collins, and C. M. Wolfe. Free-exciton energy spectrum in GaAs. *Physical Review B*, 13: 761, 1976. doi:10.1103/PhysRevB.13.761.

[75] O. Gywat, H. J. Krenner, and J. Berezovsky. *Spins in Optically Active Quantum Dots*. Wiley-VCH, first edition, 2010.

[76] M. Bayer. Exciton Complexes in Self-Assembled In(Ga)As/GaAs Quantum Dots. In P. Michler, editor, *Single Quantum Dots: Fundamentals, Applications and New Concepts*. Springer, first edition, 2003.

[77] M. Kroutvar, Y. Ducommun, D. Heiss, M. Bichler, D. Schuh, G. Abstreiter, and J. J. Finley. Optically programmable electron spin memory using semiconductor quantum dots. *Nature*, 432:81, 2004. doi:10.1038/nature03008.

[78] K. De Greve, P. L. McMahon, D. Press, T. D. Ladd, D. Bisping, C. Schneider, M. Kamp, L. Worschech, S. Höfling, A. Forchel, and Y. Yamamoto. Ultrafast coherent control and suppressed nuclear feedback of a single quantum dot hole qubit. *Nature Physics*, 7:872, 2011. doi:10.1038/nphys2078.

[79] J. J. Finley, P. W. Fry, A. D. Ashmore, A. Lemaître, A. I. Tartakovskii, R. Oulton, D. J. Mowbray, M. S. Skolnick, M. Hopkinson, P. D. Buckle, and P. A. Maksym. Observation of multicharged excitons and biexcitons in a single InGaAs quantum dot. *Physical Review B*, 63:161305, 2001. doi:10.1103/PhysRevB.63.161305.

[80] D. V. Regelman, E. Dekel, D. Gershoni, E. Ehrenfreund, A. J. Williamson, J. Shumway, A. Zunger, W. V. Schoenfeld, and P. M. Petroff. Optical spectroscopy of single quantum dots at tunable positive, neutral, and negative charge states. *Physical Review B*, 64:165301, 2001. doi:10.1103/PhysRevB.64.165301.

[81] M. Atatüre, J. Dreiser, A. Badolato, A. Högele, K. Karrai, and A. Imamoglu. Quantum-Dot Spin-State Preparation with Near-Unity Fidelity. *Science*, 312: 551, 2006. doi:10.1126/science.1126074.

[82] E. A. Chekhovich, A. B. Krysa, M. S. Skolnick, and A. I. Tartakovskii. Light-polarization-independent nuclear spin alignment in a quantum dot. *Physical Review B*, 83:125318, 2011. doi:10.1103/PhysRevB.83.125318.

[83] J. Puebla, E. A. Chekhovich, M. Hopkinson, P. Senellart, A. Lemaitre, M. S. Skolnick, and A. I. Tartakovskii. Dynamic nuclear polarization in InGaAs/GaAs and GaAs/AlGaAs quantum dots under nonresonant ultralow-power optical excitation. *Physical Review B*, 88:045306, 2013. doi:10.1103/PhysRevB.88.045306.

[84] D. N. Krizhanovskii, A. Ebbens, A. I. Tartakovskii, F. Pulizzi, T. Wright, M. S. Skolnick, and M. Hopkinson. Individual neutral and charged $In_xGa_{1-x}As$-GaAs quantum dots with strong in-plane optical anisotropy. *Physical Review B*, 72:161312, 2005. doi:10.1103/PhysRevB.72.161312.

[85] E. A. Chekhovich, M. N. Makhonin, J. Skiba-Szymanska, A. B. Krysa, V. D. Kulakovskii, M. S. Skolnick, and A. I. Tartakovskii. Dynamics of optically induced nuclear spin polarization in individual $InP/Ga_xIn_{1-x}P$ quantum dots. *Physical Review B*, 81:245308, 2010. doi:10.1103/PhysRevB.81.245308.

[86] H. W. van Kesteren, E. C. Cosman, W. A. J. A. van der Poel, and C. T. Foxon. Fine structure of excitons in type-II GaAs/AlAs quantum wells. *Physical Review B*, 41:5283, 1990. doi:10.1103/PhysRevB.41.5283.

[87] M. Bayer, A. Kuther, A. Forchel, A. Gorbunov, V. B. Timofeev, F. Schäfer, J. P. Reithmaier, T. L. Reinecke, and S. N. Walck. Electron and Hole g Factors and Exchange Interaction from Studies of the Exciton Fine Structure in $In_{0.60}Ga_{0.40}As$ Quantum Dots. *Physical Review Letters*, 82:1748, 1999. doi:10.1103/PhysRevLett.82.1748.

[88] M. Bayer, G. Ortner, O. Stern, A. Kuther, A. A. Gorbunov, A. Forchel, P. Hawrylak, S. Fafard, K. Hinzer, T. L. Reinecke, S. N. Walck, J. P. Reithmaier, F. Klopf, and F. Schäfer. Fine structure of neutral and charged excitons in self-assembled In(Ga)As/(Al)GaAs quantum dots. *Physical Review B*, 65: 195315, 2002. doi:10.1103/PhysRevB.65.195315.

[89] J. G. Tischler, A. S. Bracker, D. Gammon, and D. Park. Fine structure of trions and excitons in single GaAs quantum dots. *Physical Review B*, 66: 081310, 2002. doi:10.1103/PhysRevB.66.081310.

[90] A. S. Bracker, D. Gammon, and V. L. Korenev. Fine structure and optical pumping of spins in individual semiconductor quantum dots. *Semiconductor Science and Technology*, 23:114004, 2008. doi:10.1088/0268-1242/23/11/114004.

[91] P. W. Fry, I. E. Itskevich, D. J. Mowbray, M. S. Skolnick, J. J. Finley, J. A. Barker, E. P. O'Reilly, L. R. Wilson, I. A. Larkin, P. A. Maksym, M. Hopkinson, M. Al-Khafaji, J. P. R. David, A. G. Cullis, G. Hill, and J. C. Clark. Inverted Electron-Hole Alignment in InAs-GaAs Self-Assembled Quantum Dots. *Physical Review Letters*, 84:733, 2000. doi:10.1103/PhysRevLett.84.733.

[92] J. Stark. Beobachtungen über den Effekt des elektrischen Feldes auf Spektrallinien. I. Quereffekt. *Annalen der Physik. Vierte Folge.*, 43 (348):965, 1914. doi:10.1002/andp.19143480702.

[93] D. A. B. Miller, D. S. Chemla, T. C. Damen, A. C. Gossard, W. Wiegmann, T. H. Wood, and C. A. Burrus. Band-Edge Electroabsorption in Quantum Well Structures: The Quantum-Confined Stark Effect. *Physical Review Letters*, 53: 2173, 1984. doi:10.1103/PhysRevLett.53.2173.

[94] A. M. Bonch-Bruevich and V. A. Khodovoi. Current Methods for the Study of the Stark Effect in Atoms. *Soviet Physics Uspekhi*, 10:637, 1968. doi:10.1070/PU1968v010n05ABEH005850.

[95] H. J. Krenner, M. Sabathil, E. C. Clark, A. Kress, D. Schuh, M. Bichler, G. Abstreiter, and J. J. Finley. Direct Observation of Controlled Coupling in an Individual Quantum Dot Molecule. *Physical Review Letters*, 94:057402, 2005. doi:10.1103/PhysRevLett.94.057402.

[96] A. J. Bennett, R. B. Patel, J. Skiba-Szymanska, C. A. Nicoll, I. Farrer, D. A. Ritchie, and A. J. Shields. Giant Stark effect in the emission of single semiconductor quantum dots. *Applied Physics Letters*, 97:031104, 2010. doi:10.1063/1.3460912.

[97] A. Laucht, F. Hofbauer, N. Hauke, J. Angele, S. Stobbe, M. Kaniber, G. Bö, P. Lodahl, M.-C. Amann, and J. J. Finley. Electrical control of spontaneous emission and strong coupling for a single quantum dot. *New Journal of Physics*, 11:023034, 2009. doi:10.1088/1367-2630/11/2/023034.

[98] M. T. Rakher, N. G. Stoltz, L. A. Coldren, P. M. Petroff, and D. Bouwmeester. Externally Mode-Matched Cavity Quantum Electrodynamics with Charge-Tunable Quantum Dots. *Physical Review Letters*, 102:097403, 2009. doi:10.1103/PhysRevLett.102.097403.

[99] R. B. Patel, A. J. Bennett, I. Farrer, C. A. Nicoll, D. A. Ritchie, and A. J. Shields. Two-photon interference of the emission from electrically tunable remote quantum dots. *Nature Photonics*, 4:632, 2010. doi:10.1038/nphoton.2010.161.

[100] B. Alén, F. Bickel, K. Karrai, R. J. Warburton, and P. M. Petroff. Stark-shift modulation absorption spectroscopy of single quantum dots. *Applied Physics Letters*, 83:2235, 2003. doi:10.1063/1.1609243.

[101] A. J. Bennett, M. A. Pooley, R. M. Stevenson, M. B. Ward, R. B. Patel, A. Boyer de la Giroday, N. Sköld, I. Farrer, C. A. Nicoll, D. A. Ritchie, and A. J. Shields. Electric-field-induced coherent coupling of the exciton states in a single quantum dot. *Nature Physics*, 6:947, 2010. doi:10.1038/nphys1780.

[102] A. Schwan, B.-M. Meiners, A. Greilich, D. R. Yakovlev, M. Bayer, A. D. B. Maia, A. A. Quivy, and A. B. Henriques. Anisotropy of electron and hole g-

factors in (In,Ga)As quantum dots. *Applied Physics Letters*, 99:221914, 2011. doi:10.1063/1.3665634.

[103] M. Bayer, O. Stern, A. Kuther, and A. Forchel. Spectroscopic study of dark excitons in $In_xGa_{1-x}As$ self-assembled quantum dots by a magnetic-field-induced symmetry breaking. *Physical Review B*, 61:7273, 2000. doi:10.1103/PhysRevB.61.7273.

[104] C. E. Pryor and M. E. Flatté. Landé g Factors and Orbital Momentum Quenching in Semiconductor Quantum Dots. *Physical Review Letters*, 96: 026804, 2006. doi:10.1103/PhysRevLett.96.026804.

[105] K. J. Nash, M. S. Skolnick, P. A. Claxton, and J. S. Roberts. Diamagnetism as a probe of exciton localization in quantum wells. *Physical Review B*, 39: 10943, 1989. doi:10.1103/PhysRevB.39.10943.

[106] S. N. Walck and T. L. Reinecke. Exciton diamagnetic shift in semiconductor nanostructures. *Physical Review B*, 57:9088, 1998. doi:10.1103/PhysRevB.57.9088.

[107] A. Kuther, M. Bayer, A. Forchel, A. Gorbunov, V. B. Timofeev, F. Schäfer, and J. P. Reithmaier. Zeeman splitting of excitons and biexcitons in single $In_{0.60}Ga_{0.40}As$/GaAs self-assembled quantum dots. *Physical Review B*, 58: R7508, 1998. doi:10.1103/PhysRevB.58.R7508.

[108] T. M. Godden, J. H. Quilter, A. J. Ramsay, Yanwen Wu, P. Brereton, I. J. Luxmoore, J. Puebla, A. M. Fox, and M. S. Skolnick. Fast preparation of a single-hole spin in an InAs/GaAs quantum dot in a Voigt-geometry magnetic field. *Physical Review B*, 85:155310, 2012. doi:10.1103/PhysRevB.85.155310.

[109] D. Heiss, S. Schaeck, H. Huebl, M. Bichler, G. Abstreiter, J. J. Finley, D. V. Bulaev, and D. Loss. Observation of extremely slow hole spin relax-

ation in self-assembled quantum dots. *Physical Review B*, 76:241306, 2007. doi:10.1103/PhysRevB.76.241306.

[110] B. D. Gerardot, D. Brunner, P. A. Dalgarno, P. Öhberg, S. Seidl, M. Kroner, K. Karrai, N. G. Stoltz, P. M. Petroff, and R. J. Warburton. Optical pumping of a single hole spin in a quantum dot. *Nature*, 451:441, 2008. doi:10.1038/nature06472.

[111] A. J. Ramsay, S. J. Boyle, R. S. Kolodka, J. B. B. Oliveira, J. Skiba-Szymanska, H. Y. Liu, M. Hopkinson, A. M. Fox, and M. S. Skolnick. Fast Optical Preparation, Control, and Readout of a Single Quantum Dot Spin. *Physical Review Letters*, 100:197401, 2008. doi:10.1103/PhysRevLett.100.197401.

[112] B. Urbaszek, X. Marie, T. Amand, O. Krebs, P. Voisin, P. Maletinsky, A. Högele, and A. Imamoglu. Nuclear spin physics in quantum dots: An optical investigation. *Reviews of Modern Physics*, 85:79, 2013. doi:10.1103/RevModPhys.85.79.

[113] R. K. Harris, E. D. Becker, S. M. Cabral de Menezes, R. Goodfellow, and P. Granger. NMR nomenclature. Nuclear spin properties and conventions for chemical shifts. *Pure and Applied Chemistry*, 73:1795, 2001. doi:10.1351/pac200173111795.

[114] P. Maletinsky, M. Kroner, and A. Imamoglu. Breakdown of the nuclear-spin-temperature approach in quantum-dot demagnetization experiments. *Nature Physics*, 5:407, 2009. doi:10.1038/nphys1273.

[115] C. Latta, A. Srivastava, and A. Imamoglu. Hyperfine Interaction-Dominated Dynamics of Nuclear Spins in Self-Assembled InGaAs Quantum Dots. *Physical Review Letters*, 107:167401, 2011. doi:10.1103/PhysRevLett.107.167401.

[116] A. Abragam. *The principles of nuclear magnetism*. Oxford University Press, first edition, 1961.

[117] J. Fischer, W. A. Coish, D. V. Bulaev, and D. Loss. Spin decoherence of a heavy hole coupled to nuclear spins in a quantum dot. *Physical Review B*, 78: 155329, 2008. doi:10.1103/PhysRevB.78.155329.

[118] J. Schliemann, A. V. Khaetskii, and D. Loss. Electron spin dynamics in quantum dots and related nanostructures due to hyperfine interaction with nuclei. *Journal of Physics: Condensed Matter*, 15:R1809, 2003. doi:10.1088/0953-8984/15/50/R01.

[119] C. Testelin, F. Bernardot, B. Eble, and M. Chamarro. Hole-spin dephasing time associated with hyperfine interaction in quantum dots. *Physical Review B*, 79:195440, 2009. doi:10.1103/PhysRevB.79.195440.

[120] E. A. Chekhovich, M. M. Glazov, A. B. Krysa, M. Hopkinson, P. Senellart, A. Lemaître, M. S. Skolnick, and A. I. Tartakovskii. Element-sensitive measurement of the hole-nuclear spin interaction in quantum dots. *Nature Physics*, 9:74, 2013. doi:10.1038/nphys2514.

[121] D. Gammon, A. L. Efros, T. A. Kennedy, M. Rosen, D. S. Katzer, D. Park, S. W. Brown, V. L. Korenev, and I. A. Merkulov. Electron and Nuclear Spin Interactions in the Optical Spectra of Single GaAs Quantum Dots. *Physical Review Letters*, 86:5176, 2001. doi:10.1103/PhysRevLett.86.5176.

[122] B. Eble, C. Testelin, P. Desfonds, F. Bernardot, A. Balocchi, T. Amand, A. Miard, A. Lemaître, X. Marie, and M. Chamarro. Hole-Nuclear Spin Interaction in Quantum Dots. *Physical Review Letters*, 102:146601, 2009. doi:10.1103/PhysRevLett.102.146601.

[123] P. Fallahi, S. T. Yilmaz, and A. Imamoglu. Measurement of a Heavy-Hole Hyperfine Interaction in InGaAs Quantum Dots Using Resonance Fluorescence. *Physical Review Letters*, 105:257402, 2010. doi:10.1103/PhysRevLett.105.257402.

[124] E. A. Chekhovich, A. B. Krysa, M. S. Skolnick, and A. I. Tartakovskii. Direct Measurement of the Hole-Nuclear Spin Interaction in Single InP/GaInP Quantum Dots Using Photoluminescence Spectroscopy. *Physical Review Letters*, 106:027402, 2011. doi:10.1103/PhysRevLett.106.027402.

[125] D. Brunner, B. D. Gerardot, P. A. Dalgarno, G. Wüst, K. Karrai, N. G. Stoltz, P. M. Petroff, and R. J. Warburton. A Coherent Single-Hole Spin in a Semiconductor. *Science*, 325:70, 2009. doi:10.1126/science.1173684.

[126] J. Fischer and D. Loss. Hybridization and Spin Decoherence in Heavy-Hole Quantum Dots. *Physical Review Letters*, 105:266603, 2010. doi:10.1103/PhysRevLett.105.266603.

[127] A. W. Overhauser. Polarization of Nuclei in Metals. *Physical Review*, 92:411, 1953. doi:10.1103/PhysRev.92.411.

[128] W. D. Knight. Nuclear Magnetic Resonance Shift in Metals. *Physical Review*, 76:1259, 1949. doi:10.1103/PhysRev.76.1259.2.

[129] A. Simon, M. E. Rose, and J. M. Jauch. Polarization and Alignment of Nuclei. *Physical Review*, 84:1155, 1951. doi:10.1103/PhysRev.84.1155.

[130] J. Dreiser, M. Atatüre, C. Galland, T. Müller, A. Badolato, and A. Imamoglu. Optical investigations of quantum dot spin dynamics as a function of external electric and magnetic fields. *Physical Review B*, 77:075317, 2008. doi:10.1103/PhysRev.84.1155.

[131] A. C. Johnson, J. R. Petta, J. M. Taylor, A. Yacoby, M. D. Lukin, C. M. Marcus, M. P. Hanson, and A. C. Gossard. Triplet-singlet spin relaxation via nuclei in a double quantum dot. *Nature*, 435:925, 2005. doi:10.1038/nature03815.

[132] F. H. L. Koppens, J. A. Folk, J. M. Elzerman, R. Hanson, L. H. Willems van Beveren, I. T. Vink, H. P. Tranitz, W. Wegscheider, L. P. Kouwenhoven, and

L. M. K. Vandersypen. Control and Detection of Singlet-Triplet Mixing in a Random Nuclear Field. *Science*, 309:1346, 2005. doi:10.1126/science.1113719.

[133] S. Nadj-Perge, V. S. Pribiag, J. W. G. van den Berg, K. Zuo, S. R. Plissard, E. P. A. M. Bakkers, S. M. Frolov, and L. P. Kouwenhoven. Spectroscopy of Spin-Orbit Quantum Bits in Indium Antimonide Nanowires. *Physical Review Letters*, 108:166801, 2012. doi:10.1103/PhysRevLett.108.166801.

[134] C. W. Lai, P. Maletinsky, A. Badolato, and A. Imamoglu. Knight-Field-Enabled Nuclear Spin Polarization in Single Quantum Dots. *Physical Review Letters*, 96:167403, 2006. doi:10.1103/PhysRevLett.96.167403.

[135] M. S. Kuznetsova, K. Flisinski, I. Y. Gerlovin, I. V. Ignatiev, K. V. Kavokin, S. Y. Verbin, D. R. Yakovlev, D. Reuter, A. D. Wieck, and M. Bayer. Hanle effect in (In,Ga)As quantum dots: Role of nuclear spin fluctuations. *Physical Review B*, 87:235320, 2013. doi:10.1103/PhysRevB.87.235320.

[136] J. A. McNeil and W. G. Clark. Nuclear quadrupolar spin-lattice relaxation in some III-V compounds. *Physical Review B*, 13:4705, 1976. doi:10.1103/PhysRevB.13.4705.

[137] S. W. Brown, T. A. Kennedy, D. Gammon, and E. S. Snow. Spectrally resolved Overhauser shifts in single GaAs/Al_xGa_{1-x}As As quantum dots. *Physical Review B*, 54:R17339, 1996. doi:10.1103/PhysRevB.54.R17339.

[138] B. Eble, O. Krebs, A. Lemaître, K. Kowalik, A. Kudelski, P. Voisin, B. Urbaszek, X. Marie, and T. Amand. Dynamic nuclear polarization of a single charge-tunable InAs/GaAs quantum dot. *Physical Review B*, 74:081306, 2006. doi:10.1103/PhysRevB.74.081306.

[139] J. Baugh, Y. Kitamura, K. Ono, and S. Tarucha. Large Nuclear Overhauser Fields Detected in Vertically Coupled Double Quantum Dots. *Physical Review Letters*, 99:096804, 2007. doi:10.1103/PhysRevLett.99.096804.

[140] E. A. Laird, C. Barthel, E. I. Rashba, C. M. Marcus, M. P. Hanson, and A. C. Gossard. Hyperfine-Mediated Gate-Driven Electron Spin Resonance. *Physical Review Letters*, 99:246601, 2007. doi:10.1103/PhysRevLett.99.246601.

[141] T. R. Carver and C. P. Slichter. Polarization of Nuclear Spins in Metals. *Physical Review*, 92:212, 1953. doi:10.1103/PhysRev.92.212.2.

[142] G. Lampel. Nuclear Dynamic Polarization by Optical Electronic Saturation and Optical Pumping in Semiconductors. *Physical Review Letters*, 20:491, 1968. doi:10.1103/PhysRevLett.20.491.

[143] P.-F. Braun, B. Urbaszek, T. Amand, X. Marie, O. Krebs, B. Eble, A. Lemaitre, and P. Voisin. Bistability of the nuclear polarization created through optical pumping in $In_{1-x}Ga_xAs$ quantum dots. *Physical Review B*, 74:245306, 2006. doi:10.1103/PhysRevB.74.245306.

[144] P. Maletinsky, C. W. Lai, A. Badolato, and A. Imamoglu. Nonlinear dynamics of quantum dot nuclear spins. *Physical Review B*, 75:035409, 2007. doi:10.1103/PhysRevB.75.035409.

[145] A. I. Tartakovskii, T. Wright, A. Russell, V. I. Fal'ko, A. B. Van'kov, J. Skiba-Szymanska, I. Drouzas, R. S. Kolodka, M. S. Skolnick, P. W. Fry, A. Tahraoui, H.-Y. Liu, and M. Hopkinson. Nuclear Spin Switch in Semiconductor Quantum Dots. *Physical Review Letters*, 98:026806, 2007. doi:10.1103/PhysRevLett.98.026806.

[146] J. Skiba-Szymanska, E. A. Chekhovich, A. E. Nikolaenko, A. I. Tartakovskii, M. N. Makhonin, I. Drouzas, M. S. Skolnick, and A. B. Krysa. Overhauser effect in individual $InP/Ga_xIn_{1-x}P$ dots. *Physical Review B*, 77:165338, 2008. doi:10.1103/PhysRevB.77.165338.

[147] E. A. Chekhovich, M. N. Makhonin, K. V. Kavokin, A. B. Krysa, M. S. Skolnick, and A. I. Tartakovskii. Pumping of Nuclear Spins by Optical Excitation

of Spin-Forbidden Transitions in a Quantum Dot. *Physical Review Letters*, 104:066804, 2010. doi:10.1103/PhysRevLett.104.066804.

[148] A. Imamoglu, E. Knill, L. Tian, and P. Zoller. Optical Pumping of Quantum-Dot Nuclear Spins. *Physical Review Letters*, 91:017402, 2003. doi:10.1103/PhysRevLett.91.017402.

[149] F. Klotz, V. Jovanov, J. Kierig, E. C. Clark, M. Bichler, G. Abstreiter, M. S. Brandt, J. J. Finley, H. Schwager, and G. Giedke. Asymmetric optical nuclear spin pumping in a single uncharged quantum dot. *Physical Review B*, 82: 121307, 2010. doi:10.1103/PhysRevB.82.121307.

[150] A. Russell, V. I. Fal'ko, A. I. Tartakovskii, and M. S. Skolnick. Bistability of optically induced nuclear spin orientation in quantum dots. *Physical Review B*, 76:195310, 2007. doi:10.1103/PhysRevB.76.195310.

[151] A. Ulhaq, Q. Duan, E. Zallo, F. Ding, O. G. Schmidt, A. I. Tartakovskii, M. S. Skolnick, and E. A. Chekhovich. Vanishing electron g factor and long-lived nuclear spin polarization in weakly strained nanohole-filled GaAs/AlGaAs quantum dots. *Physical Review B*, 93:165306, 2016. doi:10.1103/PhysRevB.93.165306.

[152] J. Hildmann, E. Kavousanaki, G. Burkard, and H. Ribeiro. Quantum limit for nuclear spin polarization in semiconductor quantum dots. *Physical Review B*, 89:205302, 2014. doi:10.1103/PhysRevB.89.205302.

[153] S. Bandyopadhyay and M. Cahay. *Introduction to Spintronics*. CRC Press, second edition, 2016.

[154] A. V. Khaetskii and Y. V. Nazarov. Spin relaxation in semiconductor quantum dots. *Physical Review B*, 61:12639, 2000. doi:10.1103/PhysRevB.61.12639.

[155] S. Amasha, K. MacLean, I. P. Radu, D. M. Zumbühl, M. A. Kastner, M. P. Hanson, and A. C. Gossard. Electrical Control of Spin Relaxation in a Quantum Dot. *Physical Review Letters*, 100:046803, 2008. doi:10.1103/PhysRevLett.100.046803.

[156] A. V. Khaetskii and Y. V. Nazarov. Spin-flip transitions between Zeeman sublevels in semiconductor quantum dots. *Physical Review B*, 64:125316, 2001. doi:10.1103/PhysRevB.64.125316.

[157] R. Hanson, L. P. Kouwenhoven, J. R. Petta, S. Tarucha, and L. M. K. Vandersypen. Spins in few-electron quantum dots. *Reviews of Modern Physics*, 79:1217, 2007. doi:10.1103/RevModPhys.79.1217.

[158] D. Heiss, M. Kroutvar, J. J. Finley, and G. Abstreiter. Progress towards single spin optoelectronics using quantum dot nanostructures. *Solid State Communications*, 135:591, 2005. doi:10.1016/j.ssc.2005.04.039.

[159] D. J. Hilton and C. L. Tang. Optical Orientation and Femtosecond Relaxation of Spin-Polarized Holes in GaAs. *Physical Review Letters*, 89:146601, 2002. doi:10.1103/PhysRevLett.89.146601.

[160] V. N. Golovach, A. Khaetskii, and D. Loss. Phonon-Induced Decay of the Electron Spin in Quantum Dots. *Physical Review Letters*, 93:016601, 2004. doi:10.1103/PhysRevLett.93.016601.

[161] A. S. Bracker, E. A. Stinaff, D. Gammon, M. E. Ware, J. G. Tischler, A. Shabaev, A. L. Efros, D. Park, D. Gershoni, V. L. Korenev, and I. A. Merkulov. Optical Pumping of the Electronic and Nuclear Spin of Single Charge-Tunable Quantum Dots. *Physical Review Letters*, 94:047402, 2005. doi:10.1103/PhysRevLett.94.047402.

[162] P.-F. Braun, X. Marie, L. Lombez, B. Urbaszek, T. Amand, P. Renucci, V. K. Kalevich, K. V. Kavokin, O. Krebs, P. Voisin, and Y. Ma-

sumoto. Direct Observation of the Electron Spin Relaxation Induced by Nuclei in Quantum Dots. *Physical Review Letters*, 94:116601, 2005. doi:10.1103/PhysRevLett.94.116601.

[163] M. V. G. Dutt, J. Cheng, B. Li, X. Xu, X. Li, P. R. Berman, D. G. Steel, A. S. Bracker, D. Gammon, S. E. Economou, R.-B. Liu, and L. J. Sham. Stimulated and Spontaneous Optical Generation of Electron Spin Coherence in Charged GaAs Quantum Dots. *Physical Review Letters*, 94:227403, 2005. doi:10.1103/PhysRevLett.94.227403.

[164] J. R. Petta, A. C. Johnson, J. M. Taylor, E. A. Laird, A. Yacoby, M. D. Lukin, C. M. Marcus, M. P. Hanson, and A. C. Gossard. Coherent Manipulation of Coupled Electron Spins in Semiconductor Quantum Dots. *Science*, 309:2180, 2005. doi:10.1126/science.1116955.

[165] F. H. L. Koppens, C. Buizert, K. J. Tielrooij, I. T. Vink, K. C. Nowack, T. Meunier, L. P. Kouwenhoven, and L. M. K. Vandersypen. Driven coherent oscillations of a single electron spin in a quantum dot. *Nature*, 442:766, 2006. doi:10.1038/nature05065.

[166] A. Faribault and D. Schuricht. Spin decoherence due to a randomly fluctuating spin bath. *Physical Review B*, 88:085323, 2013. doi:10.1103/PhysRevB.88.085323.

[167] F. H. L. Koppens, K. C. Nowack, and L. M. K. Vandersypen. Spin Echo of a Single Electron Spin in a Quantum Dot. *Physical Review Letters*, 100:236802, 2008. doi:10.1103/PhysRevLett.100.236802.

[168] D. Press, K. De Greeve, P. L. McMahon, T. D. Ladd, B. Friess, C. Schneider, M. Kamp, S. Höfling, A. Forchel, and Y. Yamamoto. Ultrafast optical spin echo in a single quantum dot. *Nature Photonics*, 4:367, 2010. doi:10.1038/nphoton.2010.83.

[169] C. Bulutay. Quadrupolar spectra of nuclear spins in strained $In_xGa_{1-x}As$ quantum dots. *Physical Review B*, 85:115313, 2012. doi:10.1103/PhysRevB.85.115313.

[170] N. A. Sinitsyn, Y. Li, S. A. Crooker, A. Saxena, and D. L. Smith. Role of Nuclear Quadrupole Coupling on Decoherence and Relaxation of Central Spins in Quantum Dots. *Physical Review Letters*, 109:166605, 2012. doi:10.1103/PhysRevLett.109.166605.

[171] A. Bechtold, D. Rauch, F. Li, T. Simmet, P.-L. Ardelt, A. Regler, K. Müller, N. A. Sinitsyn, and J. J. Finley. Three-stage decoherence dynamics of electron spin qubits in an optically active quantum dot. *Nature Physics*, 11:1005, 2015. doi:10.1103/10.1038/nphys3470.

[172] W. M. Witzel and S. Das Sarma. Multiple-Pulse Coherence Enhancement of Solid State Spin Qubits. *Physical Review Letters*, 98:077601, 2007. doi:10.1103/PhysRevLett.98.077601.

[173] L. Cywinski, W. M. Witzel, and S. Das Sarma. Pure quantum dephasing of a solid-state electron spin qubit in a large nuclear spin bath coupled by long-range hyperfine-mediated interactions. *Physical Review B*, 79:245314, 2009. doi:10.1103/PhysRevB.79.245314.

[174] F. K. Malinowski, F. Martins, P. D. Nissen, E. Barnes, M. S. Rudner, S. Fallahi, G. C. Gardner, M. J. Manfra, C. M. Marcus, and F. Kuemmeth. Notch ltering the nuclear environment of a spin qubit. arXiv:1601.06677, 2016.

[175] G. Burkard, D. Loss, and D. P. DiVincenzo. Coupled quantum dots as quantum gates. *Physical Review B*, 59:2070, 1999. doi:10.1103/PhysRevB.59.2070.

[176] I. T. Vink, K. C. Nowack, F. H. L. Koppens, J. Danon, Y. V. Nazarov, and L. M. K. Vandersypen. Locking electron spins into mag-

netic resonance by electron-nuclear feedback. *Nature Physics*, 5:764, 2009. doi:10.1038/nphys1366.

[177] R. de Sousa and S. Das Sarma. Electron spin coherence in semiconductors: Considerations for a spin-based solid-state quantum computer architecture. *Physical Review B*, 67:033301, 2003. doi:10.1103/PhysRevB.67.033301.

[178] H. Bluhm, S. Foletti, I. Neder, M. Rudner, D. Mahalu, V. Umansky, and A. Yacoby. Dephasing time of GaAs electron-spin qubits coupled to a nuclear bath exceeding 200 μs. *Nature Physics*, 7:109, 2011. doi:10.1038/nphys1856.

[179] S. G. Carter, S. E. Economou, A. Greilich, E. Barnes, T. Sweeney, A. S. Bracker, and D. Gammon. Strong hyperfine-induced modulation of an optically driven hole spin in an InAs quantum dot. *Physical Review B*, 89:075316, 2014. doi:10.1103/PhysRevB.89.075316.

[180] A. Greilich, S. G. Carter, D. Kim, A. S. Bracker, and D. Gammon. Optical control of one and two hole spins in interacting quantum dots. *Nature Photonics*, 5:702, 2011. doi:10.1038/nphoton.2011.237.

[181] A. V. Kuhlmann, J. Houel, A. Ludwig, L. Greuter, D. Reuter, A. D. Wieck, M. Poggio, and R. J. Warburton. Charge noise and spin noise in a semiconductor quantum device. *Nature Physics*, 9:570, 2013. doi:10.1038/nphys2688.

[182] P. Maletinsky, A. Badolato, and A. Imamoglu. Dynamics of Quantum Dot Nuclear Spin Polarization Controlled by a Single Electron. *Physical Review Letters*, 99:056804, 2007. doi:10.1103/PhysRevLett.99.056804.

[183] J. Ishihara, M. Ono, G. Sato, S. Matsuzaka, Y. Ohno, and H. Ohno. Magnetic Field Dependence of Quadrupolar Splitting and Nuclear Spin Coherence Time in a Strained (110) GaAs Quantum Well. *Japanese Journal of Applied Physics*, 50:04DM03, 2011. doi:10.1143/JJAP.50.04DM03.

[184] M. N. Makhonin, K. V. Kavokin, P. Senellart, A. Lemaître, A. J. Ramsay, M. S. Skolnick, and A. I. Tartakovskii. Fast control of nuclear spin polarization in an optically pumped single quantum dot. *Nature Materials*, 10:844, 2011. doi:10.1038/nmat3102.

[185] M. A. Ruderman and C. Kittel. Indirect Exchange Coupling of Nuclear Magnetic Moments by Conduction Electrons. *Physical Review*, 96:99, 1954. doi:10.1103/PhysRev.96.99.

[186] I. I. Rabi, J. R. Zacharias, S. Millman, and P. Kusch. A New Method of Measuring Nuclear Magnetic Moment. *Physical Review*, 53:318, 1938. doi:10.1103/PhysRev.53.318.

[187] I. I. Rabi, S. Millman, P. Kusch, and J. R. Zacharias. The Molecular Beam Resonance Method for Measuring Nuclear Magnetic Moments. The Magnetic Moments of ${}_3\mathrm{Li}^6$, ${}_3\mathrm{Li}^7$ and ${}_9\mathrm{F}^{19}$. *Physical Review*, 55:526, 1939. doi:10.1103/PhysRev.55.526.

[188] F. Bloch, W. W. Hansen, and Martin Packard. Nuclear Induction. *Physical Review*, 69:127, 1946. doi:10.1103/PhysRev.69.127.

[189] F. Bloch. Nuclear Induction. *Physical Review*, 70:460, 1946. doi:10.1103/PhysRev.70.460.

[190] E. M. Purcell, H. C. Torrey, and R. V. Pound. Resonance Absorption by Nuclear Magnetic Moments in a Solid. *Physical Review*, 69:37, 1946. doi:10.1103/PhysRev.69.37.

[191] L. Allen and J. H. Eberly. *Optical Resonance and Two-Level Atoms*. Dover, reprint edition, 1987.

[192] C. P. Slichter. *Principles of Magnetic Resonance*. Springer, corrected third edition, 1996.

[193] P. K. Madhu and A. Kumar. Direct Cartesian-Space Solutions of Generalized Bloch Equations in the Rotating Frame. *Journal of Magnetic Resonance*, 114: 201, 1995. doi:10.1006/jmra.1995.1127.

[194] D. M. Pozar. *Microwave Engineering*. Wiley, fourth edition, 2012.

[195] M. A. Pooley. *Components for quantum computing based on optical transitions in single quantum dots*. PhD thesis, University of Cambridge, 2012. http://www.repository.cam.ac.uk/handle/1810/245335.

[196] J. R. Klauder and P. W. Anderson. Spectral Diffusion Decay in Spin Resonance Experiments. *Physical Review*, 125:912, 1962. doi:10.1103/PhysRev.125.912.

[197] R. de Sousa and S. Das Sarma. Theory of nuclear-induced spectral diffusion: Spin decoherence of phosphorus donors in Si and GaAs quantum dots. *Physical Review B*, 68:115322, 2003. doi:10.1103/PhysRevB.68.115322.

[198] M. M. Maricq and J. S. Waugh. NMR in rotating solids. *Journal of Chemical Physics*, 70:3300, 1979. doi:10.1063/1.437915.

[199] E. L. Hahn. Spin Echoes. *Physical Review*, 80:580, 1950. doi:10.1103/PhysRev.80.580.

[200] R. I. Dzhioev and V. L. Korenev. Stabilization of the Electron-Nuclear Spin Orientation in Quantum Dots by the Nuclear Quadrupole Interaction. *Physical Review Letters*, 99:037401, 2007. doi:10.1103/PhysRevLett.99.037401.

[201] M. J. Stanley, C. Matthiesen, J. Hansom, C. Le Gall, C. H. H. Schulte, E. Clarke, and M. Atatüre. Dynamics of a mesoscopic nuclear spin ensemble interacting with an optically driven electron spin. *Physical Review B*, 90: 195305, 2014. doi:10.1103/PhysRevB.90.195305.

[202] A. Schweiger and G. Jeschke. *Principles of Pulse Electron Paramagnetic Resonance*. Oxford University Press, first edition, 2001.

[203] L. Viola and S. Lloyd. Dynamical suppression of decoherence in two-state quantum systems. *Physical Review A*, 58:2733, 1998. doi:10.1103/PhysRevA.58.2733.

[204] L. Cywinski, R. M. Lutchyn, C. P. Nave, and S. Das Sarma. How to enhance dephasing time in superconducting qubits. *Physical Review B*, 77:174509, 2008. doi:10.1103/PhysRevB.77.174509.

[205] A. M. Raitsimring, K. M. Salikhov, B. A. Umanskii, and Y. D. Tsvetkov. Instantaneous diffusion in the electron spin echo of paramagnetic centers stabilized in a solid host. *Soviet Physics Solid State*, 16:492, 1974.

[206] K. M. Salikhov and Y. D. Tsvetkov. Electron Spin-Echo Studies of Spin-Spin Interactions in Solids. In L. Kevan and R. N. Schwartz, editors, *Time Domain Electron Spin Resonance*. John Wiley & Sons, first edition, 1979.

[207] K. M. Salikhov, S. A. Dzuba, and A. M. Raitsimring. The Theory of Electron Spin-Echo Signal Decay Resulting from Dipole-Dipole Interactions between Paramagnetic Centers in Solids. *Journal of Magnetic Resonance*, 42:255, 1981. doi:10.1016/0022-2364(81)90216-X.

[208] V. V. Kurshev, A. M. Raitsimring, and Y. D. Tsvetkov. Selection of Dipolar Interaction by the "2+1" Pulse Train ESE. *Journal of Magnetic Resonance*, 81:441, 1989. doi:10.1016/0022-2364(89)90080-2.

[209] A. M. Tyryshkin, S. Tojo, J. J. L. Morton, H. Riemann, N. V. Abrosimov, P. Becker, H.-J. Pohl, T. Schenkel, M. L. W. Thewalt, K. M. Itoh, and S. A. Lyon. Electron spin coherence exceeding seconds in high-purity silicon. *Nature Materials*, 11:143, 2012. doi:10.1038/nmat3182.

[210] J. S. Waugh, L. M. Huber, and U. Haeberlen. Approach to High-Resolution nmr in Solids. *Physical Review Letters*, 20:180, 1968. doi:10.1103/PhysRevLett.20.180.

[211] W. K. Rhim, D. D. Elleman, and R. W. Vaughan. Enhanced resolution for solid state NMR. *Journal of Chemical Physics*, 58:1772, 1973. doi:10.1063/1.1680944.

[212] P. Mansfield, M. J. Orchard, D. C. Stalker, and K. H. B. Richards. Symmetrized Multipulse Nuclear-Magnetic-Resonance Experiments in Solids: Measurement of the Chemical-Shift Shielding Tensor in Some Compounds. *Physical Review B*, 7:90, 1973. doi:10.1103/PhysRevB.7.90.

[213] R. J. Harrison and P. L. Sagalyn. Trace Relations for Tensors Relating Electric Fields and Elastic Strains to Nuclear Quadrupole Effects. *Physical Review*, 128:163, 1962. doi:10.1103/PhysRev.128.1630.

[214] R. K. Sundfors. Experimental gradient-elastic tensors and chemical bonding in III-V semiconductors. *Physical Review B*, 10:4244, 1974. doi:10.1103/PhysRevB.10.4244.

[215] P. J. Knijn, P. J. M. van Bentum, E. R. H. van Eck, C. Fang, D. L. A. G. Grimminck, R. A. de Groot, R. W. A. Havenith, M. Marsman, W. L. Meerts, G. A. de Wijs, and A. P. M. Kentgens. A solid-state NMR and DFT study of compositional modulations in $Al_xGa_{1-x}As$. *Physical Chemistry Chemical Physics*, 12:11517, 2010. doi:10.1039/C003624B.

[216] I. Kegel, T. H. Metzger, A. Lorke, J. Peisl, J. Stangl, G. Bauer, K. Nordlund, W. V. Schoenfeld, and P. M. Petroff. Determination of strain fields and composition of self-organized quantum dots using x-ray diffraction. *Physical Review B*, 63:035318, 2001. doi:10.1103/PhysRevB.63.035318.

[217] M. Sztucki, T. U. Schülli, T. H. Metzger, E. Beham, D. Schuh, and V. Chamard. Direct determination of strain and composition in InGaAs nanoislands using anomalous grazing incidence x-ray diffraction. *Superlattices and Microstructures*, 36:11, 2004. doi:10.1016/j.spmi.2004.08.025.

[218] M. Ono, G. Sato, J. Ishihara, S. Matsuzaka, Y. Ohno, and H. Ohno. Nuclear spin coherence time in a strained GaAs quantum well. *AIP Conference Proceedings*, 1399:685, 2011. doi:10.1063/1.3666562.

[219] J. Haase and M. S. Conradi. Sensitivity enhancement for NMR of the central transition of quadrupolar nuclei. *Chemical Physics Letters*, 209:287, 1993. doi:10.1016/0009-2614(93)80109-3.

[220] D. Gammon, S. W. Brown, E. S. Snow, T. A. Kennedy, D. S. Katzer, and D. Park. Nuclear Spectroscopy in Single Quantum Dots: Nanoscopic Raman Scattering and Nuclear Magnetic Resonance. *Science*, 277:85, 1997. doi:10.1126/science.277.5322.85.

[221] S. N. Shevchenko, S. Ashhab, and F. Nori. Landau-Zener-Stückelberg interferometry. *Physics Reports*, 492:1, 2010. doi:10.1016/j.physrep.2010.03.002.

[222] N. Bar-Gill, L. M. Pham, C. Belthangady, D. Le Sage, P. Cappellaro, J. R. Maze, M. D. Lukin, A. Yacoby, and R. Walsworth. Suppression of spin-bath dynamics for improved coherence of multi-spin-qubit systems. *Nature Communications*, 3:858, 2012. doi:10.1038/ncomms1856.

[223] E. W. Hansen, X. Gong, and Q. Chen. Compressed Exponential Response Function Arising From a Continuous Distribution of Gaussian Decays - Distribution Characteristics. *Macromolecular Chemistry and Physics*, 214:844, 2013. doi:10.1002/macp.201200715.

[224] J. T. Muhonen, J. P. Dehollain, A. Laucht, F. E. Hudson, R. Kalra, T. Sekiguchi, K. M. Itoh, D. N. Jamieson, J. C. McCallum, Dzurak A. S., and A. Morello. Storing quantum information for 30 seconds in a nanoelectronic device. *Nature Nanotechnology*, 9:986, 2014. doi:10.1038/nnano.2014.211.

[225] G. A. Álvarez, A. Ajoy, X. Peng, and D. Suter. Performance comparison of

dynamical decoupling sequences for a qubit in a rapidly fluctuating spin bath. *Physical Review A*, 82:042306, 2010. doi:10.1103/PhysRevA.82.042306.

[226] H. Y. Carr and E. M. Purcell. Effects of Diffusion on Free Precession in Nuclear Magnetic Resonance Experiments. *Physical Review*, 94:630, 1954. doi:10.1103/PhysRev.94.630.

[227] S. Meiboom and D. Gill. Modified Spin-Echo Method for Measuring Nuclear Relaxation Times. *Review of Scientific Instruments*, 29:688, 1958. doi:10.1063/1.1716296.

[228] V. V. Kurshev and T. Ichikawa. Effect of Spin Flip-Flop on Electron-Spin-Echo Decay Due to Instantaneous Diffusion. *Journal of Magnetic Resonance*, 96:563, 1992. doi:10.1016/0022-2364(92)90341-4.

[229] J. G. Powles and P. Mansfield. Double-pulse nuclear-resonance transients in solids. *Physics Letters*, 2:58, 1962. doi:10.1016/0031-9163(62)90147-6.

[230] U. Haeberlen and J. S. Waugh. Coherent Averaging Effects in Magnetic Resonance. *Physical Review*, 175:453, 1968. doi:10.1103/PhysRev.175.453.

[231] H. Kimura, K. Nakamura, A. Eguchi, H. Sugisawa, K. Deguchi, K. Ebisawa, E. Suzuki, and A. Shoji. Structural study of α-amino-acid crystals by 1H CRAMPS NMR spectroscopy. *Journal of Molecular Structure*, 447:247, 1998. doi:10.1016/S0022-2860(98)00329-9.

[232] T. D. Ladd, D. Maryenko, Y. Yamamoto, E. Abe, and K. M. Itoh. Coherence time of decoupled nuclear spins in silicon. *Physical Review B*, 71:014401, 2005. doi:10.1103/PhysRevB.71.014401.

[233] D. P. Burum and W. K. Rhim. Analysis of multiple pulse NMR in solids. III. *Journal of Chemical Physics*, 71:944, 1979. doi:10.1063/1.438385.

[234] G. A. Álvarez and D. Suter. Measuring the Spectrum of Colored Noise by Dynamical Decoupling. *Physical Review Letters*, 107:230501, 2011. doi:10.1103/PhysRevLett.107.230501.

[235] K. Khodjasteh and D. A. Lidar. Fault-Tolerant Quantum Dynamical Decoupling. *Physical Review Letters*, 95:180501, 2005. doi:10.1103/PhysRevLett.95.180501.

[236] G. S. Uhrig. Keeping a Quantum Bit Alive by Optimized π-Pulse Sequences. *Physical Review Letters*, 98:100504, 2007. doi:10.1103/PhysRevLett.98.100504.

[237] G. S. Uhrig. Exact results on dynamical decoupling by π pulses in quantum information processes. *New Journal of Physics*, 10:083024, 2008. doi:10.1088/1367-2630/10/8/083024.

[238] M. J. Biercuk, H. Uys, A. P. VanDevender, N. Shiga, W. M. Itano, and J. J. Bollinger. Experimental Uhrig dynamical decoupling using trapped ions. *Physical Review A*, 79:062324, 2009. doi:10.1103/PhysRevA.79.062324.

[239] A. Ajoy, G. A. Álvarez, and D. Suter. Optimal pulse spacing for dynamical decoupling in the presence of a purely dephasing spin bath. *Physical Review A*, 83:032303, 2011. doi:10.1103/PhysRevA.83.032303.

[240] N. Bar-Gill, L. M. Pham, A. Jarmola, D. Budker, and R. L. Walsworth. Solid-state electronic spin coherence time approaching one second. *Nature Communications*, 4:1743, 2011. doi:10.1038/ncomms2771.

[241] W. A. B. Evans. On Some Applications of the Magnus Expansion in Nuclear Magnetic Resonance. *Annals of Physics*, 48:72, 1968. doi:10.1016/0003-4916(68)90270-4.

[242] U. Haeberlen. *High Resolution NMR in Solids - Selective Averaging. Supplement I: Advances in Magnetic Resonance*. Academic Press, first edition, 1976.

[243] I. J. Lowe. Free Induction Decays of Rotating Solids. *Physical Review Letters*, 2:285, 1959. doi:10.1103/PhysRevLett.2.285.

[244] W. A. B. Evans and J. G. Powles. A time-dependent Dyson expansion - the nuclear resonance signal in a rotating single crystal. *Proceedings of the Physical Society*, 92:1046, 1967. doi:10.1088/0370-1328/92/4/327.

[245] W. Magnus. On the Exponential Solution of Differential Equations for a Linear Operator. *Communications on Pure and Applied Mathematics*, 7:649, 1954. doi:10.1002/cpa.3160070404.

[246] L. Viola, E. Knill, and S. Lloyd. Dynamical Decoupling of Open Quantum Systems. *Physical Review Letters*, 82:2417, 1998. doi:10.1103/PhysRevLett.82.2417.

[247] S. A. Moiseev and V. A. Skrebnev. Short-cycle pulse sequence for dynamical decoupling of local fields and dipole-dipole interactions. *Physical Review A*, 91:022329, 2015. doi:10.1103/PhysRevA.91.022329.

[248] W. K. Rhim, D. D. Elleman, L. B. Schreiber, and R. W. Vaughan. Analysis of multiple pulse NMR in solids. II. *Journal of Chemical Physics*, 60:4595, 1974. doi:10.1063/1.1680944.

[249] W. K. Rhim, D. D. Elleman, and R. W. Vaughan. Analysis of multiple pulse NMR in solids. *Journal of Chemical Physics*, 59:3740, 1973. doi:10.1063/1.1680545.

[250] R. W. Vaughan, D. D. Elleman, L. M. Stacey, W. K. Rhim, and J. W. Lee. A

Simple, Low Power, Multiple Pulse NMR Spectrometer. *Review of Scientific Instruments*, 43:4356, 1972. doi:10.1063/1.1685924.

[251] S. Nadj-Perge, S. M. Frolov, E. P. A. M. Bakkers, and L. P. Kouwenhoven. Spin-orbit qubit in a semiconductor nanowire. *Nature*, 468:1084, 2010. doi:10.1038/nature09682.

[252] G. de Lange, Z. H. Wang, D. Ristè, V. V. Dobrovitski, and R. Hanson. Universal Dynamical Decoupling of a Single Solid-State Spin from a Spin Bath. *Science*, 330:60, 2010. doi:10.1126/science.1192739.

[253] J. Medford, L. Cywinski, C. Barthel, C. M. Marcus, M. P. Hanson, and A. C. Gossard. Scaling of Dynamical Decoupling for Spin Qubits. *Physical Review Letters*, 108:086802, 2012. doi:10.1103/PhysRevLett.108.086802.

[254] L. Cywinski. Dynamical-decoupling noise spectroscopy at an optimal working point of a qubit. *Physical Review A*, 90:042307, 2014. doi:10.1103/PhysRevA.90.042307.

[255] A. E. Dementyev, D. Li, K. MacLean, and S. E. Barrett. Anomalies in the NMR of silicon: Unexpected spin echoes in a dilute dipolar solid. *Physical Review B*, 68:153302, 2003. doi:10.1103/PhysRevB.68.153302.

[256] S. Watanabe and S. Sasaki. ^{29}Si Nuclear-Spin Decoherence Process Directly Observed by Multiple Spin-Echoes for Pure and Carrier-Less Silicon. *Japanese Journal of Applied Physics*, 42:L1350, 2003. doi:10.1143/JJAP.42.L1350.

[257] M. B. Franzoni and P. R. Levstein. Manifestations of the absence of spin diffusion in multipulse NMR experiments on diluted dipolar solids. *Physical Review B*, 72:235410, 2005. doi:10.1103/PhysRevB.72.235410.

[258] D. Li, A. E. Dementyev, Y. Dong, R. G. Ramos, and S. E. Barrett. Generating

Unexpected Spin Echoes in Dipolar Solids with π Pulses. *Physical Review Letters*, 98:190401, 2007. doi:10.1103/PhysRevLett.98.190401.

[259] C. D. Ridge, L. F. O'Donnell, and J. D. Walls. Long-lived selective spin echoes in dipolar solids under periodic and aperiodic π-pulse trains. *Physical Review B*, 89:024404, 2014. doi:10.1103/PhysRevB.89.024404.

[260] D. Li, Y. Dong, R. G. Ramos, J. D. Murray, K. MacLean, A. E. Dementyev, and S. E. Barrett. Intrinsic origin of spin echoes in dipolar solids generated by strong π pulses. *Physical Review B*, 77:214306, 2008. doi:10.1103/PhysRevB.77.214306.

[261] D. Burstein. Stimulated Echoes: Description, Applications, Practical Hints. *Concepts in Magnetic Resonance*, 8:269, 1996. doi:10.1002/(SICI)1099-0534(1996)8:4<269::AID-CMR3>3.0.CO;2-X.

[262] E. D. Ostroff and J. S. Waugh. Multiple spin echoes and spin locking in solids. *Physical Review Letters*, 16:1097, 1966. doi:10.1103/PhysRevLett.16.1097.

[263] P. Mansfield and D. Ware. Nuclear resonance line narrowing in solids by repeated short pulse r.f. irradiation. *Physics Letters*, 22:133, 1966. doi:10.1016/0031-9163(66)90545-2.

[264] M. H. Levitt and R. Freeman. NMR population inversion using a composite pulse. *Journal of Magnetic Resonance*, 33:473, 1979. doi:10.1016/0022-2364(79)90265-8.

[265] M. H. Levitt and R. Freeman. Compensation for pulse imperfections in NMR spin-echo experiments. *Journal of Magnetic Resonance*, 43:65, 1981. doi:10.1016/0022-2364(81)90082-2.

[266] E. Baudin. Controlling the dipole-dipole interaction using NMR composite rf pulses. *Journal of Chemical Physics*, 141:054202, 2014. doi:10.1063/1.4891481.

[267] M. Garwood and L. DelaBarre. The Return of the Frequency Sweep: Designing Adiabatic Pulses for Contemporary NMR. *Journal of Magnetic Resonance*, 153:155, 2001. doi:10.1006/jmre.2001.2340.

[268] S. Capuani, F. De Luca, L. Marinelli, and B. Maraviglia. Coherence-Transfer Processes by Adiabatic Pulses. *Journal of Magnetic Resonance A*, 121:1, 1996. doi:10.1006/jmra.1996.0129.

[269] J. N. Eckstein, A. I. Ferguson, and T. W. Hänsch. High-Resolution Two-Photon Spectroscopy with Picosecond Light Pulses. *Physical Review Letters*, 40:847, 1978. doi:10.1103/PhysRevLett.40.847.

[270] T. Udem, R. Holzwarth, and T. W. Hänsch. Optical frequency metrology. *Nature*, 416:233, 2002. doi:10.1038/416233a.

[271] A. M. Waeber, M. Hopkinson, I. Farrer, D. A. Ritchie, J. Nilsson, R. M. Stevenson, A. J. Bennett, A. J. Shields, G. Burkard, A. I. Tartakovskii, M. S. Skolnick, and E. A. Chekhovich. Few-second-long correlation times in a quantum dot nuclear spin bath probed by frequency-comb NMR spectroscopy. *Nature Physics*, 12:688, 2016. doi:10.1038/nphys3686.

[272] J. M. Elzerman, R. Hanson, L. H. Willems van Beveren, B. Witkamp, L. M. K. Vandersypen, and L. P. Kouwenhoven. Single-shot read-out of an individual electron spin in a quantum dot. *Nature*, 430:431, 2004. doi:10.1038/nature02693.

[273] C. Barthel, D. J. Reilly, C. M. Marcus, M. P. Hanson, and A. C. Gossard. Rapid Single-Shot Measurement of a Singlet-Triplet Qubit. *Physical Review Letters*, 103:160503, 2009. doi:10.1103/PhysRevLett.103.160503.

[274] V. V. Kurshev and T. Ichikawa. Effect of spin flip-flop on electron-spin-echo decay due to instantaneous diffusion. *Journal of Magnetic Resonance*, 96:563, 1991. doi:10.1016/0022-2364(92)90341-4.

[275] J. H. van Vleck. The Dipolar Broadening of Magnetic Resonance Lines in Crystals. *Physical Review*, 74:1168, 1948. doi:10.1103/PhysRev.74.1168.

[276] G. E. Pake and E. M. Purcell. Line shapes in nuclear paramagnetism. *Physical Review*, 74:1184, 1948. doi:10.1103/PhysRev.74.1184.

[277] R. K. Sundfors. Exchange and Quadrupole Broadening of Nuclear Acoustic Resonance Line Shapes in the III-V Semiconductors. *Physical Review*, 185: 458, 1969. doi:10.1103/PhysRev.185.458.

[278] A. Pines and J. S. Waugh. Quantitative Aspects of Coherent Averaging. Simple Treatment of Resonance Offset Processes in Multiple-Pulse NMR. *Journal of Magnetic Resonance*, 8:354, 1972. doi:10.1016/0022-2364(72)90053-4.